Examining the influence of lineage relationships upon mammalian excitatory neocortical development

Sophie Nixon

Thesis submitted for the degree of Doctor of Philosophy

St Anne's College

University of Oxford

Hilary Term 2017

Abstract

The mammalian neocortex comprises a diverse population of excitatory neurons that perform distinct roles in the neocortical circuit. These neurons are born from a heterogeneous population of progenitor cells during embryonic development and it is increasingly being recognised that individual progenitors can impart specific functional characteristics to their offspring. For example, clonally-related sister neurons in mouse neocortex are biased to form gap junctions with one another early in development, to form synaptic connections with one another as they mature, and to show similar response properties in the adult. This highlights a fundamental role for neuronal lineage in the formation of precise neocortical connectivity. However, the extent to which neuronal phenotype is determined by lineage, and the process by which this arises, is not fully understood. Nor is it known whether similar lineage relationships exist in the human neocortex. Deciphering neocortical lineage relationships has been limited by the techniques available to identify and manipulate clonally-related neurons.

In this thesis I have developed novel molecular tools for the identification and manipulation of clonally-related neurons and refined their use by *in utero* surgery in mice. I first developed a retrovirus encoding Cre recombinase and demonstrated that this can be successfully combined with reporter mice to capitalise on optogenetics for functional studies. In an effort to establish a reliable and unequivocal method of identifying clonally-related neurons, I then constructed a retrovirus encoding genetically-distinct RNA barcodes. I confirmed that the RNA barcode could be reliably retrieved from single neurons and used to determine clonal relationships in mouse neocortex and in an *in vitro* model of human neocortex derived from induced pluripotent stem cells (iPSCs). By comparing the dendritic morphology of barcoded mouse neocortical neurons, I was able to demonstrate that the dendritic arbor of clonally-related neurons is more similar than control neurons derived from different progenitors. This may contribute to specific patterns of synaptic connectivity amongst clonally-related neurons. Within the iPSC system, I demonstrate the utility of the retroviral RNA barcode and revealed that clonally-related human neocortical cells exhibit a higher probability of being gap-junction coupled. These studies advance our understanding of lineage relationships in neocortical excitatory neurons in mouse and provide the first evidence that human neocortical clones exhibit similar functional relationships to those observed in the rodent neocortex.

Acknowledgements

First and foremost I would like to thank my supervisors Professor Colin Akerman and Dr Sarah Newey, for the exceptional support, patience and scientific brilliance they have offered to me throughout my DPhil. Colin and Sarah have shown me a seemingly endless generosity with their time for which I will be forever grateful. I have evolved a clear understanding of the qualities I aspire to develop from Colin and Sarah, and I could not have asked for two more inspirational role models.

I am indebted to Dr Louise Kay for the invaluable mentorship and support she offered to me, that provided me with the knowledge and skills with which to undertake this thesis. I would like to express my gratitude to my collaborators Dr Daniel Lyngholm, Dr Feige Tang, Dr Hania Pavlou, Sophie Avery and Dr Tommas Ellender for the access to data they provided me with in the course of my DPhil. I am privileged to be able to thank my colleagues in the Akerman lab past and present for being such a friendly, intelligent and supportive group of people. I owe particular thanks to Emma Whiteley, Dr Feige Tang, Dr Kashif Mahfooz and Sophie Avery for their warmth and encouragement.

I am grateful to the BBSRC for their generosity in funding the Doctoral Training Partnership that made my DPhil possible. I would like to offer special thanks to Professor Gail Preston for her expertise in developing such a cohesive programme with which to underpin my DPhil.

Finally, I would like to thank the family and friends that supplied me with the grounding and fortification with which to keep going – whether they knew it or not. I owe a particular debt of gratitude to Anne, Kim, Terry and Marjorie for their unwavering belief in me.

Collaborations

Chapter 3

I am grateful to Sophie Avery and Dr Tommas Ellender for giving me access to their surgical records, which I combined into my analysis of mouse *in utero* surgery.

Chapter 4

I would like to thank Dr Daniel Lyngholm and Dr Louise Kay for performing the electrophysiological recordings described in Figure 4.3.

Chapter 5

I am grateful to my collaborators at the Oxford Genomics Centre, at the Wellcome Trust Centre for Human Genetics, who performed the RNA-seq that generated the data for Figure 5.3. I am also indebted to Dr Hania Pavlou who performed the analysis of these RNA-seq data.

Chapter 6

I would like to offer my sincere thanks to Dr Feige Tang for performing the gap junction assay, which generated the data that I describe in Figure 6.5 and Figure 6.6.

Contents

List of Figures

List of Tables

Abbreviations

bp: base pairs
CAG: Cytomegalovirus early enhancer/ chicken β-actin promoter
c.f.u.: colony-forming units
E: Embryonic day
(E)GFP: (enhanced) green fluorescent protein
EPSC: excitatory postsynaptic current
GABA: γ-aminobutyric acid
IPC: intermediate progenitor cell
iPSC: induced pluripotent stem cell
NPC: neural progenitor cell
oRGC: outer radial glial cell
P: postnatal day
p: plasmid
PCR: polymerase chain reaction
rpm: revolutions per minute
RR: relative risk
RT-PCR: reverse-transcription polymerase chain reaction
RV: retrovirus
SNP: short neural precursor cell
SWWTS: static warm-water thermal support
tdTom: tandemTomato
tRGC: truncated radial glial cell
vRGC: ventricular radial glial cell
WPRE: Woodchuck Hepatitis Posttranscriptional Regulatory Element

Chapter 1

General Introduction

1.1 Introduction

The neocortex is responsible for higher-order brain function, such as sensory processing and the generation of motor commands (Hejtmancik et al., 2017; Lodato & Arlotta, 2015). Understanding how neuronal circuits form in the neocortex during development is one of the grand challenges of neuroscience. Extensive efforts have been made to understand the function of the adult neocortex, from the development of Brodmann's map in 1909 to the ongoing human connectome project (Brodmann, 1910; Glasser et al., 2016). However, the fundamental structure on which the function of the adult neocortex is founded is established during development. Deciphering the rules of neocorticogenesis, therefore are likely to provide invaluable insight into the functionality of the mature brain.

The importance of neuronal progenitors in assembling the precise functional circuitry of the adult neocortex is being increasingly recognised (Montiel, Vasistha, Garcia-Moreno, & Molnár, 2016). Heterogeneity in the progenitor population is proposed to give rise to the diverse range of excitatory neuronal subtypes (Florio & Huttner, 2014; Montiel et al., 2016) and understanding the heterogeneity of excitatory neuronal progenitors is an area of active research. Ventricular radial glial cells (vRGCs) were the first excitatory neuronal progenitors to be identified and were proposed to generate the entire population of excitatory neurons in the neocortex (P Malatesta, Hartfuss, & Götz, 2000; Noctor, Flint, Weissman, Dammerman, & Kriegstein, 2001). Subsequently, it has been shown that vRGCs can also give rise to other distinct excitatory neuronal progenitor subtypes, such as intermediate progenitor cells (IPCs), short neural precursors (SNPs) and outer radial glial cells (oRGCs) (Montiel et al., 2016). These subtypes of excitatory neuronal progenitor

are defined by characteristics such as the position of their soma, their morphology and their expression of particular transcription factors (Florio & Huttner, 2014). Different progenitor subtypes have been found to vary in their neurogenic potential and thus their contribution to the adult neuronal population within, and between, species (Montiel et al., 2016). The extent to which progenitors represent discrete subtypes or a continuum is not fully understood (Lodato & Arlotta, 2015).

There are now multiple lines of evidence that excitatory neuronal progenitors influence the functional characteristics of their neuronal progeny. Clonal studies, which investigate individual lineages, have shown that “sister” neurons (originating from the same individual progenitor) within mouse visual cortex exhibit more similar functional properties than non-sister neurons (Li et al., 2012; Ohtsuki et al., 2012). Furthermore, sister neurons have been found to exhibit preferential chemical (synaptic) and electrical (gap-junction mediated) connectivity (Yu et al., 2012; Yu, Bultje, Wang, & Shi, 2009). More generally, IPCs have been shown to produce neurons with electrophysiological properties that are more similar to one another than to neurons derived from other subtypes of progenitor (Tyler, Medalla, Guillamon-Vivancos, Luebke, & Haydar, 2015). Finally, transplantation and fate-mapping studies have indicated that neuronal progenitors provide intrinsic cues to specify the laminar fate of their progeny (Desai & McConnell, 2000; Frantz & McConnell, 1996).

Investigating excitatory neuronal lineages in the neocortex generates a series of technical challenges. The tools available for unbiased, clonal labelling of single lineages can be ambiguous (Mayer, Bandler, & Fishell, 2016) and have focused on visualising the constituent cells. Clonal labelling has not capitalised on the increasing availability of functional molecular tools for investigating neocortical circuitry, such as optogenetics (Baker, Elyada, Parra-Martin, & Bolton, 2016; F. Zhang, Wang, Boyden, & Deisseroth, 2006), or new opportunities provided by single cell transcriptomics (Lake et al., 2016). Furthermore, the delivery of these molecular tools to the developing neocortex is increasingly achieved by *in utero* surgery, the effects of which are not well understood.

Investigating the development of the human neocortex poses yet further challenges. The rodent neocortex has been used extensively as a model for studying the principles of mammalian neocortical development (Montiel et al., 2016). However, there are fundamental differences between the rodent and human neocortex. Perhaps most notable is the convoluted, gyrencephalic nature of the human neocortex, which has expanded over evolution compared to the lissencephalic rodent neocortex (Montiel et al., 2016). The difference in the relative size of the neocortex between rodents and humans is proposed to arise through differences in neuronal progenitors (Fernández, Llinares-Benadero, & Borrell, 2016). There are limitations, therefore, in the rodent model in investigating human neocortical development. The advent of *in vitro* models of human neocorticogenesis using induced pluripotent stem cell (iPSCs) technology provides new opportunities for the developmental neurobiologist.

In this thesis I have developed two retroviral tools for studying excitatory neuronal lineages in the neocortex. Firstly, a retrovirus encoding Cre recombinase (Cre) to capitalise on Cre-lox technology for clonal labelling. Secondly, a retroviral library for RNA-barcoding progenitors with a variable DNA sequence that can be used to unequivocally label clones. I have assessed the effect of using *in utero* surgery to deliver these tools *in vivo* on the health of mice, and produced a refined surgical protocol based on these findings. I have used retroviral RNA-barcoding of progenitors to study unequivocal clones of excitatory neurons and revealed that clonally-related neurons in layer 2/3 of somatosensory cortex have similar dendritic arbors. Furthermore, I have demonstrated that RNA barcoding is compatible with single cell RNA-seq for studying the transcriptome of clones. I have derived human neocortical neurons from iPSCs and used RNA-barcoding retrovirus to study clones *in vitro* to reveal that clonally-related human neocortical cells exhibit preferential gap junction coupling, reminiscent of rodent neocortex.

In this work I contribute to the toolbox for the investigation of neocortical neuronal lineages and refine the surgical procedure used to apply these *in vivo* in mice. I build on a body of literature in mouse that has related neuronal lineage to neuronal function, and I

extend this relationship into a model of the developing human neocortex. In the remainder of this introductory Chapter I will review the literature that has preceded this work and provide a context for the questions that I have addressed experimentally.

1.2 Lineage relationships in excitatory neurons in the developing neocortex

Neocortical circuits are comprised of two main classes of neurons that have distinct origins in the neocortex (Marín & Müller, 2014). The first group comprises glutamatergic excitatory neurons that are generated by progenitors located in the pallium. Neuronal progenitors located at, or near, the ventricular surface generate excitatory neurons that migrate radially to form the lamination characteristic of the adult neocortex (Noctor et al., 2001). The second group comprises GABAergic inhibitory interneurons ('interneurons'), which are believed to originate in the subpallium (Marín & Müller, 2014). Excitatory and inhibitory neurons can be further subdivided into different subtypes (Marín & Müller, 2014). This raises a key question, how do progenitors give rise to different subtypes of excitatory and inhibitory neurons? The focus of this thesis is the development of neocortical excitatory neurons.

The earliest models of excitatory neurogenesis in the mouse proposed a simple schema in which neuroepithelial cells generated a single class of excitatory neurogenic progenitors called radial glia cells (RGCs; Anthony et al., 2004; Malatesta et al., 2003, 2000; Noctor et al., 2001). Excitatory neuronal progenitors have subsequently been found to be heterogeneous (**Figure 1.1**), and this substantiates the hypothesis that progenitor diversity could give rise to neuronal diversity (Florio & Huttner, 2014; Montiel et al., 2016). Progenitor diversity has also been proposed as a mechanism by which neuronal

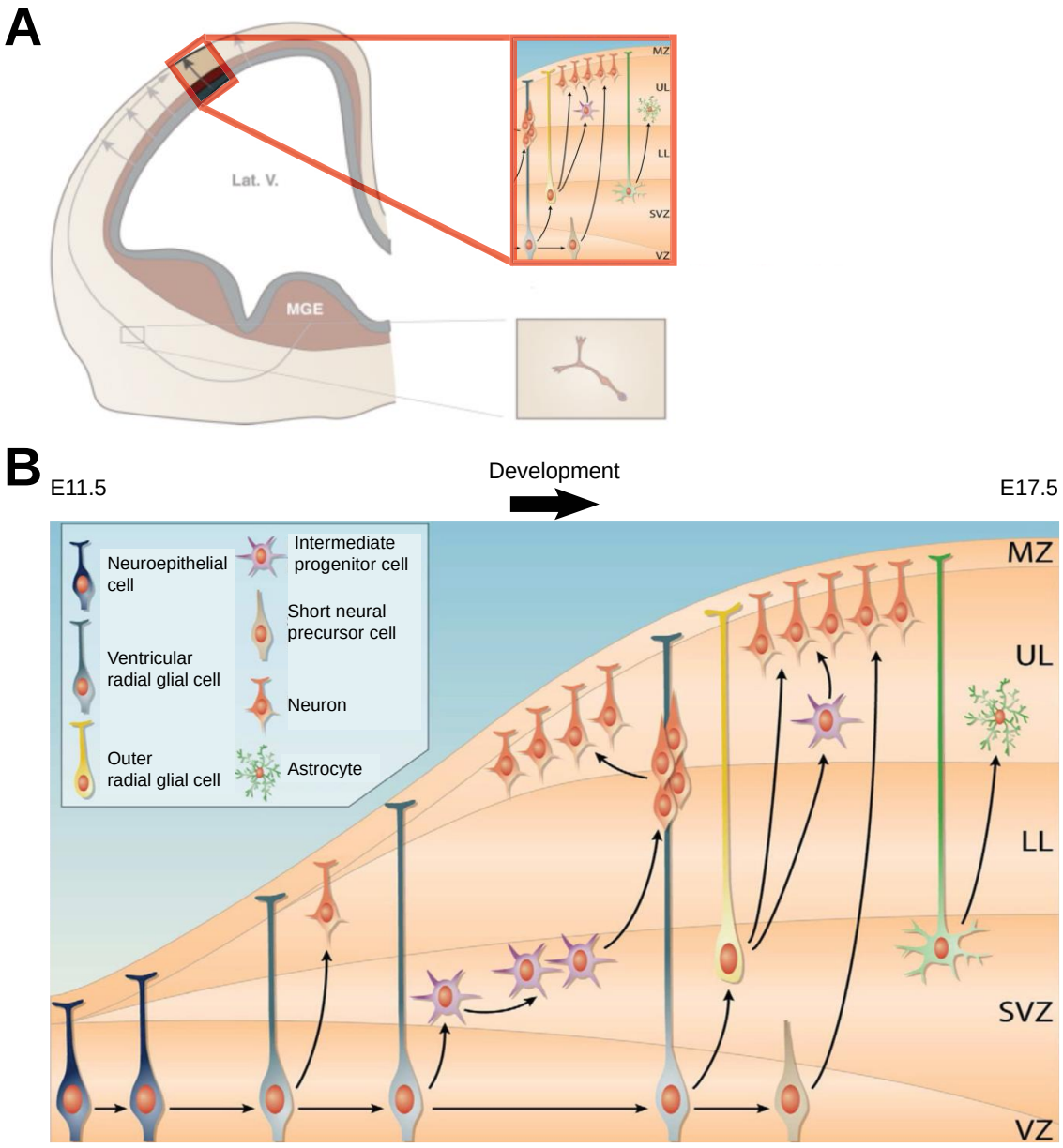

Figure 1.1: Distinct subtypes of excitatory neuronal progenitors give rise to the mammalian neocortex. (**A**) Schematic of a coronal section of one hemisphere from the brain of a mouse at embryonic day 14. In the neocortex (highlighted by the orange box) excitatory neurogenesis occurs in the VZ (dark blue) and SVZ (dark brown) surrounding the lateral ventricles (Lat V.). Neurons migrate radially (short grey arrow) to sequentially generate deep and then superficial neocortical layers. Figure adapted from Jaglin and Chelly, 2009. The inset represents part B of the figure. (**B**) Development is represented from left to right. Neuroepithelial cells divide symmetrically in early development to expand the progenitor pool before generating ventricular radial glial cells (vRGCs). vRGCs can divide asymmetrically to self-renew and generate either neurons or intermediate progenitor cells (IPCs). IPCs divide symmetrically, typically to generate neurons although some may generate further IPCs. Short neural precursor cells are located in the VZ and divide symmetrically to generate neurons. Outer radial glial cells (oRGCs) are located in the SVZ and may self-renew (not shown), generate IPCs or generate neurons. vRGCs and oRGCs can generate astrocytes at the end of neurogenesis. VZ, ventricular zone; SVZ, subventricular zone; LL, lower layers; UL, upper layers; MZ, marginal zone. Figure adapted from Franco and Müller, 2013.

numbers are controlled, since the neurogenic capacity of different subtypes of progenitor has been found to vary (Montiel et al., 2016; Reillo, de Juan Romero, Garcia-Cabezas, & Borrell, 2011).

Neurogenesis in the mouse begins at E9.5 - E10.5 with the transformation of neuroepithelial cells into radial glial cells, which have recently been termed 'ventricular' radial glial cells (vRGCs), to reflect their positioning within the VZ (Tan & Shi, 2013). During early neurogenesis, vRGCs largely divide symmetrically to produce two daughter vRGCs, thereby expanding the progenitor pool (Montiel et al., 2016). From approximately E10.5, vRGCs are believed to make the transition to asymmetric divisions, in which they self-renew and generate either another progenitor subtype or a post-mitotic excitatory neuron (Tan & Shi, 2013). Once born, the neurons migrate to take up their position within the cortical plate in an 'inside-out' fashion, in which the deeper layer neurons are generated before the neurons that reside in more superficial layers. The majority of neurons for layers 6 and layer 5 are generated between approximately E12-E13 in the mouse. And from approximately E14, neurons in layer 4 and layer 2/3 are generated (Toma & Hanashima, 2015). The extent to which heterogeneity in the excitatory neuronal progenitor pool is simply a mechanism by which neuronal numbers are controlled, or by which distinct subtypes of excitatory neurons are produced, is still unclear. In the following section I will review the literature describing the excitatory neuronal progenitor population in mammals and the current evidence for a relationship between neuronal lineage and function.

1.2.1 Distinct subtypes of excitatory neuronal progenitors

Characteristics such as the location, morphology and molecular identity have been well-used to sub-classify excitatory neuronal progenitors have been used for sub-classification

(Hansen et al., 2010; Molyneaux et al., 2015; Noctor et al., 2004; Reillo et al., 2011). The soma of progenitors may be located in the ventricular zone (VZ) or the subventricular zone (SVZ, also referred to as 'abventricular'). The SVZ is significantly more extensive in gyrencephalic than lissencephalic species, reflecting differences in the progenitor population (Montiel et al., 2016). The extensive SVZ in gyrencephalic species is further subdivided into an inner and an outer region, which are differentially populated by excitatory neuronal progenitors (Dehay, Kennedy, & Kosik, 2015; Hansen et al., 2010). Significant spatiotemporal overlap has been observed between distinct progenitor subtypes (García-García, Pino-Barrio, López-Medina, & Martínez-Serrano, 2012; LaMonica, Lui, Hansen, & Kriegstein, 2013; Shitamukai, Konno, & Matsuzaki, 2011; Tyler et al., 2015). In the following subsection I will discuss the distinct subtypes of excitatory neuronal progenitor that have been described in mammals.

Ventricular radial glial cells (vRGCs): multipotent progenitors in the VZ

vRGCs are first generated at approximately embryonic day 9.5 in mouse from neuroepithelial cells (Tan & Shi, 2013). They share considerable similarities with the neuroepithelial cells from which they derive, including apicobasal polarity and a phasic migration of their soma over the course of the cell cycle, known as interkinetic nuclear migration (IKM) (Kriegstein & Alvarez-Buylla, 2009). vRGCs play a multifaceted role in neocortical development. They can give rise to neurons directly, and produce neurons indirectly by generating other subtypes of neuronal progenitor (Martínez-Cerdeño, Noctor, & Kriegstein, 2006; Tyler & Haydar, 2013). They can also give rise to non-neuronal cells such as astrocytes (Voigt, 1989). Furthermore, they provide a scaffold on which nascent neurons migrate (Noctor et al., 2001; Noctor, Martínez-Cerdeño, & Kriegstein, 2008). The soma of vRGCs is located in the VZ, and they possess single apical and basal processes that extend towards the ventricular surface and the pia, respectively (Noctor et al., 2001).

The basal process of human vRGCs has been found to lose contact with the pial surface at midgestation and lose its radial orientation to become orientated tangentially, resulting in the endfoot of the basal process approaching the vasculature at roughly mid-cortical depth (Nowakowski, Pollen, Sandoval-Espinosa, & Kriegstein, 2016). After losing contact with the pial surface, vRGCs are renamed as truncated radial glial cells (tRGCs), and they have been found to differ in their molecular identity from vRGCs (Nowakowski et al., 2016). The function of the divergence of tRGCs from vRGCs is unknown, however it is believed that they continue to play a role in guiding neuronal migration (Nowakowski et al., 2016).

vRGCs undergo three principle types of division, which tend to occur in the following temporal order: symmetric proliferative, asymmetric, and symmetric terminal (Götz & Huttner, 2005; Noctor et al., 2008). The type of division was previously thought to be related to the angle of the mitotic cleavage relative to the ventricular surface, due its effect on the distribution of fate-determinants between daughter cells (Chenn & McConnell, 1995; Haydar, Ang, & Rakic, 2003). However, time-lapse imaging has revealed that the angle of cleavage is more closely related to progenitor subtype, and vRGCs undergo both symmetric and asymmetric divisions with a vertical cleavage plane (Noctor et al., 2008). There is variation in the types of cells that are produced from an asymmetric division of a vRGCs (Montiel et al., 2016). All asymmetric divisions of vRGCs are believed to be self-renewing, however the other daughter may be a neuron or a different subtype of progenitor that amplifies the neuronal output of a vRGC (Gal et al., 2006; Noctor et al., 2004; Tyler & Haydar, 2013; X. Wang, Tsai, LaMonica, & Kriegstein, 2011). The third type of division undertaken by a vRGC is a symmetric terminal division, which may be neurogenic or gliogenic (Götz & Huttner, 2005; Noctor et al., 2008; Voigt, 1989).

Short neural precursors (SNPs): excitatory neuronal progenitors in the VZ

SNPs (also known as apical intermediate progenitor cells) are a subtype of excitatory neuronal progenitors located in the VZ, which are molecularly-defined by their expression of tubulin alpha-1 (Tα1) (Gal et al., 2006; Stancik, Navarro-Quiroga, Sellke, & Haydar, 2010). SNPs are derived from vRGCs and arise later in the neurogenic window than vRGCs, between E13.5 and E16.5 in mouse (Gal et al., 2006). They have a similar bipolar radial morphology to vRGCs, however their basal process tends to be shorter and more variable in length and it is retracted during mitosis (Gal et al., 2006). SNPs can produce intermediate progenitor cells (IPCs, see following subsection), but they mainly produce neurons and therefore their neurogenic potential is lower than vRGCs (Stancik et al., 2010). SNPs tend to produce neurons with a different laminar phenotype than temporally-matched vRGCs, which tend to produce neurons destined for more superficial layers (Stancik et al., 2010). The difference in laminar phenotype is thought to arise due to indirect neurogenesis by vRGCs, resulting in a delayed neuronal birthdate for neurons that are generated via an IPC (Stancik et al., 2010).

Intermediate progenitor cells (IPCs): excitatory neuronal progenitors in the SVZ

IPCs are multipolar progenitors that are found in the SVZ throughout neurogenesis in the neocortex and whose numbers peak around mid-neurogenesis (Noctor et al., 2004). IPCs, like SNPs, are produced from an asymmetric division of a vRGC (or an outer radial glial cell, discussed in the next subsection) and amplify the neuronal output (Haubensak, Attardo, Denk, & Huttner, 2004; Kowalczyk et al., 2009; Noctor et al., 2004). IPCs have been defined by their expression of T-box brain-2 (Tbr2, also known as *Eomes*; Englund et al., 2005). Offspring of IPCs have been found across all neocortical layers and contribute to a substantial proportion of projection neurons (Kowalczyk et al., 2009;

Vasistha et al., 2015). The absence of apicobasal polarity in IPCs is proposed to limit IPCs to symmetric, but not asymmetric, division (Attardo et al., 2008; Noctor et al., 2008). Time lapse studies have shown that the majority of IPCs undergo a single round of mitosis in the SVZ to produce two neurons, but a minority undergo further rounds of self-amplifying divisions before undergoing neuronal differentiation (Haubensak et al., 2004; Noctor et al., 2004, 2008; Vasistha et al., 2015; Wu et al., 2005).

Outer radial glial cells (oRGCs): excitatory neuronal progenitors in the SVZ

oRGCs (also known as basal radial glial cells) are a population of highly proliferative vRGC-like progenitors located in the SVZ (A. Pollen et al., 2015). oRGCs can be defined molecularly by a transcriptional state, but not by the expression of a single gene (A. Pollen et al., 2015). This, in combination with their morphological heterogeneity, can make their identification difficult (Ostrem, Di Lullo, & Kriegstein, 2017). oRGCs are particularly numerous in the outer SVZ (oSVZ) in primates, but they can also be found in small numbers in the SVZ of rodents (Hansen et al., 2010). oRGCs have been found to contribute directly to the development of the oSVZ through the local production of growth factors and potentiation of growth factor signalling (A. Pollen et al., 2015). oRGCs possess a long, basal process that contacts the pial surface, similar to vRGCs, although oRGCs can be either unipolar or bipolar (Betizeau et al., 2013). This polarity depends on their apical process, which is short or absent in humans and of variable length in other species, although it never contacts the ventricular surface (Betizeau et al., 2013; Hansen et al., 2010; LaMonica et al., 2013). oRGCs can occur by direct conversion of a vRGC that delaminates from the ventricular surface, or they can be produced by mitosis of a vRGC (Gertz, Lui, LaMonica, Wang, & Kriegstein, 2014). oRGCs exhibit phasic migration of their soma, called mitotic somal translocation (MST). Interestingly, the direction of MST is highly variable, representing a significant difference from the IKM of vRGCs (Betizeau et

al., 2013; Hansen et al., 2010). Furthermore, the distance undertaken by the somata in MST can correlate with the degree of gyrencephaly, although the significance of this is not known (Ostrem et al., 2017).

The proliferative behaviour of oRGCs is more similar to vRGCs than other progenitor subtypes. oRGCs can divide symmetrically or asymmetrically, self-proliferate, undergo indirect neurogenesis through the production of IPCs, generate neurons directly, and generate glia (Betizeau et al., 2013; Gertz et al., 2014; A. Pollen et al., 2015). oRGCs have been found to give rise to a substantial proportion of layer 2/3 excitatory neurons in humans (Hansen et al., 2010). The proliferative output of oRGCs is highly species-specific (Simone A Fietz et al., 2010; Gertz et al., 2014; Ostrem, Lui, Gertz, & Kriegstein, 2014). In rodents, most divisions are symmetric, terminal and neurogenic (Kosodo et al., 2008; Wu et al., 2005). In both primates and ferrets oRGCs are proliferative - in primates they are primarily neurogenic, whereas in ferrets they are primarily gliogenic (Betizeau et al., 2013; Reillo et al., 2011). oRGCs are proposed to contribute to the massive tangential expansion of upper neocortical layers that produces the gyrencephalic cortex (Hansen et al., 2010; Lukaszewicz et al., 2005; Wang et al., 2011; **Figure 1.2**). A single oRGC can produce hundreds of neurons in humans and complex, divergent lineages have been proposed to arise through multiple rounds of proliferative divisions by oRGCs (Betizeau et al., 2013). Since oRGCs exhibit molecular and morphological heterogeneity, and have a highly divergent qualitative and quantitative cellular output across species, they may represent a group of excitatory neuronal progenitor subtypes, rather than a single subtype.

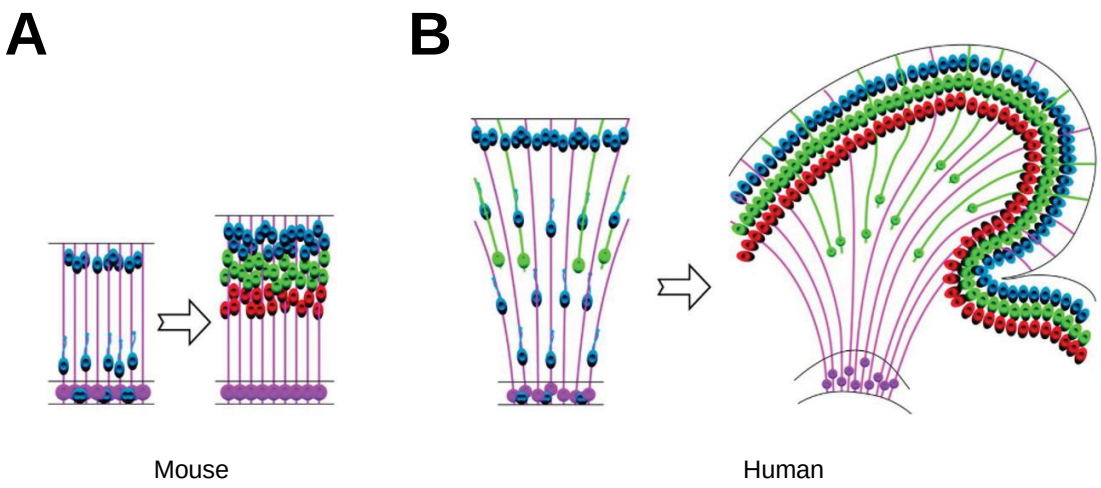

Figure 1.2: The role of oRGCs in the tangential expansion of the neocortex in gyrencephalic species. (**A**) In lissencephalic species such as the mouse the radial fibres of vRGCs (purple; somata located in the VZ at the bottom of the schematic) are parallel to one another. Migrating neurons (blue) follow a predominantly radial migratory path towards the pial surface (top of the schematic). Development is represented from left to right in figure part A and B. (**B**) In gyrencephalic species such as the human, the scaffold of radial fibres can diverge towards the pial surface. Migratory neurons (blue) may therefore be dispersed laterally, resulting in tangential expansion of the upper neocortical layers relative to the lower neocortical layers. oRGCs in the SVZ (green) contribute to the migratory scaffold in the upper neocortical layers. Figure adapted from Reillo et al., 2011.

1.2.2 The relationship between the lineage and function of excitatory neurons in the neocortex

A seminal observation in our understanding of the influence of lineage on neocortical microcircuitry was the observation that clonally-related excitatory neurons, derived from the same individual progenitor, are more likely to form synaptic connections with one another than non-clonally related neurons (Yu et al., 2012, 2009). There is now a growing body of evidence revealing a relationship between the lineage of a neuron and diverse aspects of neocortical function, including the intrinsic electrical properties of a neuron (Tyler et al., 2015) and its stimulus response properties (Li et al., 2012; Ohtsuki et al., 2012; **Figure 1.3**).

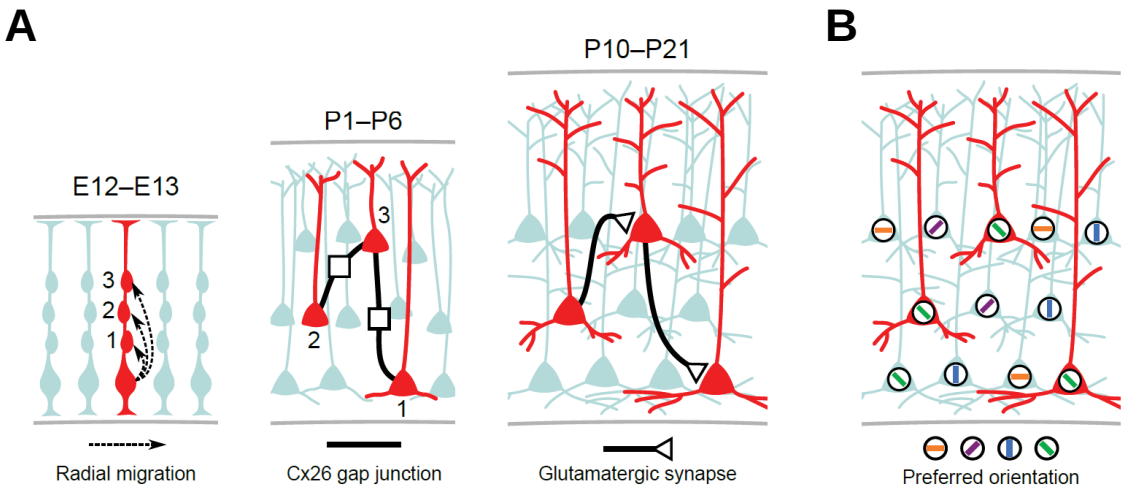

Figure 1.3: The influence of lineage on neuronal function in the neocortex. (**A**) Schematic depicting excitatory neurogenesis in the mouse neocortex (development is represented from left to right; the pial surface is at the top). Clonally-related 'sister' pyramidal neurons in the VZ near the ventricular surface and migrate radially to sequentially form deep and then superficial neocortical layers (**left**). Sister neurons exhibit preferential gap-junction coupling mediated by connexin 26 (Cx26) in the first postnatal week (**centre**; Yu et al., 2012). Sister neurons develop preferential synaptic connections with one another in the later postnatal period (**right**; Yu et al., 2009). (B) Neurons in layer 2/3 of the visual cortex in mouse exhibit more similar stimulus selectivity (Li et al., 2012; Ohtsuki et al., 2012). Figure adapted from Muldal, 2016

Studies of neuronal lineage can be broadly divided into two perspectives. Firstly, the progeny of entire neuronal progenitor subtypes can be examined, or secondly, the neuronal progeny of single progenitor cells (clones) can be investigated. The first strategy, investigating specific progenitor subtypes, can identify general rules governing the phenotype of neurons produced by a particular subtype of progenitor (Tyler et al., 2015). However, this strategy requires that progenitor subtypes are identified *a priori*, which is limited by the depth of our understanding of progenitor diversity and methods of targeting specific progenitor subtypes. The second strategy, investigating the progeny of individual progenitors (clonal studies), can elucidate precise progenitor-neuron relationships which may be distinct from progenitor subtype (Yu et al., 2009). This thesis will focus on the application of clonal studies to investigate neuronal lineage relationships. It is worth noting that the concept of a 'lineage relationship' and a 'clonal relationship' is subjective. Fundamentally, all cells in an animal could be viewed as lineage-related. In the context of

this thesis a lineage relationship constitutes, in its broadest terms, cells that derive from non-stem progenitors that are capable of direct neurogenesis, such as vRGCs, IPCs and SNPs. The term ‘clone’ is used to refer to a specific subset of lineage relationships. These are identified experimentally as the progeny that derive from a single labelled neuronal progenitor and they are therefore defined by the timing of experimental labelling. In the following subsection I will review the existing literature that documents the relationship between neuronal lineage and function.

The role of excitatory neuron lineage in the instruction of circuit assembly in the neocortex

At a general level, the influence of lineage upon neocortical function can be seen in the laminar specification of excitatory neurons (Douglas & Martin, 2004). In the canonical neocortical circuit, excitatory neurons in deep layers (L5 and L6) are primarily responsible for projection to subcortical targets and the contralateral hemisphere, whereas superficial layers predominantly form local intra-cortical connections (Douglas & Martin, 2004; Harris & Shepherd, 2015; K. D. Miller, 2016). There is evidence supporting two different theories by which progenitors can generate neurons with a specific laminar phenotype. The first theory is that the progressive differentiation and fate-restriction of multipotent progenitors leads to the temporal production of specific neuronal subtypes. The second theory is that the neurogenic pool comprises quiescent, *ab ovo* fate-restricted progenitors that are competent to produce a single neuronal subtype, which are activated in the appropriate temporal window. Early studies using recombinant retrovirus to label neuronal lineages supported the progressive fate-restriction hypothesis by demonstrating that there is sequential production of lower and then upper layer neurons within the same lineage (M. B. Luskin, Pearlman, & Sanes, 1988). This was corroborated by transplantation studies, that also demonstrated that neurogenic plasticity of progenitors is unidirectional (Desai & McConnell, 2000; Frantz & McConnell, 1996; Shen et al., 2006). However, other i*n vivo*

fate-mapping and *in vitro* clonal analysis studies have indicated the existence of fate-restricted progenitor pools (Franco et al., 2012). General relationships have also been found between progenitor subtype and neuronal function. For example, IPC-derived layer 2/3 pyramidal neurons have been found to differ from non-IPC derived neurons in their electrophysiological properties (Tyler et al., 2015). Furthermore, IPC-derived and non-IPC derived neurons appear to differ in their dendritic morphology (Tyler et al., 2015). IPC-derived layer 2/3 neurons exhibited significantly lower apical dendritic branching complexity and length than equivalent non-IPC derived neurons (Tyler et al., 2015).

More recent work, particularly from Song-Hai Shi's group, has revealed even more powerful examples of a relationship between neuronal lineage and function. In two related studies, Yu et al. (2009, 2012) demonstrated that clonally-related excitatory neurons (deemed 'sisters') exhibit biased gap-junction coupling in early development, which instructs the formation of preferential synaptic connectivity (Yu et al., 2012, 2009). In these studies, Yu et al. (2009) labelled neocortical clones in mice using low titre injection of replication-incompetent retrovirus at the peak of neurogenesis. Yu et al. (2009) then performed quadruple patch-clamp recording of labelled sister neurons in radially-aligned clones, and adjacent non-labelled control neurons, in brain slices of adult mice. These experiments revealed that sister neurons within radially-aligned clones exhibit preferential, unidirectional synaptic connectivity. Yu et al. (2012) performed follow-up work in young mice to reveal that sister neurons also exhibited preferential electrical coupling, mediated by gap junctions, in the early postnatal period. Yu et al. (2012) suggested that the preferential synaptic connectivity between sister neurons is dependent upon the early communication via gap junctions (Yu et al., 2012). A pair of complementary studies demonstrated that lineage also influences the function of excitatory neurons in layer 2/3 of mouse visual cortex. Ohtsuki et al. (2012) and Li et al. (2012) independently revealed that clonally-related excitatory neurons in layer 2/3 tend to exhibit more similar stimulus selectivity (Li et al., 2012; Ohtsuki et al., 2012). Furthermore, Li et al. (2012) demonstrated that this phenomenon is mediated by gap-junction coupling, corroborating the role of gap

junctions in mediating the relationship between neuronal lineage and function observed by Yu et al. (2009, 2012).

1.3 Techniques for investigating excitatory neuronal lineage relationships in the developing mammalian neocortex

Studies of lineage relationships in mammalian neocorticogenesis can vary in two fundamental ways. Firstly the model system that is used, and secondly the method of clonal labelling. The models of neocorticogenesis and the methods of clonal labelling employed in lineage studies will be discussed in this section.

1.3.1 The mouse is a versatile and accessible model of mammalian neocorticogenesis

The mammalian neocortex has a distinct cytoarchitecture. A common feature across mammals is a basic six-layered structure which forms the basis of the canonical neocortical circuit, plus a distinct areal arrangement resulting from anatomical and functional parcellation (Brodmann, 1910; P Rakic, 1988; Ramon y Cajal, 1909; Rash & Grove, 2006). Mammals broadly share a schema of excitatory neurogenesis in which nascent neurons migrate radially from major sites of excitatory neurogenesis in the VZ and SVZ (Arnold et al., 2008; Cheung et al., 2010; Hansen et al., 2010; Howard et al., 2008; Kolasinski et al., 2013; Kornack & Rakic, 1995; Noctor et al., 2001; Stancik et al., 2010; Tamamaki, Nakamura, Okamoto, & Kaneko, 2001). Considering the broad similarity in excitatory neurogenesis in the neocortex across mammals, the rodent has many advantages over other mammalian species as an experimental model. Advantages of the

rodent model include ease of access, economy, speed of neurodevelopment and experimental versatility (Montiel et al., 2016). Moreover, there has been considerable investment in the generation of transgenic mouse strains for the investigation of neurodevelopment (Madisen et al., 2012; NIH Blueprint, 2011).

There are however significant species differences in neocortical development that limit the extent to which a rodent model can be used to understand other mammalian species, notably the human. Possibly the most remarkable developmental difference between the rodent and human neocortex is the tangential expansion and gyrification of the neocortex in humans. Yet the differences in rodent and human excitatory neurogenesis are qualitative as well as quantitative. For example, the rodent SVZ is primarily composed of IPCs, whereas the primate SVZ is primarily composed of oRGCs (Betizeau et al., 2013; Martínez-Cerdeño et al., 2012; Noctor et al., 2004; Shitamukai et al., 2011; X. Wang et al., 2011). This is reflected by the greater neurogenic contribution from the SVZ in humans than in rodents (Betizeau et al., 2013; Cheung et al., 2010; Hansen et al., 2010; Smart, Dehay, Giroud, Berland, & Kennedy, 2002; Zecevic, Chen, & Filipovic, 2005). Enlargement of the SVZ and the subsequent increase in abventricular neurogenesis has been proposed to bypass potential restrictions placed on neurogenesis that may be imposed by the surface area of the ventricular zone (Hansen et al., 2010). Enlargement of the SVZ is facilitated by the transition from a continuous to a discontinuous radial glial scaffold at midgestation in humans, where vRGCs detach from the pial surface and become tRGCs (Nowakowski et al., 2016). This allows for disproportionate tangential expansion of the supragranular layers, which is believed to occur through the amplification of oRGCs (Nowakowski et al., 2016). The full implications of this divergence from rodent neocorticogenesis is not yet known, but it provides an intriguing example of the difference between the developing rodent and human neocortex. Understanding the differences between these diverse mammalian species is an exciting area of developmental neuroscience.

1.3.2 iPSC technology offers a new perspective on mammalian neocorticogenesis

Recent advances in iPSC technology has the potential to provide unprecedented access to the developing human neocortex for the application of genetic and functional tools to study development. The successful production of functional excitatory neocortical neurons that form synapses *in vitro* has provided some of the most convincing evidence that this model recapitulates excitatory neocorticogenesis (Bardy et al., 2016; Kim et al., 2011; Kirwan et al., 2015; Shi, Kirwan, & Livesey, 2012; Shi, Kirwan, Smith, Robinson, & Livesey, 2012). It has been demonstrated that a diverse population of excitatory neocortical neuronal progenitors that undergo self-organisation analogous to the neural tube *in vivo* can be produced by directed differentiation of iPSCs (Karus, Blaess, & Brüstle, 2014; Kindberg et al., 2014; Mariani et al., 2012). Furthermore, neocortical neuronal progenitors derived from human iPSCs have been reported to exhibit the same temporal progression of neurogenesis that occurs *in vivo*, whereby production of upper layer neurons follows that of lower layer neurons (Camp et al., 2015; Kohwi & Doe, 2013; Shi, Kirwan, & Livesey, 2012). Similarity in the cellular diversity between neocortical cultures derived from iPSCs and human foetal cortex has been confirmed using single cell transcriptome profiling (Camp et al., 2015; Handel et al., 2016). However, although some differences have been noted between neocortical cultures derived from iPSCs and *in vivo* development. For example, iPSC-derived cerebral organoids (3D cultures) have been reported to contain a lower proportion of oRGCs than that found in the developing human neocortex. This could represent incongruence in the state of maturity between the two systems, or an intrinsic underrepresentation of basal progenitors in the current iPSC model (Camp et al., 2015). Further work is required to understand this and other potential differences in iPSC-derived neocortical progenitors, since the extent to which *in vitro* corticogenesis maps onto *in vivo* corticogenesis is not fully characterised.

One important question to ask of the iPSC-derived model of neocorticogenesis is what the implications are of isolating the tissue from the other physiological structures that would normally be present *in vivo.* For example, there is evidence that the neocortical vasculature is important in regulating neocorticogenesis (Javaherian & Kriegstein, 2009; Stubbs et al., 2009). Furthermore, there is an absence of external cortical cues, such as thalamocortical projections, which have been shown to play a role in the regulation of neocorticogenesis (Reillo et al., 2011). Despite these potential limitations of iPSCs, they offer novel opportunities to investigate human neocortical development.

1.3.3 Identification of clones in the neocortex

Successful identification of clones makes certain requirements of the cell labelling method. The principle of clonal labelling is that stable, heritable labelling of a progenitor will reliably demarcate its progeny, and that these can be discriminated from the labelled progeny of other progenitors. Flexibility in the timing of progenitor labelling is necessary to enable the investigation of potential changes over development. Versatile clonal labelling, in the sense that it is compatible with other experimental techniques such as electrophysiology and transcriptomic analysis, is advantageous. There have been many strategies employed for clonal labelling, but each of these faces limitations. For example, some clonal labelling techniques have been criticised for ambiguity in their ability to discriminate between labelled clones (Kirkwood, Price, & Grove, 1992; Mayer et al., 2016; Christopher Walsh & Cepko, 1992), whereas others are associated with a low success rate in the ability to identify the clonal label (Fuentealba et al., 2015; Golden, Fields-Berry, & Cepko, 1995). Errors in identifying clones are referred to as either a ‘lumping’ error, where true non-clones are wrongly defined as clones, or a ‘splitting’ error, where a true clone is defined as non-clonal (Christopher Walsh & Cepko, 1992). Two strategies have

been employed for clonal labelling. Firstly, the identification of clones by geometric analysis of cells labelled in a heritable manner, or secondly identification of clones by a distinct, heritable label that is unique to each clone in a brain. Identification of clones using geometric analysis and distinct labelling will be discussed in the following section. This will be followed by an overview of retroviral vectors, the most common method of delivering clonal labels.

Identification of clones using geometric analysis

The use of geometric analysis for the identification of neocortical clones relies on labelling a small number of progenitors in a single brain with a reporter such as a fluorophore, so that clones can be discriminated by analysing the spatial distribution of labelled cells (M. B. Luskin et al., 1988; Noctor et al., 2001; Price, Turner, & Cepko, 1987). Progenitors can be labelled by direct delivery of a label (such as a replication-incompetent retrovirus) to the developing brain by *in utero* surgery, or through low-frequency recombination in transgenic reporter mice (Espinosa, Tea, & Luo, 2014; Price & Thurlow, 1988). Clones of excitatory or inhibitory neurons can be labelled by these methods (Brown et al., 2011; Gao et al., 2014; Woodruff, Xu, Anderson, & Yuste, 2009; Yu et al., 2009).

There are multiple challenges to the geometric identification of clones. For example, titrating the frequency of labelling events in order to label a single progenitor in a brain is necessary to achieve unequivocal identification of a clone, but achieving this labelling frequency is technically difficult and inefficient (Grove, Kirkwood, & Price, 1992). Yet labelling more than one progenitor per brain may lead to lumping errors (Mayer et al., 2016; Turrero García, Mazzola, & Harwell, 2016). Establishing the labelling frequency that avoids lumping errors is subjective and it relies on preconceived notions about the size and distribution of clones. Furthermore, there is evidence that geometric analysis is

subject to lumping errors even following very low frequency labelling (Ciceri et al., 2013; M. Luskin, Parnavelas, & Barfield, 1993; Mayer et al., 2015).

Comparing the labelling frequency used to identify clones between different studies can be difficult due to variability in the way that this is reported. For example, clonal labelling frequency has been reported as the number of clones (Costa, Bucholz, Schroeder, & Götz, 2009), the total number of labelled cells (C Walsh & Cepko, 1988), the number of clones per mm^2 (Noctor et al., 2001), and the titre of the retrovirus according to titre-testing *in vitro* (M. Luskin et al., 1993). A clonal labelling frequency ranging from 10^3 to 10^7 infectious retroviral particles per rodent embryo has been reported, which either reflects four orders of magnitude differences in the interpretation of clonal labelling, or differences in the methods used to establish the titre of retrovirus (M. Luskin et al., 1993; Maria C. Mione, Cavanagh, Harris, & Parnavelas, 1997; Noctor et al., 2001, 2004; Price & Thurlow, 1988).

Establishing the specific spatial criteria used to define clones is another area of subjectivity in the geometric identification of clones. The lateral distance between labelled cells (parallel to the pia) has been relied on to identify clones using geometric analysis in the literature and is based on the assumption that clones of excitatory neurons are predominantly radially arranged (Li et al., 2012; Ohtsuki et al., 2012; Yu et al., 2009). A limit on the maximum lateral spread ranging from 120 μm to 1 mm has been reported (Li et al., 2012; Yu et al., 2009). Some studies have also used a restriction on the proximity of a putative clone, to other labelled cells that are not included in the putative clone (M. Luskin et al., 1993). Clones have been found to disperse over 500 μm laterally, and even up to 1 mm when relying upon geometric methods (Gao et al., 2014; Ohtsuki et al., 2012; Yu et al., 2009).

Ideally, the criteria employed for geometric identification of clones would be based on exhaustive understanding of the migratory patterns of excitatory neurons. Unequivocal characterisation of excitatory neuronal migration patterns can be provided by time-lapse imaging (Noctor et al., 2004), but these studies are restricted to relatively short time-

course experiments *in vitro*. Other methods of identifying the migration of clones have relied on clonal labelling, rendering this a circular argument (Kornack & Rakic, 1995; M. B. Luskin et al., 1988; Maria C. Mione et al., 1997; Noctor et al., 2001; Ohtsuki et al., 2012; Price & Thurlow, 1988). Reliance on geometric identification of clones may, therefore, have biased the investigation of lineages to a subset that conform to the expectation that excitatory neuronal clones are dispersed radially in the neocortex. Nevertheless, important inferences have been made about the behaviour of clones identified by geometric analysis (Li et al., 2012; Yu et al., 2012, 2009).

Identification of clones with a distinct label

Labelling a progenitor with a distinct, heritable, label that is unique in a single brain is a way of ensuring that clonally-related cells can be identified, regardless of their spatial distribution (Golden et al., 1995; Jefferis & Livet, 2012). The probability that a progenitor is labelled by a particular label, therefore, should be low enough to render two progenitors in a brain unlikely to receive the same label by chance (Golden et al., 1995). This depends on having a sufficiently large pool of distinct labels relative to the number of clones that are labelled in a single brain, and it is affected by the relative frequency of each label in the actual pool of labels ('library') that is delivered to the brain. The quantity of distinct labels in the library is often referred to as the 'complexity'. Combinatorics has been used to generate distinct labels composed of either variable DNA sequences (often referred to as barcodes) or multiple fluorophores (Golden et al., 1995; Jefferis & Livet, 2012). Occasionally, DNA barcoding and combinatorial fluorophore labelling have been used in tandem (Beier, Samson, Matsuda, & Cepko, 2011; Cornils et al., 2014). In the following paragraphs I will review the literature on DNA barcoding and combinatorial fluorophore labelling, in turn.

Clonal labelling in the neocortex using DNA barcodes was pioneered by Cepko and colleagues (Christopher Walsh & Cepko, 1992). Cepko and colleagues (1992) developed a library of retroviral vectors carrying a short, variable DNA sequence to label progenitors in the developing brain. The barcode was retrieved from labelled neurons in tissue fragments by PCR amplification and identified based on the size and restriction digest pattern (Christopher Walsh & Cepko, 1992). The design of the initial DNA barcode developed by Cepko and colleagues generated a library complexity of around 80 different labels (Christopher Walsh & Cepko, 1992). This relatively low complexity placed limits on the labelling frequency that could be used, and the barcode design faced potential caveats such as biases that may be associated with variability in the length of the barcode sequence (Kirkwood et al., 1992; Christopher Walsh & Cepko, 1992). Cepko and colleagues subsequently improved the barcode design to consist of a variable DNA sequence of uniform length, identified by DNA sequencing, which is still in use today (Golden et al., 1995; Harwell et al., 2015; Mayer et al., 2015). The improved DNA barcode yielded a library complexity of around 10^4 - 10^5 distinct barcodes of approximately equal representation, enabling a high confidence in identifying clones (Golden et al., 1995; Harwell et al., 2015; Mayer et al., 2015). The improved barcode library designed by Cepko and colleagues has been used to identify interneuron lineages that undergo significant tangential migration, demonstrating its ability to identify clones regardless of their pattern of migration (Harwell et al., 2015; Mayer et al., 2015, 2016). Furthermore, the sensitivity of DNA barcoding has revealed lumping errors in geometrically-identified clones (Mayer et al., 2015; McCarthy, Turnbull, Walsh, & Fishell, 2001; Turrero García et al., 2016; C. Walsh & Cepko, 1993).

DNA barcoding, however, is subject to technical challenges. For example, a persistently high failure rate in retrieving the DNA barcode from single neurons of around 50 % has pervaded since its inception (Fuentealba et al., 2015; Golden et al., 1995; Harwell et al., 2015). Production of a retroviral DNA barcode library is a multi-step process that may result in cumulative library biases and loss of complexity. This may compromise

the expectation that neurons carrying the same barcode are clones (Golden et al., 1995; Kirkwood et al., 1992; C Walsh & Reid, 1995). Furthermore, the necessity to harvest cells for PCR amplification of the barcode limits the amount of further analysis that can be performed. Although progress has been directed towards lineage tracing using DNA labels, these refined techniques have not yet been advanced for use in mammals (McKenna et al., 2016; Peikon, Gizatullina, & Zador, 2014)

Combinatorial fluorophore expression can generate distinct labels that can be used to identify clones (García-Moreno, Vasistha, Begbie, & Molnár, 2014; Jefferis & Livet, 2012). The number of distinct labels that can be generated is limited by the ability to resolve individual fluorophores (Cai, Cohen, Luo, Lichtman, & Sanes, 2013; García-Moreno et al., 2014; Loulier et al., 2014). Subcellular targeting of fluorophores has been employed to increase the number of distinct labels (García-Moreno et al., 2014; Loulier et al., 2014). The intensity of fluorophore expression has also been used in some studies to further discriminate distinct labels (Figueres-Oñate, García-Marqués, & López-Mascaraque, 2016). Nevertheless, combinatorial fluorophore labelling has been predominantly limited to around 100 distinct labels at most (Cai et al., 2013; Jefferis & Livet, 2012). Clonal labelling using a distinct fluorophore label has tended to rely on stochastic, Cre-mediated expression of a subset of fluorophores by progenitors, often based on the Brainbow constructs, in a heritable manner (Cai et al., 2013; García-Moreno et al., 2014; Jefferis & Livet, 2012; Loulier et al., 2014). This has been achieved by acute delivery of constructs *in vivo* that are integrated into the genome of a progenitor, and by using transgenic mice encoding multiple fluorophores (García-Moreno et al., 2014; Jefferis & Livet, 2012). Combinatorial fluorophore labelling can be technically demanding. For example, the CLoNe method pioneered by García-Moreno et al. (2014) involves the electroporation of a cocktail of twelve floxed-STOP labelling vectors, each carrying one of four fluorophores and one of three subcellular localisation signals, a cell-type targeted Cre recombinase, and a transposase (García-Moreno et al., 2014). Lumping errors may occur if the mixture contains too much, or too little, fluorophore. Too little fluorophore and most

labels will comprise one or two fluorophores, too much fluorophore and most labels will comprise all fluorophores. Splitting errors may occur if a progenitor underwent mitosis before transposase-mediated integration of fluorophores into the genome had occurred, due to division of non-integrated transgenes between daughter cells. Furthermore, since techniques used to deliver fluorophores acutely tend to result in a high labelling frequency, identifying the fluorophore label of an individual cell may be complicated by surrounding labelled cells (Mishchenko, 2010).

The use of retroviral vectors to deliver clonal labels

Replication-incompetent retroviral vectors (referred to simply as 'retroviral vectors' in this thesis) have been used to deliver simple labels for the identification of neocortical clones by geometric analysis, and to deliver DNA barcodes (Price et al., 1987; Christopher Walsh & Cepko, 1992). Retroviral vectors can only transduce mitotic cells (D. G. Miller, Adam, & Miller, 1990; Roe, Reynolds, Yu, & Brown, 1993). RNA contained in the retroviral vector is transcribed and integrated into the genome of a daughter cell, resulting in heritable labelling (D. G. Miller et al., 1990; Roe et al., 1993). These factors render retroviral vectors highly suited to clonal labelling. Neocortical clones are labelled by the injection of retrovirus into the ventricles of the developing brain in order to transduce mitotic progenitors near the ventricular surface (Cepko et al., 1998).

The use of retroviral vectors for clonal labelling relies on a set of assumptions about their behaviour, which have not been thoroughly tested. For instance, it has been speculated that the aggregation of retroviral virions could result in infection of adjacent progenitors, resulting in lumping errors in the geometric identification of clones (Fields-Berry, Halliday, & Cepko, 1992). The use of retroviral vectors to deliver DNA barcodes for clonal studies has been based on the assumption that only one barcode is packaged into each virion and that a progenitor is transduced by a single virion. However, there is

evidence that this might not always be the case (Eckwahl, Sim, Smith, Telesnitsky, & Wolin, 2015; Garcia et al., 2009; Onafuwa-Nuga, King, & Telesnitsky, 2005; Rulli et al., 2007).

Limitations in retroviral labelling of clones have hampered the investigation of lineage relationships. Retroviral silencing may result in a failure to identify some neurons that comprise a clone (Gal et al., 2006; Mayer et al., 2015). Low, and variable, expression levels that result from insertion of a single transgene at a random location in the genome can hinder the morphological identification of labelled neurons (Cepko et al., 1998; Golden et al., 1995). This also poses an obstacle to the use of retroviral vectors to deliver functional tools, such as optogenetics (Baker et al., 2016; F. Zhang et al., 2006), for studying the influence of clonal relationships on synaptic connectivity.

1.4 *In utero* surgery provides access to the developing brain

The use of retroviral vectors for clonal labelling in the neocortex relies on the ability to deliver retrovirus to the developing brain *in vivo*. Access to the developing brain is provided by *in utero* surgery, which allows retrovirus to be delivered into the fluid-filled ventricles of the embryonic brain, adjacent to the proliferative VZ of the neocortex (Price & Thurlow, 1988). *In utero* surgery can be used to deliver other molecular tools to facilitate diverse genetic manipulations and even multiple manipulations in parallel (García-Moreno et al., 2014; Saito & Nakatsuji, 2001; Telley et al., 2016). Recently, *in utero* surgery has been used to deliver a CRISPR/ Cas9-based tool to knock-in genes in the developing brain, highlighting the versatility that it offers (Tsunekawa et al., 2016). *In utero* surgery enables genetic manipulation to be achieved rapidly and with good spatiotemporal resolution, without the costly and laborious generation of transgenic mouse lines (Saito,

2006; Saito & Nakatsuji, 2001). It represents, therefore, a powerful technique in developmental biology.

Despite the number of studies reliant on *in utero* surgery in the literature, the surgical procedure itself has rarely been studied and there is considerable variability in the surgical methods that are reported (Pierfelice & Gaiano, 2010; Punzo & Cepko, 2008; Szczurkowska et al., 2016). However, there is a shortage of information on which to develop a best-practice, evidence-based surgical protocol, which represents a missed opportunity to refine the procedure. *In utero* surgery has the potential to disrupt developmental processed and introduce experimental variability, yet the adverse effects of this procedure on the dam and offspring are not well characterised. Consequently, it is difficult to appreciate the extent to which *in utero* surgery affects the health of surgical animals. In this thesis I will characterise the morbidity and mortality of the pregnant female mouse (dam) and her embryos between surgery and littering. In the following section, I will review the current literature on *in utero* surgery in mice.

1.4.1 Adverse effects of *in utero* surgery

In utero surgery involves an incision through the abdominal wall (referred to as a 'laparotomy'), usually through the midline in rodents, in order to gain access to the abdominal cavity and to exteriorise the uterus (Hau & Van Hoosier, 2003). Laparotomy is an invasive procedure that carries a risk of severe adverse events (Bajwa & Bajwa, 2013; Hau & Van Hoosier, 2003; Xing, Culbertson, Wen, & Franz, 2013). Punzo et al. (2008) report a strain-dependent mortality rate of up to 20 % for the dam following *in utero* surgery in mice (Punzo & Cepko, 2008). Notably, the experience of the surgeon in that study was inversely correlated with the mortality rate of the dam (Punzo & Cepko, 2008). The causes of deaths were not reported, but the correlation with surgeon experience suggests that

the mortality rate could be minimised by identifying and correcting the technical aspects of the surgery (Punzo & Cepko, 2008).

In utero surgery has been shown to cause embryonic death via inflammatory disruption of maternal immune tolerance to the developing embryos, which is essential for the maintenance of pregnancy (Krzymowski & Stefańczyk-Krzymowska, 2012; Wegorzewska et al., 2014). Wegorzewska et al. (2014) examined embryonic death (resorption) following *in utero* surgery and injection of sterile phosphate-buffered saline at midgestation (Wegorzewska et al., 2014). The authors revealed that this procedure increased embryonic resorption from 3 % to 34 %, and discovered that this arose through an inflammatory immune response in the uterus of the dam (Wegorzewska et al., 2014). Interestingly, the rate of resorption was greater in litters produced from crosses of different mouse strains, than for litters produced from crosses of the same mouse strain (Wegorzewska et al., 2014). The authors interpret this as evidence of a disruption to maternal immunotolerance in the aetiology of embryonic death (Wegorzewska et al., 2014). Other studies have reported a birth rate ranging from 60 % – 90 % of embryos that were alive at the time of surgery (Punzo & Cepko, 2008; Saito, 2006; Shimogori & Ogawa, 2008). However, these studies have not established the baseline incidence of embryonic death, meaning that the rates cannot be directly attributed to *in utero* surgery. Furthermore, Punzo et al. (2008) revealed a correlation between embryonic survival and the age of embryos at the time of surgery, with later surgery associated with a lower birth rate (Punzo & Cepko, 2008).

Reports of adverse effects following *in utero* surgery in rodents is sparse in the literature. Unsurprisingly, there is evidence for pain following laparotomy in mice, indicated by behavioural and physiological measures, lasting up to three days following surgery (Arras et al., 2007; Jirkof et al., 2010). The severity of the pain response is reduced by the provision of analgesia in the post-operative period (Arras et al., 2007; Jirkof et al., 2010). Secondary septic peritonitis is a serious complication of abdominal surgery that is occasionally reported to result from poor aseptic technique following laparotomy in

humans (Holzheimer, Muhrer, L'Allemand, Schmidt, & Hennecking, 1991; Simmen, Heinzelmann, & Largiadèr, 2008). Septic peritonitis following *in utero* surgery in rodents has not been reported in the literature. However, there is evidence for poor aseptic technique in the literature (Dixit et al., 2011; Haddad-Tóvolli, Szabó, Zhou, & Alvarez-Bolado, 2013; Itah, Gitelman, Tal, & Davis, 2004; Pierfelice & Gaiano, 2010). For example, sterile surgical drapes are often absent or poorly implemented, and removed before wound closure (Ge, 2012; Itah et al., 2004; Pierfelice & Gaiano, 2010; Walantus, Castaneda, Elias, & Kriegstein, 2007). This results in the suture material contacting the animal's fur, predisposing the animal to septic peritonitis, wound dehiscence and surgical site infection (Riou, Cohen, & Johnson, 1992; Simmen et al., 2008). Furthermore, experimental models of maternal inflammation, which could arise through poor aseptic technique, have been shown to perturb neurodevelopment (Smith, Li, Garbett, Mirnics, & Patterson, 2007; Helen B Stolp et al., 2011). Whether or not poor asepsis during surgery affects neurodevelopment is not known.

A predisposition for rodents to undergo dehiscence of the laparotomy wound due to self-removal of sutures is often reported anecdotally in the literature (Dixit et al., 2011; Szczurkowska et al., 2016). 'Tight' suture placement has been recommended in the literature to discourage self-removal of sutures by rodents (Dixit et al., 2011; Szczurkowska et al., 2016), despite a considerable body of evidence that this practice is painful and detrimental to wound healing (Diener, Voss, Jensen, Büchler, & Seiler, 2010; J Höer et al., 2002; Jörg Höer, Klinge, Schachtrupp, Töns, & Schumpelick, 2001; Sagi, Papp, & DiPasquale, 2008; Zografos, Martis, Morris, & Anonymous, 1992). However, laparotomy wound dehiscence in rodents has not been investigated in the literature. This aspect of *in utero* surgery therefore represents another point for potential refinement.

1.5 The aims of this thesis

The experimental aims of this thesis are fourfold:

- In Chapter 3, I will characterise the baseline incidence of morbidity and mortality in mice following *in utero* surgery. I will then investigate refinements to the surgical methodology and use these data to develop an improved protocol for *in utero* surgery in mice.
- In Chapter 4, I will develop two novel retroviral tools for clonal labelling in the developing neocortex. The aim of the first tool is to increase the reliability and versatility of clonal labelling using retroviral vectors. The aim of the second tool is to develop a method of unequivocally identifying clonally-related cells using an RNA barcode.
- In Chapter 5, I will use the refined *in utero* surgery (Chapter 3), in order to apply my novel clonal-labelling tool (Chapter 4) to the developing brain of mice. I will use my RNA-barcoding retrovirus to unequivocally identify clones and thereby investigate the influence of clonality on the dendritic morphology of excitatory pyramidal neurons.
- In Chapter 6, I will apply my RNA-barcoding retrovirus (Chapter 4) to an in vitro model of the developing human neocortex derived from iPSCs. I will examine whether clonally-related neurons exhibit a tendency to form preferential gap junction coupling, reminiscent of observations made in mouse neocortex.

Chapter 2

Materials and Methods

Materials

2.1 Animals

C57BL/6J mice were purchased from Charles River Laboratories. Ai9 reporter mice (B6.Cg-Gt(ROSA)26SOR$^{tm9(CAG-tdTomato)HZE}$/J) were bred in-house from stocks available from the Jackson Laboratory as stock number 007909. Floxed-STOP P_2X_2-ATP receptor mice were generated in the laboratory of Professor Gero Miesenböck and provided by Professor Simon Butt, Department of Physiology, Anatomy and Genetics, University of Oxford (Anastasiades et al., 2016).

2.2 Buffers, solutions and cell culture media

All chemicals used were purchased from Sigma-Aldrich unless otherwise stated. Lennox LB and Lennox LB-Agar were purchased from Invitrogen. All cell culture media, supplements, reagents and foetal calf serum were from Life Technologies unless otherwise stated. All solutions and media were made up in deionised (dH_2O) and autoclaved or filter sterilised where necessary.

2.3 Molecular Biology Reagents

All restriction enzymes and modifying enzymes were purchased from New England Biolabs. The source of other reagents used is listed in the relevant sections of this chapter.

2.4 Plasmid vectors

The following vectors were sourced as follows (Table 2.1):

Vector	Generates virus	Source	Reference
CAG-GFP	RV-GFP	CAG-GFP was a gift from Fred Gage (Addgene plasmid # 16664). See **Figure 2.1.**	**Zhao et al., 2006**
paavCAG-iCre	Not generated	paavCAG-iCre was a gift from Jinhyun Kim (Addgene plasmid # 51904)	Druckmann et al., 2014
pVSV-G.	Encodes the retroviral envelope protein VSV-G. Used to generate all retroviruses	Takara Bio Europe as Part of the Retro-X Universal Packaging System.	
pEYFP-C1	Not applicable	Clontech	
CAG-tdTom	RV-tdTom	CAG-tdTom was a gift from Dr Louise Kay, Akerman Group, Department of Pharmacology, University of Oxford. See **Figure 2.2**.	

The following vectors were generated in the course of this thesis (Table 2.2):

Vector	Generates Virus	Notes
pRV-iCre	RV-iCre	GFP replaced by iCre in CAG-GFP. See section 2.8.2 and **Figure 2.1**.
pRV-tdTom-barcode library	RV-tdTom-barcode	Insertion of a pool of double-stranded oligonucleotides downstream of tdTom in vector CAG-GFP. See Section 2.8.3, **Figure 2.2** and **Figure 4.5.**

2.5 Oligonucleotides

The oligonucleotides used in this thesis were generated by Sigma-Genosys (Table 2.3).

	Forward (5' – 3')	**Reverse (5' – 3')**
MCS1	GCGGGATCCTGCTCCGGACTCAGATCTCGA	AACAACCGGTGCTACCCGGGCCCGCGGTAC
MCS2	CCTAGGAAGCTTACGCGTGCGGCCGCTTAATTAAGCATGC	GCATGCTTAATTAAGCGGCCGCACGCGTAAGCTTCCTAGG
iCre	GAGCCGTCCGGATGACTGATTGATGCCACCATGGTGCCCAAGAAGA	CTCCCGCCTAGGTCAGTCCCCATCCTCGAGCA
tdTom	CATGTAGCACCGGTCGTCATGGTGAGCAAGGGCGAG	GGCCGCGCGGGTTTAAACGAGACCTACAGGAACAGGTGGT
Barcode	CTAGGAAGTAANNATCNNGATSSAAANNGGTNNAACNNTGTAAAACGACGGCCAGTGAA	CGCGTTCACTGGCCGTCGTTTTACANNGTTNNACCNNTTTSSATCNNGATNNTTACTTC
Barcode 1	GAGCTGTACAAGTAAGTCTCG	CCATACGGGAAGCAATAGCAT
Barcode 2	None	GGCATTAAAGCAGCGTATCC

2.6 Mammalian cell lines

GP2-293 is a HEK 293-based retroviral packaging cell line supplied by Takara Bio Europe as part of the Retro-X Universal Packaging System. NIH-3T3 cells were obtained from European Collection of Authenticated Cell Cultures (ECACC). The human induced pluripotent stem cell (iPSC) line SFC180-01-01 was obtained from StemBANCC's (http://stembancc.org/; Morrison et al., 2015) Birmingham Repository for iPSCs. SFC180-01-01 was derived from patient 180, a 60 year old female with no history of mental health problems, diabetes or migraine.

Methods

2.7. *In utero* surgery and acute cortical slice preparation

2.7.1 Animals

All experiments were approved by the University of Oxford Animal Welfare and Ethical Review Board under Home Office licence in accordance with the Animals (Scientific Procedures) Act 1986, UK. The University of Oxford guidelines for the care and use of animals in research were followed. All animal experiments were performed using C57BL/6J mice unless otherwise stated.

2.7.2 Protocol for *in utero* surgery

A detailed surgical protocol including all refinements is available in Appendix 1. In brief, midday on the day that the vaginal plug was observed was considered to be embryonic day 0.5 (E0.5) and the day of birth postnatal day 0 (P0). Timed-pregnant dams were induced and maintained under anaesthesia with isofluorane (Zoetis) and prepared for midline laparotomy. The uterus was exteriorised and a volume either retrovirus, plasmid DNA or 10mM carboxyfluorescein succinimidyl ester [(CellTrace CFSE, Life Technologies) alone or in a 50:50 ratio with CytoTell Blue (Stratech Scientific)], each with 0.05 % v/v fast-green dye (Sigma-Aldrich), was introduced into the left ventricle of the embryo with a pulled glass micropipette using a Picospritzer (General Valve Company) with visual confirmation of placement. The total volume injected per pup was ~ 1 µl.

For the electroporation only, Tα1-Cre and CβA-FLEx constructs were injected as a 1:1 ratio of plasmid DNA (each 3 µg/µl, so final concentration of both constructs was 1.5 µg/µl). The anode of a Tweezertrode (Genetronics) was placed over the dorsal telencephalon outside the uterine muscle. Five pulses (50 ms duration separated by 950

ms) at 42V (at E14.5 and E15.5), 40V (at E13.5) and 38V (at E12.5) with a BTX ECM 830 pulse generator (Genetronics).

After completion of all intraventricular injections the uterus was lavaged with warmed, sterile Hartmann's solution (Dechra Pharmaceuticals) and replaced into the abdomen. The abdominal incision was closed in two layers. Mice were recovered from anaesthesia and allowed to litter down naturally. Pre- and post-operative analgesia was provided as documented in Chapter 3, Figure 3.5 B.

2.7.3 Acute cortical slice preparation

Postnatal mice were deeply anaesthetised with isofluorane (Zoetis) and killed by cervical dislocation. Brains were rapidly dissected on ice and placed in an ice cold solution of cutting artificial cerebrospinal fluid (cutting ACSF; 1 mM $CaCl_2$, 5 mM $MgCl_2$, 4 mM KCl, 26 mM $NaHCO_3$, 8 % w/v D-sucrose) bubbled with 95 % oxygen, 5 % carbon dioxide. Brains were sliced coronally (250μm) using a vibratome (Microm HM 650V, Thermo Scientific). Slices were placed in room-temperature ACSF (24 mM NaCl, 2.5 mM KCl, 1.25 mM KH_2PO_4, 26 mM $NaHCO_3$, 2 mM $MgSO_4$, 2.5 mM $CaCl_2$, 10 mM D-glucose, and 4 mM D-sucrose) bubbled with 95 % oxygen, 5 % carbon dioxide and protected from light.

2.8 Construction of retroviral expression vectors (Table 2.2)

2.8.1 Standard conditions for DNA subcloning

The following standard sub-cloning reaction conditions were used unless otherwise stated:

• PCR amplification of target DNA for sub-cloning was performed using a high-fidelity polymerase (Phusion High-Fidelity DNA Polymerase, New England BioLabs) according to the manufacturer's protocol.

• Restriction Digests of plasmid vectors and PCR products were performed using 500ng-10ug purified DNA in a total reaction volume of 50ul according to the recommended protocol (New England Biolabs). Double digests were performed sequentially with the DNA from the first enzyme digest purified using the QIAquick PCR Cleanup Kit (Qiagen) or QIAquick Gel Extraction Kit (Qiagen) prior to the second restriction digest.

• Restriction digests and PCR products were visualized by agarose gel electrophoresis using horizontal slab gels. Samples were separated on 1-2 %(w/v) agarose in 1x TAE (40mM Tris acetate, 1mM EDTA) with 0.1□g/ml ethidium bromide (Invitrogen) at 80-120V. DNA fragments, along with a 1kb DNA ladder (Invitrogen) were visualised on an ultra-violet trans-illuminator.

• Digested plasmid vectors were prepared for ligation by treating with Antarctic Phosphatase (AP, NEB). Briefly, 5.5μl of 10x AP buffer and 1.2 μl AP was added to a 50μl restriction digest and incubated for 1 hour at 37^{o}C. The treated vector was then run on an agarose gel and the relevant DNA band excised from gel and cleaned up using QIAquick Gel Extraction Kit (Qiagen).

• DNA ligation was performed using DNA Ligation Mighty Mix (Takara) following a standard protocol using 50ng of plasmid DNA and a vector: insert ratio of approximately 1:3 in a 20ul final reaction volume. Ligations were incubated at 16^{o}C for 30 minutes - overnight.

• 2-10ul of the ligation reaction was transformed into competent *E. coli* (MAX efficiency Stbl2 Competent Cells, Invitrogen) using the manufacturer's protocol. Bacteria were plated onto LB agar plates supplemented with 100ug/ml ampicillin and grown over night at 37^{o}C.

• Identification of bacterial colonies containing the insert of interest was performed using colony PCR or restriction digests of purified plasmid DNA.

• Small scale plasmid purification ('miniprep') was performed by selecting a single bacterial colony containing the plasmid of interest which was grown overnight in 2-5 ml LB broth supplemented with 100μg/ml ampicillin (LB-Amp) at 37 ^{o}C with shaking (230 rpm). Plasmids were purified using the QIAprep Spin Miniprep kit (Qiagen).

• Large scale plasmid preparation ('maxiprep') was generated by inoculating a 2-5 ml started culture of a single bacterial colony into 150ml LB-Amp, which was shaken over night at 37^{o}C. Plasmids were purified using the QIAfilter Plasmid Maxi Kit (Qiagen)

2.8.2 Construction of pRV-iCre retroviral vector

The retroviral vector pRV-iCre (**Figure 2.1**) was generated as follows:

• The multiple cloning site 1 (MCS1) from the mammalian expression vector pEYFP-C1 (Clontech) was PCR amplified using primers MCS1 Forward and MCS1 Reverse. The PCR product was digested with BamHI and AgeI alongside the Moloney murine leukaemia

virus (MoMLV)-derived pCLNCX retroviral expression vector CAG-GFP (Addgene plasmid # 16664). MCS1 was subcloned into the digested vector into sites immediately upstream (5') of the GFP coding sequence to create CAG-MCS1-GFP intermediate vector.

• A second MCS (MCS2) was then inserted downstream (3') of GFP in vector CAG-MCS1-GFP. This was created by annealing two single stranded oligonucleotides, MCS2 Forward and MCS2 Reverse. The two primers were dissolved in annealing buffer (10mM Tris, pH 7.5, 50mM NaCl), diluted to a concentration of 10µm before being mixed at equimolar concentrations and annealed by heating in a thermocycler using the following conditions:

1. 95^{o}C for 2 minutes
2. Δ -5^{o}C per 5 minutes x 5
3. Δ -10^{o}C per 5 minutes x 4
4. Hold at 4^{o}C

Double stranded MCS2 and the CAG-MCS1-GFP vector were then digested with PmeI, and MCS2 was ligated into CAG-MCS1-GFP immediately downstream of GFP to create CAG-MCS1-GFP-MCS2.

• iCre was PCR amplified from vector paavCAG-iCre (Addgene plasmid 51904) using primers iCre Forward and iCre Reverse, and both iCre PCR product and CAG-MCS1-GFP-MCS2 were digested with BspeI and AvrII. iCre was ligated into the digested vector to produce the CAG-MCS1-iCre-MCS2 vector, referred to as pRV-iCre in this thesis (**Figure 2.1**).

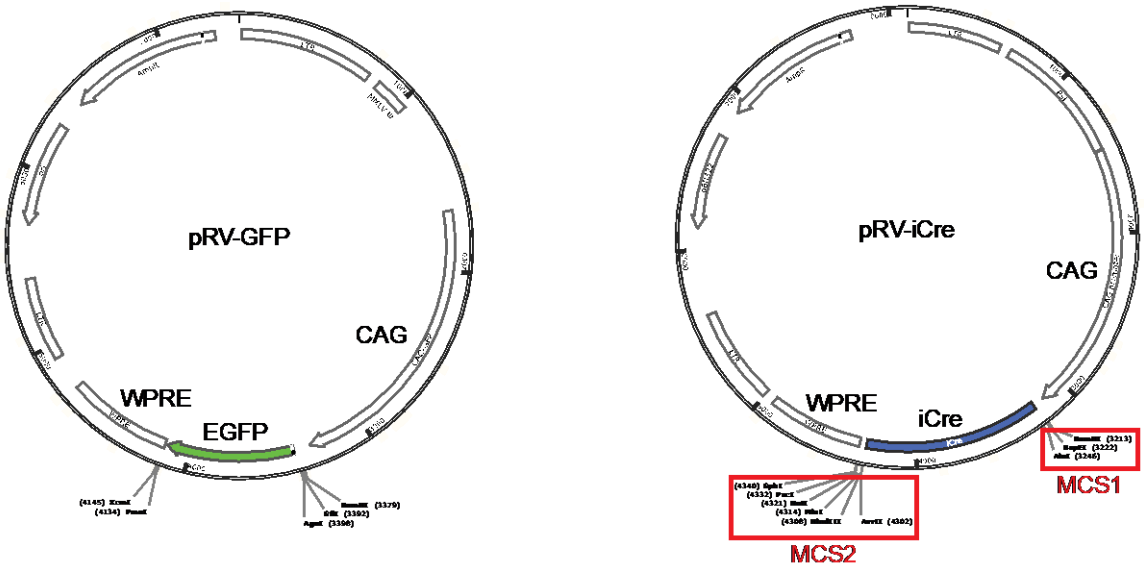

Figure 2.1: Generation of pRV-iCre retroviral vector. RV-GFP plasmid, based on the pCLNCX retroviral expression vector (a gift from Fred Gage, Addgene plasmid # 16664; **left**), was used to generate pRV-iCre (**right**). Multiple cloning sites MCS1 and MCS2 were inserted upstream and downstream of EGFP, respectively, to generate an intermediate vector. The intermediate vector was digested with restriction sites based in the two multiple cloning sites in order to remove EGFP. iCre was then inserted in place of EGFP.

2.8.3 Construction of pRV-tdTom-barcode library

The pRV-tdTom-barcode library (**Figure 2.2** and **Figure 4.5**) was created by inserting a pool of genetically distinct, double-stranded barcode oligonucleotides downstream (3') of the sequence encoding the fluorescent protein tandem tomato (tdTom) in the retroviral expression vector backbone CAG-GFP. The following steps describe the process:

• Cloning of the barcode library into pRV-tdTom required the insertion of a MCS downstream of tdTom. MCS2 was generated by annealing two single stranded oligonucleotides, MCS2 Forward and MCS2 Reverse, as described in Section 2.8.2. MCS2 and pRV-tdTom were both digested with PmeI, and MCS2 was ligated into pRV-tdTom immediately downstream of tdTom, to create the intermediate vector pRV-tdTom-MCS2 (**Figure 2.2 A**).

• The single stranded complimentary oligonucleotide primers Barcode Forward and Barcode Reverse were annealed by following the protocol described in Section 2.8.2. The resulting pool of genetically distinct double stranded barcode oligonucleotides and pRV-tdTom-MCS2 were digested with AvrII and MluI and the barcode pool was ligated into the retroviral expression vector at a molar ratio of 3:1 (**Figure 2.2 B**). This reaction was set up with 50 ng of vector and 660 pg barcode in a total volume of 20 µl.

• Three parallel transformation reactions were then set up using 1 µl of the ligation reaction into 100 µl MAX efficiency Stbl2 Competent Cells (**Figure 2.2 C**). The entire pooled transformation reactions were plated onto five large, 150 mm diameter LB agar plates supplemented with 100 µg/ml ampicillin. Approximately 7500 colonies were counted to have grown after overnight incubation at 37 ^{o}C. Colonies were harvested by adding 5 ml LB to each plate and rocking for 20 minutes to wash off the bacteria. Pooled colonies were placed into a final volume of 450 ml LB/ampicillin and grown for further 12 hours at 37 ^{o}C

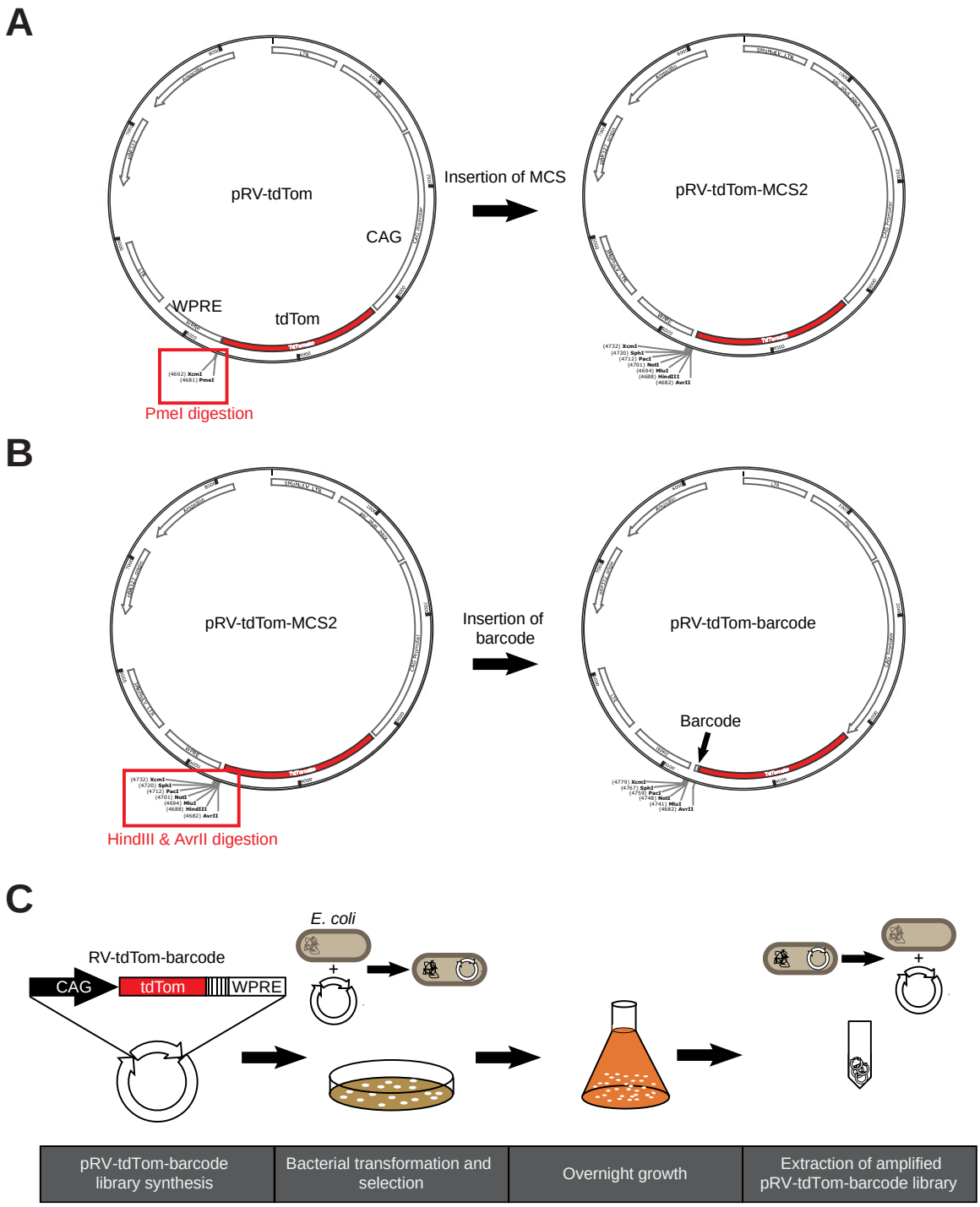

Figure 2.2. Generation of pRV-tdTom-barcode library. (**A**) The pRV-tdTom retroviral expression vector (a gift from Dr Louise Kay) was digested with Pme1, located between tdTom and WPRE, and a multiple cloning site (MCS2) was inserted to create pRV-tdTom-MCS2. (B) pRV-tdTom-MCS2 was then digested sequentially with HindIII and AvrII, located in MCS2, in order to insert the barcode between tdTom and WPRE. This created the pRV-tdTom-barcode library of genetically-distinct plasmids. (**C**) pRV-tdTom-barcode was transformed into competent *E. coli* to amplify the library. Transformed E.coli underwent overnight incubation for antibiotic selection on agar plates supplemented with ampicillin. Colonies were then washed off and incubated for a further 12 hours in liquid media. The amplified pRV-tdTom-barcode library was then extracted and purified.

with shaking at 220 rpm. pRV-tdTom-barcode plasmid DNA was then purified using the QIAfilter Plasmid Maxi Kit using three Maxi columns.

2.9 Retrovirus production and titration

2.9.1 Culturing of mammalian cell lines

The GP2-293 cell line is a HEK (Human Embryonic Kidney) 293-based retroviral packaging cell line. The essential viral packaging genes gag and pol are stably integrated while the viral envelope must be supplied in trans. The NIH/3T3 cell line is derived from mouse embryonic fibroblast cells. Both cell lines were grown in T-75 flasks (Corning) in DMEM + GlutaMAX (containing 4.5 g/l D-glucose and pyruvate) and 10 %v/v foetal calf serum (FCS). Cells were trypsinised every 3-4 days on reaching 90 % confluency. Cells were maintained in a 37 ^{o}C incubator humidified with 5 % carbon dioxide.

2.9.2 Retrovirus production

The following retroviral plasmid vectors were used for retrovirus production: pRV-iCre, pRV-tdTom, pRV-tdTom-barcode and CAG-GFP. Replication incompetent Moloney murine leukaemia virus (MoMLV) was produced by co-transfection of the GP2-293 packaging cell line containing *gag* and *pol* genes, with retroviral vector plasmid(s) and the pVSV-G envelope plasmid (provided as part of the Retro-X Universal Packaging System, Takara Bio Europe; **Figure 4.6**). GP2-293 cells were plated in a T75 tissue culture flask such that they achieved 80-90 % confluency the following day. Transfection was achieved using Lipofectamine 2000 (Thermo Fisher Scientific): 70 µg RV plasmid DNA and 30 µg pVSV-G envelope plasmid DNA were mixed with 1 ml Opti-MEM Reduced Serum Medium. In a separate tube, 75 µl Lipofectamine 2000 was mixed with 1 ml Opti-MEM and incubated for 5 minutes at room temperature. The two solutions were combined and

incubated at room temperature for 20 minutes. DNA-liposome complexes were added to the flask containing cells and 5ml complete medium. Cells were incubated for 4 hours in the incubator before removing the DNA-liposome complexes and replacing with 7 ml fresh complete medium.

Medium containing RV particles was harvested 24 hours after removal of the DNA-liposome complexes, and replaced with a further 7 ml complete medium. This was harvested a further 24 hours later. Retroviral supernatants were centrifuged for 5 minutes at 3000 rpm in a Heraeus Megafuge 8 table top centrifuge fitted with a swinging bucket rotor to remove cell debris and then and passed through a 0.22 μm filter (Nalgene SFCA, Thermo Fisher Scientific). This preparation (known as RV-supernatant) was used in a subset of experiments as indicated in the results chapters. For most experiments, RV-supernatants were concentrated by ultracentrifugation. RV supernatants were placed into 8 ml conical bottomed, heat sealable tubes (Beckman Coulter) and loaded into SW41TI swinging bucket rotor, and centrifuged in a Beckman L8-70M Ultracentrifuge at 23,000 rpm for 2 hours at 4 ^{o}C. The resulting viral pellet was re-suspended in 10 μl Opti-MEM containing 1: 200 dilution DNase I (IU/μl, Amplification Grade, Sigma-Aldrich) and 8 μg/ml Polybrene (hexadimethrine bromide, Sigma-Aldrich) before overnight incubation at 4^{o}C. Aliquots (2 μl and 5 μl) of the concentrated retrovirus were stored at -8 0^{o}C and removed immediately before use.

2.9.3 Retroviral titre testing

NIH/3T3 mouse embryonic fibroblast cells were used for titre testing retrovirus. Cells were plated at 8 x 10^4 cells per well on 18mm coverslips (VWR) in 12 well plates (Costar). The following day, cells were incubated overnight with concentrated retrovirus which was subject to ten-fold serial dilutions from 1: 1 x 10^3 to 1 x 10^7 in complete medium. Two replicates (coverslips) were performed at each dilution. The following day, the medium was replaced and cells were incubated for a further 72 hours before being fixed in 4 %

w/v paraformaldehyde (PFA) for 20 minutes prior to three five minute washes in phosphate-buffered saline (PBS). Coverslips were mounted in Vectashield mounting media (Vector Laboratories) and imaged under epifluorescence using an Olympus BX40 Epifluorescence microscope fitted with UPlanFL 10X and 20X Olympus air objectives, a cooled CCD camera (Orca ER, Hamamatsu) and HCImage imaging software. The number of fluorescently labelled colonies were counted on the two coverslips transduced with the lowest titre of retrovirus in which labelled colonies were present, the number of colonies averaged, and the retroviral titre was expressed as a number of colony forming units (c.f.u.) per ml of concentrated virus.

2.10 Characterisation of the RV-iCre retrovirus

2.10.1 Imaging study of RV-tdTom and RV-iCre

In utero surgery was performed at E12.5 as described in Section 2.7.2 in Ai9 reporter mice (B6.Cg-Gt(ROSA)26SOR$^{tm9(CAG\text{-}tdTomato)HZE}$/J) that encode floxed-stop CAG-tdTom at the *ROSA26* locus. Mice were injected with either RV-tdTom or RV-iCre at approximately 2000 c.f.u/embryo. Acute cortical slices were taken between P14 and P21 according to Section 2.7.3. Two animals (one animal injected with each retrovirus) were prepared simultaneously for imaging with a Zeiss Examiner Z1 confocal microscope, fitted with 458 nm, 488 nm, 514 nm and 631 nm laser lines and Zen 2.1SPZ imaging software (Zeiss). Confocal imaging settings were determined by examining two cortical slices from each animal and designed to avoid fluorophore saturation. These settings were then kept unchanged and cortical slices from each animal were imaged alternately using a 20X objective (Zeiss). Images were taken centred over the soma of spatially separated labelled neurons with a 1 µm z-step and a total z-stack depth of 50 µm.

In order to quantify the strength of fluorophore labelling for the comparison of RV-tdTom and RV-iCre, the mean pixel intensity over the soma of labelled cells was measured from Z-stacks that were collapsed using the maximum intensity projection function in Fiji (Schindelin et al., 2012). Somata were drawn around manually for analysis.

2.10.2 Functional characterisation of RV-iCre in the floxed-STOP P_2X_2-ATP receptor mouse

In utero surgery was performed at E12.5 as described in Section 2.7.2 in floxed-STOP P_2X_2-ATP receptor mice (Anastasiades et al., 2016) in order to inject approximately 1000 c.f.u./ embryo of RV-iCre. The following procedures were carried out by Dr Daniel Lyngholm in the Department of Physiology, Anatomy and Genetics at the University of Oxford: acute cortical slices were taken before P7 according to Section 2.7.3 and allowed to rest at room temperature for approximately 60 minutes before electrophysiological recording. Whole-cell patch-clamp recordings were performed at room temperature in high divalent ACSF using borosilicate glass microelectrodes (1.2mm outer diameter, 0.69 inner diameter; Harvard Apparatus, UK) pulled to 6-9 MΩ resistance using a Sutter P-97 horizontal puller and filled with a potassium-based internal solution (128 mM K-gluconate, 4 mM NaCl, 0.5 mM Li-GTP, 5 mM Mg-ATP, 0.0001 mM $CaCl_2$, 10 mM HEPES and 1 mM glucose). Excitatory postsynaptic currents (EPSCs) were recorded in voltage clamp at -70 mV holding potential. Optogenetic laser light activation of fluorescently labelled neurons was performed according to Anastasiades et al., 2016. In brief, a standard ultraviolet laser LSPS set up (Anastasiades & Butt, 2012) was used to focally release DMNPE-caged ATP (100 μm; adenosine 5'-triphosphate, P^3-(1-(4,5-dimethoxy-2-nitrophenyl)ethyl) ester, disodium salt; Life Technologies, UK) across the extent of the target grid. The emitted power of the DPSL-355/30 laser (Rapp Optoelectronic GmbH) was optimised to evoke action potentials in the retrovirally labelled neuron only when focused at the laser target spot immediately above the labelled cell soma.

2.11 Single cell collection for barcode retrieval using single cell RT-PCR and RNA-seq

2.11.1 Cell collection set-up

Live cells were collected either from coverslips, or from acute mouse cortical slices. Coverslips or brain slices were placed in a custom-made perfusion chamber on a standard electrophysiology rig equipped with a micromanipulator (Sutter Instrument Company), and an upright microscope (Olympus BX51 WI) equipped with a 20X water immersion objective (Olympus), epifluorescence and Dodt gradient contrast imaging (Luigs and Neumann). For RNA-seq single cell collections, the tubing on the rig was completely replaced. Cultured cells were perfused with a HEPES-based ACSF (140 mM NaCl, 5mM KCl, 2 mM $CaCl_2$, 10 mM HEPES ($C_8H_{18}N_2O_4S$), 10 mM glucose), whereas acute cortical slices were perfused with standard ACSF (24 mM NaCl, 2.5 mM KCl, 1.25 mM KH_2PO_4, 26 mM $NaHCO_3$, 2 mM $MgSO_4$, 2.5 mM $CaCl_2$, 10 mM D-glucose, and 4 mM D-sucrose). Both solutions were bubbled with 95 % oxygen, 5 % carbon dioxide. All solutions were either purchased as RNase free or made up with new chemicals and DEPC-treated distilled H_20. Single cell collection and preparation areas were cleaned with either 10 % v/v bleach or RNaseZap (Thermo Fisher Scientific) followed by RNase-free ethanol (Sigma-Aldrich), and equipment was UV-treated weekly.

2.11.2 Cell collection

Thin-walled borosilicate glass capillaries (1.5 mm outer diameter; Harvard Apparatus) were pulled using a Flaming Brown micropipette puller (Sutter Instrument Company) to obtain an aperture of approximately 10 µm. For single cell RT-PCR experiments, the micropipette was pre-filled with approximately 2 µl Resuspension Solution supplemented with 1:10 dilution of Lysis Enhancer (both solutions are components of the CellsDirect OneStep qRT-PCR Kit, Thermo Fisher Scientific) and 1 U/µl RNase inhibitor (RiboLock

RNase inhibitor, Thermo Fisher Scientific) and passed through a 0.22 µm filter. For single cell RNA-seq experiments from acute cortical slices, the micropipette was filled with 2 µl Smart-seq2 cell lysis buffer (0.2 % v/v Triton X-100 (Sigma-Aldrich) containing 2U/µl RNase inhibitor (Takara)) (Picelli et al., 2014). Fluorescently labelled cells were approached with positive pressure and then aspirated into the micropipette with light suction sustained over 1-2 minutes until the entire cellular contents were visualised to have entered the pipette. Pressure was equilibrated and then fixed as the pipette was withdrawn from the perfusion chamber. The contents of the micropipette were transferred blindly into a 0.2 ml PCR tube (Greiner Bio-one) for RT PCR, or a prototype single PCR tube (4titude) for RNA-seq, by application of strong positive pressure once the tip was located near the bottom of the PCR tube. To ensure the cell was transferred, the tip of the micropipette was finally broken off or ground into the bottom of the PCR tube. Samples were stored on dry ice for up to 2 hours and then stored at -80 ^{o}C until processing, which was no later than one month, and usually within a week, from collection. RNA-seq tubes were transferred to a rigid, fully skirted frame for 96 samples (4titude) and the location of each cell recorded. A sample of ACSF from the perfusion chamber (‘bath solution’) and collection solution were taken as a negative controls for single cell PCR experiments. For RNA-seq, a sample of Smart-seq2 cell lysis buffer was collected as a negative control. In some experiments, non-fluorescent cells were also harvested as negative controls.

2.11.3 Single cell RT-PCR and barcode identification

Samples were removed from -80 ^{o}C storage and centrifuged at 3000 rpm in a microcentrifuge (Eppendorf) for one minute at 4 ^{o}C. Samples were then placed in a PCR thermocycler (Veriti thermocycler, Applied Biosystems) pre-heated to 65^{o}C and incubated for ten minutes to induce cell lysis. Samples were treated with DNase (RNase-free DNase I, Thermo Fisher Scientific) by adding 5 µl DNase I and 1.6 µl 10X DNase buffer (Thermo Fisher Scientific) followed by 5 minutes incubation at 25 ^{o}C. The reaction was halted by

the addition of 4 µl of 25mM EDTA and incubation at 70 °C for 10 minutes. First strand synthesis was performed with random hexamers using the Superscript III First Strand Supermix according to the manufacturer's instructions (Thermo Fisher Scientific) using the entire cell lysate or a no-cell control. Two rounds of semi-nested PCR amplification were then performed, and included a positive (relevant RV plasmid DNA) and a negative (no DNA) control. Platinum Taq DNA Polymerase (Thermo Fisher Scientific) was used for the first PCR amplification in a standard reaction mixture with a total volume of 50 µl, including 5 µl first strand product and 0.2 µM each of primers Barcode1 Forward and Barcode1 Reverse). The following thermocycling conditions were used:

1. 94°C for 2 minutes

Then, 35 cycles of:

2. 94°C for 20s
3. 57.5°C for 30s
4. 72°C for 2 minutes

Followed by:

5. 72°C for 7 minutes
6. 4°C hold

2.5 µl of the primary PCR product was used in the second PCR amplification in a total volume of 25 µl using RedTaq ReadyMix (Sigma-Aldrich). The primers used for this reaction were Barcode1 Forward and Barcode2 reverse at a final concentration of 0.4 µM each. The same thermocycling conditions were used as the primary PCR amplification, but with 30 cycles of amplification.

The product of the second PCR amplification was analysed by gel electrophoresis and resulting PCR products extracted using the QIAquick Gel Extraction Kit (Qiagen). Samples were submitted to Source Bioscience for Sanger sequencing with primer Barcode2 Reverse. Barcode sequences in which the Phred (quality of sequence) score was below 40 for any of the barcode positions, or in which there were errors in the fixed loci in the barcode sequence, were discarded from analysis. Sequences in which there

was superimposition of nucleotide peaks at the variable, but not the fixed, positions were deemed to contain more than one barcode sequence. The barcode sequence was manually identified from sequencing traces. Custom Matlab software (Mathworks) was used to compare newly-identified barcode sequences with the database in order to identify sequence matches.

2.12 Study of clonal neuronal morphology using RV-tdTom-barcode *in vivo*

2.12.1 *In utero* surgery and tissue preparation

In utero surgery was performed between E11.5 and E13.5 according to Section 2.7.2 and RV-tdTom-barcode retrovirus was diluted for injection in order to inject either ~ 250 c.f.u/ embryo or ~ 1000 c.f.u/embryo, depending on the experiment. Mice were examined postnatally between P14 and P28 and acute cortical slices were prepared according to

2.12.2 Imaging protocol for clonal analysis

Acute cortical slices were imaged on Zeiss Examiner Z1 confocal microscope, with a 20X water immersion objective (Zeiss). Z-stacks were taken over fluorescently labelled cells using a 0.5 µm z-step covering the entirety of the visible dendritic arbor. Following imaging, cells were collected and processed for barcode identification as described in Section 2.11.

2.12.3 Morphological analysis of neurons

Z-stacks were collapsed in Fiji (Schindelin et al., 2012) using the standard deviation projection function. Images were imported into NeuronJ (Meijering et al., 2004) and the dendritic arbor was traced manually and then the total dendritic length was determined using the ‘measure’ function. The dendritic tracing was then opened in Fiji (Schindelin et

al., 2012) and Sholl analysis was performed using 10μm increments in the radius. These steps were then repeated for the apical and dendritic arbors, which were identified subjectively, separately. The enclosing radius and radius at which there were the maximum number of intersections were identified from the Sholl profile manually, and the SRI was taken from the Sholl analysis.

2.13 Single Cell RNA-seq using RV-tdTom-barcode *in vivo*

2.13.1 Single cell RNA-seq

Single cell RNA-seq was performed by the facility at the Oxford Genomics Centre, which is located at the Wellcome Trust Centre for Human Genetics, University of Oxford. Briefly, one 96 well plate containing 6 lysed single cells isolated from acute cortical slices transduced with RV-tdTom-barcode and stored at -80^{o}C was submitted to the Oxford Genomics Centre. Smart-seq2 methods detailed in Picelli et al., 2014 were used to lyse, reverse transcribe, PCR amplify and construct sequencing cDNA libraries. The prepared libraries were subjected to paired end sequencing over one lane of a HiSeq 4000 flow cell (Illumina) on a HiSeq 4000 DNA sequencing instrument (Illumina).

2.13.2 Sequence read processing and barcode identification

Analysis of RNA-seq data was performed by Dr Hania Pavlou, (Computational Analysis and Training Fellow, MRC Weatherall Institute for Molecular Medicine, University of Oxford). Briefly, sequence read quality was assessed with FastQC (Andrews, 2010), and trimmed for Nextera transposase sequence contamination using Trimmomatic (Bolger et al., 2014). Trimmed reads were aligned to the mouse genome (mm10 assembly including ERCC and tdTomato-barcode sequences) using STAR (v2.4.2a) (Dobin et al., 2013), with default settings except for switching off the number of mismatches per pair filter (--

outFilterMismatchNmax 999) and instead implementing a ratio of mismatches per pair (--outFilterMismatchNoverLmax 0.03), which is scaled to the read length. Reads overlapping the tdTomato-barcode reference sequence were isolated, and subsequently aligned using MAFFT under the G-INS-i model with 1000 iterations (Katoh et al., 2002). Consensus barcode sequences were identified by locating fixed upstream sequence.

2.14 Clonal studies in iPSC-derived human neocortical cells

2.14.1 Culturing of human iPSCs

The SFC180-01-01 iPSC line was derived from patient 180, a 60 year old female with no history of mental health problems, diabetes or migraine. iPSCs were cultured in 6 well plates (Corning) coated with Geltrex LDEV-free hESC-Qualified Reduced Growth Factor Basement Membrane Matrix (diluted 1:100 in Knock-out DMEM). Cells were maintained in mTesR1 Medium (Stem Cell Technologies) and cells were subject to full medium changes every day. Once cells reached approximately 90 % confluency, they were passaged using Versene (EDTA, Lonza) and split in a 1:2 or 1:3 ratio. Cells were plated in mTesR1 containing 10μM ROCK inhibitor (RI) Y-27632 (Tocris) for the first 24 hours.

2.14.2 Cortical differentiation of iPSCs

Cortical differentiation of iPSCs was performed using a protocol based on Shi et al., 2012. iPSCs at 70-90 % confluence were passaged 2:1 (2 wells of a 6 well plate onto 1 well) onto Geltrex and maintained in mTeSR1+ RI medium overnight. The following day (Day 0), 100 % confluent wells were washed once in PBS and transferred into 2 ml Neural Induction Medium (NIM) (50 % v/v DMEM:F12 + Glutamax, 50 % v/v Neurobasal, 2.5 μg/ml insulin (Sigma), 50 μM 2-mercaptoethanol, 0.5x non-essential amino acids; 0.5 mM sodium pyruvate (Sigma) 1x N2 supplement, 1x B27 supplement, 25 U/μl penicillin/

streptomycin, 1 mM glutamine, 10 µM SB431542 (Tocris), 1 µM dorsomorphin (Tocris)). Neural induction medium was changed every day for 12 days. At D12, the differentiated neuroepithelial cell sheet was lifted in large clumps (visible by eye) by dispase treatment: 0.2 ml dispase (10 mg/ml) was added to each well containing 2 ml NIM and incubated for 10-20 minutes at 37 ^{o}C until the cell sheet lifted off. The cells were transferred to a 15 ml tube and the clumps allowed to sink to the bottom by gravity. The supernatant was removed and the cell clumps were washed twice with 8 ml NIM, using gravity to collect cells. Cells were resuspended gently in 4 ml NIM and plated as visible clumps onto 2 wells of a 6 well plate coated with laminin (1:2 split). The following day, the medium was changed to neural maintenance medium (NMM; NIM without SB43152 and dorsomorphin) containing 20 ng/ml FGF2 (Peprotech) to promote neural progenitor cell (NPC) rosette formation. NMM + FGF2 was changed every day for the next 3 days. After 4 days of FGF2 treatment (Day 17), rosettes were lifted gently with dispase (split 1:2) and plated onto laminin-coated wells in NMM. Rosettes were also be plated onto poly-L-ornithine/laminin coated glass coverslips for immunolabelling studies. NPCs were fed every 2 days with NMM, dispased every 3-4 days (1:2 split) until D25 - D26 when neurons start to appear. At this point, cells were lifted with Accutase (Sigma; 1:1 split) and dissociated into a single cell suspension. For Accutase treatment, cells were washed once with PBS and 0.5 ml Accutase was added to each well and incubated for 5 minutes at 37 ^{o}C. Cells were flushed off the well and removed to a 15 ml tube containing 10 ml NMM. Cells were centrifuged at 300 g for 5 minutes, the supernatant removed and the wash repeated. Cells were resuspended in NMM and plated onto laminin coated wells. NPCs and neurons were passaged 1:2 with Accutase every 2-4 days when cells reached 90 % confluence. At approximately D35, NPCs and neurons were plated for the final time onto poly-ornithine/laminin coated glass coverslips. NMM was changed 3 times a week and 100 µg/ml laminin was included with the medium every seven days.

2.14.3 Immunolabelling of iPSC-derived NPCs and neurons

Coverslips of NPCs or neurons were fixed with 4 % w/v paraformaldehyde in PBS for 20 minutes at room temperature, washed three times with PBS and permeabilised with 0.3 % v/v Triton X-100 for 10 minutes. Coverslips were incubated with a blocking solution (10 % v/v normal goat serum in PBS) for 1 hour before applying primary antibodies. The following primary antibodies were diluted in 2 % v/v normal goat serum/ PBS (host species, dilution and source are noted in brackets): Pax6 (rabbit; 1:500; Covance), Tuj1 (mouse; 1:2000; BioLegend), Nkx2.1 (mouse; 1:500; Millipore), Tbr2 (rabbit; 1:500; Abcam), phosphohistone H3 (rabbit; 1:500; Millipore), Tbr1 (rabbit; 1:500; Abcam), Ctip2 (rat; 1:250; Abcam), SATB2 (mouse; 1:100; Abcam), MAP2a (mouse; 1:1000; Millipore), GAD67 (mouse; 1:400; Millipore), synaptophysin (mouse; 1:500; Synaptic Systems). Antibodies were incubated for 2 hours at room temperature or overnight at 4 ^{o}C. Following washing coverslips 3 times for 5 minutes with PBS, cells were incubated with appropriate combinations of Alex-488 or Alexa-568-conjugated secondary antibodies (goat anti-rabbit, goat-anti-mouse or goat anti-rat; Life Technologies) for 1 hour at room temperature. Coverslips were washed once with PBS and incubated for 10 minutes with DAPI nuclear stain (Molecular probes) diluted 1:10000 in PBS. Coverslips were then washed a further three times with PBS and mounted in Prolong Diamond Anti-fade Mounting solution (Thermo Fisher Scientific). Cells were imaged on an Olympus BX40 Epifluorescence microscope with UPlanFL 20X and 40X Olympus air objectives and HCImage imaging software.

2.14.4 Clonal studies in iPSC-derived human neocortical progenitors using RV-tdTom-barcode

Cultures at D30-D35 post induction were transduced by overnight incubation with RV-tdTom-barcode (ranging from 4 x 10^3 c.f.u./ml to 100 c.f.u./ml). Transduction media was replaced with fresh NMM the following day and cells were cultured up to a further 90 days.

Coverslips were then transferred to a perfusion chamber on a Zeiss Examiner Z1 confocal microscope, and fluorescently labelled cells were imaged using a 20X water immersion objective (Zeiss) prior to cell collection and barcode retrieval according to Section 2.11. Z-stacks of collected images were collapsed in Fiji (Schindelin et al., 2012) using the standard deviation projection function. For experiments documenting clone size, the number of fluorescently labelled cells was counted manually on images of coverslips transduced with low titre retrovirus (100 - 125 c.f.u./ml).

2.14.5 Gap junction tracing in iPSC-derived neocortical cells

Gap-junction tracing was performed by Dr Feige Tang in the Akerman Group in the Department of Pharmacology, University of Oxford. Neuronal progenitor cells were plated at a density of 2 x 10^5 cells/ml and transduced with RV-tdTom-barcode at a titre of 100 c.f.u./ml as described in section 2.13.4. For dye transfer studies, the cell-impermeant fluorochrome Alexa Fluor 488 (Thermo Fisher, Molecular weight: 570) was introduced into fluorescently-labelled neuronal cells through a glass micropipette (Biochrom Ltd) either by whole cell patch clamp or single-cell electroporation. Dye was dissolved in intracellular solution (K-gluconate 140 mM; NaCl 6 mM; EGTA 1 mM; HEPES 10 mM; MgATP 4 mM; Na3GTP 0.4 mM; pH 7.3, osmolarity 290 mM) at a concentration of 1mM.

Target cell loading

Whole cell patch clamp technique: 8-10 MΩ glass micropipettes were used to obtain a whole cell patch configuration. Dye was injected intracellularly by application of brief hyperpolarizing voltage pulses.

Single-cell electroporation: 35-50 MΩ glass micropipettes were used for electroporation. The micropipette tip was brought into contact with the cell soma and train of pulses (100Hz

for 3 seconds; pulse amplitude 2 V, pulse duration 1 ms) was applied using an Axoporator 800A (Molecular device Co.)

Gap-junction connection assay

5 minutes was allowed for dye diffusion. Epifluorescence (using a 470 nm excitation, 525 nm emission, filter) was then used to identify dye-coupled cells using a 20X objective. Images were taken in order to identify co-localisation of tdTom expression and Alexa Fluor 488 dye and to measure the distance between coupled cells.

Cell number estimate

At the end of each experiment, if the distance between the target cell and the furthest coupled cell was under 300 µm, a count was made of the total number of cells in the area covered by a circle which was centred on the cell soma and had a radius equal to the maximum distance between the target cell and a gap-junction coupled cell. If the radius was over 300 µm, the cell number was estimated based on counts made of the number of cells in a 215 µm x 215 µm area under a 40X objective from fixed coverslips at a range of age (**Figure 2.3**). The cell number could then be estimated using the formula for the line of best fit ($r^2 = 0.9$; linear regression) to generate the following equation:

$$cell\ number\ in\ 215\ \mu m\ x\ 215\ \mu m\ area = 1.93\ x\ culture\ age + 58.4$$

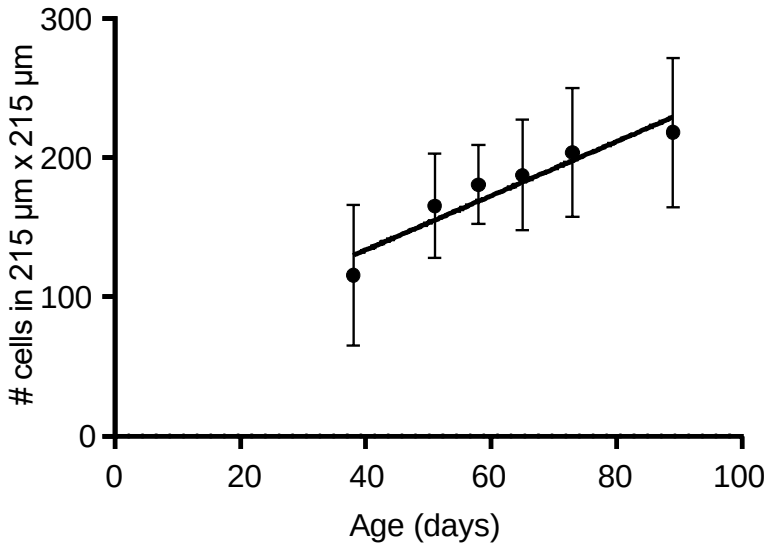

Figure 2.3: Estimating cell numbers for calculating the probability of gap-junction coupling. The number of cells in a 215 µm x 215 µm area were counted from fixed coverslips under light microscopy using 40X magnification. A line of best fit was calculated in order to generate an equation to estimate the number of cells on live coverslips for calculating the probability of gap-junction coupling ($r^2 = 0.9$; linear regression).

2.15 Statistics

Data analysis was performed using either custom software in Matlab (Mathworks) or GraphPad Prism version 6.0 (GraphPad Software). Data are presented as mean ± SEM and two-tailed tests were used as standard. Specific statistical tests are reported in the text. The following symbolism is used to indicate statistical significance, defined as $p < 0.05$: *, $p < 0.05$; **, $p < 0.01$; ***, $p < 0.001$.

Chapter 3

Assessment and refinement of *in utero* surgery in mice

3.1 Introduction

In utero surgery provides unprecedented access to the developing embryo. It has facilitated insights into development by enabling rapid and flexible genetic manipulation without the need for the generation of transgenic strains (Lo Turco, Manent, & Sidiqi, 2009; C. Wang & Mei, 2013). A further advantage is its versatility in enabling multiple manipulations to be performed with spatiotemporal flexibility in embryos from a range of species (Lo Turco et al., 2009). The ability to differentially manipulate individual embryos, and leave unmanipulated littermates as controls, provides a powerful method of controlling for genetic background and developmental environment. *In utero* surgery has successfully been used to deliver tools to up-regulate or down-regulate gene expression (Bai et al., 2003; Young-Pearse, Suth, Luth, Sawa, & Selkoe, 2010), to express transgenes (Sanes, 1989), to dye-label cohorts of cells (Telley et al., 2016) and to deliver cells for allotransplantation (Carletti, Grimaldi, Magrassi, & Rossi, 2004). However, an experimental risk of *in utero* surgery is the potential variability that may arise from performing surgical manipulations on individual animals. Despite its increasing popularity, the protocol for *in utero* surgery is variable in the literature. Furthermore, *in utero* surgery is a complex and invasive surgical procedure, necessitating general anaesthesia of the pregnant female (dam), incision into the abdominal cavity (laparotomy) and exteriorisation of the gravid uterus (Saito & Nakatsuji, 2001). The physiological effects of this procedure on the dam are not well characterised, nor are the efficacy of measures taken to minimise these effects well documented. Parallels drawn from literature in humans indicate that surgery during pregnancy poses a significant risk to the health of the pregnant female and

her developing offspring (Bajwa & Bajwa, 2013; Duncan, Pope, Cohen, & Greer, 1986), but the risk of these events in rodents is unknown. Consequently, there is little foundation on which to develop an evidence-based surgical protocol or to assess surgical practice, replacing a missed opportunity to refine the use of animals in research.

In this chapter I set out to perform an analysis of surgical records from my host laboratory over a six year period in order to characterise the morbidity (disease) and mortality (death) of pregnant female mice and their offspring between *in utero* surgery and littering down. Specifically, I aimed to establish:

- What is the nature and incidence rate of morbidity and mortality of the dam and her offspring in the seven days following *in utero* surgery?
- Can measures be taken to reduce the frequency and severity of inadvertent intra-operative hypothermia and post-operative wound dehiscence, to which rodents are likely to be predisposed?
- Can refinement of the surgical protocol reduce the incidence of post-operative morbidity and mortality following *in utero* surgery?

3.2 Results

3.2.1 *In utero* surgery is a powerful method for delivering molecular tools to the developing brain.

In utero surgery was performed in mice between embryonic day (E) 11.5 and E15.5 (**Figure 3.1 A**) as part of a series of experiments in the Akerman group, at the University of Oxford, investigating neocortical development. Timed-pregnant mice were anaesthetised with isofluorane to gain access to the embryos by exteriorisation of the gravid uterus through a midline laparotomy incision (**Figure 3.1 B**). *In utero* intraventricular injection of the embryonic brain was used to deliver DNA by electroporation or using replication-incompetent retroviral vectors, or it was used to deliver cell-permeable carboxyfluorescein ester dyes. The laparotomy incision was closed in two layers (muscle and skin) and animals were recovered from surgery in order to litter down naturally. Successful manipulation was confirmed by examining the postnatal brains of offspring for the presence of fluorescently-labelled neurons. For instance, labelling of layer 2/3 pyramidal neurons in the neocortex was successfully achieved by electroporation of a plasmid DNA encoding EGFP or by injection of retrovirus encoding tdTomato (**Figure 3.1 C**).

This risk of dam mortality was assessed over a six year period, during which the protocol for *in utero* surgery was refined. To characterise the baseline level of mortality of dams and their offspring using a standard surgical protocol, data from the first two years of the assessment period was pooled for evaluation. Data from the last two years of the assessment period were pooled in order to characterise the efficacy of the refinements (**Figure 3.1 D**).

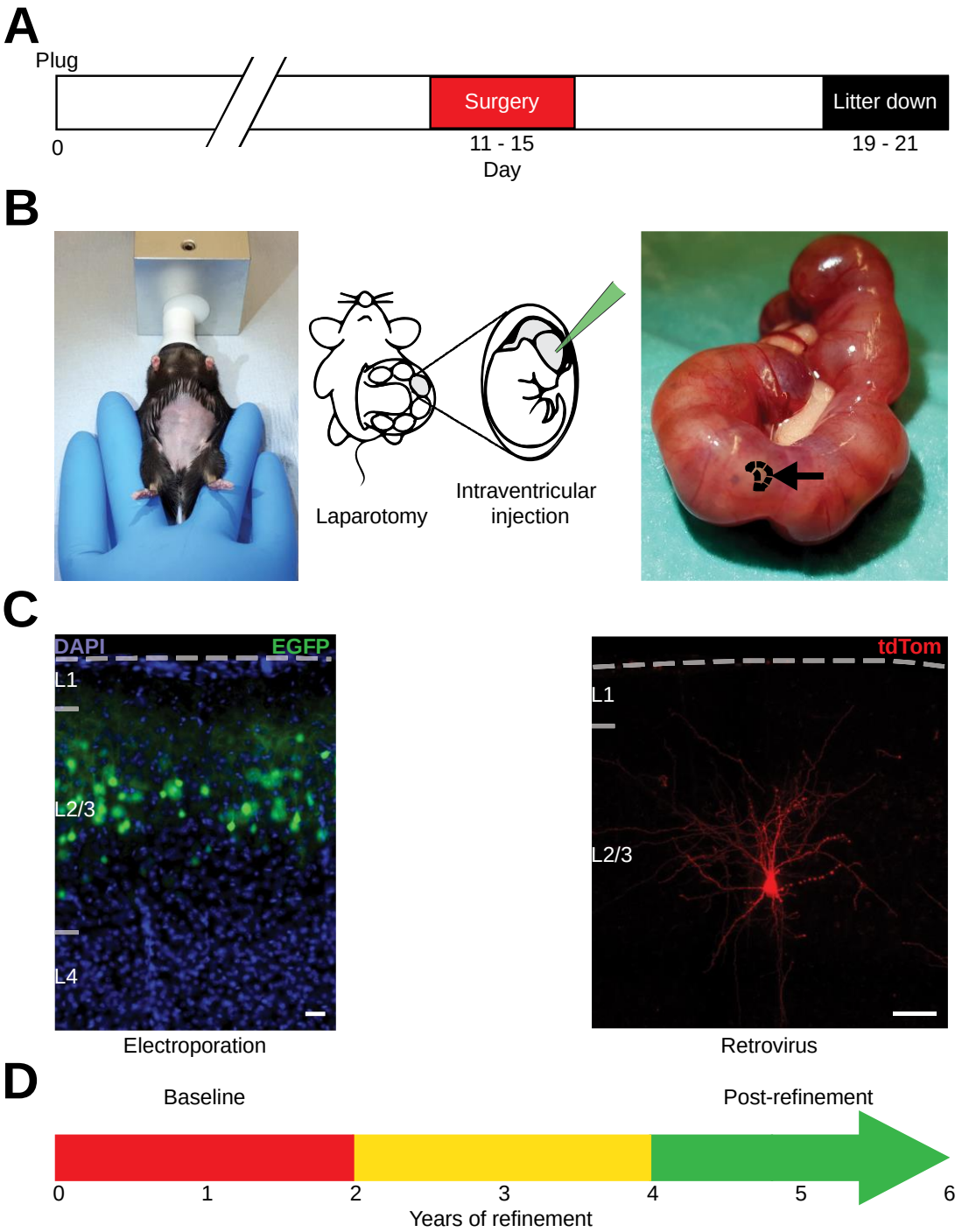

Figure 3.1: *In utero* surgery enables manipulation of gene expression in the developing mouse neocortex. (**A**) Timeline of *in utero* surgery. The day of plugging was designated day 0. Surgery was performed between E11.5 and E15.5. Dams were recovered from surgery in order to litter down naturally. (**B**) Anaesthetic set up demonstrating a dam in dorsal recumbency prepared for surgery. Anaesthesia is maintained by delivery of isofluorane by nose cone. A glove filled with warm water (38 – 40^{o}C) is placed to provide thermal support (**left**). Schematic demonstrating placement of an intraventricular injection into the embryonic brain accessed by a laparotomy incision (**centre**). Gravid uterus exteriorised during surgery demonstrating the dye-filled lateral ventricle of the brain (outlined by the dashed line, indicated by the arrow, **right**). (**C**) *In utero* surgery was used to label layer 2/3 neocortical neurons by electroporation of plasmid DNA (**left**) or by retrovirus (**right**). Scale bars 50 μm. (**D**) The protocol for *in utero* (cont.)

3.2.2 *In utero* surgery carries a risk of dam mortality that is significantly associated with surgical technique

Three surgeons performed surgery over the first two years of the study. Surgical records were assessed in order to determine the mortality rate, which would constitute the baseline. Dams littered down 5.8 ± 0.2 days following surgery (gestation length 19.3 ± 0.7 days, n = 70). The overall incidence of death of the female in the seven days following surgery was 18 % (n = 266, **Figure 3.2 A**). No instances of intra-operative death were recorded, but post-operative dam mortality occurred throughout the seven day time window. Death was categorised as 'unexpected', when the dam was found dead without prior morbidity being observed. Alternatively, death was categorised as the fulfilment of a humane endpoint, in cases where the dam was killed because morbidity levels had exceeded a predetermined threshold. This was implemented in accordance with the guidance of the UK Animals (Scientific Procedures) Act (1986), when morbidity level was deemed likely to lead to unacceptable pain, suffering and/or distress. Fulfilment of a humane endpoint constituted a greater cause of dam mortality than unexpected death (overall rate 15 % and 3 %, respectively). Significant variation was revealed in the incidence of dam mortality between individual surgeons (surgeon A: humane endpoint = 27 %, unexpected death = 4 %, n = 113; surgeon B: humane endpoint = 3 %, unexpected death = 0, n = 69; surgeon C: humane endpoint = 9 %, unexpected death = 4 %, n = 84; C^2 (4, n = 266) = 20.36, p = 0.0004, chi-square test; **Figure 3.2 B**).

Fulfilment of a humane endpoint could be further classified by the nature of the causal morbidity, termed 'threshold morbidity'. Non-specific malaise was the most common threshold morbidity in the seven days following surgery (11 % of all dams, 29/266 dams). Non-specific malaise was a descriptive classification defined by the presence of

(Figure 3.1 cont.) surgery was refined over a six year period. Mortality rates for the dam and embryos during the first two and last two years were pooled for analysis to characterise the mortality rate at baseline and post-refinement, respectively.

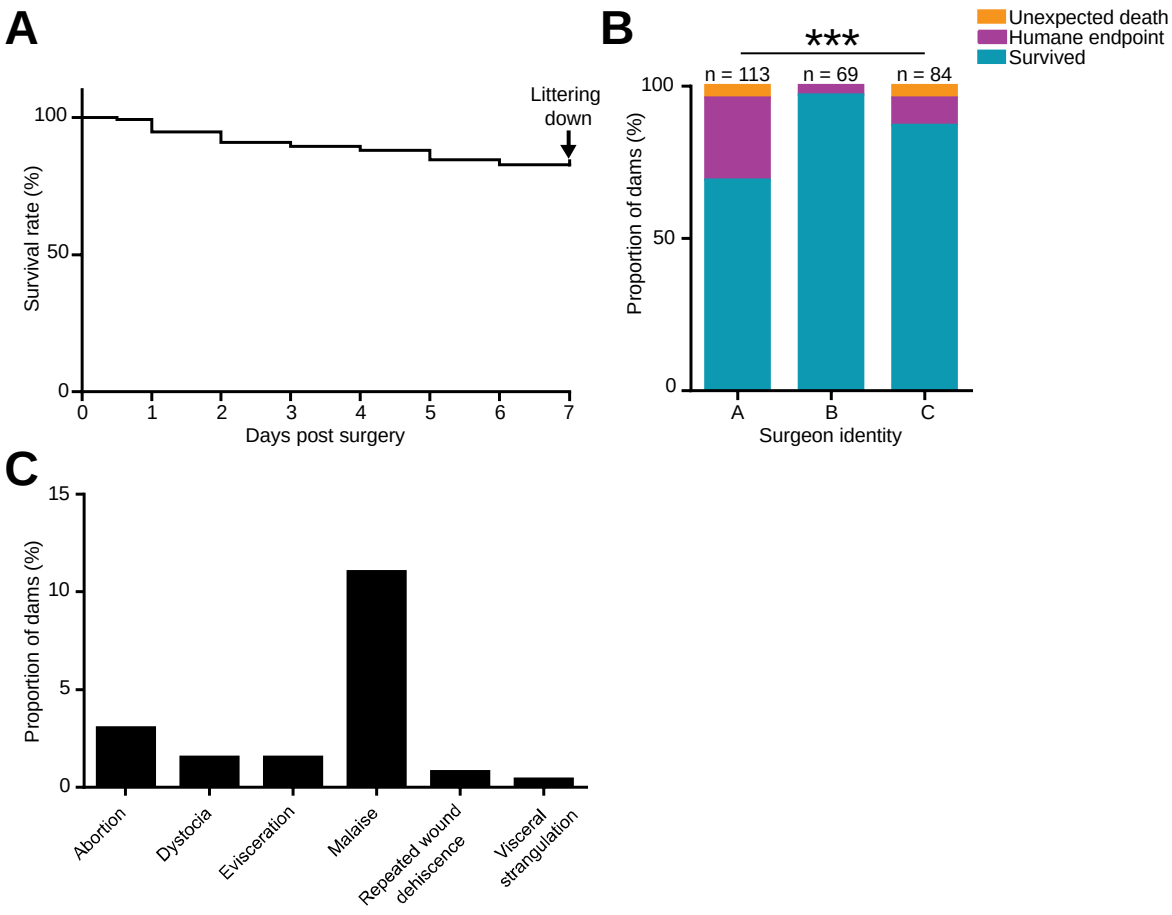

Figure 3.2: *In utero* surgery carries a risk of post-operative dam morbidity and mortality that is significantly associated with surgeon technique. (**A**) There was a low risk of dam death in the seven days following surgery (18 % death by day seven, 48/266). (**B**) There was significant variation in the incidence of dam mortality between surgeons (surgeon A: humane endpoint = 27 %, unexpected death = 4 %; surgeon B: humane endpoint = 3 %, unexpected death = 0; surgeon C: humane endpoint = 9 %, unexpected death = 4 %; C^2 (4, n = 266) = 20.36, p = 0.0004, chi-square test). Mortality was manifest as either unexpected death, when the dam was found dead, or because the dam was killed due to morbidity that passed the threshold for a humane end point. (**C**) Non-specific malaise was the most common threshold post-operative morbidity, occurring in 11 % (29/266) of all dams. Other causes of threshold morbidity occur at rates of less than 5 % (13/266) of all dams.

one or more symptoms of inappetance, reluctance to move, piloerection, hunched posture, and presence of a facial grimace that did not improve with combined analgesia with meloxicam and buprenorphine (**Figure 3.2 C**). Other post-operative morbidities occurred at an individual incidence rate of under 5 % of all dams.

3.2.3 *In utero* surgery carries a risk of embryonic death that is associated with surgical technique

The next target for investigation was to explore whether *in utero* surgery was also correlated with a risk of embryonic death. Two goals were identified: firstly, to characterise the relationship between *in utero* surgery and embryonic mortality, and secondly, to explore associations between procedural variables and embryonic mortality. Dam records were analysed from animals with, or without, *in utero* surgery. Birth rate (litter size) was used as a proxy for embryonic death rate, as embryonic death could manifest as resorption (Flores, Hildebrandt, Kühl, & Drews, 2014). Significantly fewer pups were born from dams that underwent surgery than from control dams that did not undergo surgery (non-surgery: mean = 7.3 ± 0.3 pups, n = 46; surgery: mean = 5.4 ± 0.4 pups, n = 24; t (57.7) = 4.0, p = 0.0002; unpaired t test with Welch's correction, **Figure 3.3 A**). Surgery litters were 74 ± 4 % of the size of non-surgery litters, therefore the embryonic death rate attributable to *in utero* surgery was estimated to be 26 ± 4 %. To investigate the relationship between surgery and litter size at the level of the individual dam, the change in litter size between a dam's first and second litters was analysed. There was no significant difference between the size of the first and second litters in dams that did not undergo surgery (non-surgery/non-surgery (n = 8): litter 1 mean = 7.1 ± 0.6 pups, litter 2 mean = 6.5 ± 0.7; t (7) = 0.8, p = 0.4); paired t test). However, in dams that underwent surgery during their second pregnancy, the second litter was significantly smaller than the

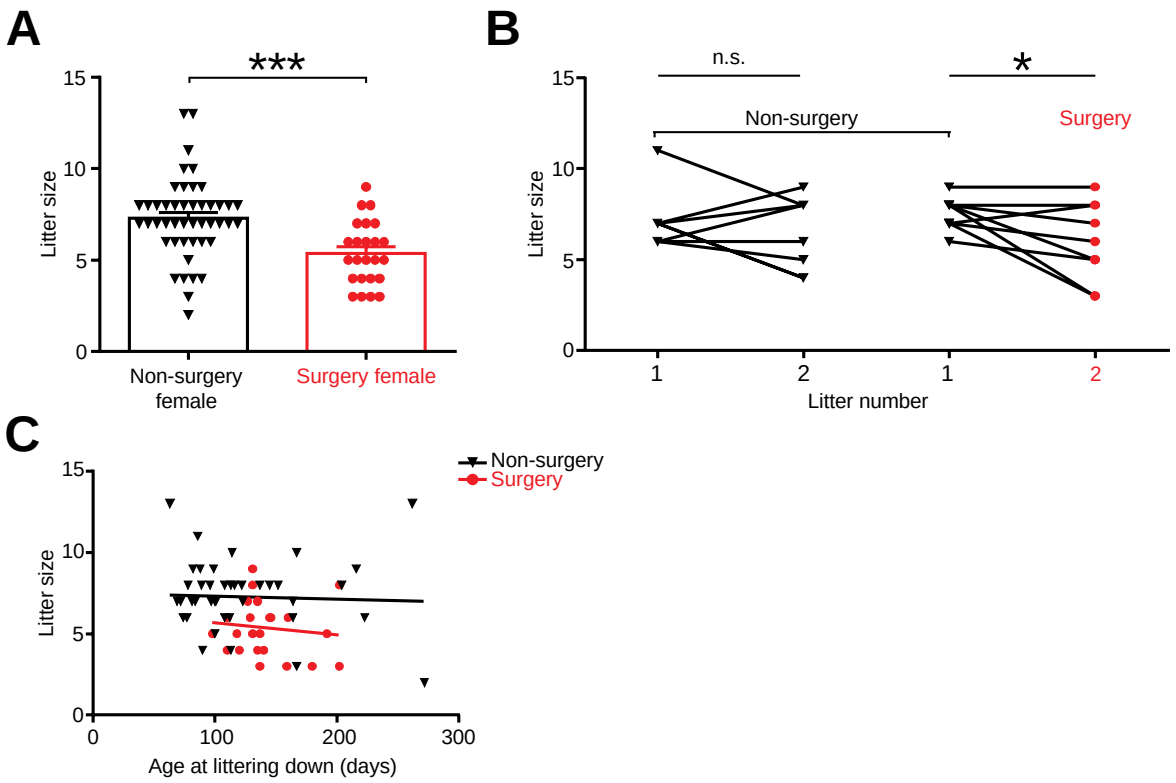

Figure 3.3: *In utero* surgery carries a risk of death to embryos that is unrelated to dam age. (**A**) Significantly fewer pups were born from dams that underwent surgery than dams that did not undergo surgery (non-surgery: mean = 7.3 ± 0.3 pups, n = 46; surgery: mean = 5.4 ± 0.4 pups, n = 24; t (57.7) = 4.0, p = 0.0002, unpaired t test with Welch's correction). (**B**) There was a significant decrease in litter size between litters in dams that underwent surgery during their second pregnancy, but not in those that did not (non-surgery/non-surgery (n = 8): litter 1 mean = 7.1 ± 0.6 pups, litter 2 mean = 6.5 ± 0.7; non-surgery/surgery (n = 9): litter 1 mean = 7.6 ± 0.3, litter 2 mean = 6 ± 0.7; t (8) = 2.33, p = 0.0485, paired t test). (**C**) Litter size at birth was not significantly correlated with dam age at littering in either the surgery or non-surgery groups (non-surgery: r (46) = - 0.04, p = 0.79; surgery: r (24) = - 0.12, p = 0.57; Pearson correlation coefficient).

first litter (non-surgery/surgery (n = 9): litter 1 mean = 7.6 ± 0.3, litter 2 mean = 6 ± 0.7; t (8) = 2.33, p = 0.0485, paired t test; **Figure 3.3 B**). Birth rate was not correlated with the age of the dam at littering down, either with or without surgery (non-surgery: r (56) = - 0.04, p = 0.79; surgery: r (24) = - 0.12, p = 0.57; Pearson correlation coefficient; **Figure 3.3 C**). In summary, these findings confirm that *in utero* surgery is associated with a risk of embryonic death, estimated at a rate of 26 %.

Heterogeneity in the surgical protocol presented the opportunity to explore whether aspects of the procedure were correlated with birth rate. Firstly, variables that related to aspects of the embryonic protocol were evaluated to establish whether these exhibited a relationship with birth rate. Specifically, the molecular manipulation protocol, the stage of embryonic development at the time of surgery, and the proportion of the litter that was injected, were all assessed using the records of a single surgeon. The molecular manipulation protocol consisted of either injection and electroporation of plasmid DNA, or injection with replication-incompetent retrovirus, or injection of carboxyfluorescein ester dyes. The molecular manipulation was not associated with differences in litter size at birth (electroporation: mean = 5.3 ± 0.5 pups, n = 16; retrovirus: mean = 5.8 ± 0.4 pups, n = 24; single dye: mean = 4.5 ± 1.0 pups, n = 4; two dyes: mean = 4.0 ± 0.8 pups, n = 5; F (3, 45) = 1.47, p = 0.24; one-way ANOVA; **Figure 3.4 A**), indicating that there was no relationship between the specific substances delivered to the embryonic brain and mortality. Litter size at birth was, however, found to vary as a function of the embryonic stage at the time of surgery (E11.5: mean = 5.7 ± 0.5 pups, n = 3; E12.5 pups: mean = 4.6 ± 0.3 pups, n = 31; E13.5: mean = 5.5 ± 0.4 pups, n = 30; E14.5: mean = 6.2 ± 0.4 pups, n = 30; E15.5: mean = 5.9 ± 0.4 pups, n = 12; F (4, 102) = 2.76, p = 0.03; one-way ANOVA; **Figure 3.4 B**). Litter size was significantly greater following surgery at E14.5 in comparison to surgery at E12.5 (p = 0.016; Tukey's post hoc test for multiple comparisons). These represented the only developmental stages between which litter size differed significantly. There was no linear trend between developmental stage and the rate of embryonic mortality (p = 0.4, one-way ANOVA with post-test for linear trend).

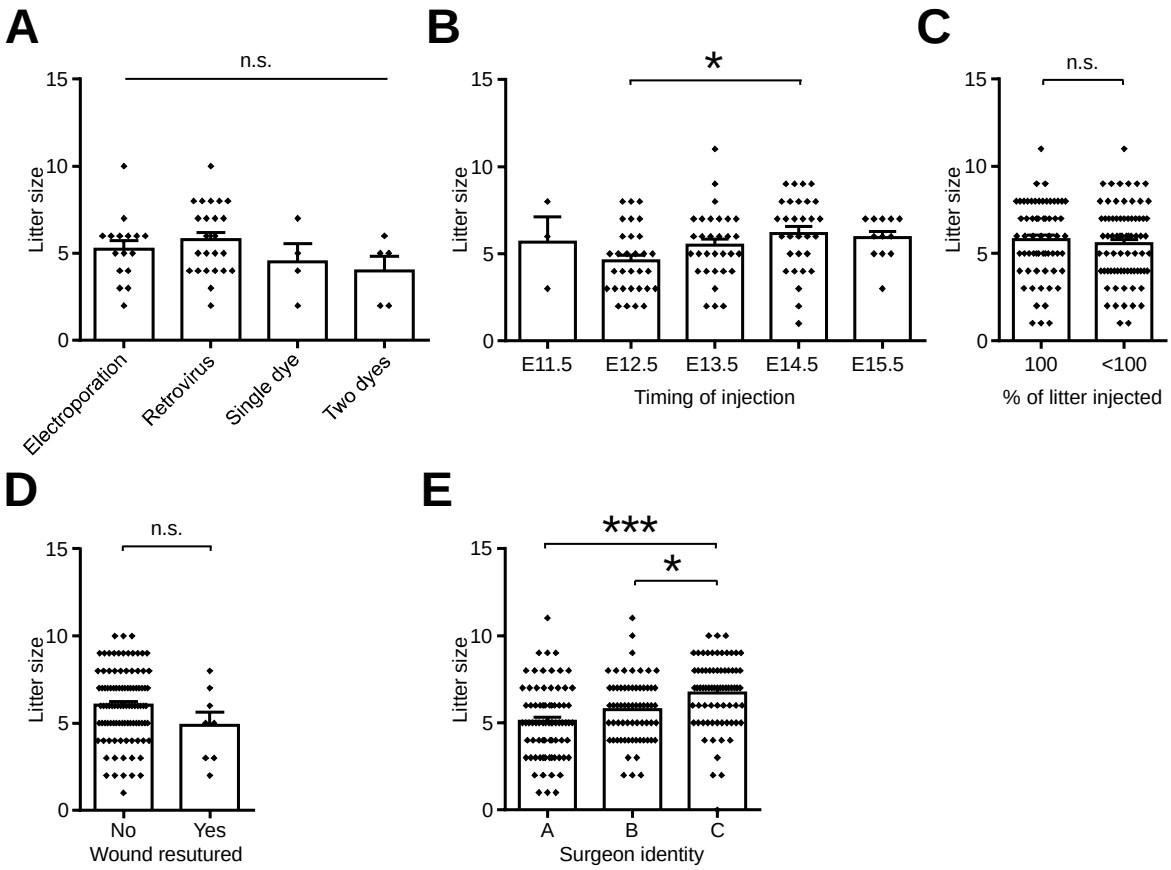

Figure 3.4. Surgical technique is significantly correlated with the risk of embryonic death following *in utero* surgery. (**A**) The technique for molecular manipulation of the embryonic brain was not associated with the litter size at birth (electroporation: mean = 5.3 ± 0.5 pups, n = 16; retrovirus: mean = 5.8 ± 0.4 pups, n = 24; single dye: mean = 4.5 ± 1.0 pups, n = 4; two dyes: mean = 4.0 ± 0.8 pups, n = 5; $F(3, 45) = 1.47$, $p = 0.24$; one-way ANOVA). (**B**) Litter size at birth varied as a function of the stage of embryonic development at the time of surgery (E11.5: mean = 5.7 ± 0.5 pups, n = 3; E12.5: mean = 4.6 ± 0.3 pups, n = 31; E13.5: mean = 5.5 ± 0.4 pups, n = 30; E14.5: mean = 6.2 ± 0.4 pups, n = 30; E15.5: mean = 5.9 ± 0.4 pups, n = 12; $F(4, 102) = 2.76$, $p = 0.03$; one-way ANOVA). Litter size was significantly greater following surgery at E14.5 compared to surgery at E12.5 ($p = 0.016$, Tukey's post hoc test for multiple comparisons), although those were the only ages where a difference was observed. (**C**) Litter size at birth was not associated with whether or not all of the litter were injected (100 % injected: mean 5.8 ± 0.3 pups, n = 62; < 100 % injected: mean = 5.6 ± 0.3 pups, n = 74; $t(134) = 0.063$, $p = 0.53$, unpaired t test). (**D**) Whether or not the dam was subjected to wound resuturing was not associated with litter size at birth (no resuturing: mean = 6.0 ± 0.2 pups, n = 104; resuturing: mean = 4.9 ± 0.7 pups, n = 8; $t(110) = 1.56$, $p = 0.12$, unpaired t test). (**E**) Variation in the litter size at birth was associated with different surgeons (surgeon A: mean = 5.1 ± 0.2 pups, n = 77; surgeon B: mean = 5.8 ± 0.2 pups, n = 65; surgeon C: mean = 6.7 ± 0.2 pups, n = 72; $F(2, 211) = 12.99$, $p < 0.0001$; one-way ANOVA; surgeon A vs C: $p < 0.0001$; surgeon B vs C: $p = 0.01$; post hoc Tukey's test for multiple comparisons).

To further understand whether the relationship between surgery and embryonic mortality was a consequence of the general surgical procedure itself, or intraventricular injection specifically, I next assessed the relationship between the proportion of the litter that was injected and the birth rate. The decision as to the proportion of the total number of embryos that would be injected was made at the time of surgery. This depended on factors such as how easily the embryos located nearest the cervix could be accessed without excessive physical manipulation. Records were divided into two groups: either those in which all embryos were injected (100 % of embryos injected, n = 62 dams), or those in which part of the litter was injected (77 ± 2 % of embryos injected, n = 74 dams). There was no significant difference in the litter size at birth when all embryos were injected, compared to cases where only part of the litter was injected ($t(134) = 0.063$, $p = 0.53$; unpaired t test; **Figure 3.4 C**). This suggested that intraventricular injection itself, is not associated with embryonic mortality.

I hypothesised that wound dehiscence necessitating resuturing of the dam may pose a risk of embryonic mortality due to maternal stress and the necessity for a second anaesthetic. To examine this hypothesis, the embryonic birth rate for dams that did, and did not, undergo resuturing was compared. There was no significant difference in litter size at birth between females that underwent resuturing, and those that did not (no resuturing: mean = 6.0 ± 0.2 pups, n = 104; resuturing: mean = 4.9 ± 0.7 pups, n = 8; $t(110) = 1.56$, $p = 0.12$, unpaired t test; **Figure 3.4 D**). This indicated that subjecting the dam to a second, short, anaesthetic episode did not increase the risk of embryonic mortality.

Following on from the observation that surgeon technique was associated with dam mortality rate, it was postulated that surgeon technique may also be correlated with embryonic mortality. To evaluate the relationship between surgeon technique and embryonic mortality, the birth rates following surgery performed by three surgeons were compared. Significant variation in the litter size following *in utero* surgery was revealed between surgeons (surgeon A: mean = 5.1 ± 0.2 pups, n = 77; surgeon B: mean = 5.8 ±

0.2 pups, n = 65; surgeon C: mean = 6.7 ± 0.2 pups, n = 72; $F(2, 211) = 12.99$, $p < 0.0001$; one-way ANOVA; surgeon A vs C: $p < 0.0001$; surgeon B vs C: $p = 0.01$; post hoc Tukey's test for multiple comparisons; **Figure 3.4 E**). These data indicate that embryonic survival following *in utero* surgery is significantly associated with surgeon technique.

3.2.4 Refinement to the surgical protocol reduces the incidence of intra-operative morbidity

In order to minimise the effect of *in utero* surgery on the health of the dam and her offspring, specific targets for improvement to the surgical protocol were identified and general refinements were made (**Figure 3.5 A**). Steps were taken to improve intra-operative asepsis, and the analgesic protocol was developed to minimise intra- and post-operative pain, and therefore reduce the anaesthetic requirement. Surgeon training was formalised to improve the standard and consistency of the surgical technique and to educate on specific procedures such as titration of anaesthetic delivery. Finally, a formalised system of post-operative monitoring was employed in order to ensure the prompt identification of morbidity. The standard analgesic protocol was expanded to add buprenorphine to the existing meloxicam-based protocol in order to provide multimodal analgesia (Parker, Austin, Wilkerson, & Carbone, 2011). The duration of analgesic provision was also extended to include pre-emptive analgesia and three days of post-operative analgesia (**Figure 3.5 B**). Furthermore, a subset of refinements were evaluated in terms of their ability to minimise two key adverse events that posed a particularly high risk of occurrence to the individual: inadvertent intra-operative hypothermia and post-operative wound dehiscence (**Figure 3.5 C**).

Inadvertent intra-operative hypothermia represents a potential source of serious physiological disturbance (Doufas, 2003). The frequency and severity of this adverse

A

General refinement	Goal
Use large, sterile surgical drapes	Maintenance of intra-operative asepsis
Provide pre-operative analgesia	Anaesthetic-sparing, prevention of central pain sensitisation
Titrate delivery of anaesthetic agent	Minimise maternal & embryonic physiological disruption
Increase post-operative analgesic provision	Minimise physiological & behavioural stress
Improve surgeon training	Improve outcome and consistency
Increase frequency of post-operative monitoring	Improve identification of humane endpoints

B

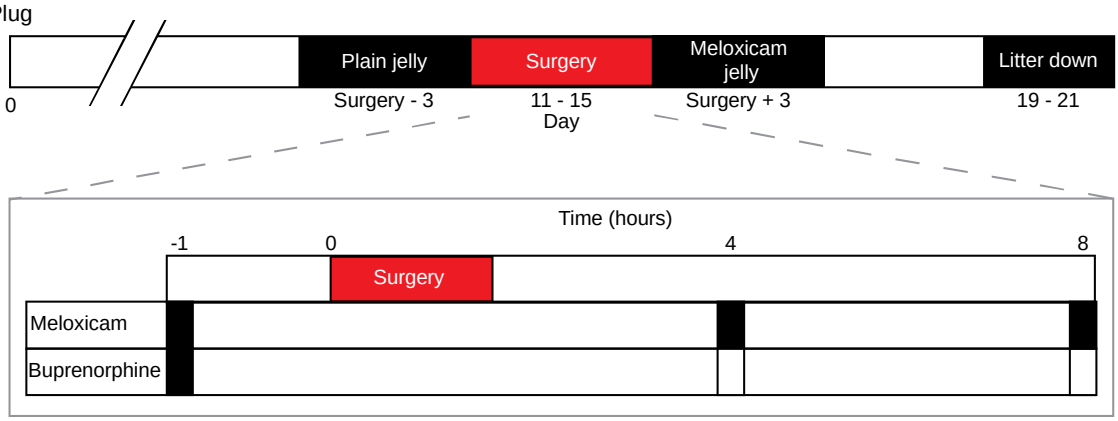

Time (hours)	Drug	Dosage (mg/kg)	Route of administration
-1	Meloxicam	5	Subcutaneous injection
-1	Buprenorphine	0.1	Subcutaneous injection
0	Surgery		
4 - 6	Buprenorphine	0.1	Oral /subcutaneous injection
8 - 12 (optional)	Buprenorphine	0.1	Oral /subcutaneous injection
24	Meloxicam	5	Oral
48	Meloxicam	5	Oral
72	Meloxicam	5	Oral

C

Evaluated refinements	Goal
Minimise anaesthetic duration Use water-resistant surgical drapes Apply static warm water thermal support	Minimise intra-operative hypothermia
Suture pattern for skin wound closure	Minimise the occurrence of wound dehiscence

Figure 3.5: A refined protocol for *in utero* surgery in mice. (**A**) Putative refinements were made to the surgical protocol over the course of the six year investigation period in order to address the goals listed. (**B**) Schematic depicting the improved protocol for post-operative analgesia based on administration of multimodal analgesic comprising meloxicam and buprenorphine. Mice were administered plain jelly for three days prior to surgery in order to habituate to the novel foodstuff, which was used to deliver analgesia post-operatively. Pre-emptive analgesia was administered parenterally around 30 minutes to 1 hour before the induction of anaesthesia. Post-operative, multimodal analgesia was administered either orally or parentally based on assessment of the individual animal for the first 24 hours following surgery. Meloxicam monotherapy was extended to three days post-operatively. (**C**) A subset of putative refinements were selected to undergo a systematic evaluation of their effectiveness.

event is unknown during *in utero* surgery in mice. To characterise the change in core body temperature of the dam during surgery, a rectal temperature probe was used over the course of *in utero* surgery and under a range of different surgical conditions. Body temperature measurements were obtained immediately after the onset of anaesthesia and at the offset of anaesthetic delivery. In a subset of dams, the core body temperature was also recorded at five minute intervals throughout the procedure. Mice were placed on a heat pad set at 40 ^{o}C during surgery and were recovered from anaesthesia in a warming cabinet set at 36 ^{o}C until either resumption of grooming behaviour or a maximum duration of 30 minutes.

All mice exhibited a decrease in body temperature over the course of anaesthesia, which lasted 44 ± 1 minutes on average (n = 30). The mean decrease in core body temperature of 2.9 ± 0.3 ^{o}C represented a reduction in core body temperature from 37.9 ± 0.1 ^{o}C, at the onset of anaesthesia, to 34.0 ± 0.4 ^{o}C at the offset of anaesthesia. The magnitude of the change in body temperature was significantly correlated with the duration of anaesthesia ($r(30) = -0.5$, $p = 0.0029$, Pearson's correlation coefficient; **Figure 3.6 A**). Consequently, it was proposed that a longer duration of anaesthesia and greater decrease in body temperature would be associated with a slower recovery from anaesthesia. This hypothesis was tested by examining the relationship between these variables and the latency to the animal exhibiting grooming behaviour (indicating resumption of normal behaviour after regaining consciousness). Latency to grooming following return to consciousness was 16 ± 1 minutes across all surgeries (n = 30). The duration of anaesthesia was not correlated with the latency to grooming ($p = 0.7$, Pearson's

(**Figure 3.6 cont. from page 71**) drape: $r(10) = -0.98$, $p < 0.0001$; water-permeable drape: $r(10) = 0.99$, $p < 0.0001$; Pearson's correlation coefficient). (**E**) Application of a water-resistant, rather than a water-permeable, drape caused a significant reduction in the change in core body temperature during anaesthesia (water-permeable drape: mean = -5.3 ^{o}C ± 0.3 ^{o}C, n = 12; water-resistant: mean = -2.2 ^{o}C ± 0.2 ^{o}C, n = 18; $t(27.31) = 9.50$, $p < 0.0001$; unpaired t test with Welch's correction). (**F**) Application of SWWTS caused a significant reduction in the magnitude of the change in core body temperature during anaesthesia when used in conjunction with a water-permeable drape. (SWWTS absent: mean = - 4.4 ^{o}C ± 0.2 ^{o}C, n = 17; SWWTS present: mean = - 2.8 ^{o}C ± 0.4 ^{o}C, n = 13; $t(20.43) = 3.53$, $p = 0.002$; unpaired t test with Welch's correction). Lines of best fit for all plots were calculated by linear regression.

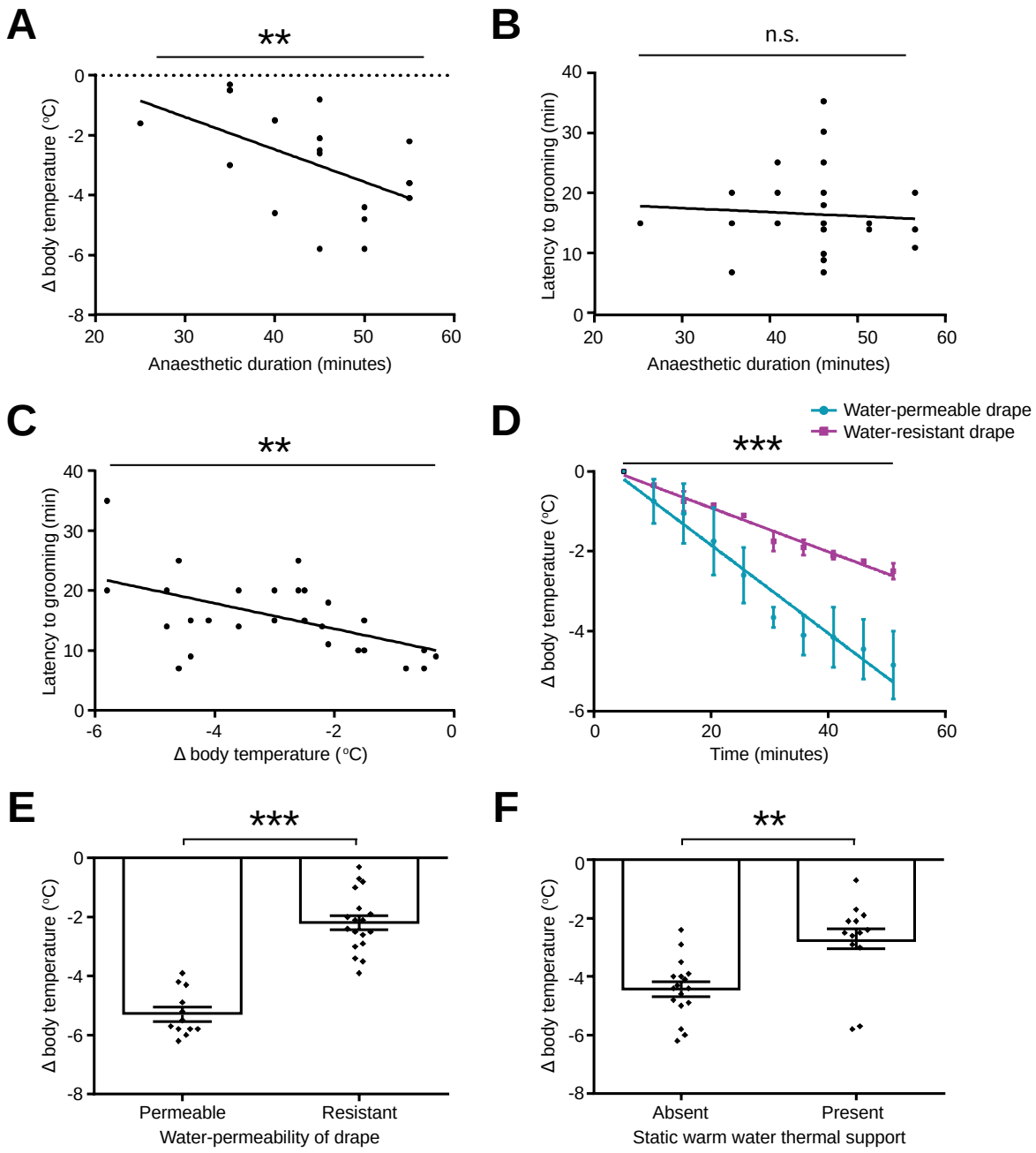

Figure 3.6: Surgical refinements significantly reduce the severity of intra-operative hypothermia in mice undergoing laparotomy for *in utero* surgery. (**A**) The magnitude of the change in core body temperature was significantly correlated with anaesthetic duration (r (30) = - 0.5, p = 0.003, Pearson's correlation coefficient). (**B**) There was no correlation between anaesthetic duration and the latency to first grooming after return to consciousness (p = 0.7, Pearson's correlation coefficient). (**C**) Latency to grooming following return to consciousness was significantly correlated with the magnitude of the change in core body temperature during anaesthesia (r (30) = - 0.5, p = 0.0029, Pearson's correlation coefficient). (**D**) Application of a water-resistant, rather than a water-permeable, drape significantly reduced the rate of change of body temperature during anaesthesia (n = 3 water-permeable, n = 3 water-resistant, F 1, 36 = 21.06, p < 0.0001, linear regression). Duration of anaesthesia with either a water-resistant or a water-permeable drape was significantly positively correlated with the magnitude of the change in core body temperature during the anaesthetic (water-resistant (cont. on page 70)

correlation coefficient; **Figure 3.6 B**). However, the magnitude of the change in body temperature was significantly correlated with the latency to grooming behaviour ($r(30) = -0.5$, $p = 0.0029$, Pearson's correlation coefficient; **Figure 3.6 C**). This indicated that minimising the change in a dam's core body temperature during anaesthesia is a mechanism by which resumption of normal behaviour could be accelerated.

The next step therefore, was to examine whether the decrease in core body temperature during anaesthesia could be attenuated. Two methods were assessed in terms of their ability to change core body temperature during anaesthesia. Firstly, the application of a water-resistant, rather than a water-permeable, drape, in order to reduce heat loss by evaporation. Secondly, the provision of static warm water thermal support (SWWTS) as supplementary heating (see Figure 3.1 B). Evaporation is a significant source of heat loss during anaesthesia due to the application of cleaning solution and opening of the abdomen to expose viscera (Díaz & Becker, 2010). However, it was proposed that evaporation resulting from saturation of the animal with lavage solution during surgery could be reduced by the application of a water-resistant drape, rather than the conventional water-permeable drape. This hypothesis was tested by recording the dam's body temperature every five minutes in a subset of surgeries in which either a water-resistant or a water-permeable drape was used. Body temperature decreased during surgery with both types of drape and was significantly correlated with the duration of anaesthesia (water-resistant drape: $n = 3$, $r(10) = -0.98$, $p < 0.0001$; water-permeable drape: $n = 3$, $r(10) = 0.99$, $p < 0.0001$; Pearson's correlation coefficient). However, the use of a water-resistant, rather than a water-permeable, drape significantly reduced the rate at which body temperature declined during anaesthesia ($F(1, 36) = 21.06$, $p < 0.0001$, linear regression; **Figure 3.6 D**). Over the duration of anaesthesia, application of a water-resistant drape was correlated with a significant reduction in the magnitude of the change in core body temperature when compared to a water-permeable drape (water-permeable drape: mean = $-5.3^{o}C \pm 0.3^{o}C$, $n = 12$; water-resistant: mean = $-2.2^{o}C \pm 0.2^{o}C$, $n = 18$; $t(27.31) = 9.50$, $p < 0.0001$, unpaired t test with Welch's correction; **Figure 3.6 E**). This

supports the use of a water-resistant drape as a refinement for reducing intra-operative heat loss.

Supplementary heating is recommended to mitigate the decrease in body temperature during anaesthesia (Gargiulo et al., 2012). Although a heat mat was provided as standard for animals undergoing anaesthesia, mice still experienced the significant decrease in core body temperature described above. For this reason, the effect of providing further supplementary heating in the form of SWWTS was assessed. SWWTS is a simple and commonly-used method of providing supplementary heating to rodents (colloquially known as 'hot hands'), which involves placing a glove filled with warm water alongside the animal to provide heat by radiation (Uhlig et al., 2015). However, the efficacy of this intervention is unknown. This was evaluated by applying SWWTS to a subset of surgeries in which a water-permeable drape was employed. Provision of SWWTS was associated with a significant reduction in the change in core body temperature during anaesthesia (SWWTS absent: mean = - 4.4 ± 0.2 ^{o}C, n = 17; SWWTS present: mean = - 2.8 ± 0.4 ^{o}C, n = 13t (20.43) = 3.53, p = 0.002; unpaired t test with Welch's correction, **Figure 3.6 F**). This supports the application of SWWTS as an effective method of supplementary heating. In summary, these data demonstrate that a significant reduction in core body temperature occurs during *in utero* surgery in mice, and that measures can be taken to reduce the change in core body temperature.

3.2.5 Refinement to the method of skin closure reduces the incidence of wound dehiscence

Surgery wound dehiscence is often mentioned in conjunction with *in utero* surgery in rodents (Szczurkowska et al., 2016). However, this relationship has not been systematically documented. This was performed by analysing records of wound

dehiscence following *in utero* surgery in the Akerman group. Most instances of wound dehiscence occurred one day post-operatively (26 %, 31/121 dams; **Figure 3.7 A**) and all occurred within two days of surgery. The occurrence of wound dehiscence following the initial surgical protocol, in which skin was closed with a horizontal mattress suture pattern, was 33 % across three experienced surgeons (40/121 surgeries). The incidence of wound dehiscence did not vary significantly between surgeons (surgeon A: 35 %, 24/68; surgeon B: 20 %, 3/15; surgeon C: 34 %, 13/38; C^2 (2, n = 121) = 0.5, p = 0.8; chi-square test). This indicated that surgical technique was not associated with the rate of wound dehiscence, at least between these surgeons. There was a low incidence (3 % of all dams, 4/121) of total wound dehiscence, in which there was dehiscence of both the muscle and skin layers of wound closure leading to evisceration. The remaining cases of wound dehiscence (30 % of all dams, 37/121) involved the skin layer only.

In order to ascertain the optimal technique for wound closure, the relationship between the suture pattern and the incidence of wound dehiscence was analysed. Three suture patterns were assessed in year four to six of the refinement period: (i) horizontal mattress sutures (recommended in the original surgical protocol), (ii) simple interrupted sutures and (iii) intradermal sutures (**Figure 3.7 B**). Horizontal mattress and simple interrupted sutures were classified together as transdermal sutures, traversing the thickness of the skin and resulting in a portion of the suture being sited externally. In contrast, intradermal sutures were located entirely within the skin, thereby positioning the suture completely internally. The first assessment was to compare the two types of

---

(Figure 3.7 cont. from page 75) sutures. (**C**) The pattern of transdermal suture (horizontal mattress or simple interrupted suture pattern) was not correlated with the incidence of wound dehiscence (simple interrupted: dehiscence = 28 %, 17/60 dams; horizontal mattress: dehiscence = 18 %, 17/94 dams; p = 0.2, Fisher's exact test). (**D**) Intradermal suture placement was protective against wound dehiscence in comparison to transdermal sutures (transdermal: dehiscence = 20 %, 5/25 dams; intradermal: 4 %, 2/55 dams; RR 0.18 95 % CI 0.04 – 0.9, p = 0.03, Fisher's exact test). (**E**) Wound dehiscence was less likely in animals that had already undergone an episode of wound dehiscence (no previous dehiscence: 30 %, 33/109 dams; previous dehiscence: 12 %, 4/33 dams; RR 0.4, 95 % CI 0.2 – 1.0, p = 0.04, Fisher's exact test). (**F**) The risk of dehiscence of both the skin and muscular layers resulting in evisceration was not associated with a history of wound dehiscence (no previous dehiscence: 3 %, 3/109 dams; previous dehiscence: 3 %, 1/33 dams; p = 1, Fisher's exact test).

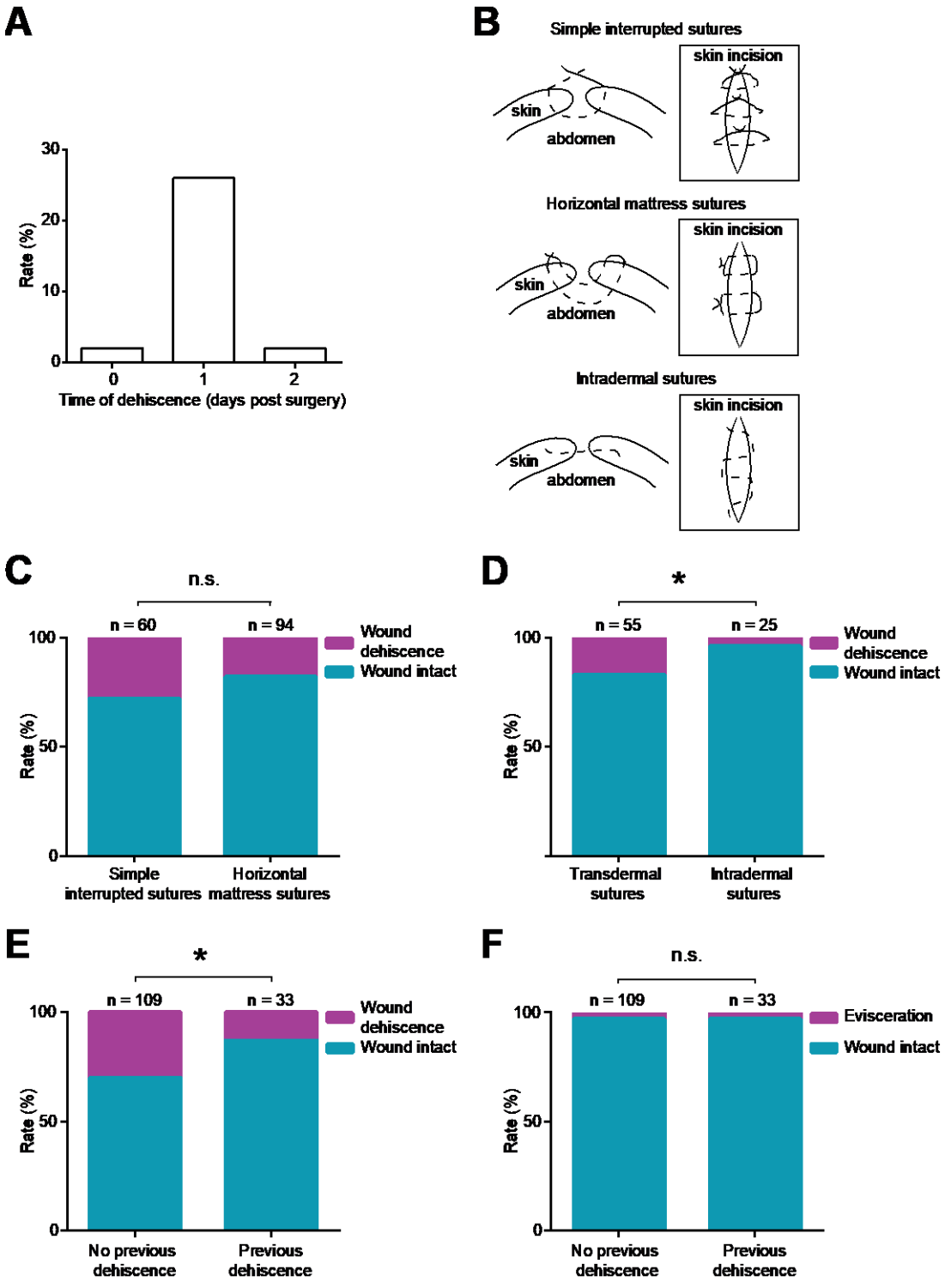

Figure 3.7. Intradermal suture placement is protective against laparotomy wound dehiscence. (**A**) Episodes of wound dehiscence after transdermal suture placement occurred in the early post-operative period. The highest incidence of wound dehiscence was on the first day following surgery (26 %, 31/121 of all dams). (**B**) Schematic of the suture patterns used for closure of the laparotomy skin incision. Transdermal sutures in a simple interrupted or horizontal mattress pattern were initially used for skin closure. Intradermal sutures were proposed to reduce the incidence of wound dehiscence due to their entirely internal positioning, in contrast to transdermal (cont. on page 74)

transdermal suture pattern with respect to the incidence of wound dehiscence. No association was found between the pattern of transdermal wound closure (horizontal mattress or simple interrupted) and the incidence of wound dehiscence (simple interrupted: dehiscence = 28 %, 17/60 dams; horizontal mattress: dehiscence = 18 %, 17/94 dams; p = 0.2, Fisher's exact test, **Figure 3.7 C**). I proposed that intradermal suture placement, however, would be associated with a lower incidence of wound dehiscence by reducing the potential for the animal to disrupt the sutures. Indeed, wound closure with intradermal sutures was associated with a significant reduction in the incidence of wound dehiscence from 21 % to 4 % of all dams for a single surgeon that tested this suture pattern (transdermal: dehiscence = 20 %, 5/25 dams; intradermal: 4 %, 2/55 dams; RR 0.18 95 % CI 0.04 – 0.9, p = 0.03, Fisher's exact test; **Figure 3.7 D**). This confirms the efficacy of intradermal suture placement for skin wound closure as a measure of reducing the incidence of wound dehiscence.

Wound dehiscence occasionally led to two sequelae that exceed the threshold for a humane endpoint: either a second episode of wound dehiscence or evisceration. Evisceration occurred due to dehiscence of the wound in the abdominal musculature, in addition to skin wound dehiscence. The rate of these outcomes was examined independently to establish whether a history of wound dehiscence in a dam is associated with the risk of subsequent dehiscence (i.e. a second dehiscence). In fact, the risk of wound dehiscence was lower in animals that had already experienced an episode of wound dehiscence (no previous dehiscence: 30 %, 33/109 dams; previous dehiscence: 12 %, 4/33 dams; RR 0.4, 95 % CI 0.2 – 1.0, p = 0.04, Fisher's exact test; **Figure 3.7 E**). Finally, the relationship between wound dehiscence history and evisceration was evaluated. The risk of evisceration was not associated with a history of skin wound dehiscence (no previous dehiscence: 3 %, 3/109 dams; previous dehiscence: 3 %, 1/33 dams p = 1, Fisher's exact test; **Figure 3.7 F**). This suggests that experiencing an episode of dehiscence is not a risk factor for, or indicator of, the probability of evisceration. These findings confirm that wound dehiscence is a common post-operative complication of *in*

utero surgery in mice in which the skin wound is closed with transdermal sutures. Furthermore, this risk can be diminished by closing the skin incision with intradermal sutures.

3.2.6 Refinement of the protocol for *in utero* surgery improves outcomes for experienced and newly-trained surgeons

The surgical protocol was refined iteratively over a number of years and the overall impact of these measures on the health and welfare of animals receiving surgery was investigated in two ways. First, by evaluating the outcomes of surgeries performed by experienced surgeons. And second, by evaluating the outcome of surgeries performed by newly-trained surgeons. In order to quantify the efficacy of the modified protocol (Appendix 1), surgical records were examined to compare the dam outcome and embryonic survival before, and after, refinements were implemented. Baseline data comprised surgical outcomes for the first two years of the refinement period. Corresponding post-refinement measures were obtained from the last two years of the refinement period (**Figure 3.8 A**). Records selected for analysis were restricted to those from two surgeons who were experienced before the implementation of refinements, so as to minimise potential confounds resulting from changes in surgeon experience over time.

The survival rate of dams following *in utero* surgery performed by experienced surgeons was found not to differ significantly between baseline and post-refinement (baseline: humane endpoint: 11 %, 4/38, unexpected death: 0/38; post-refinement: humane endpoint: 5 %, 4/84, unexpected death: 2 %, 2/84; $p = 0.07$, C^2 test; **Figure 3.8 B**). However, refinements were associated with an increase in embryonic survival. Surgery litters born after refinement were significantly larger than surgery litters born before refinement (baseline: mean = 4.9 ± 0.2, n = 93; post-refinement: mean = 6.4 ± 0.2,

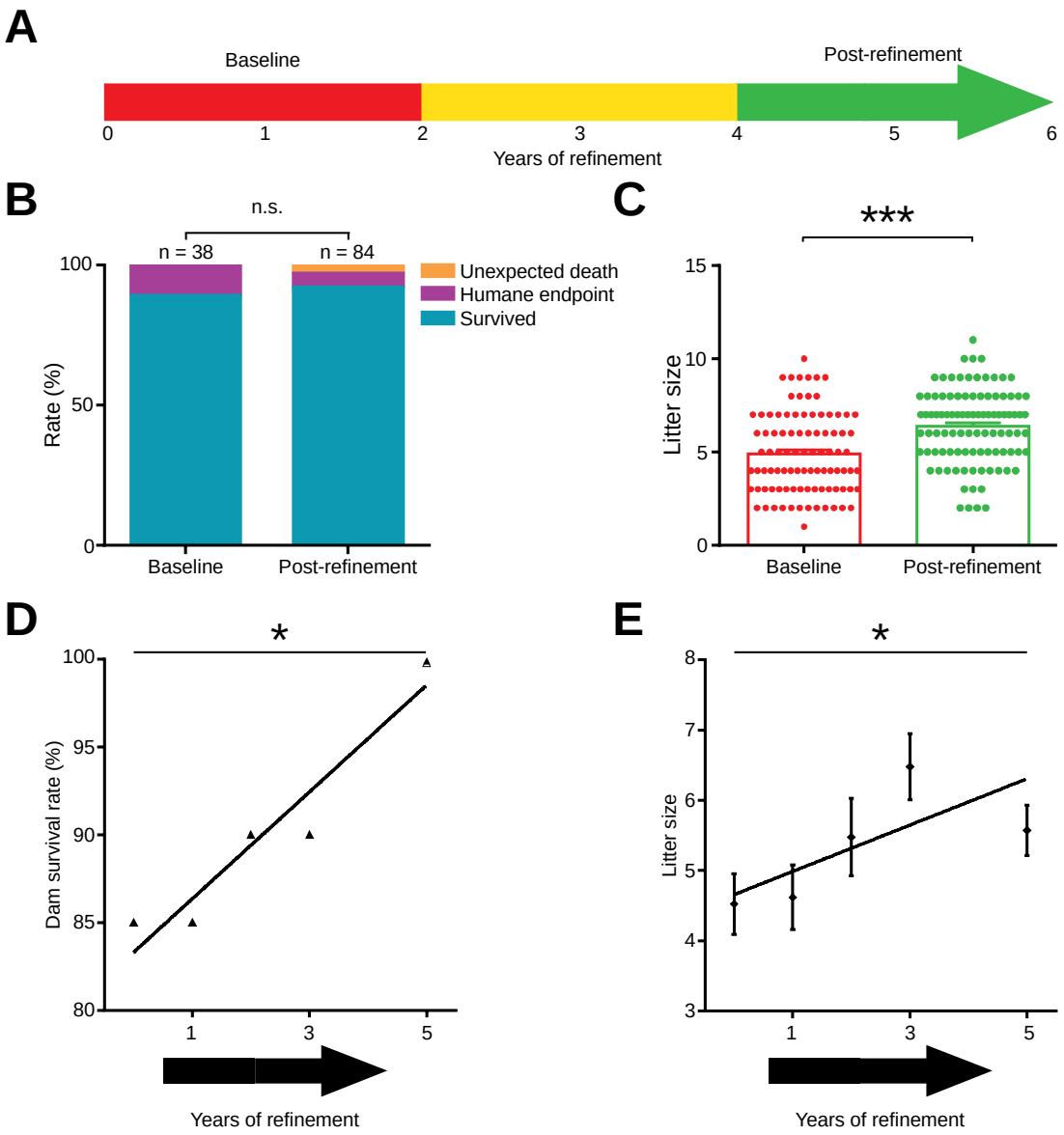

Figure 3.8: Refinement of *in utero* surgery improves post-operative mortality rates. (**A**) Timeline of the period over which *in utero* surgery was assessed. Dam and embryonic morbidity and mortality was pooled over the first two and last two years in order to provide data for baseline and post-refinement, respectively. (**B**) The survival rate of dams following *in utero* surgery performed by two experienced surgeons did not change significantly over the refinement period (baseline: humane endpoint: 11 %, 4/38, unexpected death: 0/38; post-refinement: humane endpoint: 5 %, 4/84, unexpected death: 2 %, 2/84; $p = 0.07$, C^2 test). (**C**) For procedures performed by experienced surgeons, litter size significantly increased over the refinement period (baseline: mean = 4.9 ± 0.2, n = 93; post-refinement: mean = 6.4 ± 0.2, n = 97; $p < 0.0001$; one-way ANOVA with Tukey's post hoc test for multiple comparisons). (**D**) The survival rate of dams from the first twenty surgeries performed by newly-trained surgeons showed a significant increase over the duration of the refinement period ($R^2 = 0.91$, $F(1, 3) = 31.15$, $p = 0.01$, linear regression). (**E**) The size of litters born following the first twenty surgeries performed by a newly-trained surgeon showed a significant increase over the duration of the refinement period ($R^2 = 0.059$, $F(1, 96) = 5.97$, $p = 0.016$, linear regression), equating to an increase of 0.3 ± 0.1 pups per litter, per year (95 % CI 0.06 to 0.6). Each point in (D) and (E) represents the first twenty surgeries performed by a newly-trained surgeon.

n = 97; $p < 0.0001$; one-way ANOVA with Tukey's post hoc test for multiple comparisons; **Figure 3.8 C**). This indicated that for experienced surgeons, the refined surgical protocol significantly improved the mortality rate of embryos, but not dams.

In order to test the impact of the surgical refinements on the learning curve of newly-trained surgeons, the survival rate of dams and embryos for the first 20 surgeries performed by newly-trained surgeons were evaluated. Five surgeons were trained over the refinement period, with no more than one surgeon trained per year. The survival rate of dams from the first twenty surgeries performed by a newly-trained surgeon showed a significant linear increase over the duration of the refinement period ($R^2 = 0.91$, $F(1, 3) = 31.15$, $p = 0.01$, linear regression). This represented an increase from 85 % survival of dams from the new surgeon trained in 2011, to 100 % survival of dams from the new surgeon trained in 2016 (**Figure 3.8 D**). Moreover, the size of litters born following the first twenty surgeries performed by a newly-trained surgeon showed a significant linear increase over the duration of the refinement period ($R^2 = 0.059$, $F(1, 96) = 5.97$, $p = 0.016$, linear regression; **Figure 3.8 E**). This equated to an increase of 0.3 ±0.1 pups per litter, per year (95 % CI 0.06 to 0.6). Furthermore, when both dam survival and birth rate were factored together, surgical refinement represented a cumulative increase of 34 ± 3 % in the yield of pups per surgery performed by experienced surgeons (from 4.4 ± 0.2 pups per surgery at baseline to 5.9 ± 0.2 pups per surgery post-refinement) and 45 ± 3 % amongst newly trained surgeons (from 3.8 ± 0.2 pups per surgery at baseline to 5.6 ± 0.2 pups per surgery post-refinement). These data demonstrate that refinement of the surgical protocol resulted in an improvement in the health and welfare of animals undergoing *in utero* surgery, which was most effective for newly trained surgeons.

3.3 Discussion

In this chapter I have described a protocol for *in utero* surgery in mice and characterised the risk of morbidity and mortality to the dam and her offspring following surgery. I have investigated the incidence of two surgery-associated morbidities to which rodents are particularly susceptible: namely, inadvertent intra-operative hypothermia and post-operative wound dehiscence. I have identified factors that are associated with the occurrence of these events and characterised measures taken to mitigate the risk of their occurrence. Finally, I have produced a refined surgical protocol and demonstrated its efficacy in improving the survival of the dam and her offspring following surgery.

3.3.1 Morbidity and mortality of the dam following *in utero* surgery

In utero surgery posed a demonstrable risk to the dam of either unexpected death, or fulfilment of a humane endpoint of 18 % in the seven days following surgery. This is higher than the death rate of 7 % following *in utero* surgery reported in the only comparable study of dam survival following *in utero* surgery (Punzo & Cepko, 2008). These differences could be explained by subjectivity in the definition, and identification, of threshold morbidity that constitutes a humane endpoint. This is likely to lead to variation between institutions and individuals. It is also possible that differences between Punzo and Cepko (2008) and the present study could be explained by differences in the underlying data included. For example, it is possible that the death rate of dams in the study of Punzo and Cepko constituted only the category that would be classified as ‘unexpected death’ in the current study (Punzo & Cepko, 2008). In my data, the rate of unexpected death ranged from 0 – 4 % across three experienced surgeons who used the original surgical protocol, which is closer to the 7 % reported by Punzo and Cepko (Punzo & Cepko, 2008). Finally, strain

differences may also contribute to the difference in survival rates across the two studies. Punzo and Cepko performed *in utero* surgery across three mouse strains, but reported survival only for the CD1 strain. These authors noted that the CD1 strain had a higher survival rate than the C57BL/6 dams, and it was the C57BL/6 strain that was used exclusively in the present study. Further work is necessary to establish the extent to which strain differences are associated with a variation in mortality rate, and to explore whether the mortality rate following *in utero* surgery observed in the present study is comparable to rates observed in other research groups.

As highlighted above, the majority of cases of death of the dam arose due to the development of serious morbidity triggering enforcement of a humane endpoint (threshold morbidity, necessitating Schedule 1 killing of the dam (A(SP)A, 1986)). Specific diagnoses were not determined in most cases of serious morbidity, which were identified by physical examination alone. These cases were therefore described by the primary, non-specific presenting symptom of malaise, and the cause of these cases of morbidity was unknown. It is likely that this population represents a heterogeneous group of surgery-associated pathologies, which could include diseases that cannot be diagnosed by gross examination (such as septic peritonitis), and diseases for which diagnosis is difficult (such as adhesion-associated pain; Polymeneas et al., 2001; Simmen et al., 2008).

Sub-threshold dam morbidity was not specifically assessed and is rarely identified, probably due to the conservatism in ensuring good standards of animal welfare that means that few cases of morbidity are classified as sub-threshold. Wound dehiscence was a specific case of sub-threshold morbidity that was investigated and will be discussed further in a subsequent section. In brief, wound dehiscence occurred in 33 % of all dams prior to refinement, which resulted in a significant number of animals having to undergo a second episode of anaesthesia for wound repair. A subset of these cases (9 % of cases of wound dehiscence) constituted threshold morbidity, either due to repeated wound dehiscence or evisceration. Unexpectedly, no cases of wound infection or incisional herniation were identified. This is despite these representing common laparotomy-

associated morbidities in humans, occurring at rates of 25 % and 11 % of laparotomies, respectively (Diener et al., 2010; Mudge & Hughes, 1985; Pinkney et al., 2013). This interspecies differences could be attributable to the nature of rodent physiology, or to external factors. For example, it is possible that wound infection and incisional herniation are less likely to be diagnosed in rodents. Furthermore, it is likely that most dams do not live long enough following surgery to develop incisional herniation, which is a post-operative complication that can occur more than a year following surgery in humans (Mudge & Hughes, 1985). The short lifespan of dams also limits the relevance of other delayed post-operative complications such as infertility and adhesion formation that pose a significant risk following laparotomy in humans (Barmparas et al., 2010; Chen, Teigen, Reynolds, Johnson, & Fowler, 1998; Polymeneas et al., 2001).

3.3.2 Mortality of the embryos following *in utero* surgery

Embryonic mortality can manifest as resorption, abortion or still birth. Overt embryonic death may not be identified due to the lack of external signs of resorption, and cannibalism of dead pups that are aborted or still born (Hau & Van Hoosier, 2003). The difference in the birth rate between surgery and non-surgery litters was therefore used as a proxy for embryonic death. Birth rate was significantly lower following surgery, and the death rate attributable to *in utero* surgery was estimated to be 26 %. This is comparable to the embryonic death rate of 20 % reported by Punzo et al. (2008) following *in utero* surgery, and within the range of 10 – 40 % reported in other studies (Saito & Nakatsuji, 2001; Shimogori & Ogawa, 2008). The figure reported by Punzo et al. is likely to represent an overestimation of embryonic death rate compared to the present study, because it is calculated from the difference between the number of embryos present at the time of surgery and the number born (Punzo & Cepko, 2008). Therefore, this includes the low

level of embryonic death that occurs between mid-gestation and birth in non-surgery dams (The Jackson Laboratory, 2016b). The true difference in embryonic death rate between the current study and Punzo et al. is likely to be greater than the 6 % indicated. Again, it is likely that mouse strain is a confounding factor between the two studies as both the endogenous death rate and surgery-associated death rate have been shown to exhibit inter-strain differences (Punzo & Cepko, 2008; The Jackson Laboratory, 2016b).

Characterising birth rates made it possible to assess factors that influence litter size following surgery. There was no association between dam age and birth rate within the confines of the relatively narrow age window (between 8 weeks and 8 months of age) used here. Factors associated with the embryonic injections also showed little association with birth rate. Neither the nature of the brain manipulation, nor the proportion of the litter that underwent intraventricular injection, was related to birth rate. This suggested that embryonic mortality is more likely to be linked to the anaesthesia and laparotomy, rather than the procedure performed on the embryos.

The difference in birth rate between surgery at E14.5 and E12.5 was the only significant relationship revealed by analysis of the procedural variables. The effect of age was also examined by Punzo and Cepko (2008), where the authors revealed that later surgery was associated with a higher risk of embryonic death than earlier surgery. However, the composition of these data differed from the current study, in which birth rate was only assessed from litters in which pups were born and therefore abortions were not included (Punzo & Cepko, 2008).

3.3.3 Inadvertent intra-operative hypothermia in mice

All dams exhibited a decrease in core body temperature over the course of anaesthesia. There is neither a strict definition of hypothermia in mice, nor a thorough understanding of

the correlation between body temperature and changes in physiology. This means it is not possible to define the threshold between a non-pathological and a pathological decrease in body temperature. Instead, the definition of intraoperative hypothermia in humans can be extrapolated to the current study in order to estimate the extent of hypothermia experienced by dams during *in utero* surgery. A decrease in core body temperature from 37^{o}C to 36^{o}C is deemed to constitute clinically-relevant hypothermia in humans (Hart, Bordes, Hart, Corsino, & Harmon, 2011). Since the core body temperature of rodents is similar to humans (Talan, 1984; The Jackson Laboratory, 2016a), a decrease of 1^{o}C in the core body temperature of dams can also be assumed to be physiologically relevant. Applying this criterion to these data, 87 % of dams experienced clinically significant hypothermia. In fact, the mean decrease in core body temperature was 2.9 ± 0.3 ^{o}C.

Redistribution of heat from the core to the periphery is a significant and unavoidable cause of the decrease in core body temperature during the first hour of anaesthesia, which is likely to contribute to the duration-dependent hypothermia observed in the present study (Díaz & Becker, 2010; Hart et al., 2011). Furthermore, the rate of heat loss was likely to have been exacerbated by the necessity to perform surgery in a laminar flow hood, accelerating heat loss by convection and evaporation (Díaz & Becker, 2010). The efficacy of switching from a water-permeable to a water-resistant drape suggests that, as expected, saturation of the animal during surgery and the resulting evaporation was a significant cause of the hypothermia experienced by mice during *in utero* surgery.

The provision of active heating devices, using forced air warming or circulating warm water for example, is the gold-standard method of supporting thermoregulation during anaesthesia (Leung, Lai, & Wu, 2007; Rembert, Smith, & Hosgood, 2004; Taylor, 2007). However, the necessity for expensive equipment and hindrance to abdominal access that these devices can pose is likely to result in their underuse. A simple and commonly used substitute in rodent anaesthesia is to place a glove filled with warm water (SWWTS) in close proximity to the animal, in order to provide heat by radiation (Hau & Van Hoosier, 2003). This measure was demonstrated to be effective in reducing the

magnitude of the change in core body temperature. However, one significant drawback of this method of heating in comparison to active systems is the gradual cooling of the water to room temperature. Indeed, it is possible that this intervention is detrimental once the water has reached room temperature, since the water may then act as a heat sink. Further work is necessary to establish whether this is the case. Furthermore, there are other simple interventions that may reduce the incidence of inadvertent intraoperative hypothermia that warrant investigation. For example, pre-warming an animal (prior to the induction of anaesthesia) has been shown in other paradigms of anaesthesia to be effective in reducing the decrease in core body temperature associated with redistribution of heat from the core to the periphery (Andrzejowski, Hoyle, Eapen, & Turnbull, 2008; Hart et al., 2011).

The effect of intraoperative hypothermia on behaviour in the immediate post-operative period was evident. The magnitude of the temperature decrease was correlated with the latency to the resumption of grooming behaviour following recovery of consciousness. A relationship between the core body temperature and latency to grooming could be explained by the delayed drug metabolism that has been associated with, even mild, intraoperative hypothermia (Hart et al., 2011). Animals in which recovery was prolonged may therefore represent a population that are susceptible to anaesthetic overdose. These data provide evidence that intraoperative hypothermia is an important consideration for *in utero* surgery in mice that can be mitigated by simple measures, including minimising the duration of anaesthesia, employing water-resistant surgical drapes and providing supplementary heating in the form of SWWTS. The relationship between intraoperative hypothermia and post-operative morbidity in this paradigm remains an important subject for future study.

3.3.4 Laparotomy wound dehiscence following *in utero* surgery

In accordance with anecdotal reports of a high rate of wound dehiscence in rodents, wound dehiscence occurred in 33 % of dams that underwent the original surgical protocol. A second episode of anaesthesia for wound repair was necessary in the majority of these animals. Wound dehiscence was associated with a low level of serious morbidity: a small number of animals experienced evisceration following total wound dehiscence. Furthermore, a small subset of animals experienced repeated dehiscence that constituted a humane endpoint. A history of previous wound dehiscence did not predispose an animal to either of these serious morbidities, nor was it associated with an increase in embryonic mortality. Wound repair after a single episode of dehiscence, therefore, remains justified.

The pattern of skin closure using sutures was identified as a variable that may be correlated with the rate of wound dehiscence. Different suture patterns are associated with a variable degree of pain in other species (Cassie, Chatterjee, Mehta, & Haworth, 1988; Sylvestre, Wilson, & Hare, 2002), and internal and external suture patterns present differential susceptibility to removal by the animal. Unsurprisingly, intradermal sutures were associated with an almost complete reduction in the incidence of wound dehiscence. The pattern of external suture, however, was not associated with the incidence of wound dehiscence. Although intradermal sutures are technically more challenging and come at the cost of a slightly longer anaesthetic (Sylvestre et al., 2002), the significant decrease in dehiscence rate provides good justification for the use of this suture method.

Self-removal of sutures was occasionally observed directly by animal care staff. However, in most cases the animal was found with the wound already dehisced. Three factors support self-removal as the primary cause of wound dehiscence. Firstly, in most cases only the skin wound dehisced and incisional herniation was never reported. Therefore it was unlikely that dehiscence was due to the placement of insecure sutures. Secondly, no predisposing morbidity, such as surgical site infection, was identified.

Thirdly, the proclivity for rodents to chew at their sutures has been noted by ourselves and others (Cepko et al., 1998; Szczurkowska et al., 2016). This raises an interesting question: why does the tendency of rodents to remove sutures extend only to sutures in the skin? Very few cases involved dehiscence of sutures in the musculature, despite dams being presented with the access and opportunity once the skin has dehisced. One attractive explanation is the lack of motivation to remove sutures in the muscle, if discomfort is an instigating factor for self-removal of sutures. This theory is supported by the time-course of wound dehiscence, in which most animals were found dehisced in the first morning following surgery. Due to the short duration of effect of buprenorphine of 4 – 6 hours (Gades, Danneman, Wixson, & Tolley, 2000), only meloxicam analgesia is likely to be effective overnight. Therefore animals would be predicted to experience a peak in post-operative pain in the first night following surgery. The observation that dams experiencing one episode of dehiscence and wound repair were unlikely to experience a second episode of dehiscence, is also consistent with the idea that discomfort is the major trigger for wound dehiscence. Firstly, it suggests that there is not a constant behavioural drive for dams to remove their sutures, as this would not be expected to change over time. Secondly, it indicates that the stimulus for most cases of wound dehiscence is directly related to the surgical procedure: the longer the time that has elapsed since surgery, the lower the drive for wound dehiscence. Taken together, these observations suggest that wound dehiscence is indeed a strong indicator of wound-associated pain. The results highlight the potential for further refinement of the analgesic protocol, which could be the focus of future investigation.

3.3.4 The importance of surgical technique

Over the six year period of review, significant inter-surgeon variability was noted in the rate of dam morbidity and mortality, and in embryo mortality, following surgery. This was despite the fact that surgeons used the same surgical protocol and engaged in mutual observation and information exchange. The specific aspects of surgical technique responsible for these variations was not identified, but may be attributed to different levels of skill in aspects such as aseptic technique, dexterity, tissue handling and anaesthetic management. At the end of the refinement period the outcome measures between the experienced surgeons and newly-trained surgeon were comparable: the dam mortality rates were 92 % and 100 %, respectively, and the birth rate following surgery was 6.4 ± 0.2 and 5.5 ± 0.4 pups per litter, respectively. Combining dam mortality rate and embryonic birth rate, this corresponds to 5.9 pups and 5.5 pups per surgery for experienced and newly-trained surgeons, respectively. These findings offer further evidence for the importance of investing in surgeon training in order to attenuate inter-surgeon differences.

3.3.5 Refinement to the surgical protocol

Comparison of mortality rates revealed that refinement reduced the rate of embryonic death following *in utero* surgery performed by experienced surgeons. Dam mortality rate was unchanged, which may reflect the small potential for improvement from the already-low pre-refinement mortality rate of 11 %. Overall, refinement increased the yield of pups per surgery by 34 %. This would constitute a reduction in the number of dams required for experimentation. Furthermore, it may reflect a decrease in the physiological disruption resulting from surgery that may be evident in more subtle aspects of physiology beyond a reduction in mortality. Further work is necessary to establish whether other measures of

dam and embryonic health are correlated with refinement. The benefits of the refined protocol were most evident amongst newly-trained surgeons, which may reflect a combination of the more prescriptive nature of the new protocol, the extension of the formalised training of new surgeons and the greater effectiveness of learning good habits from the offset. Cumulatively, a reduction in the mortality of both dams and embryos over the first twenty surgeries following training using the refined protocol represented a 45 % increase in the yield of pups per surgery. The refined surgical protocol is detailed in Appendix 1.

Chapter 4
Development of novel retroviral tools for the investigation of neuronal lineage and function in the developing neocortex

4.1 Introduction

The definitive identification of neuronal clones in the neocortex is a challenging problem in neuroscience. This is traditionally addressed by delivering a heritable label to neuronal progenitors using replication incompetent retroviral vectors (Price et al., 1987). Clones can be identified by applying geometric criteria to labelled cells that derive from a small number of transduced progenitors, using the assumption that clonally-related neurons will be spatially clustered. 'Lumping errors' may occur when cells from more than one clone are spatially clustered and, therefore, are assumed to represent a single clone. This could arise through bias in the distribution of independently-labelled cells. For example, it has been speculated that the aggregation of retroviral virions could lead to the infection of adjacent progenitors (Cepko et al., 1998), resulting in artificial clustering of independently-labelled neurons. Conversely, 'splitting errors' may occur if a neuron migrates away from other members of the clone.

An alternative method of clonal labelling is using retroviral vectors to deliver a unique label to progenitors (Golden et al., 1995). The label is heritable and, therefore, common to members of the clone that are generated subsequent to transduction (Golden et al., 1995). This confers the ability to discriminate clones regardless of their geometric distribution, resulting in clonal labelling that is more resistant to lumping and splitting errors (Mayer et al., 2016). The confidence with which this inference can be made depends on the 'complexity' (i.e. the number of unique labels) of the 'library' (i.e. the total pool of labels), and the relative frequency of each label in the pool. Clonal labelling using variable

oligonucleotide sequences (DNA barcodes) to generate combinatorial complexity has achieved around 10^4 - 10^5 genetically unique DNA labels (Golden et al., 1995; Harwell et al., 2015; Mayer et al., 2015). However, DNA barcodes can be difficult to identify from single cells and failure rates of around 50 % are typical (Fuentealba et al., 2015; Harwell et al., 2015). This may result in an underestimation of clone size, or a systematic failure to identify entire clones (Harwell et al., 2015; Mayer et al., 2015). The use of barcoding for the identification of clones has been based on the assumption that only one RNA label is packaged into each virion and that a progenitor is transduced by a single virion. However, there is evidence for erroneous packaging of host RNA during retrovirus generation (Eckwahl et al., 2015; Garcia et al., 2009; Golden et al., 1995; Onafuwa-Nuga et al., 2005; Rulli et al., 2007), which could lead to more than one barcode being packaged into a virion. The extent to which this affects clonal labelling is unknown. A further limitation of current techniques is that the requirement for low frequency labelling to identify clones has been associated with low transgene expression levels (Cepko et al., 1998; Golden et al., 1995). Moreover, clonal labelling techniques have not harnessed the power of functional tools such as optogenetics or advances in single cell analysis, which would facilitate detailed investigation of relationships between clonality and function.

In this chapter I set out to develop two molecular tools for studying clonal relationships. The first is a retrovirus encoding Cre recombinase (Cre) to enable the manipulation of individual clones using Cre-lox technology to improve the performance and versatility of clonal labelling. The second is a retroviral library barcoded with a short, variable oligonucleotide sequence that is transcribed within a cell, enabling barcode retrieval by the amplification and sequencing of either DNA or RNA. I propose that this RNA barcoding could offer a favourable success rate in identifying the label of single cells and greater compatibility with downstream analysis than traditional DNA barcoding. Specifically, my aims were to establish the following:

- Can a Cre-encoding retrovirus achieve recombination in transduced neurons?
- Can functional manipulation of neurons be achieved with Cre-encoding retrovirus?
- Can a retroviral RNA barcode library be produced that can be identified from single cells?
- Does an RNA-barcoding retrovirus enable identification of clonally related cells?

4.2 Results

4.2.1 Improved fluorophore expression in transduced neocortical neurons can be achieved by application of an iCre recombinase-encoding retrovirus in a floxed-STOP tdTom mouse strain

The current application of retroviral labelling in clonal studies of excitatory neocortical neurons relies on low-titre infection by retrovirus, usually encoding a fluorophore, in order to sparsely label progenitors in the developing neocortex. Integration of a single copy of the retrovirally-delivered transgene at a variable location within the host cell genome has been associated with low transgene expression levels (Cepko et al., 1998; Golden et al., 1995; **Figure 4.1 A**). I proposed that a Cre-encoding retrovirus would confer an advantage over standard retroviral labelling techniques by offering improved levels of reporter gene expression and greater versatility through compatibility with a range of floxed reporter mouse strains. I used codon-improved Cre recombinase (iCre), as this has been reported to provide improved expression and greater resistance to epigenetic silencing than the prokaryotic coding sequence (Shimshek et al., 2002). Thus, I set out to test the hypothesis that an iCre-encoding retrovirus (RV-iCre) injected into a floxed-STOP reporter mouse strain would lead to iCre-mediated recombination in transduced neurons and result in strong expression of a reporter gene from

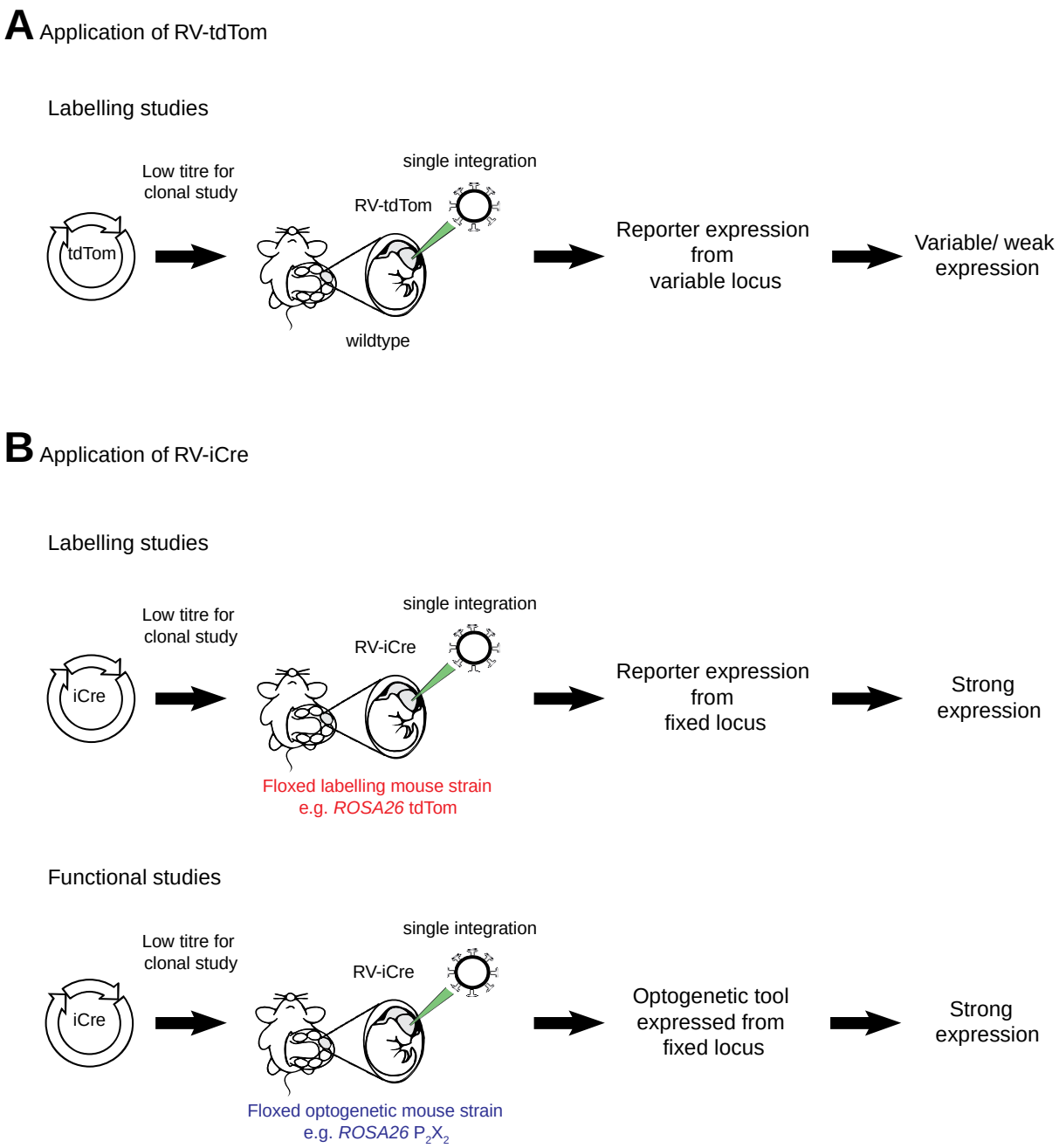

Figure 4.1: An iCre retrovirus is predicted to offer advantages over standard retroviral clonal labelling techniques. (**A**) Current clonal labelling techniques rely on low-titre infection with a labelling transgene encoding fluorescent proteins such as tdTom. However, single integration of RV-tdTom at a variable location in the genome of an infected cell can result in weak fluorophore expression, which limits clonal studies. (**B**) I predicted that infection of floxed-STOP reporter mice with RV-iCre would cause recombination in infected cells, activating expression of a reporter gene from both alleles of a constitutive, ubiquitous locus such as *ROSA26* resulting in strong fluorophore labelling. RV-iCre could be used in a variety of floxed mouse strains to provide versatile clonal labelling and the opportunity to use molecular tools for studying neuronal circuits, such as optogenetics.

a fixed, ubiquitous locus. Furthermore, I tested whether RV-iCre could be used in combination with an optogenetic reporter mouse, which would offer new opportunities for functional studies of neuronal clones (**Figure 4.1 B**).

I created the CAG-iCre retroviral vector by PCR amplification of iCre from paavCAG-iCre (a gift from Jinhyun Kim; Addgene plasmid number 51904), which I subcloned into the Moloney murine leukaemia virus (MoMLV)-derived pCLNCX retroviral expression vector containing CAG-GFP (a gift from Fred Gage, Addgene plasmid number 16664), in place of the GFP transgene. Replication-incompetent retrovirus was subsequently produced by transfection of GP2-293 retroviral packaging cells with CAG-iCre retroviral transfer plasmid and VSV-G envelope plasmid.

To compare fluorophore expression between RV-iCre and standard retroviral labelling of neurons in mouse neocortex, either RV-iCre or retrovirus encoding tdTom driven by the CAG promoter (RV-tdTom) was injected into the lateral ventricles of the embryonic brain of tdTom conditional reporter mice (Ai9) at embryonic day 12.5 (E12.5). These mice carry floxed-STOP tdTom driven by the CAG promoter at the *ROSA26* locus. Mice were recovered from anaesthesia and allowed to develop (**Figure 4.2 A**). Mice injected with RV-iCre or RV-tdTom were sacrificed at postnatal day 30 - 35 (P30 - 35) and acute brain slices were prepared and imaged using a confocal microscope under identical conditions. In neurons transduced with RV-tdTom, tdTom was expressed from the single retroviral transgene, which was integrated into the genome at an unknown position. No recombination of the genomic floxed-STOP tdTom would occur under these conditions, therefore the prediction was that this would result in variability in fluorophore expression levels between transduced neurons, depending on the site of the transgene integration. In neurons transduced with RV-iCre, iCre would also be expressed from the retroviral transgene at an unknown position in the genome. However, in any neuron with sufficient iCre activity, recombination of the floxed-STOP tdTom would be expected to result in strong, biallelic tdTom expression from the *ROSA26* locus (**Figure 4.2 B**).

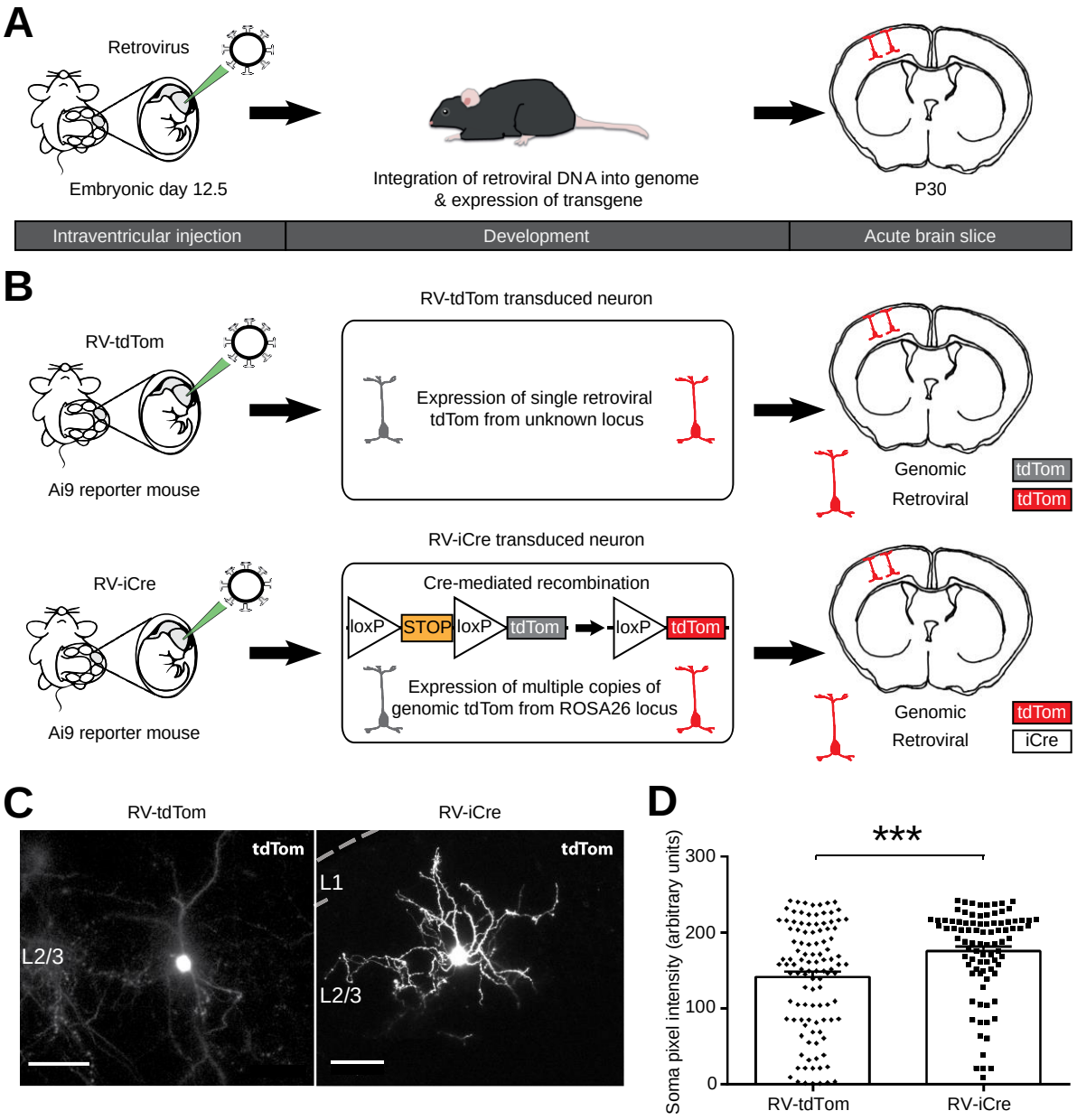

Figure 4.2: An iCre retrovirus facilitates improved fluorophore expression levels. (**A**) Embryonic Ai9 reporter mice encoding floxed-STOP tdTom at the *ROSA26* locus were injected with either RV-tdTom or RV-iCre. Acute cortical slices were imaged at P30-35 under identical conditions to compare the fluorophore expression resulting from infection with RV-tdTom and RV-iCre. (**B**) In mice injected with RV-tdTom, transduced neurons would be labelled by tdTom expressed from the retroviral transgene at an unknown locus in the genome. No recombination of the genomic floxed-STOP tdTom would occur. In mice injected with RV-iCre, sufficient iCre activity in transduced neurons would lead to recombination of the genomic floxed-STOP tdTom leading to strong, biallelic fluorophore expression from the *ROSA26 locus*. (**C**) Neurons could be identified by tdTom expression following transduction with either RV-tdTom or RV-iCre. Neurons seen here are in neocortical layer 2/3 (L2/3). Scale bar 50 µm, dashed line represents the pia. (**D**) The soma of neurons transduced by RV-iCre-mediated recombination had a higher mean pixel intensity than neurons transduced with RV-tdTom under comparable imaging conditions (RV-tdTom: mean = 141.5 ±6.9, n = 109; RV-iCre: mean = 175.7 ±6.1, n = 89; t (196) = 3.71, p = 0.0003, t test with Welch's correction).

As predicted, transduced neurons were successfully identified in mice injected with either RV-tdTom or RV-iCre by the expression of tdTom. Neurons labelled with tdTom could be found in animals injected with RV-tdTom and RV-iCre (**Figure 4.2 C**). To compare the brightness of neuronal labelling between RV-tdTom and RV-iCre, the mean pixel intensity over the somata of fluorescently-labelled neurons was calculated. Neurons transduced by RV-iCre had a significantly higher pixel intensity over their soma than neurons transduced with RV-tdTom (RV-tdTom: mean = 141.5 ±6.9, n = 109; RV-iCre: mean = 175.7 ±6.1, n = 89; t (196) = 3.71, p = 0.0003, t test with Welch's correction; **Figure 4.2 D**). This indicated that neurons transduced by RV-iCre, in which tdTom was expressed from the *ROSA26* locus, had greater expression of tdTom than neurons transduced with RV-tdTom. Moreover, the variance in the mean pixel intensity of somata was significantly lower for neurons transduced with RV-iCre than neurons labelled with RV-tdTom (F (108, 88) = 1.54, p = 0.04; F test), indicating that the level of fluorophore expression was more uniform in neurons transduced with RV-iCre. These data indicate that RV-iCre can elicit brighter and more consistent fluorophore labelling than RV-tdTom in the Ai9 tdTom conditional reporter mouse.

4.2.2 RV-iCre enables the functional manipulation of transduced neurons in a Cre-dependent optogenetic reporter mouse

To explore whether RV-iCre could enable optogenetic activation of clonally related neurons, RV-iCre was injected into the lateral ventricles of a floxed-STOP optogenetic reporter mouse. The double-transgenic floxed P_2X_2.Ai9 mouse was used, which carries floxed-STOP P_2X_2-ATP receptor and floxed-STOP tdTom at the *ROSA26* locus. Neurons labelled by Cre-mediated recombination in this mouse express the high-conductance, ionotropic P_2X_2-ATP receptor from the *ROSA26* locus and can, therefore, be activated by focal uncaging of ATP over the soma (Anastasiades et al., 2016). This optogenetic reporter mouse was selected because of

the higher single-channel conductance of P_2X_2 compared to the microbial opsins such as channelrhodopsin-2. In the double transgenic, Cre-mediated recombination also leads to tdTom expression, enabling visual identification of transduced neurons.

RV-iCre was injected at E12.5 and acute brain slices were prepared from mice at P 7 (**Figure 4.3 A**). This developmental time point was selected in order to prevent contamination of the selective activation response by endogenous ATP-gated ion channels, which can be expressed later in development (Anastasiades et al., 2016). Sparse, tdTom-labelled neurons could be visualised in the neocortex, confirming iCre-mediated recombination of floxed-STOP tdTom in transduced neurons (**Figure 4.3 B**). ATP-uncaging over the soma of transduced neurons could successfully evoke a burst of action potential firing recorded in current clamp. No direct response could be elicited from non-transduced neurons, confirming that the response in transduced neurons was a result of P_2X_2 receptor-mediated activity and not a result of activation of endogenous ATP-gated ion channels. Up to 10 photo-activation trials were performed over individual neurons, which confirmed that reproducible action-potential firing could be reliably evoked (**Figure 4.3 C**). In a subset of recordings from non-transduced neurons, excitatory post-synaptic currents could be observed in voltage-clamp following ATP-uncaging over a tdTom-positive cell. These currents were consistent with a glutamatergic synaptic connection between the transduced, tdTom-positive neuron (pre-synaptic) and the non-transduced, recorded neuron (post-synaptic). These observations confirmed successful

(**Figure 4.3 cont. from page 99**) action potential on ten consecutive trials, recorded in current clamp. (**D**) Example voltage clamp recording of excitatory post-synaptic currents (EPSCs) recorded in a layer 4 non-transduced neuron following light-activation at ten different locations across the cortical slice. In this example, EPSCs were recorded in trials #2 and #9, consistent with a glutamatergic synaptic connection originating from a neuron at those locations. Scale bar 50 µm. (**E**) Example of an experiment in which the synaptic connectivity was explored within a putative clone of transduced neurons. The positions of the TdTom-expressing neurons within the slice were documented with a photomicrograph (left). EPSCs were recorded from one member of the putative clone ('Cell 1') and then from an adjacent non-transduced control neuron ('Cell 2') in layer 4. Photo-uncaging of ATP was performed at multiple locations across the slice, in accordance with a grid (50 µm resolution). The EPSCs recorded for each uncaging location were used to generate a heat map of synaptic inputs for Cell 1 (middle) and Cell 2 (right), in which the colour indicates the amplitude of the EPSC recorded when ATP was uncaged at that location. White dots indicate the location of the transduced cells, based on the photomicrograph. Note that some of the strongest EPSCs were recorded from locations associated with transduced cells. Scale bar 50 µm.

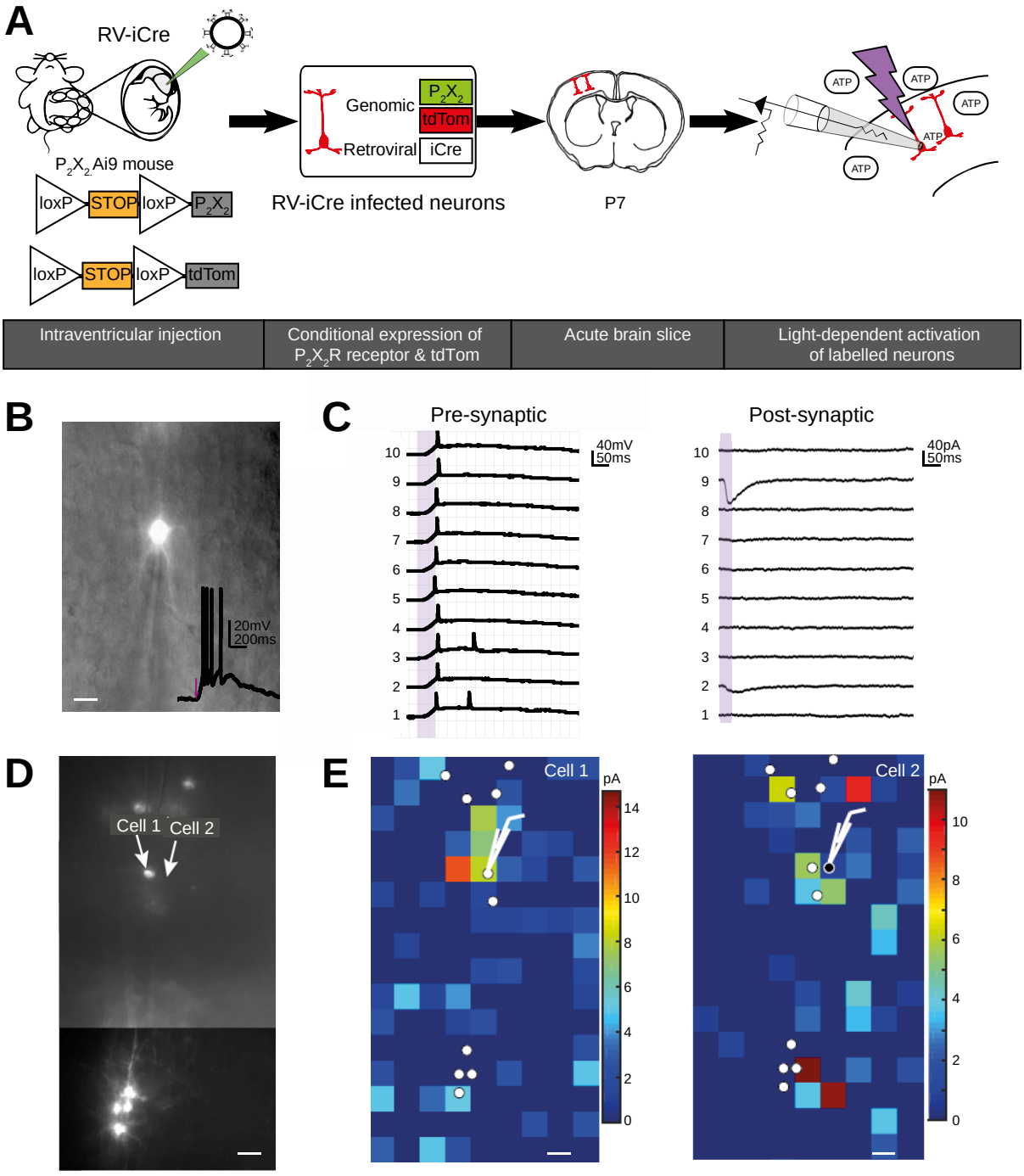

Figure 4.3: Delivering an iCre retrovirus to floxed-STOP P_2X_2-ATP receptor transgenic mouse enables light-dependent activation of clonally related neurons. (**A**) RV-iCre was injected into the lateral ventricles of double-transgenic floxed P_2X_2.Ai9 mice, which carry floxed-STOP P_2X_2-ATP receptor and floxed-STOP tdTom at the *ROSA26* locus, at E12.5. In this mouse, neurons labelled by Cre-mediated recombination were expected to express tdTom and the high-conductance, ionotropic P_2X_2-ATP receptor from the *ROSA26* locus. Transduced neurons could then be activated by focal uncaging of ATP over the soma, via the targeting of an ultraviolet (355 nm) laser spot (Anastasiades et al., 2016). Acute cortical slices were generated at P7, bathed in ACSF containing caged ATP and whole cell patch clamp recordings were used to assess the functional effects of optogenetic activation. (**B**) ATP uncaging over the soma of a transduced neuron successfully evoked a burst of action potentials in current clamp. Scale bar 20 µm. (**C**) Repeated brief photo-uncaging of ATP over the soma of a layer 2/3 retrovirally transduced neuron elicited a timed (cont. on page 98)

iCre-mediated recombination of both floxed-STOP P_2X_2 and floxed-STOP tdTom in transduced neurons, and the ability to selectively activate transduced neurons to examine synaptic connectivity.

To explore whether this approach could allow the investigation of connectivity relationships between clonally-related and unrelated neurons, ATP was sequentially uncaged over the somata of sparse, fluorescently labelled neurons constituting a putative clone, whilst recording from either a transduced neuron or an adjacent non-transduced neuron (**Figure 4.3 D - E**). This enabled the strength of connectivity between cells in the putative clone and the two recorded neurons to be mapped and compared. These data provide proof-of principle that RV-iCre could be used to investigate the functional relationships of clonally-related neurons in a conditional optogenetic reporter mouse.

4.2.3 RNA barcoding of progenitors is a strategy to improve the accuracy and versatility of clone identification

DNA barcoding of progenitors currently provides one of the most definitive methods of identifying clonally-related neurons (Golden et al., 1995; Mayer et al., 2016; Turrero García et al., 2016). This strategy involves the heritable delivery of a distinct oligonucleotide tag (barcode) to a progenitor, by using a retroviral vector to integrate the barcode into the genome. All neurons carrying the same tag are assumed to be a clone, deriving from a single labelled progenitor (**Figure 4.4 A**). Incorporation of a transgene encoding fluorescent protein into the retroviral vector enables barcoded neurons to be identified for collection and processing for barcode identification by PCR amplification and sequencing. DNA barcode identification has been associated with a low success rate in barcode identification (Fuentealba et al., 2015; Golden et al., 1995). I hypothesised that this high failure rate was due to the reliance on identification of a single copy of the barcode from the genome of a cell. I proposed RNA

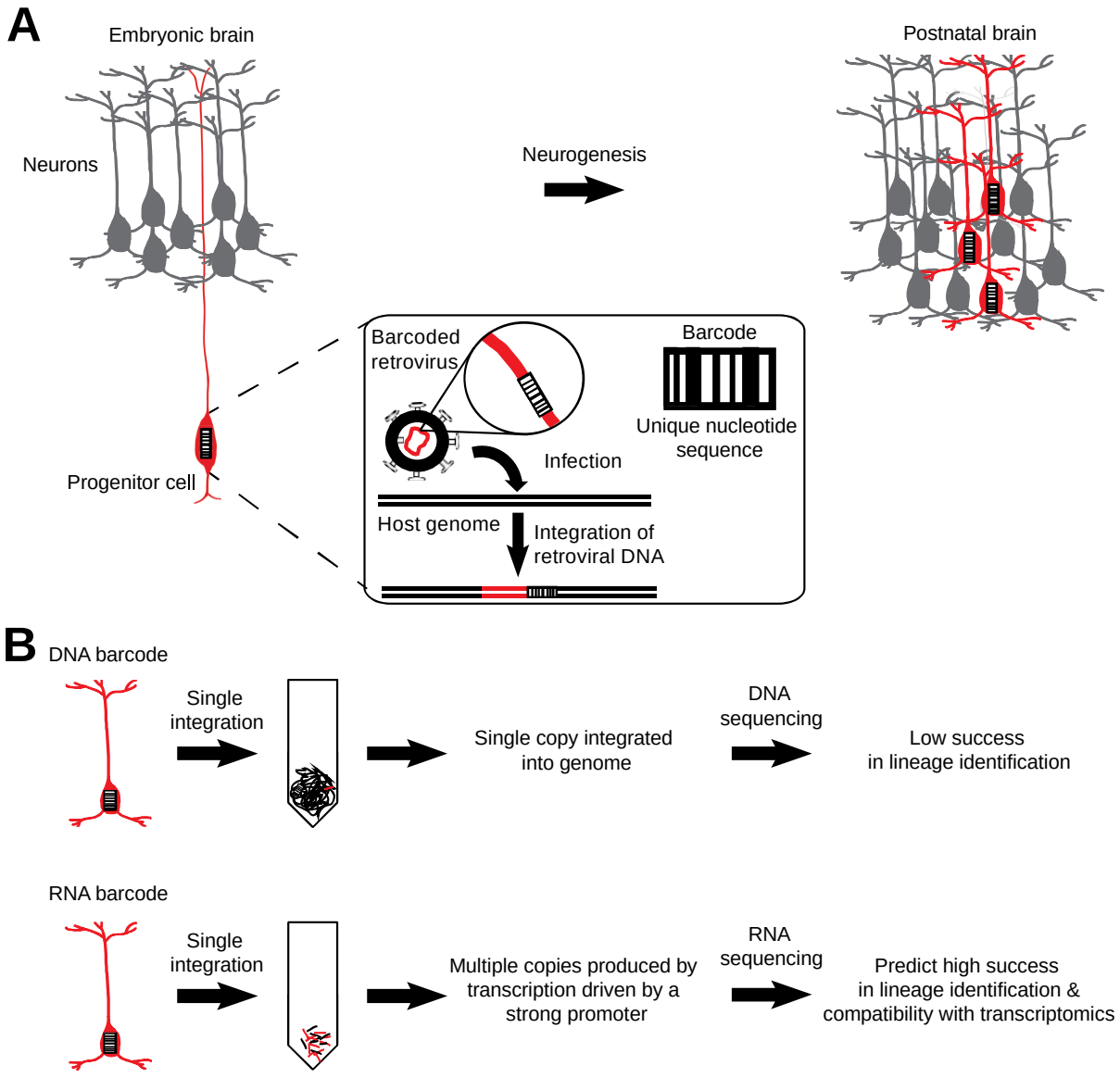

Figure 4.4: Retroviral RNA barcoding is predicted to provide greater precision and reliability than conventional clonal labelling techniques. (**A**) Progenitor barcoding is a method of clonal labelling that relies on retroviral delivery of a short, unique nucleotide sequence ('barcode') to a progenitor. The barcode will label the progenitor and its progeny in a stable and heritable manner. Retrovirally transduced neurons can be identified by incorporation of a transgene encoding a fluorescent protein into the retroviral vector, which results in fluorescent protein production in transduced neurons. In the schematic, transduced neurons are red, and non-transduced neurons are grey. (**B**) I hypothesised that the low success rate associated with identification of a DNA barcode was due to reliance on retrieving a single copy of the barcode integrated into the genome of a cell. I proposed that RNA barcoding could result in multiple copies of the barcode in a single cell by using a strong, constitutive promoter to drive transcription of the barcode. I predicted that this would offer a higher success rate of clone identification than DNA barcoding. Furthermore, RNA barcoding could offer improved opportunities for whole transcriptome analysis of clonally-related neurons through compatibility with single cell RNA sequencing technologies.

barcoding as an alternative method of progenitor barcoding to definitively identify clonally related neurons. I predicted that this would increase the number of copies of the barcode in a single cell arising through transcription of the barcode, therefore increasing the success rate of barcode retrieval from single cells (**Figure 4.4 B**). Furthermore, since RNA barcoding could be compatible with single cell whole transcriptome analysis, this could provide the opportunity to investigate the gene expression patterns of clonally related neurons.

4.2.4 RV-tdTom-barcode is a complex library of RNA-barcoding retroviral vectors

The strategy for the RNA-barcoding retroviral vector was to tag a tdTom transgene with a unique 24 base pair (bp) variable oligonucleotide sequence (barcode), so that expression of tdTom would result in amplification of the barcode by transcription and production of tdTom. The barcode was inserted into the vector immediately downstream of the tdTom stop codon so that the barcode was transcribed but not translated, thereby preserving normal function of the fluorescent protein. In order to maximise expression of tdTom-barcode, transgene expression was driven by a strong CAG promoter, and WPRE was incorporated downstream of the barcode to enhance transgene expression (Zufferey, Donello, Trono, & Hope, 1999). The resulting CAG-tdTom-barcode retroviral vector is referred to in this thesis as RV-tdTom-barcode (‘RV’ refers to retrovirus, ‘pRV’ refers to retroviral vector plasmid).

The oligonucleotide barcode design was based upon Gerrits et al. (2010) and consisted of six random oligonucleotide doublets, interspersed with fixed-base oligonucleotide triplets. The fixed triplets provided an internal standard for assessing the quality of barcode sequencing read, and the random doublets generate a theoretical library complexity of 4,194,304 unique barcodes (Gerrits et al., 2010). All stages of production were performed using a large scale, multi-parallel design to maximise library complexity. The double-stranded barcode insert was produced by annealing a pool of synthetic single-strand variable

oligonucleotide barcodes, which were ligated into a CAG-tdTom-WPRE (RV-tdTom) MoMLV-derived pCLNCX retroviral expression vector (created by Dr Louise Kay, unpublished) between the 3' extent of tdTom and the 5' extent of WPRE. This was expected to result in a complex library of genetically-distinct RV-tdTom-barcode plasmids (pRV-tdTom; **Figure 4.5 A**). Sequencing of the pRV-tdTom-barcode library confirmed superimposed peaks at the variable positions in the sequencing trace indicating different nucleotide bases at a single locus, consistent with the presence of multiple different barcodes (**Figure 4.5 B**).

The plasmid library was briefly amplified by large-scale transformation into competent *Escherichia coli*. The complexity of the pRV-tdTom-barcode library was expected to be limited by the number of bacterial clones obtained during transformation, which was estimated to be 7,500. Individual bacterial colony sequencing (n = 50) revealed that barcode sequences differed in their nucleotide sequence at the variable positions, confirming the presence of multiple different barcode sequences in the pRV-tdTom- barcode library. A subset of visually distinct bacterial colonies were found to contain more than one different barcode on sequencing, indicating that colony number provided a conservative estimate of library complexity (**Figure 4.5 C**). All sequences contained the barcode insert, and each barcode identified by sequencing of single colonies was identified no more than once. Data from individual colony sequencing trials confirmed that all possible nucleotide identities were represented at the variable positions and there was no significant difference in the representation of all four nucleotides at the ten variable positions at which these could occur (C^2 (n = 50) = 18.9, p = 0.09, chi-square test; **Figure 4.5 D**). To further investigate whether there were biases that would reduce the diversity of distinct barcodes, the number of differences between 50 barcode sequences was evaluated on a pair-wise basis and compared to a simulated dataset. The simulated dataset was derived from ten simulations of a pairwise comparison of 50 random barcodes. Pairwise comparison of the actual dataset of unique barcode sequences revealed that barcodes differed from one another at multiple variable nucleotide positions (mean 8.5 ± 0.2 positions). There was no significant difference between the actual dataset and the simulated dataset (p = 1.0, two-way ANOVA, **Figure 4.5 E**),

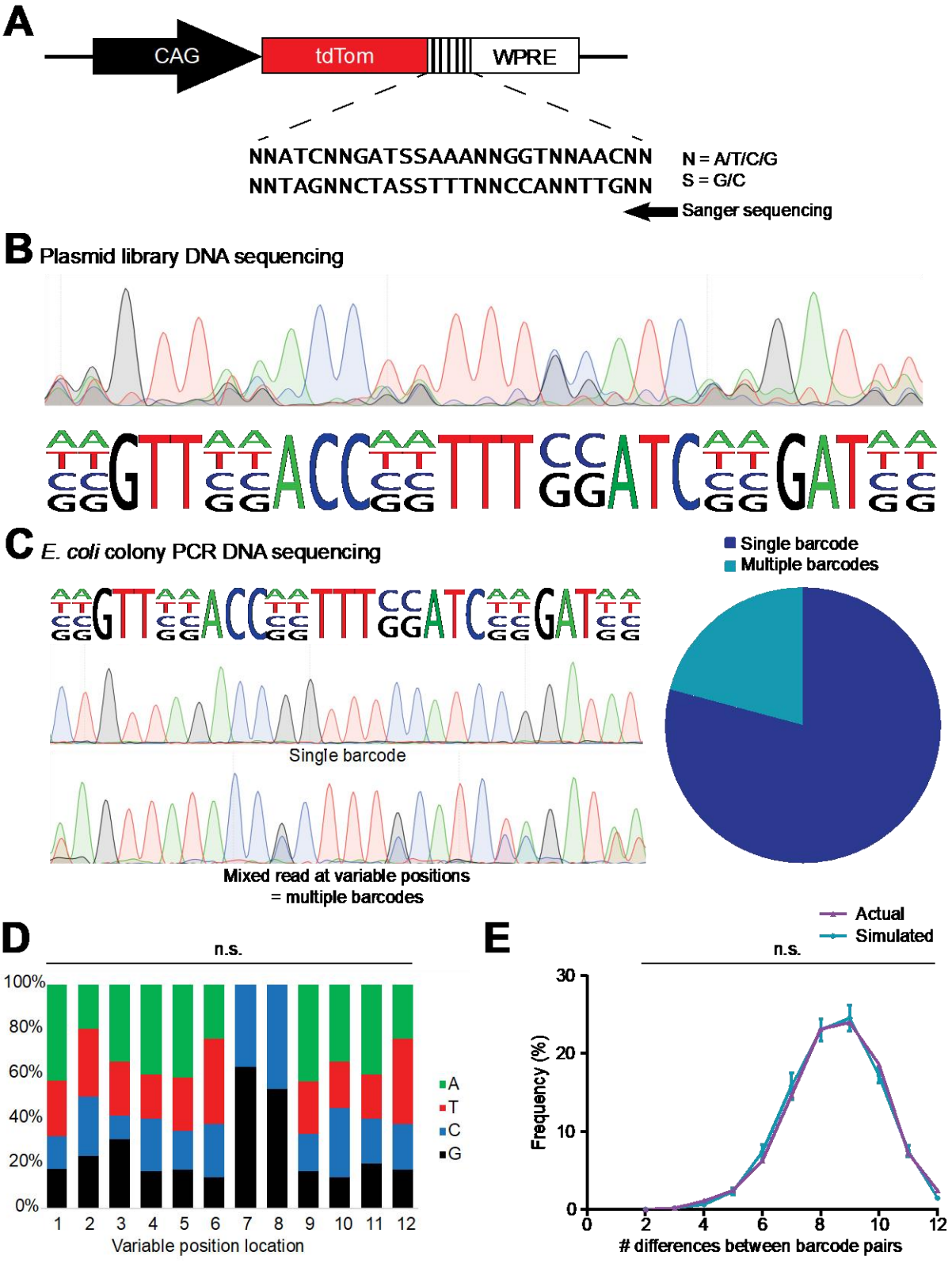

Figure 4.5: Production of a retroviral vector plasmid library barcoded with a short, variable nucleotide sequence (pRV-tdTom-barcode library). (**A**) A retroviral vector encoding a reporter gene (tdTom) was barcoded by insertion of a short, variable DNA sequence comprising fixed and variable positions between the stop codon of tdTom and the start of WPRE. This positioning of the barcode was expected to lead to inclusion of the barcode and transcription of tdTom, driven by the CAG promoter. (cont)

consistent with the idea that there was no significant bias in the synthesis of RV-tdTom-barcode plasmid. These data represent the construction and initial characterisation of the pRV-tdTom-barcode RNA-barcoding library.

4.2.5 Retrovirus can be processed to elicit a high proportion of single integration events

Successful application of RV-tdTom-barcode would rely on the labelling of a progenitor with a single barcode, since multiple barcode sequences cannot be identified by standard Sanger sequencing. Furthermore, failure to identify all the barcodes from a cell could lead to errors in identifying clones labelled with multiple barcodes. To test whether a standard protocol for the production and delivery of retrovirus could be optimised to lead to single integration events, two retroviruses encoding different fluorophores were produced and used to transduce NIH/3T3 mouse embryonic fibroblasts. This experimental design simplified the identification of multiple integration events compared to identification by barcode retrieval by enabling multiple integration events to be identified by the co-expression of different fluorophores in transduced cells.

Retroviruses encoding either GFP or tdTom were co-produced by transfection of GP2-

(**Figure 4.5 cont**) (**B**) Sequencing of plasmid library DNA demonstrated the presence of each possible base identity at the variable positions, consistent with the presence of multiple different barcode sequences within the sample. (**C**) Individual bacterial colony sequencing during library production revealed that a subset of visually distinct bacterial colonies contained more than one different barcoded plasmid, indicating that the number of bacterial colonies provided a conservative estimate of library complexity. (**D**) Data from individual colony sequencing trials confirmed that all possible nucleotide identities were represented at the variable positions (n = 50). There was no significant difference in the representation of different nucleotides at the ten variable positions at which all four bases could occur (C^2 (n = 50) = 18.9, p = 0.09, Chi-square test). (**E**) A pairwise comparison of 50 unique barcode sequences revealed that barcodes tended to differ from one another at multiple variable nucleotide positions (mean 8.5 ±0.2 positions). There was no significant difference between this dataset and a simulated dataset derived from ten simulations of a pairwise comparison of 50 random barcodes (p = 1.0, two-way ANOVA). This suggests that there is no significant bias in the creation of the barcoded retroviral plasmid library.

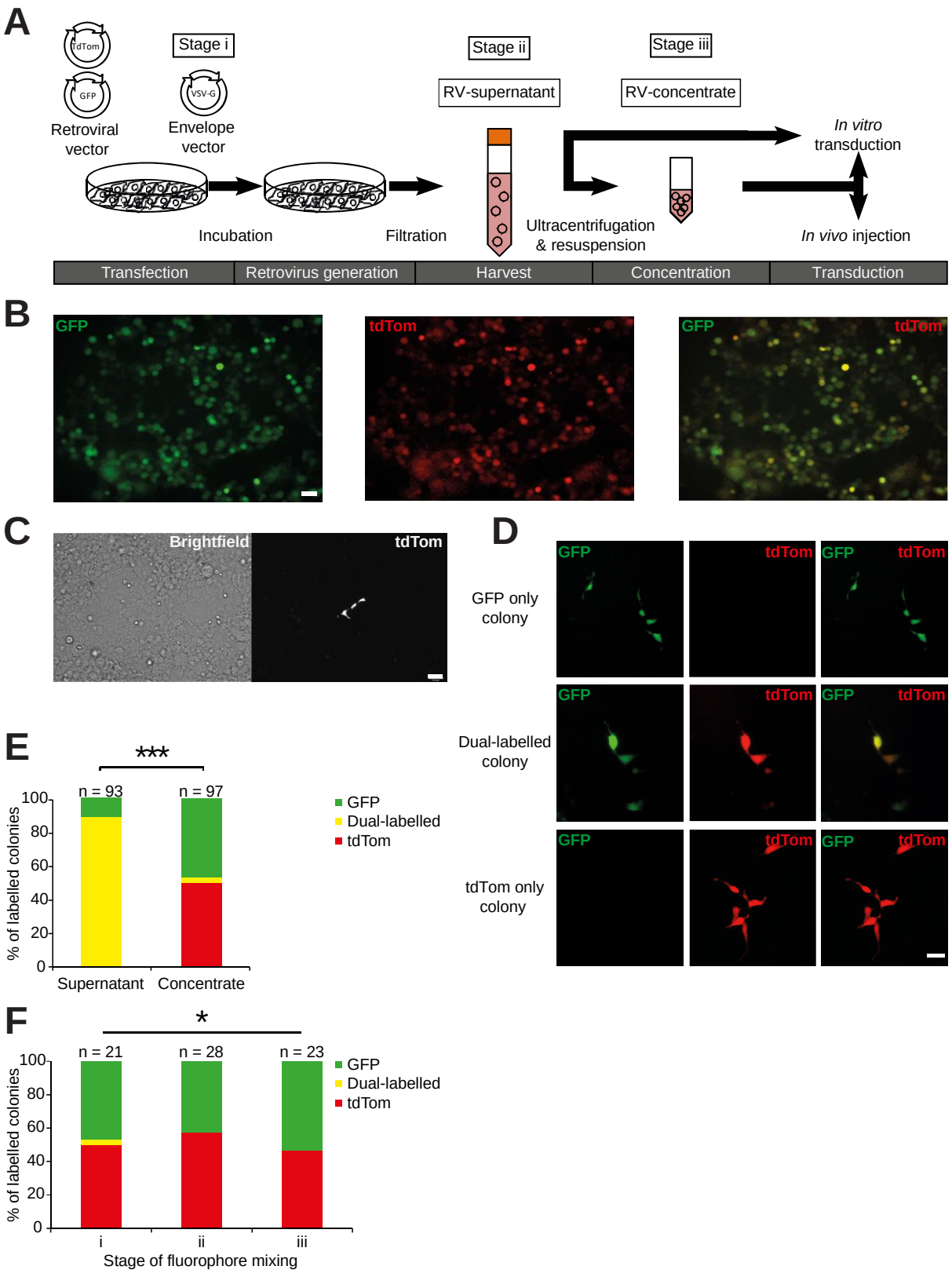

Figure 4.6: Retrovirus can be processed to elicit a low frequency of multiple integration events. (**A**) Schematic of GFP and tdTom retrovirus production. GP2-293 retroviral packaging cells were co-transfected with retroviral vector plasmid DNA and viral envelope protein (VSV-G; stage (i)). Supernatant was harvested, centrifuged, and filtered to produce RV-supernatant (stage (ii)). RV-concentrate was produced by ultracentrifugation of RV-supernatant and re-suspension of the viral pellet in a mixture of Opti-MEM, DNase and Polybrene. (cont.)

293 retroviral packaging cells with separate GFP and tdTom retroviral plasmid (pRV-GFP and pRV-tdTom) and VSV-G envelope plasmid (**Figure 4.6 A**). A high rate of co-transfection of retroviral packaging cells with pRV-tdTom and pRV-GFP was confirmed by the large proportion (over 90 %) of packaging cells that expressed both GFP and tdTom following transfection (data not shown). Retrovirus was harvested and processed as either supernatant (RV-supernatant) or concentrated retrovirus (RV-concentrate). The majority of transduced NIH/3T3 expressed both tdTom and GFP following transduction with high-titre RV-concentrate (1 - 5 x 10^4 c.f.u./ml, 70 – 80 % transduction efficiency), confirming the ability to detect multiple integration events (**Figure 4.6 B**). In contrast, sparse, spatially separated clusters of fluorescently labelled cells (colonies), resulted from low-titre transduction of NIH/3T3 cells (100 - 500 c.f.u./ml, 21.1 ± 3.79 labelled colonies per coverslip) with RV-concentrate. 98 % of colonies were over 300 µm from the nearest labelled colony and all cells within a colony expressed the same fluorophore label. This indicated that retrovirus was not biased to infect spatially-clustered cells, since these colonies constituted putative clones (**Figure 4.6 C**). Labelled colonies in this experimental paradigm exhibited one of three phenotypes: GFP-expressing only, tdTom-expressing only or dual-labelled (GFP- and tdTom-expressing; **Figure**

(**Figure 4.6 cont.**) (stage (iii)). For parts (B)-(E), pRV-GFP and pRV-tdTom were mixed at stage (i). For part (F), RV-GFP and RV-tdTom retrovirus were also separately produced and either mixed as RV-supernatant (following stage (ii)), or as RV-concentrate (following stage (iii)). (**B**) The majority of transduced NIH/3T3 expressed both tdTom and GFP following transduction with high-titre RV-concentrate (1 - 5 x 10^4 c.f.u./ml, 70 – 80 % transduction efficiency). Scale bar 100 µm. (**C**) Sparse, spatially separated clusters of fluorescently labelled cells (colonies), resulted from transduction of NIH/3T3 cells (100-500 c.f.u./ml, 21.1 ±3.79 labelled colonies per coverslip) with low-titre RV-concentrate. 98 % of colonies were over 300 µm from the nearest labelled colony and all cells within a colony expressed the same fluorophore label. Scale bar 100 µm. (**D**) Labelled colonies exhibited one of three phenotypes following low-titre transduction with RV-concentrate: GFP-expressing only, dual-labelled (GFP- and tdTom-expressing) or tdTom-expressing only. Scale bar 50 µm. (**E**) The proportion of dual-labelled colonies was significantly higher in cells transduced with RV-supernatant (88.67 ±5.67 %, n = 93), compared to RV-concentrate (3.33 ±1.67 % dual-labelled colonies, n = 97; C^2 (2, n = 190) = 152.1, $p < 0.0001$; chi-square test). (**F**) The stage of mixing was associated with the incidence of dual-labelled colonies following low-titre transduction (100-500 c.f.u./ml) with RV-concentrate. (C^2 (4, n = 72) = 10.91, $p = 0.03$, chi-square test). Dual-labelled colonies only resulted when pRV-GFP and pRV-tdTom were mixed at stage (i), when retroviral packaging cells were co-transfected with both fluorophores, but not when RV-GFP and RV-tdTom were separately produced and either mixed as RV-supernatant (stage (ii)), or as RV-concentrate (stage (iii)).

4.6 D). The presence of dual-labelled colonies indicated a subset of multiple integration events in single cells following low-titre transduction with RV-concentrate.

I hypothesised that the ultracentrifugation of retrovirus during the process of concentrating retrovirus could cause the low-frequency aggregation of retroviral virions that I had observed. To test this idea, I compared the incidence of dual-labelling following low-titre transduction of NIH/3T3 cells with either RV-supernatant or RV-concentrate. These retroviruses were produced by co-transfection of GP2-293 retroviral packaging cells with GFP and tdTom retroviral plasmid, plus the VSV-G envelope plasmid. Half of the RV-supernatant was concentrated by ultracentrifugation to produce RV-concentrate. The proportion of dual-labelled colonies was significantly higher in cells transduced with RV-supernatant, in which the majority of colonies were dual-labelled (88.67 ± 5.67 %, n = 93). By contrast, for cells transduced with RV-concentrate, the majority of colonies were labelled with either GFP or tdTom (3.33 ±1.67 % dual-labelled colonies, n = 97; C^2 (2, n = 190) = 152.1, $p < 0.0001$; chi-square test; **Figure 4.6 E**). This revealed that concentration of retrovirus significantly reduced the frequency of dual-labelling events.

Finally, to further investigate the time point at which dual-labelling events arose during retroviral production, I compared the incidence of dual labelling in cells transduced with RV-GFP and RV-tdTom that was either co-produced from retroviral packaging cells, to retrovirus that was produced and either mixed as RV-supernatant or mixed as RV-concentrate. The stage of production at which tdTom and GFP was mixed was significantly associated with the incidence of dual-labelled colonies (stage i: n = 21, stage ii: n = 28, stage iii: n = 23; C^2 (4, n = 72) = 10.91, $p = 0.03$, chi-square test; **Figure 4.6 F**). Dual-labelled colonies only resulted when retroviral packaging cells were co-transfected with both fluorophore plasmids, but not when separately-produced retrovirus (either supernatant or concentrate) was mixed. This indicates that when concentrated retrovirus is used at low titre, the frequency of multiple integration events can be kept very low. This provides a strong foundation for developing the RNA-barcoding retrovirus.

4.2.6 The barcode transcript can be retrieved from single cells transduced with RV-tdTom-barcode

The next stage was to confirm that the retroviral RNA barcode was transcribed in a cell, that this did not affect the function of the fluorescent protein, and that the barcode could be retrieved by single cell collection. To test this by proof-of-principle, NIH/3T3 cells were transduced with RV-tdTom-barcode at a high (20 %) transduction efficiency. This was expected to result in some multiple integration events in transduced cells, therefore increasing the likelihood that some barcode sequence could be retrieved. Retrovirus was produced by co-transfection of GP2-293 retroviral packaging cells with RV-tdTom-barcode plasmid and VSV-G envelope plasmid. The retrovirus was then concentrated to 1 x 10^6 c.f.u./ml.

Following 2 – 5 days after transduction, cells could be identified by expression of tdTom, confirming that fluorescent protein function had been preserved (**Figure 4.7 A**). Single cells were collected by aspiration with a glass micropipette under the control of a micromanipulator. By approaching the cell membrane and applying a small amount of negative pressure, cytoplasm containing fluorescent protein could be visualised entering the micropipette tip. Individual cells could be sequentially harvested from spatially-clustered groups of labelled cells with minimal disruption to surrounding cells, enabling the isolation of entire putative clones (**Figure 4.7 B**). Individual cells were transferred blindly into a PCR tube and samples were processed for RT-PCR amplification of the barcode, following DNase treatment, using primers located in the 3' end of tdTom and 5' end of WPRE. Amplification of RT-PCR product of the correct size was confirmed by UV visualisation following gel electrophoresis. This confirmed that the barcode sequence had been transcribed by the host cell and that the single cell had successfully been collected and the barcode amplified by RT-PCR (**Figure 4.7 C**). The DNA product was extracted, purified and sequenced using the Sanger method to identify the barcode. Barcode sequences were routinely identified in the sequencing data. Superimposed peaks corresponding to each of the possible nucleotide

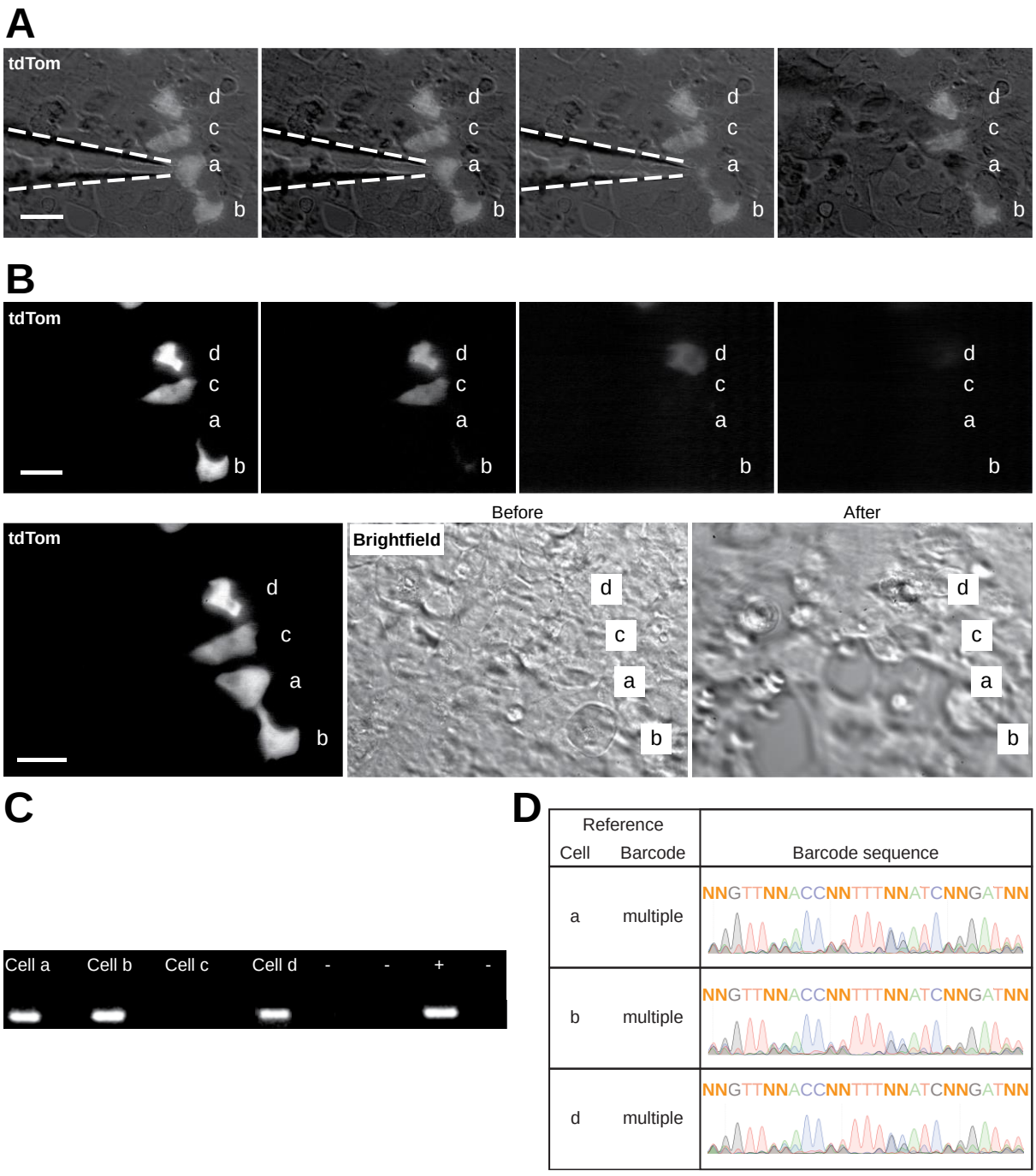

Figure 4.7: A barcoded retrovirus can be recovered following high-titre transduction of NIH/3T3 cells. NIH/3T3 cells were transduced with RV-tdTom-barcode at approximately 20 % transduction efficiency (i.e. high efficiency) and single cells were collected and processed for barcode retrieval. Scale bar 25µm. (**A**) Retrovirally-transduced cells could be identified by expression of tdTom. Cytoplasm was aspirated from single labelled cells using a glass micropipette. This could be visualised over time (left to right). (**B**) Individual cells could be sequentially harvested from spatially-clustered groups enabling the isolation of entire putative clones (top). This could be achieved with minimal disruption to surrounding cells (bottom). (**C**) Transcription of the barcode sequence in single cells was confirmed by the detection of RT-PCR product using primers directed to the transgene and the adjacent barcode from single cells. A positive control ('+', plasmid DNA) and three negative controls ('-', a sample of the collection solution, external solution and a no DNA control, left to right) confirmed no sample contamination. (**D**) The results from sequencing the RT-PCR product were consistent (cont.)

identities were consistently found at the variable positions only (**Figure 4.7 D**). These were preceded and superseded by clear, single-nucleotide peaks for the non-barcode sequence, and clear, single nucleotide peaks at the fixed positions in the barcode, which confirmed a high quality sequencing read of multiple barcode sequences. These findings were consistent with the amplification of multiple barcode sequences from multiply-transduced single cells, demonstrating successful retrieval of the RNA barcode DNA from single cells.

4.2.7 RV-tdTom-barcode can be used to identify clonally-related cells *in vitro* with a high success rate

Having established that the barcode was transcribed in single cells, RV-tdTom was used at low titre (100-500 c.f.u./ml) to establish whether it was possible to identify clones in singly-transduced cells. Fluorescently-labelled cells (**Figure 4.8 A**) were alternately harvested with adjacent, non-fluorescent control cells. The absence of contamination was confirmed by the retrieval of RT-PCR product from the fluorescently-labelled cells, but not from non-fluorescent control cells (**Figure 4.8 B**). High-quality barcode sequencing reads were successfully obtained from single cells, even those with weak fluorophore expression, indicating that barcode retrieval was robust to variability in fluorophore expression levels. Barcode sequences were identified from individual cells that differed in their nucleotide sequence at the variable positions, supporting the expectation that the RV-tdTom-barcode library contained genetically distinct tags. Analysis of the barcode sequence from single cells was used to successfully infer clonal and non-clonal relationships by the identification of identical and non-identical barcode sequences, respectively (**Figure 4.8 C**). One transduced cell (4 %; 1/24) exhibited multiple integration events, as evidenced by the presence of more than one

(**Figure 4.7 cont.**) with the recovery of multiple barcodes per cell under the conditions of high titre transduction. Sequencing traces showed multiple nucleotides at each of the variable barcode positions (represented by 'N'). Each of the fixed nucleotide positions showed a single nucleotide, as expected.

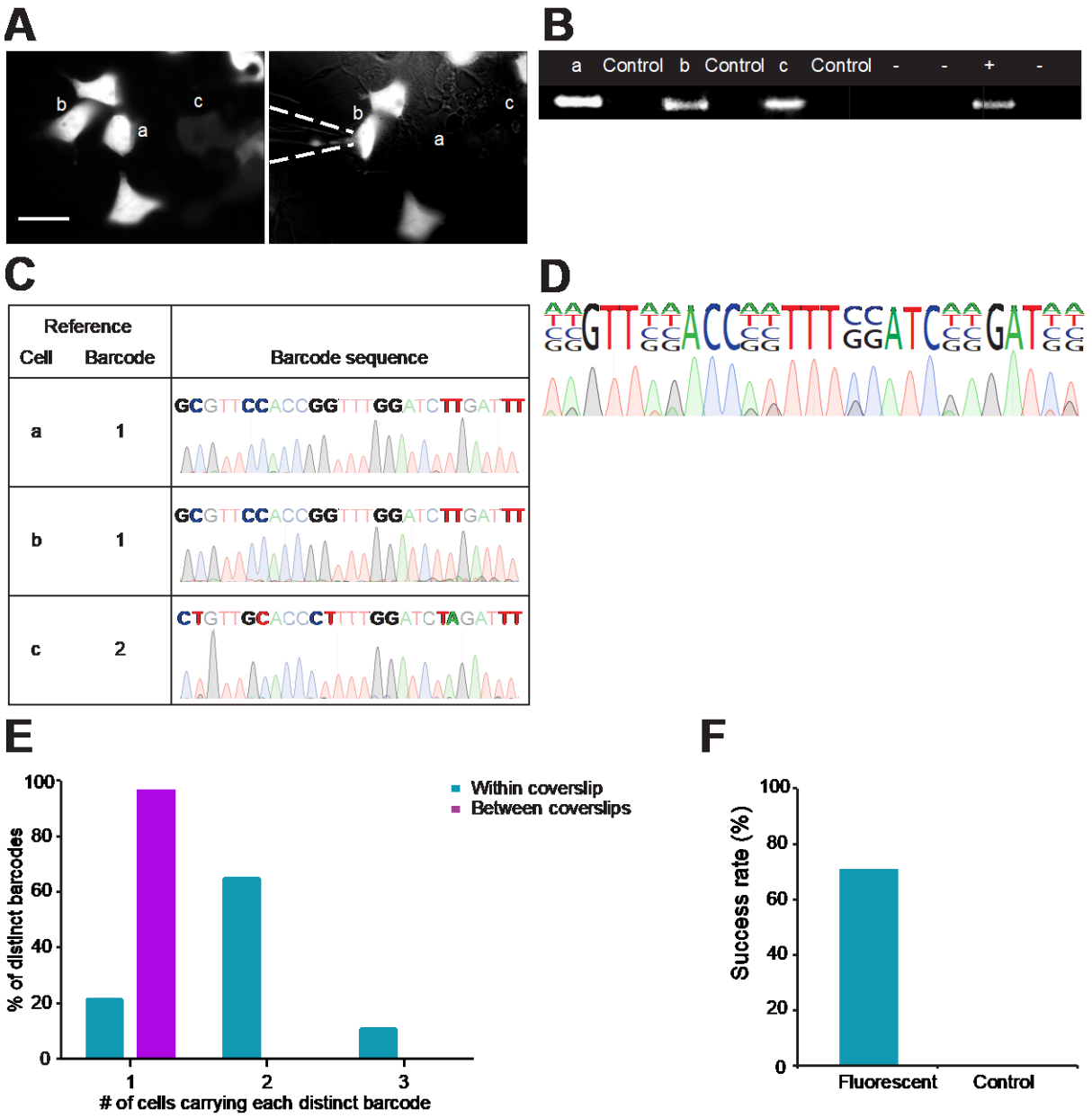

Figure 4.8: An RNA barcoding retrovirus can unequivocally identify clones in NIH/3T3 cells *in vitro.* (**A**) NIH/3T3 cells were transduced with RV-tdTom-barcode at low titre (100-500 c.f.u./ml). Fluorescence expression levels could exhibit variability between putative clones (cells 'a' and 'b' show strong expression, whilst cell 'c' shows weak expression) consistent with the idea that the retroviral transgene can insert at variable locations in the genome. Single labelled cells and adjacent non-fluorescent control cells were isolated by gentle aspiration with a glass micropipette. Scale bar 25 µm. (**B**) RT-PCR product could be obtained using primers directed to the transgene from labelled cells, but not from non-transduced control cells harvested at the same time. A positive control ('+', plasmid DNA) and three negative controls ('-', a sample of the collection solution, external solution and a no DNA control, left to right) were run in parallel. (**C**) Sequencing traces of RT-PCR product from single cells could be used to identify clones (cell 'a' and 'b') and non-clones (cell 'c') by identification of identical and non-identical barcode sequences, respectively. The successful sequencing read obtained from cell 'c', which had weak fluorophore expression, indicated that barcode could be retrieved despite variability in fluorophore expression levels. (**D**) In only one cell (4 %, 1/24) did I observe evidence for multiple nucleotides at the variable positions in the sequencing trace (cont.)

nucleotide identity peak at the variable barcode positions in the sequencing trace (**Figure 4.8 D**). No more than two nucleotide peaks were ever identified at each variable position from a single cell, suggesting that these cells were transduced with only a very small number of different barcodes. The same distinct barcode could be identified from more than one cell within a coverslip, but never from cells on different coverslips. This was consistent with a clonal labelling pattern (n = 9 unique barcodes; **Figure 4.8 E**). Furthermore, barcode sequence could be reliably retrieved from fluorescently-labelled cells (67 %; 16/24), but never from non-fluorescent, adjacent control cells (0 %; 0/8). This confirmed that the cell collection technique did not introduce lumping errors through the contamination of adjacent cells (**Figure 4.8 F**). Together therefore, these data reveal that RV-tdTom-barcode can be used to systematically study clones.

4.3 Discussion

In this chapter I have generated a retrovirus encoding iCre (RV-iCre) that can trigger recombination in transduced neocortical neurons. I have applied this tool to label neurons in the developing neocortex in two conditional reporter mouse strains. Firstly, to demonstrate that RV-iCre can generate stronger and more consistent fluorophore expression for clonal studies than retrovirus encoding a fluorophore. Secondly, to show that RV-iCre enables the optogenetic activation of transduced neurons, which could be employed in studies of connectivity in clonal neurons. I have also developed a retrovirus that can be used to identify cells with an RNA barcode. I have demonstrated that this tool

(**Figure 4.8 cont.**) The sequencing for this cell is illustrated, where it is possible to see two peaks at the variable barcode positions. The very low occurrence of this sequencing profile, was consistent with a very low number of multiple integration events in these cells. (**E**) Consistent with a clonal labelling pattern, some distinct barcodes could be retrieved from more than one cell in a coverslip, but cells on different coverslips never carried the same barcode (n = 9 distinct barcodes). (**F**) Barcode sequence could be retrieved with a high success rate from tdTom-labelled cells, but not from adjacent control cells (16/24 fluorescent cells, 0/8 non-fluorescent cells).

can be applied *in vitro* and that the RNA barcode sequence of single cells can be retrieved with a high success rate. Finally, I have shown that this tool enables the identification of clonally related cells by heritable labelling.

4.3.1 Creation and application of a retrovirus encoding iCre

Retrovirus encoding Cre offers the potential to selectively modify clonally related neurons. I constructed a retrovirus encoding iCre (RV-iCre) and demonstrated that it successfully activated recombination in transduced neurons in mouse neocortex in two floxed mouse strains. This provided a proof-of-principle that RV-iCre could be a versatile tool for investigating diverse aspects of clonal relationships. Integration of a retroviral transgene at a variable location in the genome has been associated with variable, and sometimes low, transgene expression levels (Bouard, Alazard-Dany, & Cosset, 2009; Cepko et al., 1998). This is particularly relevant in clonal studies, when retrovirus is used at a low titre in order to cause sparse labelling of cells, which is expected to result in a single integration event in a transduced cell. Consistent with this expectation, tdTom expression levels were found to be lower and more variable in the somata of neurons transduced with a retrovirus encoding tdTom, than in neurons in which tdTom was expressed from *ROSA26* following iCre-mediated recombination. The magnitude of this effect was relatively modest however (approximately 20 %), and there was considerable overlap between the brightness of somata transduced with RV-tdTom and RV-iCre. These findings revealed that retroviral labelling using RV-iCre to activate reporter expression from the *ROSA26* locus can be used to improve the strength and consistency of reporter expression compared to direct expression of a retrovirus-mediated tdTom.

One of the other rationales for developing iCre was that it could offer improved versatility over standard retroviral labelling techniques, capitalising on floxed reporter

tools. In order to demonstrate the value of RV-iCre in the investigation of neuronal circuitry, RV-iCre was tested in an optogenetic reporter mouse - the P_2X_2-ATP receptor conditional reporter (Anastasiades et al., 2016). Neurons transduced with RV-iCre activated expression of the P_2X_2-ATP receptor, enabling selective optogenetic activation of transduced neurons. The ability to harness the power of technologies such as optogenetics, to manipulate the function of neurons on a clonal basis, would be invaluable in furthering our understanding of the relationship between the lineage and function of neurons. Moreover, the Cre-lox system can be employed to achieve a wide range of targeted DNA modifications, including deletion, insertion, translocation and inversion (Tsien, 2016), which would open up the opportunity to perform diverse manipulations on clonally-related cells. RV-iCre offers significantly greater versatility therefore than traditional clonal labelling techniques.

The frequency with which cells transduced with iCre did not undergo recombination is unknown. These could include cells in which retroviral transgene expression was silenced, or cells in which there was insufficient iCre activity to cause recombination. Due to the requirement for only a single recombination event to activate expression of the reporter gene, only those cells in which iCre activity had never reached threshold in the preceding lineage would be expected to remain unlabelled. It is likely, therefore, that the majority of clones are either systematically included or excluded. This provides a further advantage over traditional retroviral clonal labelling techniques, in which individual members of a clone can independently silence retroviral expression, resulting in an underestimation of clone size (Cepko et al., 1998; Ciceri et al., 2013; Harwell et al., 2015). An estimate of the frequency with which transduced cells do not undergo recombination could be made by sampling unlabelled cells and ascertaining the presence of iCre by performing PCR amplification using primers directed to the iCre vector. Furthermore, the incidence of retroviral silencing could be assessed by single cell RT-PCR amplification of iCre from labelled cells to assay iCre expression.

It is also worth considering potential disadvantages that could be associated with the use of RV-iCre. A particular risk is Cre-associated toxicity (Silver & Livingston, 2001). Although I saw no evidence for cell death, the true number of transduced neurons observed postnatally may have been an underestimate of the infection frequency because of undetected cell death occurring as a result of iCre expression. The potential for cell toxicity could be confirmed by systematically assessing injected brains over time to quantify the proportion of transduced cells exhibiting signs of cell death, and to compare clone size with that reported in the literature (Gao et al. 2014, for example).

4.3.2 Construction and application of an RNA-barcoding retroviral vector for clonal labelling

Heritable DNA barcoding of progenitors in the developing neocortex was pioneered over twenty years ago by Cepko and colleagues, with the construction of a complex retroviral library (Golden et al., 1995). This strategy offers greater confidence in the identification of clones and avoids the biases associated with traditional geometric identification of clones. However, a persistently low success rate of around 50 % in DNA barcode retrieval from single neurons (Fuentealba et al., 2015; Golden et al., 1995; Harwell et al., 2015) hampers the characterisation of clones using this method of identification. I set out to investigate whether heritable RNA barcoding would offer an improved success rate by increasing the number of barcode copies in a single cell via transcription of the barcode driven by a strong promoter. I constructed an RNA-barcoding retrovirus to test this hypothesis by incorporating an oligonucleotide barcode immediately downstream of the tdTom fluorescent reporter transgene driven by a CAG promoter, thereby ‘tagging’ tdTom transcripts with the barcode sequence. Using this strategy, I could retrieve the barcode identity of a cell by single cell RT-PCR amplification and sequencing. I demonstrated that

the RV-tdTom-barcode library consisted of multiple different barcode sequences, which could be retrieved from single cells and used to identify clones *in vitro*. Transcription of the barcode in single cells was indicated by the reliable retrieval of barcode sequence by RT-PCR amplification following DNase treatment. Since the presence of functional tdTom fluorescent protein was used to identify transduced cells, it was assumed that transcription of the barcode did not affect production or function of the fluorescent protein.

The overall success rate of barcode retrieval was over 70 % from single NIH/3T3 cells used in the current study – higher than that reported for a DNA barcode in neocortical neurons (Fuentealba et al., 2015; Golden et al., 1995; Mayer et al., 2015). However, RNA barcoding may be sensitive to cell type-specific variation in the level of transgene expression, which may affect the success rate of barcode retrieval from different cell types. Further investigation is necessary, therefore, to establish whether this success can be recapitulated in neocortical neurons. Nonetheless, this provides promising evidence that an RNA barcode could offer a higher success rate in clone identification in the neocortex than a traditional DNA barcode.

One concern of both DNA and RNA progenitor barcoding is that, due to the scale of amplification necessary, errors in the fidelity of barcode amplification could lead to splitting errors in the identification of clones. However, consistent with the ability to identify clones, identical barcode sequences could reliably be obtained from single cells within putative NIH/3T3 cell clones, which were visually identified as discrete clusters of fluorescently-labelled cells following low-titre transduction. The composition, and complexity, of the RV-tdTom-barcode library was not performed at this stage. Therefore it was not possible to estimate the probability with which unrelated cells could carry the same barcode sequence by chance, which would constitute a lumping error. However, identical barcodes were only ever identified from putative clones, and the same barcode was never isolated from different coverslips. This supports the inference that cells carrying the same barcode were, indeed, clones. Further characterisation of the library is necessary to estimate the confidence with which clonal relationships can be inferred (see

Chapter 5). Nonetheless, these data provided the first evidence that RNA barcoding using a retrovirus could be used to unequivocally identify excitatory neuronal clones in the developing neocortex.

Chapter 5

The influence of lineage upon neuronal phenotypes in the developing mouse neocortex

5.1 Introduction

Retroviral DNA barcoding of progenitors is an established method of identifying clonally-related neurons in the developing mouse neocortex (Golden et al., 1995). DNA barcoding uses the principle that each neurogenic progenitor is labelled by a unique DNA sequence, which is inherited by its progeny. Identification of the DNA barcode from individual cells enables clonal relationships to be identified by using the assumption that all cells carrying the same barcode are clonally related. This approach provides advantages over the geometric identification of clones, as it confers the ability to confidently identify clones, regardless of their spatial arrangement.

A major drawback of DNA barcoding is the low success rate associated with identifying the barcode sequence from single cells, which is typically around 50 % or less (Fuentealba et al., 2015; Golden et al., 1995; Harwell et al., 2015; Reid & Walsh, 2002). This results in incomplete identification of clones and a limitation on the types of studies that can be performed. Furthermore, clonal-labelling by DNA barcoding is difficult to combine with techniques for single-cell whole transcriptome analysis, therefore clonal studies have not harnessed the power of methods such as RNA-seq to investigate the transcriptional signatures that link clonality and neuron function. RNA barcoding employs the same principle that clones are identified with a distinct DNA sequence delivered by retroviral vectors. However, RNA barcoding differs from DNA barcoding in that the oligonucleotide is transcribed, and therefore amplified, in individual cells. In Chapter 4

RNA barcoding was shown to reliably identify clones in NIH/3T3 cells *in vitro*. However, whether this could be recapitulated *in vivo* and whether RNA barcoding was compatible with techniques such as single-cell RNA-seq was unknown.

One of the key tasks underlying clonal studies is to understand the influence of neuronal lineage on neuronal phenotype. There is already considerable evidence for a relationship between neuronal lineage and the functional properties of a neuron. For example, clonally-related neurons exhibit more similar stimulus selectivity in visual cortex (Li et al., 2012; Ohtsuki et al., 2012), as well as biased electrical (Yu et al., 2012) and chemical (Yu et al., 2009) synaptic connectivity. An important determinant of a neuron's function is the pattern of its dendritic arbor, which determines its synaptic inputs (Arikkath, 2012). Therefore, it is possible that some of the aspects of neuronal function that have been shown to be under clonal influence arise through clonal effects on dendritic morphology. Whether this is the case is currently unknown, and deficiencies in methods of clonal labelling have hindered its investigation. In this Chapter, I set out to establish the following:

- Can RNA-barcoding retrovirus be used to identify neocortical neuronal clones?
- Is there evidence for a relationship between clonality and neuronal morphology within neocortical excitatory neurons?

5.2. Results

5.2.1 RV-tdTom-barcode enables successful identification of neocortical clones in mouse

To investigate whether RNA barcoding with RV-tdTom-barcode could be used to identify clonal relationships amongst neocortical neurons *in vivo*, low-titre RV-tdTom-barcode (between ~ 250 and ~ 1000 colony-forming units (c.f.u) per embryo) was delivered by intraventricular injection in mice between E11.5 and E13.5 to label neuronal progenitors near the ventricular surface. This was expected to lead to expression of the integrated tdTom transgene, resulting in production of tdTom fluorescent protein and amplification of the barcode sequence by transcription within the cell. Single fluorescently-labelled neurons were collected manually from acute brain slices examined postnatally by aspiration with a pulled-glass micropipette. The barcode sequence of single neurons could then be identified by single-cell RT-PCR amplification and sequencing of the barcode amplification product (**Figure 5.1 A**). All experiments in this thesis (*in vivo* and *in vitro*) were performed using a single stock of RV-tdTom-barcode retrovirus. The purpose of this was to maximise the characterisation of the RV-tdTom-barcode retroviral library, and to minimise the averaging effect that may occur if the frequency of distinct barcodes was estimated across different batches of retrovirus.

Sparse, fluorescently-labelled neurons were evident in acute brain slices across all postnatal stages examined, indicating stable and heritable expression of tdTom-barcode. Fluorescently-labelled neurons were present across all neocortical regions and layers. Excitatory neurons could be found across the depth of the cortex, displaying morphology indicative of their laminar phenotype (**Figure 5.1 B**). A population of neurons with variable morphology were found dispersed across the neocortex, consistent with

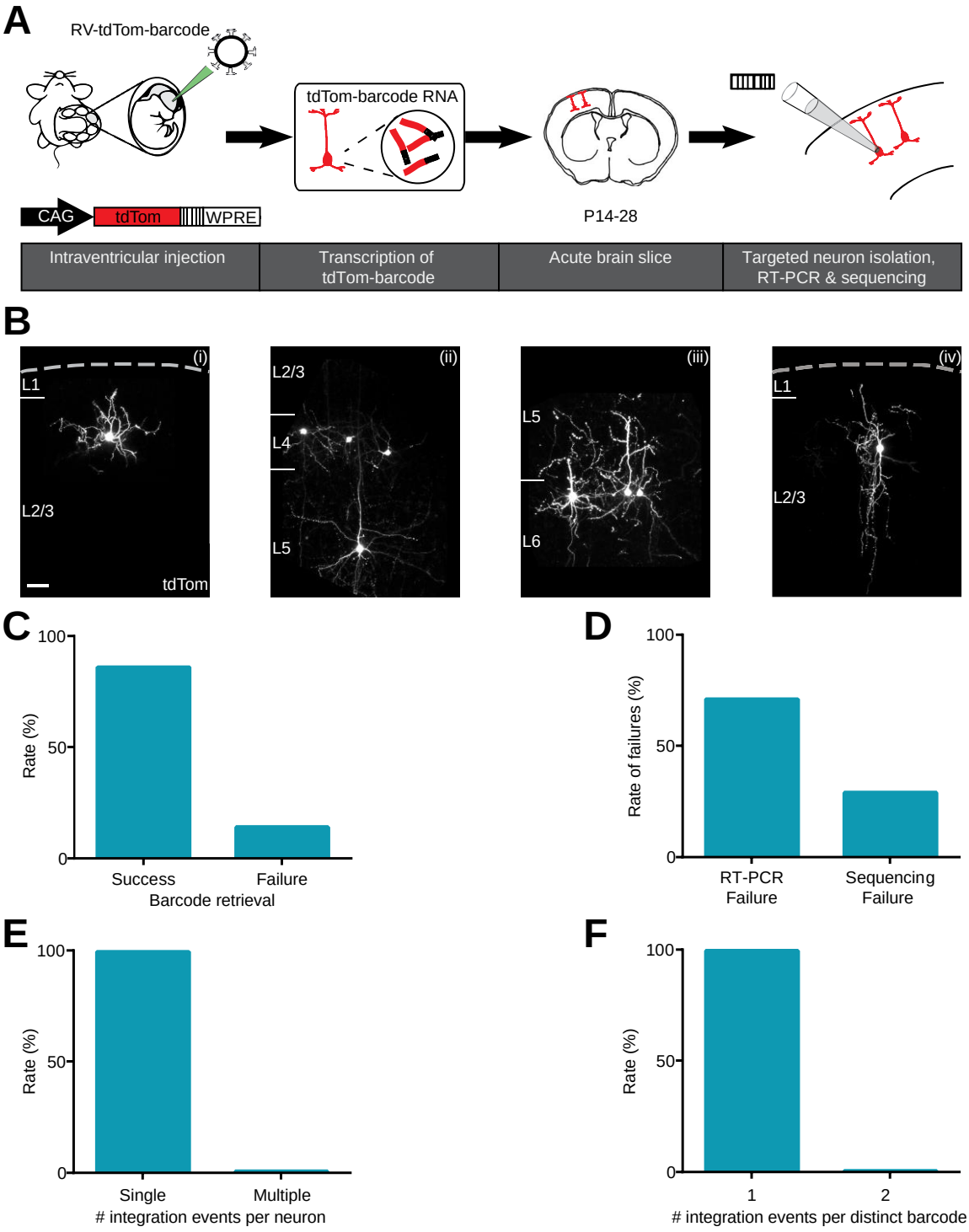

Figure 5.1: Retroviral RNA barcode can be identified from single neurons with a high success rate. (**A**) RV-tdTom-barcode was injected into the ventricles of embryonic mice between E11.5 and E13.5. Injected embryos were allowed to develop and acute cortical brain slices were generated between P14 and P28. Fluorescently-labelled neurons were collected by aspiration with a pulled-glass micropipette and processed for RT-PCR amplification and sequencing of the barcode for identification. (**B**) Fluorescently-labelled neurons were heterogeneous in their morphology and laminar positioning, consistent with labelling of diverse neuronal subtypes. Fluorescently labelled excitatory pyramidal neurons were observed in both superficial (layer 2 (L2), (**i**)) and deep (cont.)

the labelling of neocortical interneurons. These observations suggested that the tdTom barcoding retrovirus was capable of labelling diverse neuronal subtypes throughout the neocortex.

Single labelled pyramidal neurons were collected from somatosensory cortex and processed for identification of the barcode. Barcode sequence was reliably obtained from single neurons following optimisation of the protocol for RT-PCR amplification. Sequencing traces were of a high quality: the mean Phred score across the 27bp barcode read from single neurons was 52 ± 0.9 (n = 43), enabling the barcode identity of single neurons to be retrieved with a high success rate (86 %, 43/50; **Figure 5.1 C**). This established that RV-tdTom-barcode could identify a high proportion of labelled neurons within a clone. Neurons that did not yield a barcode sequence were further analysed in order to establish the source of failure. The majority of these (71 %, 5/7) were due to the failure to obtain an RT-PCR product. Failure to successfully sequence RT-PCR product of the correct size was the cause of the remaining failures (**Figure 5.1 D**). This indicated that failure of cell harvest or RT-PCR, which was likely to be affected by RNA quantity and quality, was the most likely causes of failure to identify the barcode in single neurons.

Evaluation of barcode retrieval was based on the assumption that the majority of progenitors underwent a single integration event, resulting in labelling with a single, unique barcode. To ascertain whether this was the case, the proportion of neurons exhibiting

(**Figure 5.1 cont.**) layers (L5, (**ii**); L6, (**iii**)), and exhibited morphology appropriate for their laminar phenotype. Putative excitatory spiny stellate neurons were observed in layer 4 (**ii**). In addition, morphologically-variable interneurons were found across all neocortical layers (**iv**). Dashed line represents the pia. Scale bar 50 µm. (**C**) Barcode sequence was successfully obtained from 86 % (43/50) of single neurons following optimisation of the protocol. (**D)** Of those cases that failed, the majority (5/7, 71 %) were due to the failure to obtain an RT-PCR product. Inability to successfully sequence RT-PCR product accounted for the remaining failures. (**E**) Most single neurons from which barcode sequence was successfully retrieved yielded a single barcode (> 99 %, 156/157) indicative of a single integration event in the transduced progenitor. (**F**) Across all experiments *in vitro* and *in vivo* using a single batch of RV-tdTom-barcode retrovirus, almost all distinct barcodes retrieved gave rise to a single integration event. < 1 % of barcodes gave rise to more than one (two) independent integration events, which were identified when the same unique barcode was detected in more than one experiment (n = 224 unique barcodes from 78 experiments). This small number of barcodes were discarded from analysis on the grounds that they could be overrepresented in the library.

more than one barcode sequence was assessed. Direct DNA sequencing of RT-PCR product was performed by the Sanger sequencing method, therefore it was not possible to establish the specific number of unique barcode sequences that comprised reads containing multiple barcodes. However, only one neuron out of 157 yielded multiple barcodes (< 1 %, 156/157 successfully sequenced neurons), indicative of multiple integration events in the transduced progenitor from which it was derived (**Figure 5.1 E**). Although this may represent an underestimation due to a low failure rate in the retrieval of barcodes, it suggests that there was only a very low frequency of multiple integration events in progenitors following low titre retroviral injection.

The confidence with which we can infer a clonal relationship between neurons carrying an identical barcode relies on the assumption that there is a low probability of two cells having the same barcode in the same tissue by chance. Three factors affect this assumption: the library complexity (the number of distinct barcodes), the library composition (the relative proportion of each distinct barcode within the library), and the transduction frequency (the number of independent, transduced cells in an experiment). In order to understand the confidence with which clones could be identified with RV-tdTom-barcode retrovirus, the composition of the library was characterised by examining the frequency with which different barcodes were retrieved across all experiments. For these purposes, an experiment was defined as either a brain or a culture well of cells *in vitro*, so that integration events could be definitively classed as independent events. 99 % (222/224 distinct barcodes from 78 experiments) of all unique barcodes that were retrieved, were retrieved from a single experiment (**Figure 5.1 F**). Of the remaining 1 % of barcodes, these were identified in two experiments only and were subsequently excluded from analysis on the assumption that they might be overrepresented in the library. It was difficult to estimate the composition of the library using these data for two reasons. Firstly, the data represent a relatively small sample of the library (which has a theoretical complexity of over 4 million), since the vast majority of barcodes that were retrieved were observed only once. Secondly, the unique barcodes are unlikely to be

uniformly distributed yet there is insufficient data to estimate the distribution of individual barcodes within the library. However, even if the 224 different barcodes identified represent the *entire* library, based on a likely labelling frequency of approximately 20 progenitors per brain in my experiments, the probability that the same barcode would be integrated into two progenitors is 0.008 – i.e. it has a probability of less than 1 % of occurring by chance. Furthermore, because only a small number of cells were collected from each brain, the probability that I would sample cells with the same barcode from two different progenitors was lower still. Taken together, this indicated that there was an extremely low probability that two progenitors would be labelled by the same unique barcode when RV-tdTom-barcode was used at a low titre.

In order to characterise the difference between identification of excitatory neuronal clones by geometric analysis and by RV-tdTom-barcode retrieval, two dilutions of low titre (between ~ 250 and ~ 1000 c.f.u per embryo) RV-tdTom-barcode were injected into the ventricles of embryonic mice between E11.5 and E13.5 and brains were examined between P14 and P28 (n = 52). Geometric criteria were applied to the sparsely labelled pyramidal neurons in order to identify putative geometric clones. These criteria were derived from the literature (Gao et al., 2014; M. Luskin et al., 1993; M C Mione, Danevic, Boardman, Harris, & Parnavelas, 1994; Yu et al., 2009) to define clones as clusters of fluorescently-labelled neurons that exhibited a distance of lateral spread (parallel to the pia) of less than 300 μm and that were separated laterally by more than 500 μm from other adjacent labelled cells. No restrictions were placed on the distance of their radial spread.

Across injection stages and within brains, clusters of labelled neurons were heterogeneous in their spatial arrangement, laminar position and the number of neurons included in the putative clone (**Figure 5.2 A**). Most putative clones had a broadly radial arrangement spanning the depth of the cortex, with variability in the distance of their lateral spread within the confines of the restriction used for geometric identification of clones. Some putative clones were composed of strictly linear, radial arrays, whereas other putative radial clones exhibited greater lateral dispersal. Occasionally, clusters of neurons

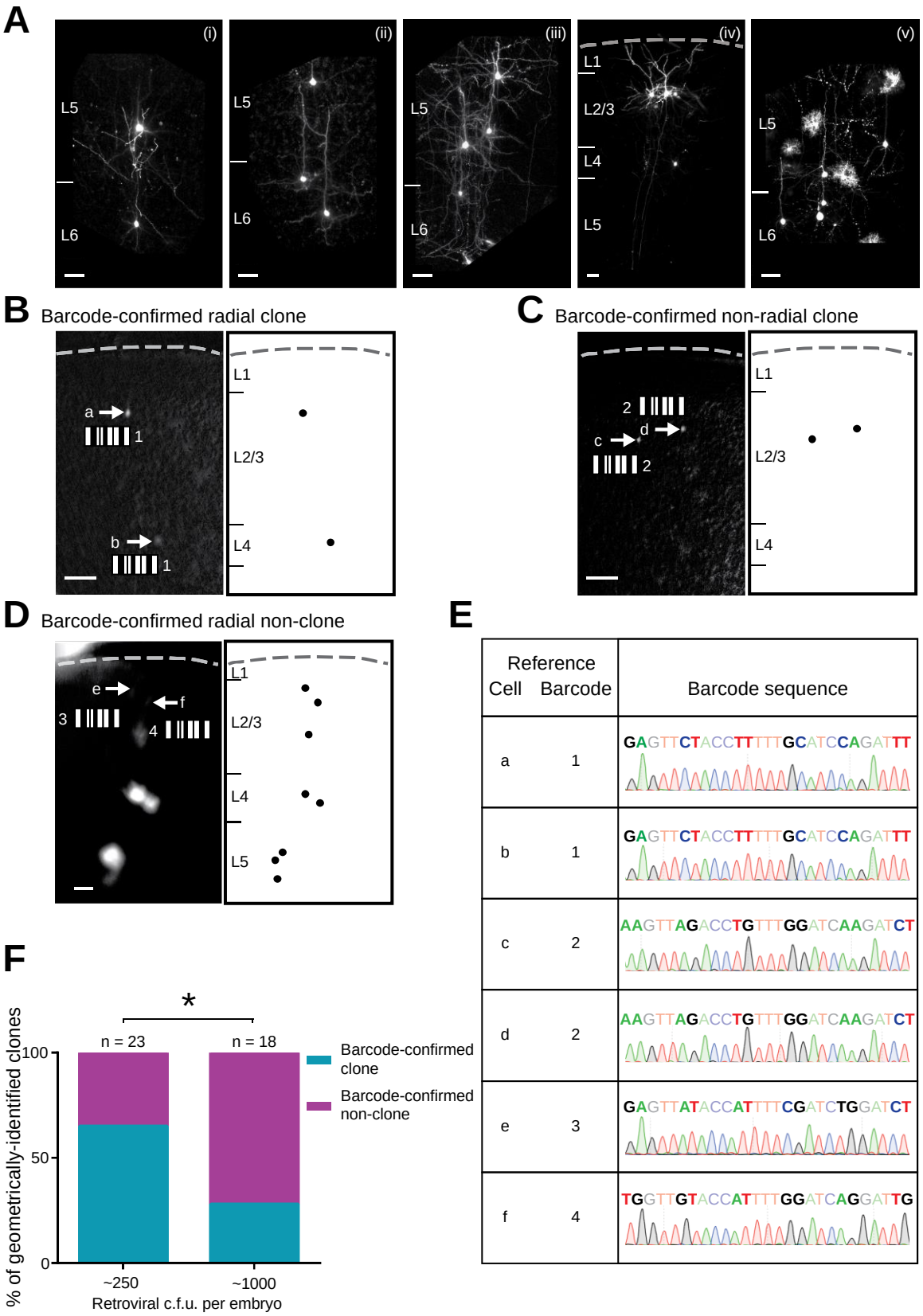

Figure 5.2: RNA barcoding retrovirus can be used to unequivocally identify clonally-related neurons in the developing mouse neocortex. Low titre (between ~ 250 and ~ 1000 c.f.u per embryo) RV-tdTom-barcode was injected into the brain ventricles of embryonic mice between E11.5 and E13.5 and acute cortical slices were prepared (cont.)

were found that exhibited greater lateral spread than radial spread. Some mixed clusters, containing both neurons and glia, were observed. The distribution of labelled cells was consistent with clonal labelling in the literature (Gao et al., 2014).

Pyramidal neurons from a subset of putative clones in somatosensory cortex were collected by aspiration with a pulled-glass micropipette (n = 18 brains). Neurons were processed by RT-PCR amplification and sequencing for barcode identification in order to establish their clonal relationships (mean 2.6 ± 0.5 distinct barcodes identified per brain). Distinct barcode sequences tended to differ from one another at multiple positions (8.5 ± 0.03 nucleotide bases of the 12 variable positions, n = 46 barcodes), therefore they could be identified unequivocally. This conveyed a high confidence in the ability to discern distinct barcode sequences, and therefore identify different clones. No neurons from different putative, geometrically-defined, clones yielded identical barcode sequences. This indicated that splitting errors (the assumption of non-clonality in neurons that are clonally-related) in clones identified using geometric criteria had not occurred. Identical barcode

(**Figure 5.2 cont.**) between P21 and P35. Neurons obtained from a single brain that yielded identical barcodes were defined as clonally related. (**A**) Putative clones were geometrically-defined as spatially-clustered groups of fluorescently-labelled cells, with under 300 µm lateral spread and greater than 500 µm separation from other labelled cells. These were heterogeneous in the number of neurons that they included, their spatial arrangement and laminar position. Radial clones varied in their lateral spread. Some formed strict, linear radial arrays (**i**), whereas others exhibited some lateral dispersal (**ii** and **iii**). Clusters of neurons were sometimes found that were predominantly spread laterally (**iv**). Occasionally, mixed clusters of neurons and glia were found (**v**). These were usually large (often > 10 cells) and spanned both deep and superficial layers. Dashed line represents the pia. Scale bar 50 µm. (**B**) Identical barcode sequences could be obtained from radial pairs of labelled pyramidal neurons, consistent with the idea that clonally-related excitatory neurons can form radial arrays. In (B) - (D): lettered arrows indicate labelled neurons and numbers indicate the identity of the unique barcode sequence. Images were collected under epifluorescence rather than confocal microscopy. The dashed line represents the pia; scale bar 100 µm. (**C**) Labelled pyramidal neurons carrying identical barcode sequences could also be found within the same neocortical layer, consistent with the idea that clones can be arranged tangentially. (**D**) Labelled pyramidal neurons within some clusters of labelled neurons yielded different barcode sequences to one another, revealing that they originated from more than one clone. (**E**) Sequencing traces from the single neurons harvested in (B) – (D) demonstrated the unequivocal identification of unique barcode sequences. (**F**) The proportion of intra-laminar, geometrically-defined clones that were confirmed to be clonally related by barcode decreased significantly when the retroviral titre was increased from ~ 250 c.f.u. per brain (250 c.f.u: 61 % of geometric clones were barcode-confirmed clones, 14/23; 1000 c.f.u: 39 % of geometric clones were barcode-confirmed clones, 7/18; p = 0.03, Fisher's exact test).

sequences could be retrieved from pairs of radially-aligned neurons from putative geometric clones, consistent with them being clonally related (**Figure 5.2 B – E**). Identical barcode sequences could also be retrieved from intralaminar neuron pairs, residing at a similar neocortical depth, from putative geometric clones. This verified that clones can form intralaminar clusters. Together, these data indicated that excitatory neuronal clones exhibited both radial and non-radial arrangements in neocortical slices. However, a subset of neuronal pairs within geometrically-identified clones yielded different barcode sequences, revealing that these neurons actually originated from different clones. This demonstrated that geometric identification of clones led to lumping errors, which was defined as the assumption of clonality in neurons that were actually non-clonally related.

Intralaminar clones that disperse laterally have presented a particular challenge for geometric methods of identifying clones (Mayer et al., 2016). To assess the relationship between retroviral transduction frequency and the confidence of geometric identification of intralaminar clones, the agreement between geometrically-identified clones and barcode-confirmed clones was related to the two retroviral titres used for transduction (~ 250 c.f.u per embryo and ~ 1000 c.f.u per embryo). These injection titres were achieved by diluting a stock of concentrated retrovirus of known titre, and led to the labelling of 28 ± 2 and 132 ± 7 neurons in somatosensory cortex, per brain, respectively. The proportion of geometrically-identified intralaminar clones that were confirmed to be clonal by barcode retrieval was significantly lower for clones in brains injected with 1000 c.f.u. of retrovirus than those injected with 250 c.f.u. (250 c.f.u: 61 % of geometric clones were barcode-confirmed clones, 14/23; 1000 c.f.u: 39 % of geometric clones were barcode-confirmed clones, 7/18; $p = 0.03$, Fisher's exact test; **Figure 5.2 F**). Moreover, even at the lower retroviral titre, 39 % of putative clones were in fact non-clonal neuronal pairs. This highlights the susceptibility of geometric identification of intralaminar clones to lumping errors, and demonstrates the utility of RNA barcoding in identifying this population of clones.

5.2.2 RNA barcoding with RV-tdTom-barcode is compatible with RNA-seq for transcription profiling of clonally-related neurons

Compatibility between progenitor barcoding and RNA-seq would offer the opportunity to compare the transcriptome of clonally-related and non-clonally related neurons. To investigate whether the RNA barcode could be retrieved by RNA-seq, six fluorescently-labelled layer 2/3 pyramidal neurons were collected from acute cortical slices using a pulled-glass micropipette and prepared for RNA-seq according to the Smart-seq2 protocol (**Figure 5.3 A**). Next-generation sequencing was then performed using the Illumina HiSeq 4000 DNA sequencing instrument. Reads were mapped with STAR v2.4.2a (Dobin et al., 2013) and aligned with MAFFT (Katoh, Misawa, Kuma, & Miyata, 2002). All six neurons were successfully sequenced, with an average read depth of $7.3 \times 10^6 \pm 8 \times 10^5$ reads per neuron (**Figure 5.3 B**). Of the total number of reads, 6917 ± 2089 reads mapped to tdTom-barcode per neuron (**Figure 5.3 C**). The depth of sequencing across the entire tdTom-barcode sequence varied, most likely because reads that mapped to a single Tomato sequence were automatically assigned to the first Tomato sequence (**Figure 5.3 D**). The read depth was sufficient to successfully identify the barcode from the consensus sequence over the barcode region by searching for the fixed nucleotide bases upstream of the barcode sequence (**Figure 5.3 E**). Identical barcode sequence was retrieved from two neurons, revealing a clonal relationship. The remaining four neurons were non-clonally related. The five distinct barcode sequences retrieved by RNA-seq differed at 7 ± 1.4 of the 12 variable nucleotide base positions but at none of the fixed positions, indicating a high confidence that RNA-seq revealed true differences between barcode sequences. These data confirm that clonal labelling with RV-tdTom-barcode can be identified by single-cell RNA-seq. This demonstrates the utility of retroviral RNA barcoding as a method of clonal labelling, and the potential to conduct transcriptomic studies in the future.

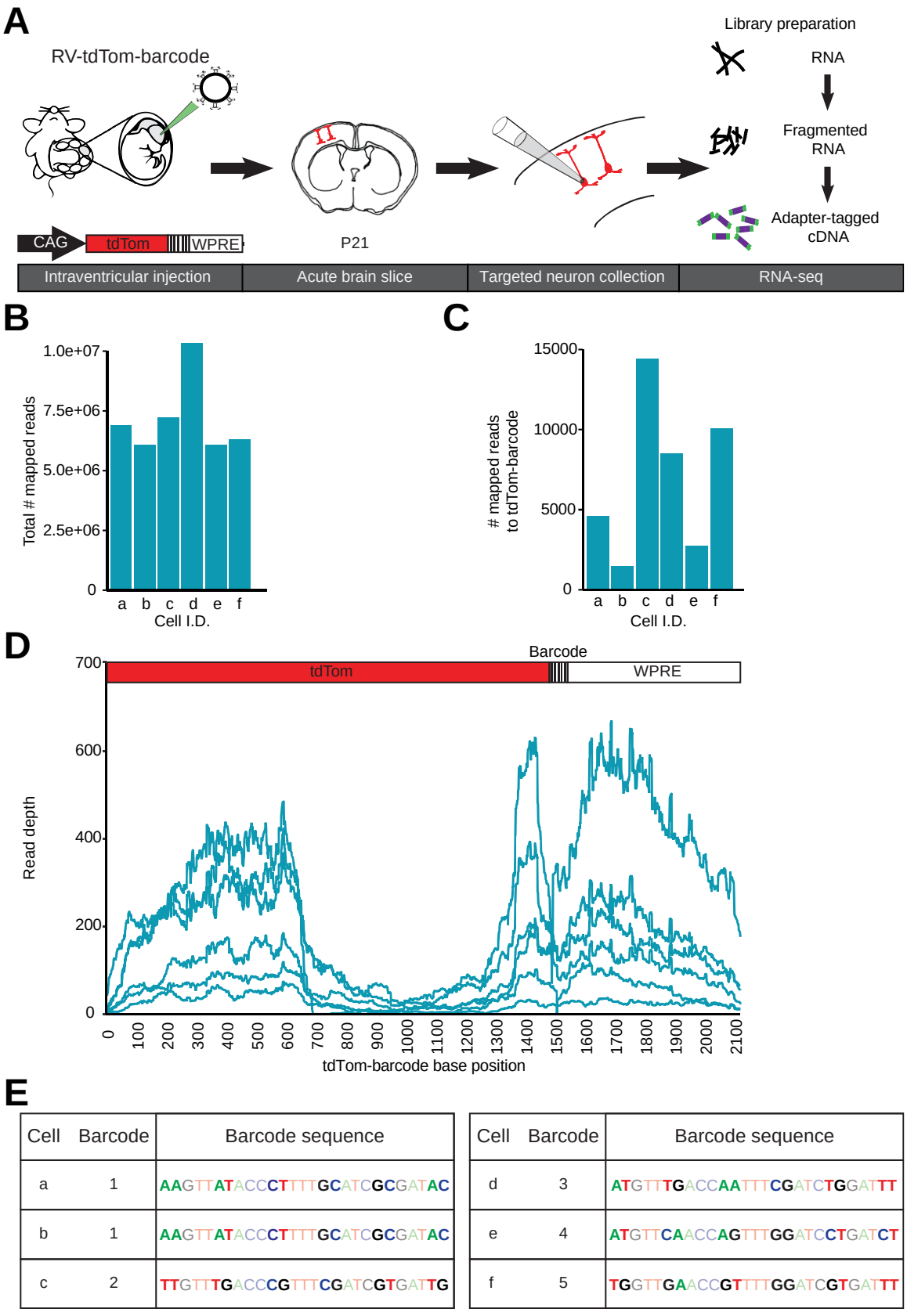

E

Cell	Barcode	Barcode sequence
a	1	AAGTTATACCCTTTTGCATCGCGATAC
b	1	AAGTTATACCCTTTTGCATCGCGATAC
c	2	TTGTTTGACCCGTTTCGATCGTGATTG

Cell	Barcode	Barcode sequence
d	3	ATGTTTGACCAATTTCGATCTGGATTT
e	4	ATGTTCAACCAGTTTGGATCCTGATCT
f	5	TGGTTGAACCGTTTTGGATCGTGATTT

Figure 5.3: RNA barcoding with RV-tdTom-barcode is compatible with RNA-seq for transcription profiling of clonally-related neurons. (**A**) RV-tdTom-barcode was injected into the ventricles of embryonic mice at E12.5. Injected embryos were allowed to develop and acute cortical brain slices were generated at P21. Six (cont.)

5.2.3 RNA barcoding reveals errors in the geometric identification of clones

To further understand the accuracy of the geometric identification of neocortical clones, the relationship between the spatial arrangement of neuron pairs and their barcode-confirmed clonal relationship was assessed using the lowest titre retrovirus (~ 250 c.f.u./ml). The lateral spread, which was the distance between somata in the direction parallel to the pial surface, and the radial spread, which was the perpendicular distance between the somata of neurons, were measured for neuron pairs comprising geometrically-defined clones. The lateral and radial spread were each divided into bins (50 μm for lateral spread, and 100 μm for radial spread) and the percentage of neuron pairs that were confirmed by barcode identification to be clonally-related was calculated.

The proportion of pairs correctly identified as clones by geometric identification changed as a function of the distance between the neurons (**Figure 5.4 A and B**). The accuracy of geometric analysis decreased as the lateral and radial spread increased, and less than half of neuron pairs that were separated by over 200 μm in either direction were clonally related. Accordingly, calculation of the Euclidean distance between neuron pairs revealed that clonally related neurons tended to be separated by a smaller Euclidean distance than non-clonally related pairs (clonal: mean = 81.0 μm ± 10.9 μm; non-clonal mean = 170.4 μm ± 29.7 μm; t (35.59) = 2.76, p = 0.009, unpaired t test with Welch's correction; **Figure 5.4 C**). Finally, in order to ascertain whether geometric analysis was biased in its ability to detect radially-aligned or non-radially aligned neuron pairs, the

(**Figure 5.3 cont.**) fluorescently-labelled pyramidal neurons in layer 2/3 of somatosensory cortex were collected by aspiration with a pulled-glass micropipette and processed for RNA-seq. Reads were mapped with STAR v2.4.2a (Dobin et al., 2013) and aligned with MAFFT (Katoh et al., 2002). (**B**) The average total number of mapped reads per neuron was $7.3 \times 10^6 \pm 8 \times 10^5$. (**C**) The average number of reads mapped to tdTom-barcode was 6917 ± 2089 per neuron. (**D**) The tdTom-barcode sequence read depth exhibited a decrease from ~ 700 to ~ 1300 bp in the tdTom sequence that was attributed to an artefact of sequence alignment. Read depths were generally high over the barcode sequence. (**E**) The barcode sequence was successfully identified from every neuron (100 %, 6/6). Identical barcode sequence was retrieved from two neurons, revealing a clonal relationship. The five distinct barcode sequences retrieved by RNA-seq differed at 7 ± 1.4 of the 12 variable nucleotide base positions but none of the fixed positions.

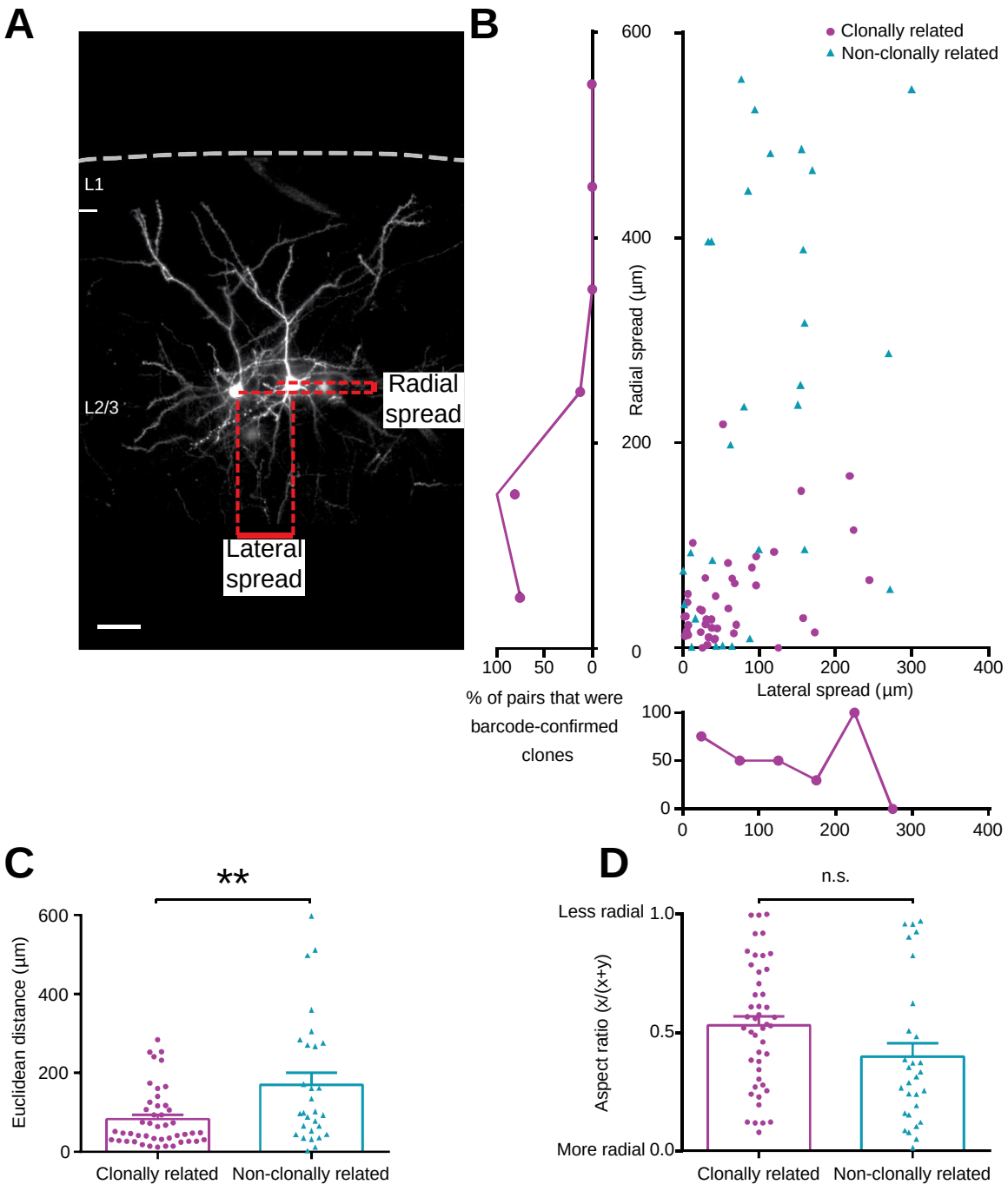

Figure 5.4: Progeny of neocortical neuronal progenitors are spatially restricted in mouse neocortex. Low titre (~ 250 - 500 c.f.u per embryo) RV-tdTom-barcode was injected into the ventricles of embryonic mice between E11.5 and E13.5 and acute cortical slices were prepared between P14 and P28. (**A**) The spatial relationship of neuronal pairs in putative (geometrically-defined) clones was analysed. Measurements of lateral spread and radial spread between neurons in pairs were taken parallel to, and perpendicular to, the pial surface, respectively. Dashed line represents the pia. Scale bar 50 µm. (**B**) The ability to identify clones using geometric criteria changed as a function of the distance of their lateral and radial spread, with fewer neuron pairs constituting barcode-confirmed clones with increasing distance. (**C**) Clonally-related pairs tended to be separated by a smaller Euclidean distance than non-clonal pairs (clonal: mean = 81.0 µm (cont.)

aspect ratio of neuron pairs was examined. This was calculated as the lateral spread divided by the sum of the lateral plus radial spread, to provide a measure of 'radialness'. No significant difference was found between the aspect ratio of confirmed clones and non-clones (clonal: mean = 0.53 ± 0.04, non-clonal: mean = 0.40 ± 0.06; t (52.86) = 1.92, p = 0.06, unpaired t test with Welch's correction). Taken together, these data provide further characterisation of the errors resulting from geometric identification of clones.

5.2.4 RV-tdTom-barcode enables the comparison of morphologically-equivalent, spatially-matched pairs of clonally related and non-clonally related pyramidal neurons

The influence of clonality on the development of the distinct dendritic morphology of an individual neuron has not been examined. The ability to unequivocally identify clones provided by RNA barcoding of progenitors, without relying on geometric identification, offers the opportunity to study the morphology of clonally related and non-clonally related neurons that share a close spatial proximity. This controls for any variation that may arise in the comparison of neurons across different neocortical areas. To further understand the relationship between clonality and neuronal morphology, the titre of RV-tdTom-barcode was titrated in order to obtain spatially-clustered pairs of labelled excitatory neurons in layer 2/3 of somatosensory cortex. This experimental design allowed the comparison of morphology between pairs of clonally related neurons, identified by their barcode label, and a control group of pairs of non-clonally related neurons matched for spatial proximity to one another.

(**Figure 5.4 cont.**) ± 10.9 µm; non-clonal mean = 170.4 µm ± 29.7 µm; t (35.59) = 2.76, p = 0.009, unpaired t test with Welch's correction). (**D**) There was no significant difference between the aspect ratio ('radialness') of confirmed clonally-related pairs and those that were non-clonal ('x' = lateral spread, 'y' = radial spread; clonal: mean = 0.53 ± 0.04, non-clonal: mean = 0.40 ± 0.06; t (52.86) = 1.92, p = 0.06, unpaired t test with Welch's correction).

The dendritic arbors of pairs of labelled neurons that were separated laterally by < 200 µm and radially by < 50 µm were imaged using a confocal microscope with a z step of 0.5 µm before being collected and processed for barcode identification to establish their clonal relationship. The dendritic arbor of each neuron was traced and Sholl analysis was performed using radius increments of 10 µm. This produced a Sholl profile for each neuron in which the number of dendritic intersections for each radius from the soma was plotted (**Figure 5.5 A**). Four specific aspects of the dendritic arbor were calculated to provide a morphological description of each neuron. The total dendritic length (i) was calculated from the dendritic tracing. Then, three further parameters were derived from the Sholl analysis (Ferreira et al., 2014): (ii) The enclosing radius (r_e), which was the radius of the largest Sholl circle centred on the soma that intersected with a dendrite, representing the distance between the soma and the furthest extent of a dendrite. (iii) The critical radius (r_c), which was the radius at which there was the greatest number of dendritic intersections, representing the distance from the soma at which there were the most dendritic branches. Finally (iv), the Schoenen Ramification Index (SRI), which was the ratio between the maximum number of dendritic intersections for a single Sholl circle and

(**Figure 5.5 cont. from page 135**) chosen to obtain intralaminar pyramidal neuron pairs, separated by under 200 µm, of which approximately 50 % were clonally related. This titre of RV-tdTom-barcode was then injected into the ventricles of embryonic mice between E11.5 and E12.5 and acute cortical slices were prepared between P21 and P35. Fluorescently-labelled pyramidal neuron pairs in layer 2/3 of somatosensory cortex were imaged using a confocal microscope, collected and processed for barcode retrieval. (**A**) Neuronal arbors were traced (**i**) and Sholl analysis was performed for each neuron using concentric circles, with radii increasing in increments of 10 µm, centred on the soma to produce a Sholl profile for each neuron (**ii**). The morphology of each neuron was then characterised by four measures (**iii**). (**B**) The combined Sholl profiles of the population of neurons from clonal and non-clonal pairs were not significantly different for any radius from the soma ($p > 0.05$ at each distance, multiple t tests with Holm-Šidák correction for multiple comparisons). (**C**) There was no significant difference between the total dendritic length of individual neurons from clonal or non-clonal pairs ($t(35.6) = 1.6$, $p = 0.1$; unpaired t test with Welch's correction). (**D**) The enclosing radius (r_e) of the dendritic arbor was not significantly different between the population of clonal or non-clonal neurons ($t(47.5) = 1.6$, $p = 0.2$; unpaired t test with Welch's correction). (**E**) The critical radius (r_c) was not significantly different between the population of clonal or non-clonal neurons ($t(50.3) = 1.6$, $p = 0.1$; unpaired t test with Welch's correction). (**F**) There was no significant difference in the dendritic complexity, assessed by the SRI, between the population of individual clonal or non-clonal neurons ($t(50.4) = 1.0$, $p = 0.3$; unpaired t test with Welch's correction).

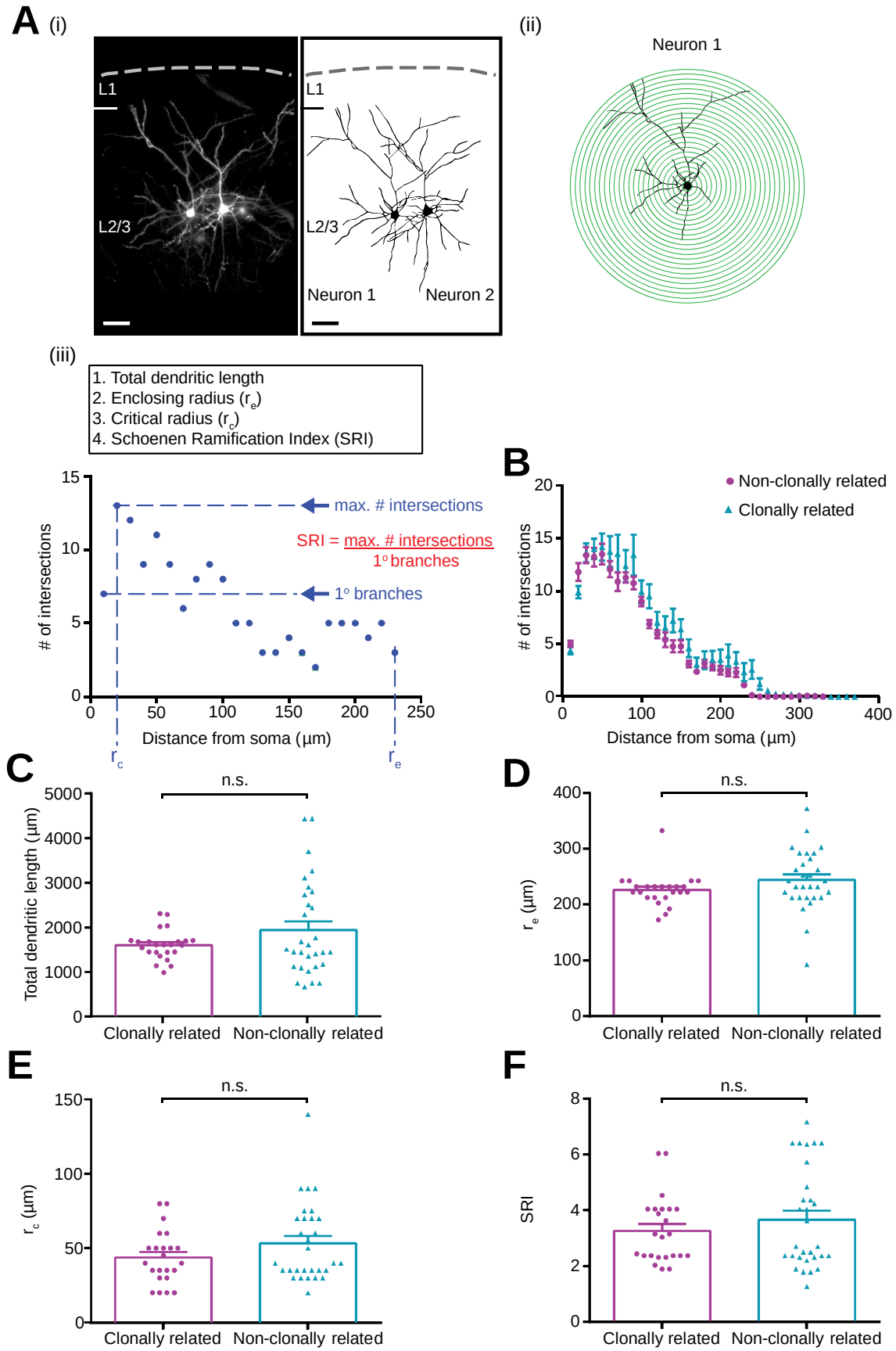

Figure 5.5: RV-tdTom-barcode labels a population of clonal and non-clonal pyramidal neuronal pairs that do not significantly differ in their dendritic morphology. The transduction titre of RV-tdTom-barcode was (cont. on page 134)

the number of primary dendrites, thus representing a measure of dendritic branching. There was no significant difference in the lateral distance between the pairs of soma of neurons in clonally-related and non-clonally related pairs (clonally related: mean = 34.1 µm ± 8.9 µm, n = 12; non-clonally related: mean = 37.7 µm ± 7.4 µm, n = 15; t (22.8) = 0.3, p = 0.8, unpaired t test with Welch's correction; data not shown).

In order to establish whether there were any differences in the morphology of the population of clonally-related and non-clonally related pyramidal neurons, the Sholl profile of neurons in each population were combined, and the number of intersections at each radius was compared. There was no significant difference in the number of dendritic intersections at any radius between neurons comprising clonally-related and non-clonally related pairs (clonally related: n = 24, non-clonally related n = 30, p > 0.05 at each distance, multiple t tests with Holm-Šidák correction for multiple comparisons; **Figure 5.5 B**). This indicated that the two populations did not differ in their general dendritic profile. There was also no significant difference in the total dendritic length of the neurons from clonally-related and non-clonally related neuron pairs (clonally-related: mean = 1602 µm ± 67 µm, n = 24, non-clonally related: mean = 1941 µm ± 195 µm, n = 30; t (35.6) = 1.6, p = 0.1; unpaired t test with Welch's correction; **Figure 5.5 C**), nor was there a difference in the enclosing radius (clonally related: mean 224 µm ± 6 µm, n = 24; non-clonally related: mean = 242 µm ± 10 µm, n = 30; t (47.5) = 1.6, p = 0.2; unpaired t test with Welch's correction; **Figure 5.5 D**). This suggested that the overall dendritic morphology was similar between the two populations. The critical radius was not significantly different between the two populations (clonally related: mean = 44 µm ± 4, n = 24; non-clonally related: mean = 53 µm ± 5 µm, n = 30; t (50.3) = 1.6, p = 0.1; unpaired t test with Welch's correction, **Figure 5.5 D**), indicating that the profile of dendritic complexity was similar. Finally, there was no significant difference in the SRI between the two groups, indicating that the degree of dendritic complexity was similar between the two populations (clonally related: mean = 3.2 ± 0.2, n = 24; non-clonally related: mean = 3.5 ± 0.3, n = 30; t (50.4) = 1.0, p = 0.3; unpaired t test with Welch's correction, **Figure 5.5 E**). Taken together, these data provide

evidence that the neurons sampled from clonally-related pairs and non-clonally related pairs were fundamentally similar in their dendritic arbors.

5.2.5 Clonally-related pyramidal neurons in layer 2/3 of somatosensory cortex have more similar dendritic arbors than non-clonally related neurons

The observation that clonally-related neuron pairs are morphologically equivalent to a matched population of non-clonally related neuron pairs provides the opportunity to compare the morphological similarity of neurons *within* pairs. The aim of this analysis was to establish whether clonally-related neurons are morphologically more similar to one another than the baseline level of similarity between spatially-matched, non-clonally related pairs of neurons. Neurons from clonally-related and non-clonally related pairs were traced (**Figure 5.6 A**) and the four measures described previously were used to quantify dendritic morphology: the total dendritic length, the enclosing radius, the critical radius, and the SRI (**Figure 5.6 B – E**). The total dendritic length was found to be significantly more similar between neurons in clonally related pairs than in unrelated pairs (clonally related: mean = 505 µm ± 66 µm, n = 12; non-clonally related: mean = 1201 µm ± 250 µm, n = 15; t (15.9) = 2.7, p = 0.02; unpaired t test with Welch's correction). Furthermore, there was a significant difference in the similarity of the SRI, which was more similar between neurons in clonally-related pairs (clonally related: mean = 0.9 ± 0.1, n = 12; non-clonally related: mean = 2.1 ± 0.3, n = 15; t (18.9) = 3.9, p = 0.001; unpaired t test with Welch's correction). Neurons in clonally-related and non-clonally related pairs were no more similar in either the enclosing radius (clonally related: mean = 23 µm ± 10 µm, n = 12; non-clonally related: mean = 53 µm ± 12 µm; t (24.7) = 1.9, p = 0.06; unpaired t test with Welch's correction) or the critical radius (clonally-related: mean = 19 µm ± 6 µm, n = 12; non-clonally related: mean = 43 µm ± 14 µm, n = 15; t (19.0) = 1.6, p = 0.1; unpaired

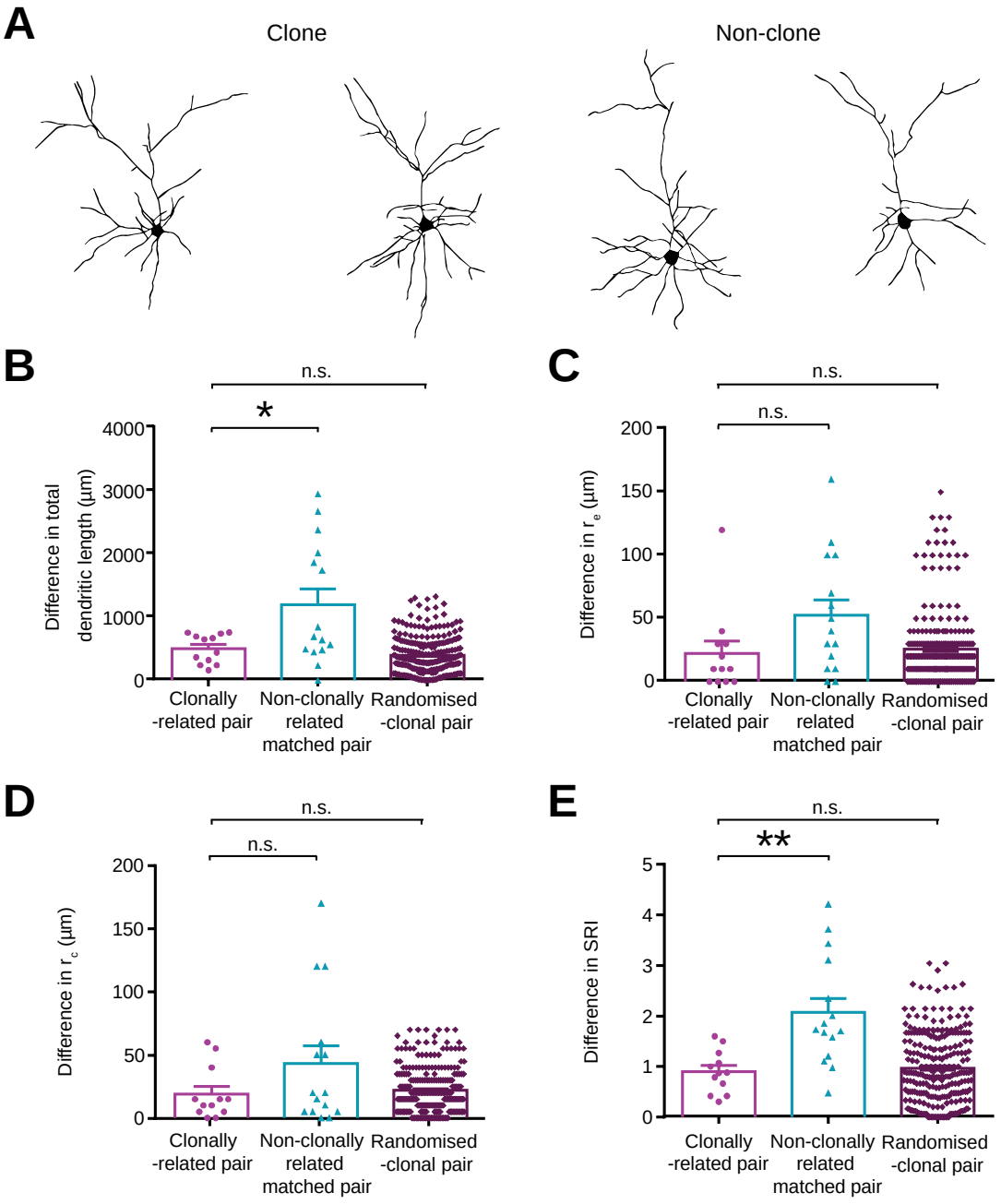

Figure 5.6: Clonally-related pyramidal neuron pairs in layer 2/3 have more similar dendritic complexity than non-clonal pyramidal neuron pairs. (**A**) Fluorescently-labelled pyramidal neurons comprising clonal or non-clonal neuron pairs from layer 2/3 were traced and Sholl analysis was performed (n = 12 clonally-related pairs, n = 15 non-clonally-related pairs). The morphology of neurons was characterised by four measures and the difference in these four measures between neurons in clonal or non-clonal pairs was calculated. A further comparison was performed between clonal pairs and randomised pairs from the population of neurons comprising clonal pairs. (**B**) The difference in the total dendritic length was significantly smaller in clonal pairs than in non-clonal pairs (t (15.9) = 2.7, p = 0.02; unpaired t test with Welch's correction) but comparable in clonal and randomised clonal pairs (t (12.7) = 1.5, p = 0.2; unpaired t test with Welch's correction). (**C**) Clonal pairs and non-clonal pairs shared a comparable difference in their enclosing radius (t (24.7) = 1.9, p = 0.06; unpaired t test with Welch's correction), as did clonal and randomised clonal pairs (t (11.7) = 0.3, p = 0.7; unpaired t test with Welch's correction). (**D**) Clonal pairs and non-clonal pairs shared a (cont.)

t test with Welch's correction). These data revealed that the overall dendritic complexity shows greater similarity between neurons in clonally related pairs, but the overall size and profile of the dendritic arbor does not.

It was possible that the significant differences in the total dendritic length and dendritic complexity reflected an effect of clonality on the dendritic arbor of a neuron, or reflected the influence of particular progenitor lineages, such as those that tend to generate pairs of neurons in layer 2/3. To establish whether the greater similarity in the neuronal dendritic arbor of clones resulted from the specific effect of clonality or a more general effect of progenitor lineage, the dendritic similarity of neurons in clonal pairs was compared to the similarity of neurons in a third group ('randomised-clonal pairs'), in which each neuron from a clonal pair was compared to every other neuron in the population of neurons comprising clonal pairs. A specific effect of clonality would be indicated by a significantly greater similarity in the neurons in clonal pairs than those in randomised-clonal pairs. There was no significant difference in either the total dendritic length (randomised-clonal pair: mean = 400 µm ± 18 µm, n = 264; t (12.7) = 1.5, p = 0.2; unpaired t test with Welch's correction), the enclosing radius (randomised-clonal pair: mean = 26 µm ± 2 µm, n = 264; t (11.7) = 0.3, p = 0.7; unpaired t test with Welch's correction), the critical radius (randomised-clonal pair: mean = 22 µm ± 1 µm, n = 264; t (11.8) = 0.5, p = 0.6; unpaired t test with Welch's correction) or the SRI (randomised-clonal pair: mean = 1.0 ± 0.04; t (14.0) = 0.6, p = 0.6; unpaired t test with Welch's correction) between neurons in clonal and randomised-clonal pairs. These data revealed that the similarity in the total dendritic length and SRI between neurons in clonal pairs is more likely to reflect an influence of particular progenitor lineages, such as those that tend to generate pairs of neurons in layer 2/3, rather than an effect of clonality per se.

(**Figure 5.6 cont.**) comparable difference in their critical radius (t (19.0) = 1.6, p = 0.1; unpaired t test with Welch's correction), as did clonal and randomised clonal pairs (t (11.8) = 0.5, p = 0.6; unpaired t test with Welch's correction). (**E**) The dendritic complexity, measured by the SRI, was more similar for neurons within clonal pairs than those within non-clonal pairs (t (18.9) = 3.9, p = 0.001; unpaired t test with Welch's correction). There was a comparable difference in the SRI within clonal and randomised clonal pairs (t (14.0) = 0.6, p = 0.6; unpaired t test with Welch's correction).

Having provided evidence for a relationship between neuronal lineage and neuronal morphology, I next examined whether this relationship was apparent across the whole dendrite or if it was specific to the apical or basal arbor (**Figure 5.7 A**). Using the same measures of dendritic arborisation as in the previous analysis, the apical and basal dendritic arbor were assessed separately (**Figure 5.7 B – E**). The total dendritic length of the apical, but not the basal, dendritic arbor was significantly more similar between neurons in clonally-related pairs than non-clonally related pairs (apical: clonally-related: mean = 174 µm ± 54 µm, n = 12; non-clonally related: mean = 447 µm ± 102 µm, n = 15; t (20.9) = 2.4, p = 0.03; unpaired t test with Welch's correction; basal: clonally related mean = 246 µm ± 79 µm, n = 12; non-clonally related mean = 563 µm ± 137 µm, n = 15; t (21.8) = 2.0, p = 0.08; unpaired t test with Welch's correction). Furthermore, clonally-related neuron pairs had a significantly more similar apical SRI than non-clonal pairs (clonally related: mean = 1.5 ± 0.5, n = 12; non-clonally related: mean = 10.1 ± 2.7, n = 15; t (14.9) = 3.1, p = 0.007, unpaired t test with Welch's correction). This was not the case for the basal dendrites, in which there was no difference in the SRI between the two populations (clonally related: mean = 2.1 ± 0.4, n = 12; non-clonally related: mean = 2.4 ± 0.5, n = 15; t (24.7) = 0.4, p = 0.7; unpaired t test with Welch's correction).

(**Figure 5.7 cont. from page 141**) (**A**) The apical (left) and basal dendrites (right) of labelled pyramidal neurons comprising clonal or non-clonal neuron pairs from layer 2/3 were traced separately and Sholl analysis was performed. The morphology of neurons was then characterised by four measures in order to compare the apical dendritic arbors of the populations of neurons that comprised clonal or non-clonal pairs. The difference in the four measures was then calculated to compare the morphological similarity of clonal and non-clonal neurons within their respective pairs. (**B**) There was significantly less difference in the total apical, but not the basal, dendritic length between neurons in clonal pairs and neurons in non-clonal pairs (apical: t (20.9) = 2.4, p = 0.03; unpaired t test with Welch's correction; basal: t (21.8) = 2.0, p = 0.08; unpaired t test with Welch's correction). (**C**) Clonal pairs and non-clonal pairs shared a comparable difference in their enclosing radius for both the apical (t (24.6) = 1.5, p = 0.2; unpaired t test with Welch's correction) and basal (t (25.0) = 0.3, p = 0.8; unpaired t test with Welch's correction) dendrites. (**D**) Clonal pairs and non-clonal pairs shared a similar difference in the critical radius for both the apical (t (23.4) = 1.4, p = 0.2; unpaired t test with Welch's correction) and the basal (t (24.7) = 0.4, p = 0.7; unpaired t test with Welch's correction) dendrites. (**E**) The apical dendritic complexity, measured by the SRI, was more similar between neurons within clonal pairs than those within non-clonal pairs (t (14.9) = 3.1, p = 0.007; unpaired t test with Welch's correction). There was no difference in the basal dendritic complexity (t (24.7) = 0.4, p = 0.7; unpaired t test with Welch's correction).

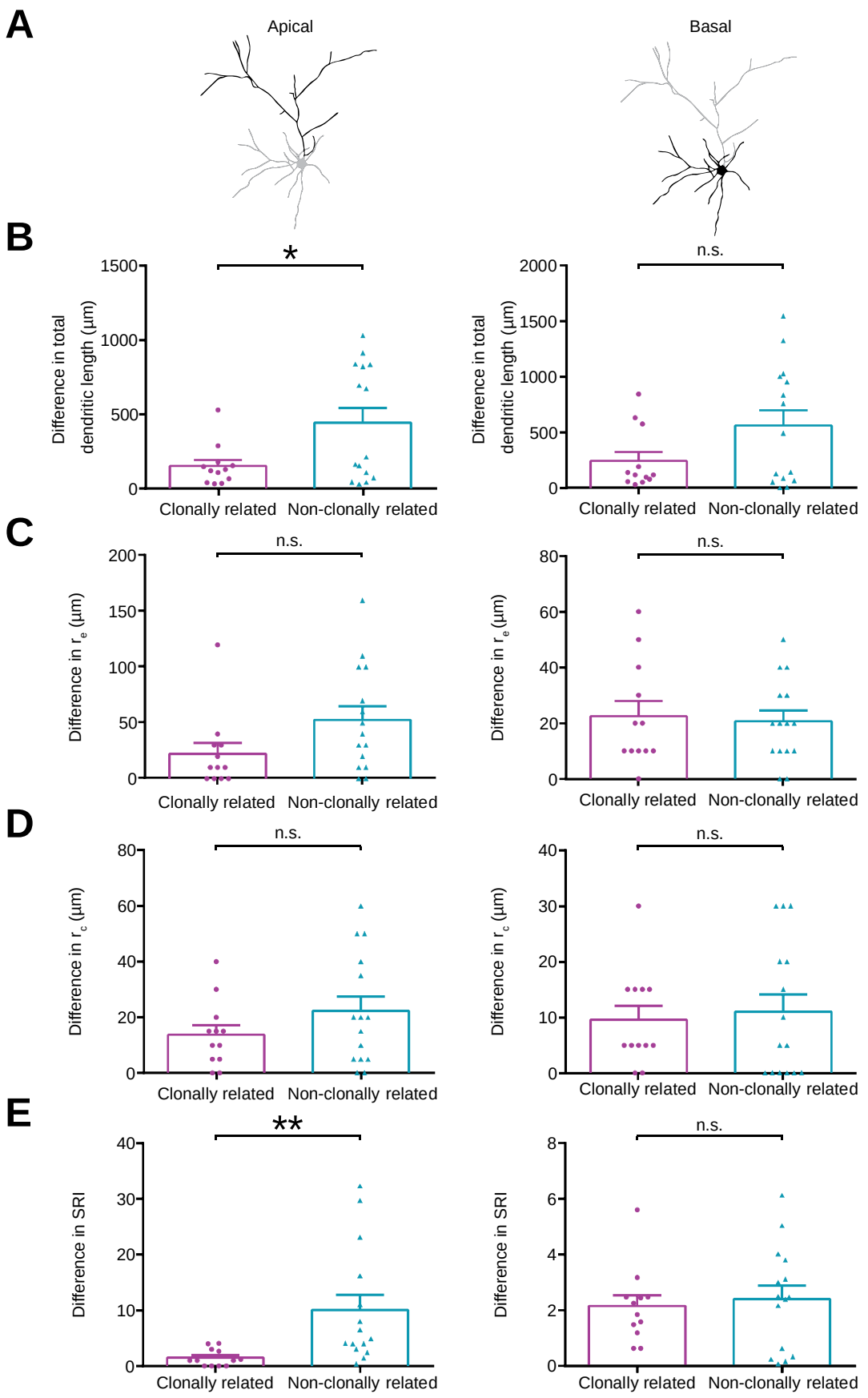

Figure 5.7: Clonally-related pyramidal neuron pairs in layer 2/3 have more similar apical dendritic complexity than non-clonal pyramidal neuron pairs. (cont. page 140)

There was no difference in the similarity of the enclosing radius of either the apical or basal dendrites between clonally-related and non-clonally related neuron pairs (apical: clonally-related: mean = 29 µm ± 15 µm, n = 12; non-clonally related: mean = 60 µm ± 15 µm, n = 15; t (24.6) = 1.5, p = 0.2; unpaired t test with Welch's correction; basal: clonally related: mean = 23 µm ± 5 µm, n = 12; non-clonally related: mean = 21 ± 4 µm, n = 15 t (25.0) = 0.3, p = 0.8; unpaired t test with Welch's correction). Nor was there a difference in the critical radius for either the apical or the basal arbors between clonally-related and non-clonally related neuron pairs (apical: clonally related: mean = 14 ± 3 µm; non-clonally related: mean = 22 ± 5 µm, n = 15; t (23.4) = 1.4, p = 0.2; unpaired t test with Welch's correction; basal: clonally related: mean = 10 µm ± 2 µm, n = 12; non-clonally related: mean = 11 µm ± 3 µm, n = 15; t (24.7) = 0.4, p = 0.7; unpaired t test with Welch's correction). Taken together, these results reveal an effect of lineage on the complexity of the apical, but not the basal, dendritic arbor.

5.3 Discussion

In this chapter I have demonstrated that a retroviral RNA barcode can be identified with a high success rate from neurons in the developing mouse cortex. Critically, this strategy confers the ability to unequivocally confirm whether neurons are clonally-related or not. I used this RNA barcoding of excitatory neuronal progenitors to investigate clones in the developing cortex. To establish the accuracy of commonly-used geometric methods, I compared clones defined using geometric criteria and clones confirmed with RNA barcoding. I also demonstrated that clonal identification by RNA barcoding was compatible with single-cell RNA-seq, which offers the opportunity to investigate the molecular basis of the relationship between clonality and dendritic arborisation. I then employed RNA barcoding to explore the relationship between clonality, lineage and

dendritic morphology in layer 2/3 pyramidal neurons in somatosensory cortex. I used the high success rate of RNA barcoding to demonstrate that clonally-related pyramidal neurons in layer 2/3 of somatosensory cortex in mouse are more similar in their dendritic morphology than unrelated neurons, and I revealed that this was likely to reflect an influence of progenitor lineage rather than a specific effect of clonality. Furthermore, I demonstrated that the relationship between neuronal lineage and dendritic arborisation was primarily attributed to greater similarity in the complexity of their apical dendritic arbor.

5.3.1 Identification of neuronal clones by an RNA-barcoding retrovirus

DNA barcoding of neuronal progenitors was pioneered over 20 years ago as a tool for studying lineage relationships (Golden et al., 1995). Although it has remained a popular method for definitively identifying clones, this method is hindered by a high failure rate of barcode retrieval, which can be over 50 % (Golden et al., 1995; Harwell et al., 2015; Reid & Walsh, 2002). In the present study, a retroviral RNA barcode was retrieved with a success rate of 86 % from cortical neurons, thereby enabling more complete identification of neuronal clones than has been achieved with DNA barcoding. The RNA-barcoding retroviral library was demonstrated to be highly complex based on the identification of 224 unique barcodes with < 1 % attributed to more than one integration event. This was equivalent to previous reports on the use of a DNA barcode library (0.7 %, 8/1210, barcodes appeared more than once in Mayer et al., 2015; 3 %, 49/1446, barcodes appeared more than once in Fuentealba et al., 2015). This provided a high level of confidence in the assumption that neurons yielding the same barcode sequence were clonally related, and therefore, a low risk of making lumping errors. Ongoing characterisation of RV-tdTom-barcode will help to further understand the composition of different barcodes in the retroviral library.

The spatial arrangement of labelled cells constituting putative, geometrically-defined neuronal clones resembled other reports in the literature (Gao et al., 2014; Maria C. Mione et al., 1997; Christopher Walsh & Cepko, 1992). Most putative radial clones exhibited some lateral dispersal, in agreement with other studies (Gao et al., 2014). Strictly-aligned, putative radial clones reported by others (Yu et al., 2012, 2009) were infrequently seen. However, the putative clones identified by geometric analysis were confirmed by barcode to represent a mixture of clones and non-clones. Furthermore, a population of non-radial barcode-confirmed clones were observed that formed intralaminar clusters. These may represent portions of radial clones that have been separated in the process of sectioning of the brain, or they may represent a subset of clones that have a distinct, non-radial arrangement. RNA barcoding offers the potential for future studies to definitively characterise the spatial distribution of clones, since it is not subject to the low success rate associated with DNA barcoding.

As expected, identification of intralaminar clones by geometric analysis and by RNA barcoding demonstrated greatest agreement at the lowest titre retrovirus employed. Titrating of retroviral transduction frequency for geometric identification of clones, and defining what constitutes a 'clonal titre', is a contentious issue (Mayer et al., 2016). Both of the titres tested in the present study (~ 250 and ~ 1000 c.f.u. per brain) could reasonably be called 'clonal' according to the literature, where titres of 10^4 to 10^6 c.f.u per brain have been reported (Noctor et al., 2001, 2004; Reid & Walsh, 2002). Even at the lowest titre, a significant proportion (39 %) of labelled neurons that fulfilled geometric criteria for being clonal (Maria C. Mione et al., 1997; Yu et al., 2009) were, in fact, non-clonal according to barcode retrieval.

However, the determination of retroviral titre is likely to show variability within and between laboratories, depending on factors such as the proliferative index of the test cells and the specific conditions used for retroviral transduction. As a result, comparing quoted retroviral titres across studies may not be informative. A more robust measure for the comparison of retroviral transduction titre between studies may be the total number of

labelled progenitors in a brain, although this in itself may be difficult to measure. It could be achieved by sacrificing sufficient animals in the early post-transduction period to be able to establish a range of confidence for the likely number of infected progenitors for a specific batch of virus. Alternatively, it could be achieved by extrapolating the likely number of transduced progenitors from the number of labelled cells observed in a brain at a later stage of development. These estimates would still require that assumptions are made about the proliferative behaviour of progenitors and the migration of their cellular offspring. Although the identification of clones by RNA barcoding is also subject to the relationship between retroviral titre and the complexity of the library, identification of clones is far more robust at the transduction frequencies commonly reported for clonal studies. RNA barcoding retrovirus can be thought of as a pool of genetically distinct retroviruses, each being injected with a probability of < 1 c.f.u per brain.

5.3.2 Clonal labelling and RNA-seq

The discovery that a retroviral RNA barcode could be retrieved by RNA-seq and used to identify clonally-related neurons offers an unprecedented opportunity to compare the transcriptome of clonally-related and non-clonally related neurons, definitively identified by retroviral RNA barcoding. The read depth achieved in the present study of over 7×10^6 mapped reads per cell is likely to be adequate for performing analysis such as cell-type identification. A minimum depth of 50,000 reads per cell has been proposed for cell-type identification of cortical neurons (A. A. Pollen et al., 2014), and a minimum of 1 million reads per cell for accurate quantification of gene expression (Svensson et al., 2017). Indeed, a comparable study involving large-scale (over 3000 cells) single-cell RNA-seq of cortical neurons (Zeisel et al., 2015) used an average read depth of 500,000 reads per cell to identify discrete subpopulations of cortical cells by transcriptome profiling. Taken

together, this suggests that the experimental protocol established here offers new opportunities to investigate the molecular mechanisms by which lineage influences neuronal function. Furthermore, it could enable a systematic examination of the relationship between clonality and the transcriptional heterogeneity of excitatory neuronal subtypes to further understand the influence of lineage on neuronal phenotype (Lake et al., 2016; Toledo-Rodriguez & Markram, 2007; Tyler et al., 2015).

5.3.3 Errors associated with the geometric identification of clones

Analysis of the spatial distribution of barcode-confirmed clones revealed that the confidence of geometric identification in identifying clones labelled with the lowest titre retrovirus (~ 250 c.f.u./ml) declined with increasing Euclidean distance between labelled neuron pairs. Surprisingly however, this was true in both the lateral and radial directions, contrary to the expectation that the ability to identify clones would be unaffected by radial dispersal. One possible explanation for this is that the sectioning of the cortex for processing may introduce distortion in the identification of radial clones due to the curvature of the cortex. It is possible that the thick sections used in the current study, in which only a proportion of the depth of the cortical slice can be resolved, may be prone to introducing splitting of radial clones.

Overall, the RNA barcoding retrovirus was shown to offer a reliable and unequivocal method of labelling neuronal clones. This opens the door to comprehensive studies of the relationship between neuronal function and clonal relationships, which have been hindered by ambiguous or unreliable clonal labelling. For example, a fundamental question in the study of clones is understanding the extent to which a progenitor influences the phenotype of its offspring. The study of intra-laminar clones is therefore an excellent model for studying the influence of clonality on neuronal phenotype by enabling the direct

comparison of clonally-related and non-clonally-related neurons, which, *a priori*, are expected to have equivalent phenotypes. This feat would be difficult to achieve with other methods of clonal analysis.

5.3.4 The relationship between clonality and the morphology of layer 2/3 pyramidal neurons in somatosensory cortex

The relationship between the geometric distribution of labelled neurons and retroviral transduction frequency could be exploited by using the ability to identify clones by their RNA barcode. Intralaminar clonal pairs of layer 2/3 pyramidal neurons could be spatially matched with labelled, non-clonal pyramidal neuron pairs by using a 'non-clonal' retroviral titre. This presented the possibility to investigate the relationship between clonality and morphology in layer 2/3 pyramidal neurons to establish whether clonally-related neurons shared a greater similarity, or dissimilarity, in the structure of their dendritic arbor.

Morphological analysis of neurons in pairs revealed that clonally-related neurons exhibited more similar dendritic arbors than matched pairs of unrelated neurons. This was due to similarity in the dendritic length and complexity of their apical arbor, rather than their basal arbor, which did not differ between the two populations. However, this similarity was found to exist at a population level within the group of clonally-related neuron pairs in layer 2/3, rather than existing solely at a clonal level. This suggests that there is a specific relationship between the population of progenitor lineages that tend to give rise to neuron pairs in layer 2/3 and the morphology of the neurons comprising those pairs. Such a relationship may lead to lineage-specific effects on the integration of synaptic inputs by pyramidal neurons, thereby giving rise to neurons with specific functional characteristics. Further work is necessary to characterise the progenitor population that gives rise to neuron pairs in layer 2/3, and to examine the relationship between lineage and function

within this population of neurons, in order to identify the implications of this morphological similarity. It will also be interesting to establish whether the relationship between lineage and morphology is also evident in other cortical laminae and in clonally-related neurons that form part of other spatial arrangements. Interestingly, a molecularly-defined subclass of neuronal progenitors, the intermediate progenitor cells (IPCs), have recently been suggested to give rise to neurons that have more similar dendritic arbors (Tyler et al., 2015). The current study presents novel evidence that progenitor lineages can inform both the spatial arrangement and the morphological phenotype of their neuronal progeny and therefore a neuron's finescale structure is, to some degree at least, inherited from its mother.

Chapter 6

Lineage relationships in human neocortical cells derived from induced pluripotent stem cells

6.1 Introduction

The study of clonal relationships in the neocortex of mice has revealed an important role for lineage in the development of neocortical function. For example, clonally related excitatory neurons have been found to exhibit biased gap-junction coupling in early development (Yu et al., 2012), and preferential synaptic connectivity later in development (Yu et al., 2009). In the visual cortex of mice, clonally-related neurons share more similar stimulus selectivity (Li et al., 2012; Ohtsuki et al., 2012), indicating that lineage relationships affect the integration of neurons into functional circuitry. A similar influence of clonality has been found in the phylogenetically-ancient *Xenopus laevis*, in which clonally-related neurons in the optic tectum were found to have more similar receptive field properties than non-clonally related neurons (Muldal, Lillicrap, Richards, & Akerman, 2014). However, if our goal is to understand how clonal relationships influence human neocortical development, we face additional challenges. The types of studies that have been employed to investigate clonal relationships are not possible in humans and therefore our understanding has lagged behind that of other species. For instance, it is not known whether clonally-related human neocortical cells exhibit the biased early gap-junction coupling seen in mouse neocortex (Yu et al., 2012).

iPSC technology offers the potential to generate a model of human neocorticogenesis *in vitro*, thereby providing the access to proliferating human neocortical progenitors that would enable the investigation of clonal relationships. Thus far however,

very few studies have investigated clonal relationships in iPSC-derived human neocortical cultures. The identification of clones in iPSC-derived human neocortical cultures is likely to be difficult as mitotic progenitors tend to be spatially-clustered (Shi, Kirwan, Smith, et al., 2012) and this would be predicted to lead to retroviral labelling that is spatially biased. Furthermore, little is known about the proliferative behaviour of progenitors in iPSC-derived human neocortical cultures, or the migratory behaviour of cells. These features of iPSC-derived human neocortical cultures mean that the iPSC-derived clones that have been identified by geometric analysis may be vulnerable to errors (Otani, Marchetto, Gage, Simons, & Livesey, 2016). For these reasons, there is the need for more definitive methods by which to determine clonal relationships in iPSC-derived human cultures.

In this chapter I set out to investigate whether retroviral RNA barcoding could be used to identify clonally-related cells in an established model of the human neocortex (Shi, Kirwan, Smith, et al., 2012). Using unequivocal identification of clones, I then tested whether a clonal relationship is associated with particular functional properties of iPSC-derived human neocortical cells. Specifically, my aims were to address the following:

- Can clones be identified reliably using RV-tdTom-barcode in iPSC-derived human neocortical cultures?
- Do clonally-related cells in iPSC-derived human neocortical cultures exhibit preferential gap junction coupling, similar to that observed in rodent neocortex?

6.2 Results

6.2.1 RV-tdTom-barcode enables successful identification of clones in iPSC-derived human neocortical neurons

The investigation of lineage relationships in an iPSC-derived model of human neocorticogenesis stands to benefit from a method for definitively identifying clonally-related cells. To establish whether RV-tdTom-barcode is suitable for this purpose, human iPSCs from the control line SFC-180-01-01 derived from a 60 year old female, were directed to generate neocortical neurons by neural induction and differentiation in adhesive cultures using an established protocol (Shi et al., 2012; **Figure 6.1 A**). Firstly, human iPSC cells were cultured in the absence of feeder cells and neural induction was initiated by dual SMAD inhibition (Shi, Kirwan, Smith, et al., 2012). Neural induction led to the formation of a neuroepithelial sheet comprising neocortical stem cells and neuronal progenitor cells (NPCs) between day 0 (D0; the first day of induction) and D12. The neuroepithelial sheet was then dissociated and cultured in the presence of mitogenic fibroblast growth factor 2 (FGF2) to promote proliferation of NPCs. FGF2 was withdrawn after two days to aid differentiation and neurogenesis, after which self-organisation of cultures into polarised neocortical rosettes was observed. Cultures were passaged repeatedly prior to final plating onto coverslips at D30 - D35 followed by a period of proliferation and maturation in order to generate neocortical neurons.

Immunocytochemical characterisation of cultures was performed to confirm the generation of excitatory neocortical neurons using markers based on previous work (Shi, Kirwan, Smith, et al., 2012). Cultures were first characterised during differentiation and neocortical rosette formation at D24. Neocortical rosettes were composed of multiple progenitor subtypes. Primary neuronal progenitors were the predominant population,

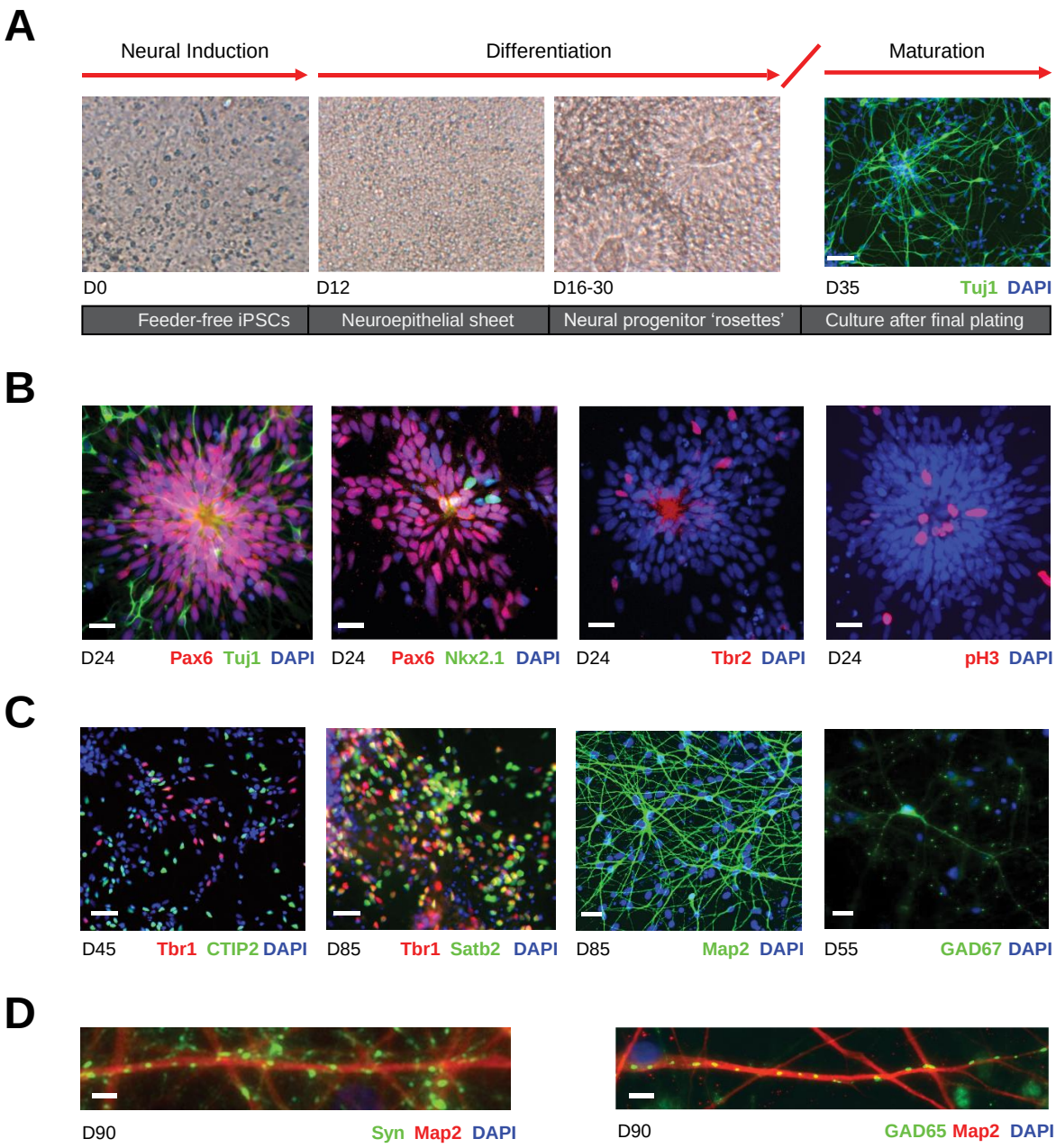

Figure 6.1: Human iPSCs directed to a cortical fate give rise to neuronal progenitors and cortical neurons. (**A**) Human cortical neurons generated using the protocol of Shi et al., 2012. Representative images (left to right) of iPSCs immediately prior to induction (D0); following formation of the neuroepithelial sheet after neural induction (D12); the generation of rosettes of NPCs (between D16 and D30); and then of neurons after final plating at D35. Scale bar 40 μm. (**B**) Cortical rosettes generated from the control iPSC line SFC180-01-01 at D24, labelled with indicated antibodies. The vast majority of cells in rosettes are Pax6 positive, indicating primary, neocortical progenitors. Tuj1-positive neurons can be observed at the periphery of the rosette. A small proportion of progenitor cells (less than 5 %) were Nkx2.1-positive, Pax6-negative interneuron progenitors. Tbr2-positive IPCs are predominantly located at the edges of rosettes. Phosphohistone H3 (pH3) positive nuclei identify progenitors undergoing mitosis. pH3-positive cells are concentrated at the apical, luminal surface of the rosette, similar to the (cont.)

indicated by Pax6 immunoreactivity (**Figure 6.1 B**). This is in agreement with Pax6-positive NPCs being the predominant population in the VZ and SVZ of the developing human neocortex (Bayatti et al., 2008). A smaller population of Tbr2-positive IPCs were observed, primarily located towards the edges of rosettes. A small proportion of progenitors (< 5 %) were Nkx2.1-positive and Pax6-negative, consistent with these cells being interneuron progenitors (Ma et al., 2013; Sussel, Marin, Kimura, & Rubenstein, 1999). The presence of Tuj1-positive neurons confirmed the onset of neurogenesis, and positive phosphohistone H3 (pH3) immunoreactivity indicated ongoing mitosis in rosettes. Consistent with the idea that the rosette structure reflects aspects of *in vivo* neurogenesis, most pH3-positive cells were located towards the apical (luminal) extent of the rosette, reminiscent of the ventricular zone (Shi, Kirwan, Smith, et al., 2012).During development *in vitro*, progenitors were found to give rise to deep and then upper layer neocortical neurons, in keeping with the temporal progression of neocorticogenesis *in vivo* (Franco et al., 2012). Neurons expressed the deep neocortical layer markers Tbr1 and CTIP2 at D45 in culture (**Figure 6.1 C**). The upper layer marker Satb2 was expressed by D85, and was occasionally co-expressed with the deep layer marker Tbr1. This is in agreement with the occasional co-expression of Satb2 and Tbr1 observed *in vivo* (Díaz-Alonso et al., 2012; Tashiro et al., 2011). The generation of extensive dendritic networks was revealed with Map2 immunostaining, which detects the dendritic arborisation of neurons. And in keeping with the observation of a small population of Nkx2.1-positive interneuron progenitors, a small proportion (< 5 %) of neurons were positive for the interneuron marker GAD67. By D90, neurons were shown to have formed excitatory synapses in culture by the presence of synaptic puncta labelled by synaptophysin

(**Figure 6.1 cont.**) situation *in vivo*. Scale bar 20 μm. (**C**) iPSC-derived neocortical neurons immunolabelled as indicated. Neurons express deep layer neocortical markers Tbr1 (layer 6) and CTIP2 (layer 5) at D45 in culture. By D85, the upper layer marker Satb2 (layers 2 - 4) is detectable. Some neurons appear to express both Tbr1 and Satb2 (scale bars 40 μm). Neurons generate extensive dendritic networks as indicted by Map2 labelling and a small percentage of neurons (< 5 %) are GAD67-positive interneurons (scale bar 20 μm). (**D**) Synaptic puncta are seen on dendrites at D90 using antibodies against synaptophysin (Syn). GAD65-positive inhibitory synapses are also present in the cultures (scale bars 5 μm).

(**Figure 6.1 D**). A subset of synapses were inhibitory in nature, indicated by GAD65 immunoreactivity.

Having confirmed that iPSC-derived cultures capture key aspects of excitatory neocorticogenesis, I set out to determine whether the RNA barcoding could be used to study human clones. Cells were incubated with serial dilutions of RV-tdTom-barcode (ranging from 4 x 10^3 c.f.u./ml to 100 c.f.u./ml) following final plating at D30 - D35 and cultures were maintained on coverslips to enable proliferation and maturation until the designated experimental time-point (D35 – D100; **Figure 6.2 A**). The coverslips were then moved to an upright microscope equipped with epifluorescence so that the cells could be first imaged and then targeted for collection. Single, fluorescently-labelled cells were collected using a glass micropipette by approaching the cell soma and applying gentle suction until the contents of the cell soma were aspirated into the pipette. The cell's contents were then expelled into a PCR tube and processed for RT-PCR and sequencing to retrieve their barcode identity. The first time-point assessed was between D35 and 45. Fluorescently-labelled cells were heterogeneous in their morphology, consistent with the labelling of diverse cell types (**Figure 6.2 B**). Putative excitatory pyramidal neurons could be identified by a triangular cell soma and slender processes, including a clear putative primary apical dendrite. Pyramidal neurons differed in the size of their soma and the complexity of their dendritic arbor, indicative of neurons at different stages of maturation. Further neuronal cell types could be identified by the presence of slender dendritic

---

(**Figure 6.2 cont. from page 155**) (**B**) and D45. Labelled cells were heterogeneous in their morphology, consistent with the labelling of diverse cell types. Putative pyramidal neurons were observed with small somata and simple dendritic morphology (i), or large somata and complex dendritic morphology (ii), indicating neurons at different stages of maturation. Other neuronal cells were observed with either fusiform (iii, single arrow), bipolar (iii, double arrow), stellate (iv) or unipolar (v, double arrow) morphology. Furthermore, gliogenesis was evident by the presence of process-bearing non-neuronal cells, consistent with reactive astrocytes (v, single arrow), and fibroblast-like non neuronal cells, consistent with immature astrocytes (vi). Scale bar 50 μm for all images. (**C**) Barcode sequences could be identified with a high success rate from single human neurons derived from iPSCs (72 %, 36/50). (**D**) The majority of failures (79 %, 11/14) were due to a failure to obtain an RT-PCR product. The remainder were due to the failure to sequence RT-PCR product. (**E**) A retroviral infection titre of < 500 c.f.u/ ml was necessary to ensure single integration events in transduced progenitors.

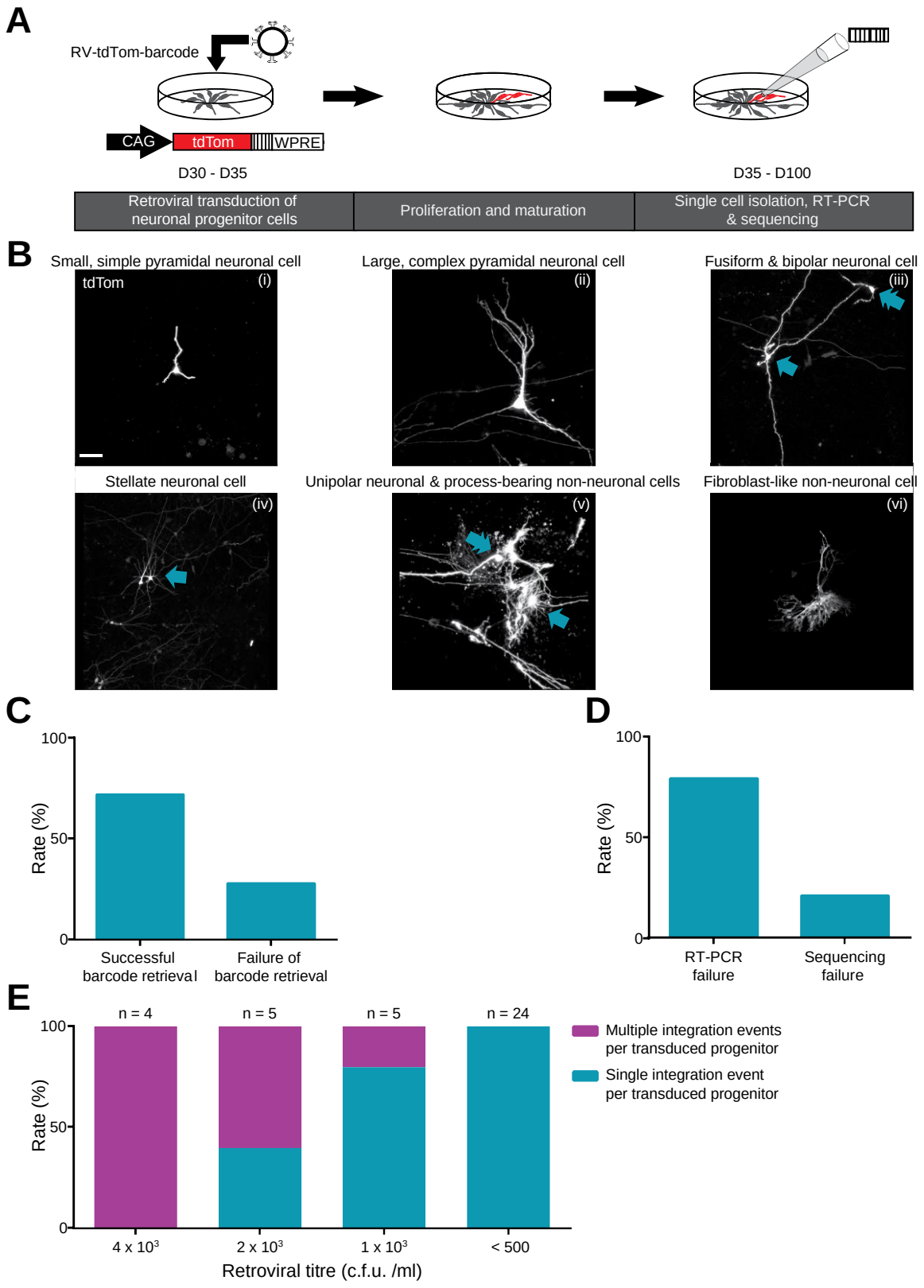

Figure 6.2: Retroviral RNA barcode can be recovered with a high success rate from single human neurons derived from iPSCs. (**A**) Following final plating at D30 – D35, neocortical NPCs derived from iPSCs were incubated with RV-tdTom-barcode for 24 hours. The cultures were allowed to proliferate and maturate before individual labelled cells were harvested for single cell RT-PCR and sequencing for barcode identification. Cultures were first assessed for barcode retrieval between D35 (cont. on page 154)

processes and were categorised as unipolar, bipolar, or stellate (multipolar) cells in accordance with previous definitions (Bardy et al., 2016). Multipolar cells were distinguished based on whether they exhibited a primary apical dendrite and a soma that tapered at both ends (fusiform cell), or they lacked a primary apical dendrite and had a rounded soma (stellate cell). Non-neuronal cells with an astrocytic appearance could be identified, consistent with the idea that gliogenesis also occurs in the cultures (Shi, Kirwan, Smith, et al., 2012).Non-neuronal cells had diverse morphologies, including fibroblast-like cells and process-bearing stellate cells, which had a larger soma than neuronal stellate cells. These groups are likely to represent immature and mature astrocytes, respectively (Y. Zhang et al., 2016). Taken together, these data reveal the morphological identification of diverse human cell types within the iPSC-derived human cultures with RV-tdTom-barcode.

Barcode sequence was recovered from single cells with a high success rate (72 %, 36/50; **Figure 6.2 C**). The majority of failures (79 %, 11/14) occurred in the steps leading up to identification of a DNA amplification product, indicating that most losses occurred in either cell harvest, reverse transcription or PCR amplification (**Figure 6.2 D**). The remaining failures were due to an inability to obtain a sequencing trace from RT-PCR DNA product. Barcode sequences were analysed to establish the transduction frequency required to obtain single integration events in NPCs (**Figure 6.2 E**). Retroviral titres over 1000 c.f.u/ml resulted in multiple integration events per progenitor, as revealed by the identification of different nucleotide bases at individual variable barcode positions in the sequencing trace from single cells (4×10^3 c.f.u./ml: 100 % of cells (4/4) multiply-transduced, 1 coverslip; 2×10^3 c.f.u./ml: 60 % of cells (3/5) multiply-transduced, 1 coverslip, 1×10^3 c.f.u./ml: 20 % of cells (1/5) multiply-transduced, 1 coverslip). In contrast, retroviral titres of under 500 c.f.u/ml reliably resulted in single integration events (< 500 c.f.u/ml: 0/24 cells multiply-transduced, 4 coverslips).

To test whether RV-tdTom-barcode could be used as a clonal labelling tool for the study of human neocorticogenesis *in vitro*, iPSC-derived neocortical cultures were

transduced with RV-tdTom-barcode at low titre (< 500 c.f.u./ml) following final plating at day D30 – D35. All fluorescently-labelled cells within clusters were harvested individually between D35 and D45, and processed for barcode identification. Clones could be routinely identified by the retrieval of identical barcode sequences from the labelled cells (**Figure 6.3 A**). Barcode identification revealed that even at low infection titre, some clusters of fluorescently-labelled cells were actually composed of more than one clone, indicating that clones could be identified regardless of their spatial distribution. To identify whether the distinct morphological cell types originated from different progenitors, clones were categorised by the morphological cell types they comprised. At this time point in the maturation of the cultures, most clones were comprised of either fusiform or bipolar cells, and a smaller proportion were comprised of unipolar, stellate, or pyramidal, cells (fusiform 38 %, 5/13; bipolar 31 %, 4/13; unipolar 8 %, 1/13; stellate 8 %, 1/13; pyramidal 8 %, 1/13; **Figure 6.3 B**). Clones consisting of more than one morphological cell type were rare (8 %, 1/13), indicating that most progenitors gave rise to a single morphological cell type, at least at this time point. Most clones comprised few cells (4 ± 0.4 barcode-confirmed cells). (**Figure 6.3 C**). These data supported the hypothesis that RV-tdTom-barcode could be used to reliably identify iPSC-derived human neocortical clones *in vitro*. Furthermore, they indicate that early NPC cultures comprise different subtypes of progenitors generating cells with distinct morphology.

Given that human neocortical progenitors can generate hundreds of neurons *in vivo* (Betizeau et al., 2013), it is desirable to study human neocortical clones over extended periods. Therefore I was keen to confirm whether RNA barcoding could be used to identify the titre at which just a single progenitor could be transduced reliably per coverslip. This would then make it possible to track clonal behaviour over extended time periods. To identify the conditions under which I could reliably transduce no more than one progenitor per coverslip, I reduced the titre of RV-tdTom-barcode and assessed the number of labelled clones per coverslip. This revealed that a retroviral titre of < 125 c.f.u./ml was required to ensure that no more than one progenitor was labelled per

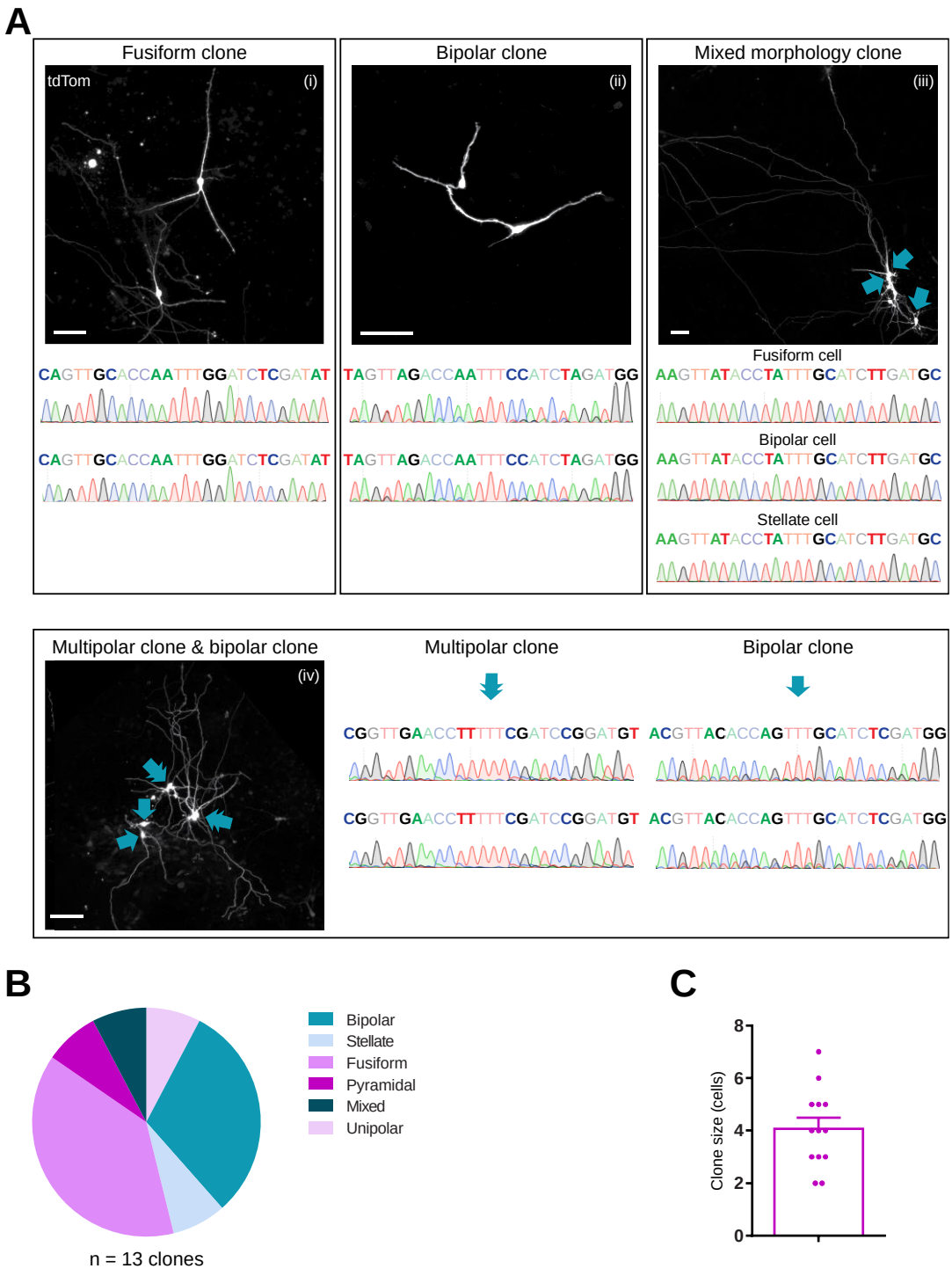

Figure 6.3: RNA barcoding retrovirus can be used to unequivocally identify clones in an iPSC-derived model of human neocorticogenesis. Following final plating at D30 – D35, neocortical iPSC-derived NPCs were incubated with low-titre RV-tdTom-barcode (24 hours at 100 – 500 c.f.u/ml). The cultures were allowed to proliferate and mature for 5-15 days (to D35-50), at which point individual labelled cells were harvested for single cell RT-PCR and sequencing for barcode identification. All scale bars 50 µm. (**A**) Retrieval of identical barcode sequences from single cells could be used to identify clonally-related cells. Clones could be found comprising different morphological cell types, including fusiform (i and iii), bipolar (ii, iii and iv) and stellate (iii and iv), cells. Clusters of (cont.)

coverslip of cells (500 c.f.u./ml: 100 % of coverslips (2/2) contained multiple clones; 250 c.f.u/ml: 50 % of coverslips (1/2) contained multiple clones; 125 c.f.u./ml: 0/3 coverslips contained multiple clones; 100 c.f.u/ml: 0/3 coverslips contained multiple clones; 6.8 ± 0.6 barcoded cells per coverslip; **Figure 6.4 A**).

Having established a retroviral titre that resulted in no more than one progenitor being labelled per iPSC culture, I used these conditions to track the behaviour of single clones over extended periods of time (up to D100 in vitro). Consistent with the labelling of no more than 1 clone at D100, 21 % of coverslips (5/24) contained zero fluorescent cells and, for those that did contain fluorescent cells, each time these were collected, they carried the same barcode (4.4 ± 0.5 barcode-confirmed cells from 5/19 coverslips). Under these conditions, long-term tracking revealed that individual clone size increased significantly between D50 and D100 ($r = 0.56$, 95 % confidence interval 0.13 to 0.82, $p = 0.01$, Spearman's Rank correlation coefficient; **Figure 6.4 B**), consistent with ongoing neurogenesis in the culture. Further, the majority of clones were dispersed by more than 400 µm (89 %, 17/19), consistent with significant dispersal of the clonally-related cells. The largest type of clone were composed of more than one morphological cell type (mixed: 37 %, 7/19; **Figure 6.4 C**). The predominance of mixed clones at later stages was in contrast to the dominance of single morphological cell-type clones in younger cultures. Fusiform cells comprised the most common single cell-type clone in older cultures (fusiform: 32 %, 6/19; bipolar: 16 %, 3/19; pyramidal: 11 %, 2/19; stellate: 5 %, 1/19; unipolar: 0/19). There was a significant relationship between clone size and morphological cell type (mixed: 33 ± 3 cells, n = 7; fusiform: 13 ± 3 cells, n = 6; bipolar: 10 ± 3; pyramidal: 7 ± 4, n = 2; stellate: 6, n = 1; $F(3, 14) = 7.0$, $p = 0.004$; one-way ANOVA; **Figure 6.4 D**), with mixed clones being significantly larger than fusiform-only, pyramidal-only and bipolar-

(**Figure 6.3 cont.**) labelled cells occasionally comprised more than one clone (iv). (**B**) Most clones were comprised of a single morphological cell type. The majority of clones were comprised of fusiform cells or bipolar cells, and a smaller proportion were comprised of unipolar, stellate, or pyramidal cells (fusiform 38 %, 5/13; bipolar 31 %, 4/13; unipolar 8 %, 1/13; stellate 8 %, 1/13; pyramidal 8 %, 1/13). Few clones consisted of more than one morphological cell type (8 %, 1/13). (**C**) Clones comprised 4 ± 0.4 barcode-confirmed cells on average.

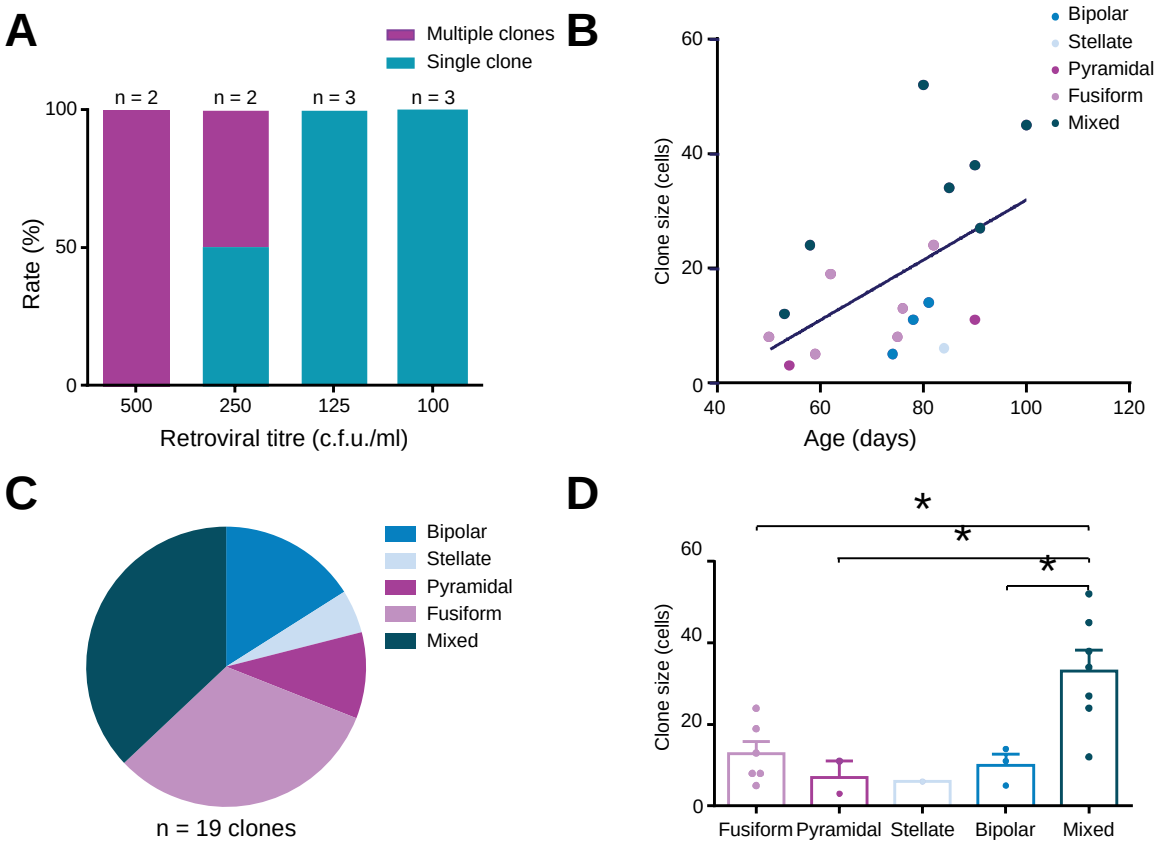

Figure 6.4: Human neocortical progenitors derived from iPSCs exhibit heterogeneous proliferative behaviour. Following final plating at D30 – D35, neocortical iPSC-derived NPCs were transduced with low-titre RV-tdTom-barcode (24 hours at 100 – 500 c.f.u/ml). The cultures were allowed to proliferate and mature before individual labelled cells were harvested for single cell RT-PCR and sequencing for barcode identification. (**A**) Application of retrovirus at < 125 c.f.u/ml ensured that a single progenitor was transduced per coverslip, confirmed by barcode identification of single cells (500 c.f.u./ml: 100 % of coverslips (2/2) contained multiple clones; 250 c.f.u./ml: 50 % of coverslips (1/2) contained multiple clones; 125 c.f.u./ml: no coverslips (0/3) contained multiple clones; 100 c.f.u/ml: no coverslips (0/3) contained multiple clones; 6.8 ± 0.9 barcoded cells per coverslip). (**B**) Clone size increased significantly over time (r = 0.56, 95 % confidence interval 0.13 to 0.82, p = 0.01, Spearman's Rank correlation coefficient). (**C**) The largest type of clone was composed of more than one morphological cell type ('mixed'; 37 %, 7/19). Clones of fusiform cells were the most common single cell-type clone (fusiform: 32 %, 6/19; bipolar: 16 %, 3/19; pyramidal: 11 %, 2/19; stellate: 5 %, 1/19; unipolar: 0/19). (**D**) There was a significant relationship between clone size and clone cell type (mixed: 33 ± 3 cells, n = 7; fusiform: 13 ± 3 cells, n = 6; bipolar: 10 ± 3; pyramidal: 7 ± 4, n = 2; stellate: 6, n = 1; F (3, 14) = 7.0, p = 0.004; one-way ANOVA), with mixed clones being significantly larger than fusiform, pyramidal and bipolar clones (mixed vs fusiform: p = 0.01; mixed vs pyramidal: 0.03; mixed vs bipolar: 0.02; no other significant differences; Tukey's post hoc test for multiple comparisons).

only clones (mixed vs fusiform: p = 0.01; mixed vs pyramidal: 0.03; mixed vs bipolar: 0.02; Tukey's post hoc test for multiple comparisons). These data indicate that, over the time window investigated, the iPSC-derived human neocortical cultures comprise a heterogeneous pool of progenitors that give rise to cells of distinct morphological subtypes, and a subpopulation of progenitors that have greater proliferative potential and produce multiple morphological cell types.

6.2.2 Cells in iPSC-derived human neocortical clones exhibit preferential gap junction coupling

One of the key advantages of an *in vitro* model of human neocorticogenesis is that it enables functional studies of clones that would be difficult to achieve in primary tissue. Having established the conditions for clonal labelling in neocortical NPCs derived from iPSCs, I set out to use this system to address whether clonally-related human neurons share similar functional properties to those that have been reported in mouse. Specifically, I tested whether the biased gap junction coupling between clonally-related neocortical cells in mouse (Yu et al., 2012), also exists in the iPSC-derived model of human neocortex.

To investigate whether human neocortical clones exhibit biased gap junction coupling *in vitro*, the first step was to confirm that a dye labelling method could be used to reveal cells that are gap-junction coupled. Cultures of human NPCs derived from iPSCs were transduced with RV-tdTom-barcode at ~ 100 c.f.u/ml immediately following final plating (D30 - D35) in order to label a single progenitor per coverslip. Gap junction coupling was assessed at D62 ± 3 by loading a single tdTom-labelled cell (the 'target' cell) with a cell-impermeant, gap-junction permeant dye (Alexa Fluor 488; **Figure 6.5 A**). Target cells were dye-loaded using a glass micropipette in whole-cell patch-clamp

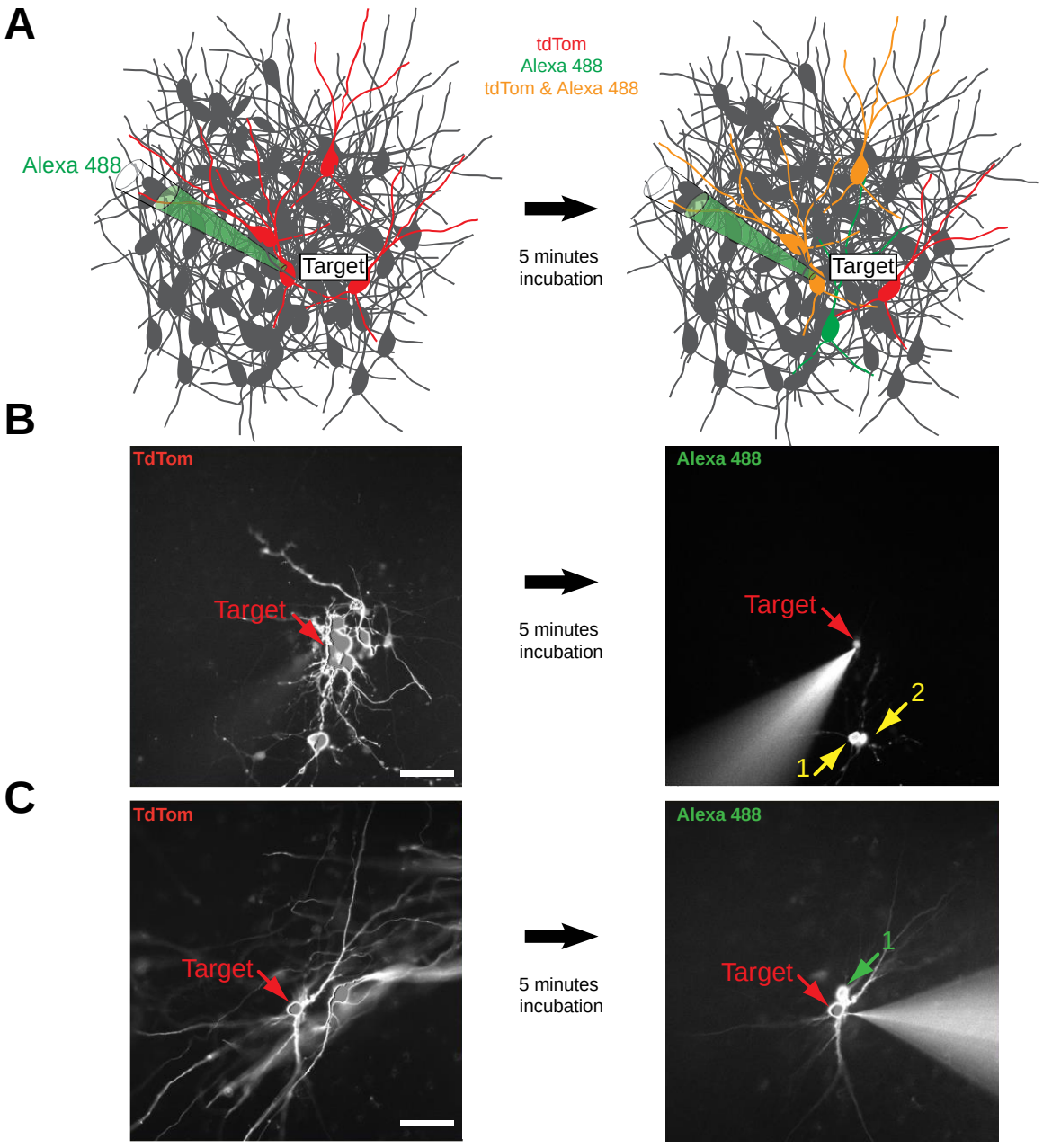

Figure 6.5: iPSC-derived human neocortical cells form gap-junction connections to clonally-related and non-clonally related cells *in vitro*. To investigate gap-junction coupling in iPSC-derived human neocortical cultures, human NPCs were transduced with RV-tdTom-barcode at ~ 100 c.f.u/ml immediately following final plating (D30 - D35), in order to label a single progenitor per coverslip. (**A**) Gap-junction coupling was assessed at D62 ± 3 by loading a single tdTom-labelled cell (the 'target' cell) with a gap-junction permeant dye (Alexa Fluor 488). Non-target cells that became dye-labelled were assumed to be gap-junction coupled. Single cells were dye-loaded using a glass micropipette in whole-cell patch-clamp configuration, and five minutes were allowed for dye diffusion before the distribution of dye-labelled cells was assessed. (**B**) Dye could be seen to diffuse to tdTom-labelled cells ('yellow' cells; arrows numbered 1 and 2), confirming that clonally-related cells could exhibit gap-junction coupling to the target cell. (**C**) On some occasions, dye diffused to non-tdTom expressing cells (arrow numbered '1'), indicating gap-junction coupling between the target cell and a non-clonally related cell. Scale bars 50 µm.

configuration or by single-cell electroporation. Five minutes were allowed for dye diffusion and those cells that became dye loaded were classified as gap-junction coupled with the target cell. Clonally-related cells could be identified that were gap junction coupled to the target cell, as indicated by co-labelling of tdTom and the green gap junction dye (**Figure 6.5 B**). Similarly, dye-labelling of tdTom-negative cells revealed the non-clonally related cells that were gap-junction coupled to the target cell (**Figure 6.5 C**).

Having confirmed that dye-loading could reveal gap junction-coupled cells, I next examined whether gap junction connections were biased to form between clonally-related cells. Most target cells were found to be couple to one or more cells in the culture (51 %, 45/89; **Figure 6.6 A**). Strikingly, the majority of these target cells were found to couple exclusively to clonally related (40 %, 36/89). In contrast, relatively few target cells were coupled with a non-clonally related cell (6 %, 5/89), and a similar proportion of target cells were coupled with both clonal and non-clonal cells (5 %, 4/ 89). Target cells that exhibited gap-junction coupling were coupled to 2 ± 0.2 cells on average. There was no significant difference in the number of coupled cells for target cells that were coupled to clones, non-clones, or both (clone-coupled: mean = 2.0 ± 0.2 cells, n = 36; Non-clone coupled: mean = 2.4 ± 0.7 cells, n = 5; clone & non-clone coupled: mean = 3.5 ± 1.2 cells, n = 4; $F(2, 43) = 2.3$, $p = 0.1$, one-way ANOVA; **Figure 6.6 B**). A similar pattern was evident when the data was analysed from the perspective of the coupled cells (i.e. not the target cells). The majority of cells that were gap-junction coupled to a target cell were clonally-related to the target cell (clonally related: 82 %, 73/90; non-clonally related: 18 %, 17/90; **Figure 6.6 C**). This bias was even more pronounced when one considered the absolute numbers of clonally- and non-clonally related cells. For each experiment the total number of clonally-related and non-clonally related cells that were located within the maximum distance between the target cell and a coupled cell was estimated (for method see 2.13.5). This revealed a substantial bias towards the formation of gap junctions between clonally-related cells (probability of clonally-related cell coupling = 76 %, 72/96; probability of a non-clonally related cell coupling: 1.9×10^{-3} %, 17/8538; $p < 0.0001$; Fisher's exact test;

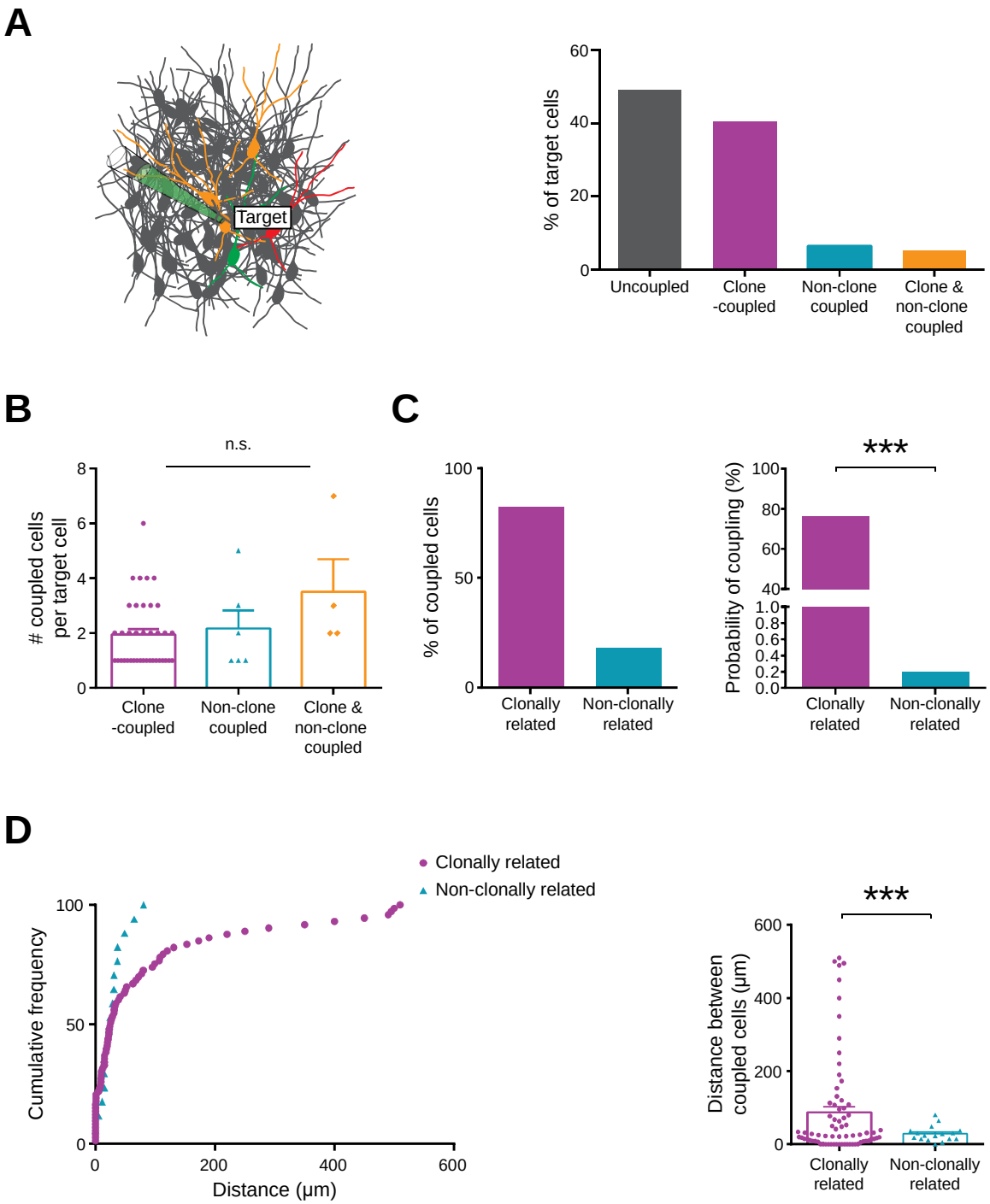

Figure 6.6: Clonally-related iPSC-derived human neocortical cells exhibit biased gap-junction coupling. To investigate gap-junction coupling in human neocortical cells, human iPSC-derived NPCs were incubated with RV-tdTom-barcode at ~ 100 c.f.u/ml following final plating (D30 - D35) in order to label a single progenitor. (**A**) Gap-junction coupling was assessed after a further 32 ± 3 days by loading a single tdTom-labelled cell (the 'target' cell) with a gap-junction permeant dye (Alexa Fluor 488; left). A minority of target cells (49 %, 44/89) were not gap-junction coupled, however most target cells were gap-junction coupled (51 %, 45/89). Target cells that were gap-junction coupled to other cells in the culture were usually coupled with a clonally-related cell (40 %, 36/89). Relatively few target cells were coupled with a non-clonally related cell (6 %, 5/89) and a small proportion of target cells were coupled with both clonal and non-clonal cells (5 %, 4/89). (**B**) There was no significant difference in the number of coupled cells (cont.)

Figure 6.6 C). Moreover, whereas gap junction coupling between non-clonally related cells exhibited a strong spatial bias towards cells in the immediate proximity to the target (connected cells were separated by no more than 80 µm), clonally-related cells were found to be capable of sustaining gap junction connections over long distances (> 400 µm). The mean distance between clonally-related coupled cells was significantly greater than the mean distance between non-clonally related coupled cells (clonally related: mean = 87 µm ± 16 µm, n = 73; non-clonally related: mean = 29 µm ± 5 µm; n = 17; t (83.4) = 3.5, p = 0.0008, unpaired t test with Welch's correction). Taken together, these data confirmed that human neocortical clones exhibit preferential gap junction coupling.

6.3 Discussion

In this chapter I have used a model of human neocorticogenesis based on the directed differentiation of iPSCs and have confirmed that this generates the cell types and temporal progression redolent of neocorticogenesis *in vivo*. I have shown that RNA barcoding using RV-tdTom-barcode can be used to identify clones in this system and I have used this approach to reveal that human neocortical progenitors exhibit diverse and sustained

(**Figure 6.6 cont.**) between target cells that were coupled to clones, non-clones, or both (clone-coupled: mean = 2.0 ± 0.2 cells, n = 36; Non-clone coupled: mean = 2.4 ± 0.7 cells, n = 5; clone & non-clone coupled: mean = 3.5 ± 1.2 cells, n = 4; F (2, 43) = 2.3, p = 0.1, one-way ANOVA). (**C**) As a result, target cells exhibited strong preferential gap-junction coupling to other tdTom-expressing clonally-related cells. The majority of gap-junction coupled cells were clonally-related to the target cell (clonally related: 82 %, 73/90; non-clonally related: 18 %, 17/90; centre). When the overall numbers of clonally and non-clonally related cells was factored for, this revealed a much higher probability (76 %, 72/96) for a clonally-related cell to be coupled with a target cell, than for a non-clonally related cell to couple with a target cell (1.9×10^{-3} %, 17/8538; p < 0.0001; Fisher's exact test; right). (**D**) Gap-junction coupling between non-clonally related cells exhibited a strong spatial bias towards cells in close proximity to the target cell, whereas gap-junction coupled clonally-related cells were found at much greater distances (> 400 µm; left). The mean distance between gap-junction coupled cells that were clonally-related was significantly greater than the distance between gap-junction coupled cells that were non-clonally related (clonally related: mean = 87 µm ± 16 µm, n = 73; non-clonally related: mean = 29 µm ± 5 µm; n = 17; t (83.4) = 3.5, p = 0.0008, unpaired t test with Welch's correction; right).

proliferative behaviour *in vitro*. Finally, I have demonstrated that human cortical cells *in vitro* form intercellular gap junction connections, which are highly biased towards clonally-related cells.

6.3.1 Clonal studies of iPSC-derived human neocortical cells using RV-tdTom-barcode

iPSC-derived human neocortical cultures contained immunocytochemically-defined excitatory progenitor subtypes, indicating that the culture was capable of giving rise to at least some of the progenitor diversity found *in vivo* (Gal et al., 2006; Montiel et al., 2016). Further evidence that the *in vitro* system recapitulates aspects of *in vivo* development was found in the temporal generation of neuronal subtypes, with lower neocortical layer neurons being born early and upper neocortical layers being born later (Shi, Kirwan, Smith, et al., 2012). A small population of Nkx2.1-positive inhibitory interneuron progenitors was noted in iPSC cultures directed to a neocortical fate. This population may reflect the small fraction of interneurons that are believed to be generated in the neocortex of humans (Hansen et al., 2013), or may indicate that a minority of progenitors adopt a subpallial phenotype.

The evidence that clones could be identified reliably using RV-tdTom-barcode is the first report of non-geometric method being employed for the identification of clones in an iPSC-based human neocortical model. Since little is known about the proliferative capacity and migratory behaviour of these cells, and mitotic cells have been observed to cluster around the lumen of rosettes (Shi, Kirwan, Smith, et al., 2012), geometric identification of clones may be vulnerable to ambiguity. Unequivocal identification of clones by retroviral RNA barcoding, therefore, provides a considerable advantage over

the use of geometric analysis to identify clones in human neocortical cultures (Otani et al., 2016).

One occasion when it is desirable to identify clones without barcode retrieval is when the objective is to monitor the development of large clones over extended periods of time. By relating the number of barcode-identified clones to retroviral infection titre, I was able to establish the titre at which only one progenitor was labelled per coverslip. This resulted in the confident identification of single clones, without exhaustive barcode retrieval or geometric analysis. This approach revealed that human NPCs continue to proliferate for extended periods of time in vitro and that they generate distinct morphological cell types, which correspond to the morphological subtypes reported by others (Bardy et al., 2016). Furthermore, the fact that some clones are comprised of just one morphological cell type, whilst other clones are comprised of mixed morphological cell types, is consistent with the idea that the cultures contain a heterogeneous population of NPCs that give rise to distinct neocortical neuronal subtypes.

6.3.2 Gap junction coupling in human neocortical cells

Dye-labelling with Alexa Fluor 488 was used to detect gap junctions between human neocortical cells *in vitro*. This dye has been shown to be broadly permeant to the range of homotypic and heterotypic gap junction channels (Weber, Chang, Spaeth, Nitsche, & Nicholson, 2004). Notably, it is permeant to channels formed by connexin 26, which plays an important role in the development of the rodent neocortex (L. A. Elias, Wang, & Kriegstein, 2007; Su et al., 2017), including the formation of biased synaptic connections between clonally-related neurons (Yu et al., 2012, 2009). Using this approach, I was able to demonstrate that clonally-related cells exhibit a pronounced bias to form gap junctions with one another. This implies that even within the context of an *in vitro* culture, clonally-

related neocortical cells are able to communicate with one another in a manner that is less common amongst non-clonally related cells. Whilst the bias in coupling was strong, it is important to acknowledge that different connexin channels exhibit differential permeability to dyes (Beltramello et al., 2003; Weber et al., 2004) and a range of connexins are expressed during development (Swayne & Bennett, 2016). Therefore further work using different dyes and other methods of assessing gap junction connections, such as electrophysiological recordings, would strengthen the assessment of gap junction coupling in iPSC-derived human neocortical cultures.

Nevertheless, the present study provides the first evidence that human neocortical cells derived from iPSCs are capable of forming gap-junction connections. Gap-junction coupling has been shown to play a role in diverse aspects of neocortical development, including the control of proliferation (Malmersjö et al., 2013) cell migration (L. A. Elias et al., 2007) and synapse formation (Yu et al., 2012). The demonstration that gap junctions were formed in this model of human neocorticogenesis, therefore, is powerful evidence that these cells are capable of exhibiting the functional behaviour expected to occur during development. Moreover, the evidence that clonally-related cells exhibit strong preferential gap junction coupling is the first time that this phenomenon has been observed outside of mouse neocortex (Yu et al., 2012). Given the importance of gap junction coupling in establishing specific synaptic connections between clonally-related neurons (Li et al., 2012; Yu et al., 2012) and in establishing functional circuitry *in vivo* (Su et al., 2017), the role of gap junction coupling in the formation of human excitatory synaptic connectivity *in vitro* is an important and timely question for future investigation.

Chapter 7

General Discussion

The aim of Chapters 3 and 4 of this thesis was to offer improvements to current methods for clonal labelling. Chapters 5 and 6 then applied these methods in order to examine the influence of neuronal lineage upon excitatory neuronal function in mouse neocortex and an iPSC-derived model of human neocorticogenesis. In the following subsection I will briefly review how these aims were addressed experimentally.

7.1 Summary of experimental findings

In Chapter 3 I began by characterising the adverse effects associated with *in utero* surgery on dam and embryo health. *In utero* surgery is widely used to perform diverse manipulations of the developing brain for the study of neurodevelopment, including the study of clonal relationships. Firstly, I characterised the baseline morbidity and mortality following a conventional surgical protocol. I discovered a risk of mortality to the dam (18 %) and her offspring (26 %), within which I found considerable inter-surgeon variability. This indicated that surgical technique is a significant factor underlying the efficacy of this procedure. Furthermore, I found that inadvertent intra-operative hypothermia and wound dehiscence occurred in a significant proportion of dams. Next, I examined a number of specific refinements of the surgical protocol. I demonstrated that both the application of a water-resistant drape and the provision of static warm-water thermal support were effective in significantly reducing the severity of intra-operative hypothermia. I showed that closure of the skin layer of the laparotomy incision with intradermal sutures was associated with a reduction in the incidence of wound dehiscence. Finally, I characterised

the impact of a series of general refinements to the protocol for *in utero* surgery (including modification of aseptic technique, analgesic provision, and surgeon training). These refinements were associated with a reduction in mortality of the dam and her offspring following surgery.

In Chapter 4 I developed two retroviral tools for investigating clonal relationships. The first of these was a retroviral vector encoding Cre recombinase. I used *in utero* surgery to deliver replication-incompetent Cre retrovirus to the developing brain of a conditional reporter mouse, which resulted in successful Cre-mediated recombination in transduced cells. I showed that Cre-mediated fluorophore expression in a transgenic reporter mouse led to a small but significant increase in fluorophore expression level, with reduced variability, compared to standard retroviral labelling. However, the primary advantage of the Cre retrovirus was in its versatility. I combined the Cre retrovirus with the optogenetic P_2X_2 receptor conditional reporter mouse and showed that this resulted in the expression of the high-conductance P_2X_2-ATP receptor in transduced neurons. This enabled the neurons to be selectively activated using light-dependent uncaging of ATP, demonstrating that conditional reporting could be used on a clonal basis with the Cre retrovirus.

The second tool I developed in Chapter 4 was an RNA barcoding retrovirus. This was intended to improve the success rate and versatility of traditional DNA barcoding. I generated a barcoded tdTom retroviral vector using a short, variable DNA sequence that was positioned immediately downstream of tdTom. The rationale for the location of the barcode was that expression of the retroviral reporter gene would lead to transcription, and therefore amplification, of the barcode sequence in single cells. I used the RNA barcoding retroviral vector to produce a library of genetically distinct retroviral virions, and demonstrated that the barcode sequence could be identified with a high success rate in NIH/3T3 cells. Furthermore, I proved that the RNA barcode could be used to identify clonally-related cells, on the basis that each clone could be identified by a common, inherited barcode, resulting from a single infection event in a progenitor.

Equipped with the RNA barcoding retrovirus and a refined protocol for its delivery *in utero*, in Chapter 5 I applied the RNA barcoding retrovirus to the developing mouse neocortex. I showed that the barcode identity of single neurons could be retrieved with a high success rate, and that neocortical clonal relationships could be identified in neurons that carried the same barcode. A pilot study demonstrated that the RNA barcode was compatible with single cell RNA-seq. Labelling of clones with the RNA barcode revealed that the geometric identification of clones with low-titre retrovirus – a method commonly used in the literature - is prone to misidentify clones. Specifically, I demonstrated that geometric identification is susceptible to lumping errors, such that some putative, geometrically-identified clones were actually polyclonal. I then used the RNA barcoding retrovirus to investigate the relationship between clonality and morphology in layer 2/3 pyramidal neurons in somatosensory cortex. I showed that clonally-related neuron pairs tended to have more similar dendritic arbors than non-clonally related neurons. These findings speak to a fundamental relationship between lineage and neuronal function.

In Chapter 6, I used RNA barcoding retrovirus to identify clones in a model of human neocorticogenesis *in vitro* derived by directed differentiation of human iPSCs to a neocortical fate. I proved that the barcode identity of single cells could be retrieved with a high success rate and that clonal relationships could be recognised in cells that shared the same barcode. This enabled me to study the proliferative nature of human neocortical progenitors derived from iPSCs, revealing that the cultures contain progenitors with a highly variable proliferative capacity. Finally, I used this combination of approaches to investigate gap-junction coupling in clonally-related human neocortical cells. By dye-labelling single members of retrovirally-labelled clones, I revealed that clonally-related human neuronal cells demonstrate biased gap-junction coupling *in vitro*. This provides the first evidence for such a functional relationship in humans.

7.2 Methodological considerations

Prior to discussing the broader implications of these findings, I will briefly review the methodological caveats and limitations that might influence the interpretation of the data and the questions that these raise.

7.2.1 Assessment of *in utero* surgery

The assessment of *in utero* surgery was focused on using morbidity and mortality as outcome measures. Morbidity and mortality offer an insight into the extent of the physiological disruption that may be caused by *in utero* surgery and they represent important indicators of the general health and welfare of dams and their offspring. However, more subtle effects, which may be relevant to the investigation of neocortical development, are likely to have been missed by the measures employed. For example, the degree of inflammatory response elicited by surgery was not characterised, despite the fact that there is considerable evidence that this may affect neurodevelopment (H B Stolp, 2013; Helen B Stolp et al., 2011). Moreover, the effect of surgery on neurodevelopment itself was not assessed. A further limitation was that dams and their offspring were only followed as far as birth, yet it is possible that *in utero* surgery could have longer-lasting effects on physiology and behaviour that could manifest later in development. Although the reduction in morbidity and mortality achieved by refinement in the present study seems likely to have a knock-on effect in the subsequent time period, this has yet to be clarified.

Another concern is that the findings from the *in utero* surgery work are limited by their context. The use of a single mouse strain in the present study was a limitation in the experimental design, since there is evidence that the effects of surgery on mortality may

vary between strains (Punzo & Cepko, 2008). However, although the absolute incidence rate of these events may differ on a strain-by-strain basis, it seems likely that the general trends I observed in C57BL/6J mice can be extrapolated to other strains. Furthermore, variability between research groups in terms of the equipment employed, experimental design and the skills of the individual, mean that the findings of the present study may differ from other paradigms of *in utero* surgery. Indeed, I discovered that surgical technique was a significant risk factor for both maternal and embryonic mortality following surgery. However, I did not establish the specific aspects of surgical technique responsible for this relationship. This highlights a clear requirement for further investigation, so that specific guidelines can be developed to reduce the risk of mortality. Nonetheless, despite the potential limitations of experimental context, it is likely that the principles of refinement determined in the present study are widely applicable to scenarios of *in utero* surgery.

The reduction in mortality rate following refinement of the surgical protocol indicated a positive effect of refinement for a subset of dams. Whether or not this represented improvements for all dams was not explored and further work is needed to establish whether the refinements documented in the current study produce measurable benefits in surviving animals. It is also the case that other potential refinements, which were not assessed in the present study, may improve the health of all dams. For example, the provision of local analgesia at the incision site was not explored, nor was a comparison of different anaesthetic protocols performed. The latter is particularly important when one wants to consider the degree to which *in utero* surgery might affect neurodevelopment. There is particular evidence in the wider literature for a detrimental effect of anaesthesia on neurodevelopment, which is specific to the anaesthetic protocol employed (Cesarovic, Arras, & Jirkof, 2014; Huang et al., 2015; Lee, Zhang, Wei, & Yu, 2015; Palanisamy, 2012). Therefore a comparison of neurodevelopmental outcomes following *in utero* surgery using different anaesthetic cocktails is warranted.

Two specific morbidities were assessed that exhibited high incidence rates amongst dams: inadvertent intra-operative hypothermia and post-operative wound

dehiscence. It was shown that provision of a static warm water supply for thermal support was effective at reducing intra-operative hypothermia, which represents an easily-implemented refinement. There are other methods of reducing hypothermia that have demonstrated efficacy without the need for costly equipment that were not assessed, such as pre-warming (Hart et al., 2011; Horn et al., 2012) and the provision of thermal insulation (Gargiulo et al., 2012; Horn et al., 2012). Furthermore, since a direct correlation between intra-operative body temperature and post-operative morbidity or survival rates was not performed, the significance of the hypothermia observed in the present study is not known. Hypothermia is correlated with morbidity in many other surgical paradigms (Flores-Maldonado, Medina-Escobedo, Ríos-Rodríguez, & Fernández-Domínguez, 2001; Hart et al., 2011; Seamon et al., 2012), but further work would be required to establish the extent and strength of this correlation following *in utero* surgery in mice.

Wound dehiscence was shown to be effectively controlled by intradermal skin closure. Although this is a more technically demanding and time consuming technique than external skin suturing (Sylvestre et al., 2002), these data indicate that the return on this investment would be considerable. It is notable however, that the comparison between internal and external skin sutures was performed within a single, experienced surgeon. Further study would be necessary to establish whether this trend remains across multiple surgeons and, particularly, those with different levels of experience. For instance, it is possible that there may be an extended learning curve associated with a surgeon learning intradermal skin closure, which could be associated with an initial increase in the rate of adverse effects. Although the limitations highlighted here indicate the need for further research, nonetheless the present study still provides new insights into the impact of in utero surgery on the health of the dam and her offspring, and offers mechanisms by which these can be minimised.

7.2.2 Retroviral labelling of clones

This thesis focussed on the use of retroviruses in order to identify and manipulate clonal cells. However, this is not the only method of clonal labelling and therefore it is prudent to consider the relative strengths and weaknesses of the different methods of clonal labelling. A possible limitation of retroviral labelling is that there may be a bias in the population of neurons that are labelled. This could arise in two ways. Firstly, it could arise through a bias in the population of progenitors that are infected. The extent to which retroviruses transduce progenitors in the SVZ (such as IPCs) is unknown, and it is possible therefore, that retroviral clones are biased to originate from progenitors in the VZ. Secondly, unwanted biases in labelling could arise from differential retroviral silencing, which could be linked to cell type or lineage (Gal et al., 2006; McCarthy et al., 2001). Although many studies have found evidence for retroviral silencing (Cepko et al., 1998; Ciceri et al., 2013; Harwell et al., 2015; Mayer et al., 2015), the population of cells in which this takes place has not been characterised. A further limitation in the characterisation of clones identified by retroviral labelling is that retroviral DNA is only integrated into a single daughter cell during infection of a mitotic progenitor, which leads to incomplete labelling of clones (Cepko et al., 1998; D. G. Miller et al., 1990).

Electroporation has recently been used in the literature for the delivery of transposon-based DNA constructs for combinatorial fluorophore labelling of clones (García-Moreno et al., 2014; Loulier et al., 2014). Retroviral labelling and electroporation of DNA constructs share some similar drawbacks: both necessitate invasive surgery, which can be disruptive to development, and both carry a risk of integration site effects, due to the unpredictable integration of a transgene at a random location in the genome. One of the major advantages of retroviral labelling for clonal analysis over DNA electroporation, however, is the heritable nature of retroviral transduction, which naturally lends itself to the labelling of clones (Cepko et al., 1998). On the other hand,

electroporated plasmid DNA is shared between daughter cells following mitosis and therefore sequentially diluted and differentially distributed during development (Buckingham & Meilhac, 2011). In order for electroporation to be used for clonal labelling, a transposase must be included into the electroporation mixture to cause the integration of episomal plasmid DNA into the genome (García-Moreno et al., 2014; Siddiqi et al., 2014). However, the dynamics of this process are not well understood. It is possible that mitosis could occur before complete integration has taken place, thereby differentially labelling clones. Alternatively, all of the episomal DNA may not integrate, again leading to the differential labelling of clones when the episomal DNA divides during mitosis.

Clonal labelling with chimeras using the MADM transgenic mice have recently been used for clonal studies (Gao et al., 2014; Li et al., 2012). MADM mice possess two reciprocally-chimeric split fluorophores that produce functional fluorescent protein upon interchromosomal recombination (Zong, Espinosa, Su, Muzumdar, & Luo, 2005). Low-frequency Cre-mediated recombination leads to the labelling of each daughter cell of a single progenitor with a different fluorophore (Zong et al., 2005). Clones are subsequently identified by geometric analysis (Gao, Sultan, Zhang, & Shi, 2013; Li et al., 2012). MADM offers an advantage over retroviral labelling in that there is no need for surgery and the entire clone, from the point of recombination, is labelled. Furthermore, the lineages of the two daughter cells labelled by MADM can be followed independently due to their differential labelling (Zong et al., 2005). However, retroviral labelling has considerably greater flexibility in the types of genetic manipulations that can be performed (as highlighted in Chapter 4). The MADM mouse by contrast, is limited to fluorophore labelling and furthermore relies on the costly maintenance of three transgenic strains (Espinosa et al., 2014). Moreover, clonal labelling with the MADM mouse is subject to the limitations of geometric analysis highlighted in Chapter 5. In summary, there are advantages and disadvantages to each of the methods of clonal labelling and the potential to use more than one technique provides flexibility. The work in this thesis demonstrates that a

retroviral strategy can offer versatility, the ability to unambiguously identify clones and the opportunity to combine clonal analysis with transcriptomic studies.

7.2.3 Models of neocorticogenesis: mouse and iPSC-derived human neocortical cells

In this thesis two models of neocorticogenesis were studied that differ in their strengths and weaknesses: the mouse, and human iPSCs directed to a neocortical fate. The mouse has served as a popular model of neocorticogenesis due to its rapid development, accessibility and the flexibility provided by the range of transgenic strains available. However, there are notable intra-species differences in neocorticogenesis that limit the extent to which the mouse can act as a universal model for mammalian neocorticogenesis. The mouse has a lissencephalic brain, therefore it is a truism that it differs developmentally from gyrencephalic mammals (Pasko Rakic, 2009). There is now strong evidence that the composition of the neocortical progenitor population varies both quantitatively and in terms of its composition between mammalian species (Betizeau et al., 2013; S. A. Fietz et al., 2012; Hansen et al., 2010; M. B. Johnson et al., 2009; Molnár & Clowry, 2012). Observations made in mouse may therefore be species-specific. For example, the relationship between clonality and dendritic morphology shown here could be restricted to mouse. However, there are many similarities in neocorticogenesis between mammalian species, such as equality in the subtypes of excitatory neuronal progenitors that have been identified (vRGCs, IPCs, oRGCs and SNPs have been found in both rodents and humans, for example (Montiel et al., 2016)). Although it is not yet clear whether the clonal influence observed in the current study is true of all neocortical progenitors, given the similarities between humans and mice, it seems reasonable to propose that there would

be an equivalent relationship between clonality and dendritic morphology in at least some human neocortical progenitors.

The second model employed in this thesis was an *in vitro* model of human neocorticogenesis derived from iPSCs. This model is both versatile and accessible, and the field has already learnt that the iPSC system is capable of recapitulating the temporal progression and neuronal cell types (including functional excitatory neurons) that one would expect from development *in vivo* (Espuny-Camacho et al., 2013; Hansen et al., 2011; Kindberg et al., 2014; Shi, Kirwan, & Livesey, 2012). However, the extent to which this model recapitulates normal development is incompletely understood. Perhaps the most significant deviation from human development in an iPSC-derived model is that it generates the neocortex in isolation. Progenitors therefore lack the communication with other physiological structures that have been shown to play a role in neurodevelopment *in vivo*, such as other parts of the central nervous system (Reillo et al., 2011), the vasculature (Javaherian & Kriegstein, 2009; Stubbs et al., 2009), and the ventricular system of the brain (Johansson, 2014). For example, bilateral enucleation has been shown to reduce the proliferation of progenitors in the oSVZ in ferrets (Reillo et al., 2011). Moreover, branch points in the vasculature have been shown to provide an environmental niche for IPCs (Javaherian & Kriegstein, 2009). The effect of removing those signals on development is unknown, therefore they may explain some of the differences that have been observed between *in vivo* and *in vitro* neocorticogenesis. For instance, there is evidence that SVZ progenitors are underrepresented in an iPSC-derived neocortical model (Camp et al., 2015). This could be explained by the absence of thalamocortical projections and their potential to regulate proliferation in the oSVZ (Reillo et al., 2011).

A further concern of the iPSC-derived model used in the present study is the relatively disorganised cytoarchitecture associated with 2D culture. A degree of self-organisation does occur *in vitro*, in that neural rosettes form and generate features that are analogous to the developing neural tube. However, multiple neural rosettes intermingle in a largely 2D fashion (Karus et al., 2014; Kindberg et al., 2014; Shi, Kirwan,

& Livesey, 2012), representing a significant deviation from normal development. It seems likely therefore that cells lack the complex cell-to-cell interactions that would be found *in vivo*. The implications of this feature of 2D culture are currently unknown. A challenge to making direct comparisons between the *in vitro* and *in vivo* systems is that iPSC-derived models are likely to lack the widespread temporal co-ordination that occurs *in vivo* (Kirwan et al., 2015). This may result in a more asynchronous development of individual clones *in vitro*. Asynchronous development may have effects on the development and maturation of the culture as a whole, and it could make it difficult to map the developmental stage of the *in vitro* model onto *in vivo* development. Indeed, it is fair to say that iPSC-based models of *in vitro* neurodevelopment are in their infancy. A growing challenge for the field is to investigate how closely the iPSC system is able to model events *in vivo*.

Finally, a limitation of the iPSC system specific to the current study is the use of a single induction of a single cell line. There is evidence for variability between cell lines and between neural inductions in how closely the iPSC model recapitulates *in vivo* development, and the rate of maturation (Bardy et al., 2016; Kirwan et al., 2015). Therefore further work is necessary to compare the behaviour of clones between cell lines and inductions. However, it seems that the fundamental characteristics of iPSC-derived neocortical cultures are repeatable (Kirwan et al., 2015; Shi, Kirwan, & Livesey, 2012) and so it seems likely that the key observation of a clonal bias in gap-junction coupling in the present study would be conserved.

7.2.4 Assessment of gap-junction coupling

In Chapter 6, a dye-based method was used to demonstrate that clonally-related human neocortical cells exhibit biased gap-junction coupling *in vitro*. Methods of assessing gap junction coupling between cells *in vitro* can be broadly categorised into two groups. Firstly,

the optical tracking of tracer molecules, such as dyes or photoactivatable fluorophores (Dakin, Zhao, & Li, 2005) that are small enough to permeate intercellular channels. Or secondly, measurements of electrical conductance between cells using whole cell patch clamp recordings (Hou, Li, & Paul, 2013). Successful detection of gap junction coupling using small molecules relies on the assumption that the compound is able to permeate all gap junction types. As acknowledged in Chapter 6, it is possible that the dye used here may be biased to label a subset of gap junctions formed by particular members of the connexin family, which differ in their permeability to molecules of different sizes (Beltramello et al., 2003). Confirmation of these findings using a smaller molecular tracer, such as serotonin (Beltramello et al., 2003), would support the findings of this study.

It is also possible that the influence of clonality on the probability of gap-junction coupling in the present study was underrepresented due to limitations in the protocol for the detection of gap junctions. This could arise through the tendency of the gap-junction coupled clonally-related cells to be separated by greater distances than the non-clonally related cells. The short time between loading a target cell and assessment of gap junction coupling (5 minutes) may have provided insufficient time for the dye to diffuse to distant cells. Nevertheless, considerable spatial separation was observed between clonally-related cells in both the iPSC system and in mouse (both > 400 μm).

Electrophysiological assessment of gap-junction coupling (MacVicar & Dudek, 1981) on the other hand, is likely to be an unbiased method of identifying gap-junction coupling. This method also provides the opportunity to quantify the degree of coupling and its directionality. A considerable limitation of this technique however, is that only very small numbers of cells can be recorded from simultaneously. Therefore, complete characterisation of the population of cells coupled to a single cell is not feasible. Furthermore, this technique does not necessarily reflect the kinetics of molecular diffusion between gap junctions. Therefore it may not accurately reflect the transfer of molecular effectors such as nutrients and metabolites (Abbaci, Barberi-Heyob, Blondel, Guillemin, & Didelon, 2008; Evans & Martin, 2002). This highlights the relative differences in the

information provided by electrophysiological and dye-based assessment of gap-junction coupling. Future work applying electrophysiological recordings would provide complimentary insight into the pronounced clonal bias in gap-junction coupling that I observed using dye labelling. Having reviewed some of the potential caveats and limitations, I will now take the opportunity to discuss the broader implications of the work in this thesis.

7.3 The influence of clonality upon mammalian neocorticogenesis

A pervading question in neuroscience is the extent to which the phenotype of a neuron is influenced by its lineage. Our understanding of the diversity of excitatory neuronal progenitors has expanded over recent years, and this diversity is proposed to contribute to events as fundamental as the development of the gyrencephalic cortex through the expansion of upper neocortical layers (Martínez-Cerdeño et al., 2006; Montiel et al., 2016; Reillo et al., 2011). Much attention has been bestowed on progenitor types and their influence on the phenotype of their neuronal offspring (Betizeau et al., 2013; Stancik et al., 2010; Tyler et al., 2015). However, relatively few studies have examined this question at the finest resolution: the relationship between a single progenitor and its offspring. Clonal analysis involves the interrogation of neurons that derive from the same progenitor in order to identify properties that are under clonal influence. In Chapter 5 and 6, I examined clonal relationships in mouse neocortex, and in an *in vitro* model of human neocorticogenesis using iPSC technology, respectively.

7.3.1 The morphological similarity of layer 2/3 pyramidal neurons in somatosensory cortex

My observation that the population of clonally-related pyramidal neuron pairs in layer 2/3 of mouse cortex have more similar dendritic morphology than non-clonally related neurons provides the first evidence of this type in neocortical neurons. It raises a series of interesting questions about the influence of a progenitor on its progeny. I will focus on the following two key questions in this discussion. Firstly, how could a progenitor influence the dendritic morphology of its offspring, and secondly, what implications does the relationship between lineage and morphology have for the functional properties of lineage-related neurons and their integration into neocortical circuitry?

Firstly, how does the influence of lineage on morphology arise during development? In this thesis, clonality was defined experimentally as a binary attribute of the relationship between two neurons which either did, or did not, arise from a single labelled progenitor at the time of retroviral transduction. The assumption *a priori* was that neurons in both the clonal and non-clonal populations were derived from equivalent neuronal progenitors. However, my observation that neurons in clonal pairs were more similar to other neurons in clonal pairs, as well as to their clonal partner, raises the likelihood that a different subgroup of progenitor tends to generate multiple neurons destined for layer 2/3 than those that tend to generate a single neuron in layer 2/3. Furthermore, this subgroup of progenitors impart specific phenotypic properties on their offspring. Nonetheless, this represents evidence that neuronal lineage influences neuronal morphology. The mechanism by which different groups of progenitors could generate neurons with distinct morphologies represents an interesting question. Clearly, any such mechanism is unlikely to be explained by a single binary difference between cells, such as the expression of a particular gene. Rather, it is more helpful to consider development as a continuum of differentiation, where progenitors become increasingly

different from one another with each round of mitosis. Through this iterative divergence, the mechanisms that regulates morphological heterogeneity could be generated. This diversity could arise through the epigenetic regulation of a large number of genes involved in determining neuronal morphology, for example. It could also arise through the asymmetric distribution of molecular effectors to daughter cells during mitosis. If this diversity exists, then the population of neuronal progenitors may not be a limited number of discrete subtypes (such as vRGCs, IPCs and oRGCs) within which progenitors are uniform. Rather, each neuronal progenitor would be a distinct branch of an ontogenetic tree, and each round of mitosis would represent a branch point. In this context, it seems likely that the clonal influence on morphology will be multifactorial, resulting from a combination of factors such as gene expression, the local environment in which neurons are born, and even gap-junction exchange of molecular effectors. Whether the group of progenitors that generated clonal pairs of neurons in layer 2/3 are a single, homogeneous subtype or a heterogeneous population of progenitors that share a common ability to influence the morphology of their offspring remains to be elucidated. The combination of clonal labelling with conditional reporting targeted to specific progenitor subtypes (using promoters such as Tbr2 to label IPCs or Tα1 to label SNPs) could be used to investigate this question. The insertion of a floxed-STOP into the RNA barcoding retrovirus would enable Cre-dependent expression of barcoded tdTom that could be injected into transgenic mice that express cell-type specific Cre. Only those neurons that were transduced with retrovirus and derived from the targeted progenitor subtype would then express the barcoded tdTom.

A vast array of molecular effectors have been associated with dendritic morphogenesis and could be under the influence of lineage through epigenetic regulation. Adhesion molecules represent a very interesting set of candidates (Arikkath, 2012; Hayashi & Takeichi, 2015). For instance, one attractive idea is that the clustered protocadherin homophilic adhesion molecules, of which there are around 60 isoforms, could provide a mechanism for generating neuronal identity under the influence of lineage.

Neurons appear to exhibit stochastic and combinatorial expression of the alpha, beta and gamma protocadherin gene clusters (Thu et al., 2014), which provides a large combinatorial complexity for the expression pattern of protocadherins in a single cell. Furthermore, the clustered protocadherins have been shown to undergo both homophilic and heterophilic cis- and trans- interactions (Nicoludis et al., 2016; Schreiner & Weiner, 2010), further increasing the diversity of distinct intercellular adhesion patterns that could be generated. The protocadherin genes have been shown to have a variety of downstream signalling pathways and they have been implicated in aspects of dendritic arborisation and synapse formation, although their function is incompletely understood (Garrett, Schreiner, Lobas, & Weiner, 2012; Lefebvre, Zhang, Meister, Wang, & Sanes, 2008; Suo, Lu, Ying, Capecchi, & Wu, 2012; Weiner & Jontes, 2013). Epigenetic modification of the protocadherin gene clusters during embryonic development has been shown to regulate the probability of isoform expression (Esumi et al., 2005; Toyoda et al., 2014). This provides a mechanism by which the subset of protocadherin isoforms expressed by a neuron could be influenced by lineage (Yao et al., 2016).

Understanding the mechanisms by which lineage-related neurons acquire their morphological similarity is an important step in understanding how a progenitor may influence the phenotype of its neuronal progeny. Insight into the mechanisms by which lineage-related neurons acquire similar morphology could be provided by examining progenitors at different stages of development. For example, if RNA-barcoding retrovirus was applied at different neurodevelopmental time-points ranging from E10.5 to E13.5, the relative influence of lineage on morphology at each time-point could be compared. If there is no difference in the degree of morphological similarity between the neuronal offspring, then this would support the idea that the local environment is a major contributor in the relationship between a progenitor and neuronal morphology. However, if layer 2/3 clones from mice injected at a later time-point (mainly ‘sisters’) were more similar than layer 2/3 clones injected at an earlier time-point (‘sisters’ and ‘cousins’), this would support the idea of there being a progressive differentiation of progenitors. This experiment would be

facilitated by the use of an RNA-barcoding Cre retrovirus, which could be applied in the MADM mouse to differentially identify each daughter lineage from a transduced progenitor. This would enable ‘sisters’ and ‘cousins’ to be identified visually.

Another experiment that is now immediately feasible, would build upon my demonstration that clonal labelling with a retroviral RNA-barcode can be combined with single-cell transcriptomic methods such as RNA-seq. This combination of approaches could be used to identify specific similarities and/or differences in gene expression amongst clonally-related and non-clonally related neurons. Single-cell RNA-seq has already been used to interrogate the expression of cell adhesion molecules across different populations of neurons, and has identified distinct expression patterns of molecules involved in circuit assembly and synapse formation (Földy et al., 2016). Analysing the expression pattern of genes that have previously been shown to play a role in the formation of dendritic morphology, such as the protocadherin gene cluster, could provide insight into the mechanism behind the morphological similarity I observed within layer 2/3 pyramidal neuron clones (Lefebvre, Kostadinov, Chen, Maniatis, & Sanes, 2012; Yagi, 2015). One could also imagine adopting a more hypothesis-free approach and using single cell RNA-seq to investigate what gene families, and what proportion of genes, exhibit a correlation with the cells’ clonal relationships. There is an emerging framework for analysing these types of data, which has led to recent progress in characterising cellular diversity in both the mouse and human neocortex (M. Johnson et al., 2015; Poulin, Tasic, Hjerling-Leffler, Trimarchi, & Awatramani, 2016; Tasic et al., 2016). The degree to which this cellular diversity at the transcriptome level may, or may not, relate to the neuron’s progenitor has not yet been examined. Finally, insight into the mechanisms by which progenitors might influence the morphology of their neuronal offspring could come from gap-junction studies. Li et al. (2012) observed that gap-junction coupling via connexin26 was instrumental in shaping a clone’s functional connectivity. To investigate whether gap-junction coupling also underlies the influence of lineage on morphology, the Cre retrovirus generated in the present study could be applied in a connexin26 conditional

reporter mouse (e.g. Schütz et al., 2011) in order to disrupt gap-junction function at a clonal level.

The second question is what are the functional implications of lineage-determined fine-scale dendritic morphology for neocortical circuits? The pattern of a neuron's dendritic arbor is critical to determining the synaptic input field of a neuron (Arikkath, 2012). Therefore, it is possible that the influence of lineage upon the dendrite represents a mechanism by which progenitors produce neurons with specific properties in terms of their integration of synaptic inputs, formation of synapses, and ultimately, function within the neural circuit. For example, clonally-related neurons in layer 2/3 of visual cortex have been shown to exhibit similar stimulus selectivity in visual cortex (Li et al., 2012; Ohtsuki et al., 2012). One possibility is that similarities in the dendritic arbor of clonally-related neurons underlies this phenomenon, by influencing the formation of specific synaptic connections between layer 2/3 pyramidal neurons and long-range inputs from the thalamus. To establish whether this is the case, the RNA-barcoding retrovirus could be used to examine whether more similar morphologies are associated with more similar functional properties. This could be assessed by performing targeted patch-clamp recordings from retrovirally-labelled neurons to assess their intrinsic electrical properties and synaptic connectivity, prior to harvesting the cell for barcode analysis. Such an experimental design could be extended by using optogenetic techniques to activate synaptic inputs from subcortical structures of other regions of cortex. This type of experiment would allow me to examine the relationship between a neuron's clonal identity and its morphology, intrinsic electrical properties and synaptic interconnectivity. A further question is whether the influence of lineage on morphology extends to translaminar clones, which have been shown to exhibit preferential connectivity (Yu et al., 2012, 2009). The RNA-barcoding retrovirus could be used to label translaminar pyramidal clones and spatially matched non-clones, and their morphology could be assessed. A positive relationship between clonality and morphology in translaminar clones would indicate that it is the effects upon morphology that underlie the formation of biased synaptic connectivity. A complimentary experiment would be to

examine the connectivity of intralaminar clonal and non-clonal neuron pairs, to establish whether the most morphologically similar are also the most likely to connect to one another.

7.3.2 Gap-junction coupling in human neocortical cells derived from iPSCs

The observation in Chapter 6 that human neocortical cells derived from iPSCs *in vitro* also exhibit biased gap junction coupling between clonally related neurons is interesting from the perspective of both the iPSC-derived model and the perspective of human neocorticogenesis. Firstly, gap-junction coupling is a key process during neocortical development (L. A. B. Elias & Kriegstein, 2008). It is involved in landmark events such as the formation of early networks (Yuste, Nelson, Rubin, & Katz, 1995) and therefore the presence of gap junctions in iPSC-derived human neocortical cells is further evidence that the *in vitro* model recapitulates aspects of *in vivo* development. Moreover, it is evidence that this model of neocorticogenesis exhibits an important feature in the formation of structured networks. Previous studies have demonstrated that iPSC-derived neurons are electrophysiologically functional (Shi, Kirwan, & Livesey, 2012), but evidence for organised synaptic connectivity is lacking. Secondly, the observations described in Chapter 6 provides the first evidence that biased gap junction coupling exists in clonally related human neocortical neurons. Biased electrical coupling is thought to give rise to biased synaptic connectivity in mouse (Yu et al., 2012). This raises the question as to whether iPSC-derived human neurons demonstrate biased synaptic connectivity. One way of investigating this would be to perform dual-patch clamp recording from pairs of clonally-related neurons and matched non-clonally related neurons, in order to establish whether clonally-related neuron pairs show a higher probability of being synaptically connected. One possible obstacle to this experiment is attaining functionally mature

synapses in an adequate proportion of neocortical neurons. However, techniques are evolving to accelerate the maturation of iPSC-derived human neurons, which are making these sorts of synaptic connectivity experiments more feasible (Lam et al., 2017; Qi et al., 2017). Dual patch-clamp recording could also be used to quantify the strength of gap-junction coupling between clonally-related neurons and its directionality. If human neurons exhibited an influence of clonality on the formation of synaptic connectivity, connexin26 could be knocked down in some members of a retrovirally-labelled clone to examine whether this influences the probability of synaptic connectivity. This could be achieved by sequential transduction of cultures, firstly with the RNA-barcoding retrovirus at final plating to label clones, and secondly with a lentivirus encoding a short-hairpin RNA to knockdown connexin26 function (Yang, Qin, & Chen, 2014) approximately 2-4 weeks later. Delay of the lentiviral transduction relative to retroviral transduction would enable the proliferation of clones. The aim of this experimental setup would be to obtain retrovirally-labelled clones in which some members of the clone were transduced with lentivirus and therefore had connexin26 function knocked down, whereas some were not. Labelling of isochronic cohorts of neurons using a fluorescent carboxyfluorescein ester dye (Telley et al., 2016) at the time of lentiviral transduction would enable the recorded neurons to be age-matched. This experiment would not only be expected to provide further insight into the role of gap-junction coupling in the formation of synaptic connections, but it may reveal novel roles for gap-junction coupling in influencing the cellular phenotypes in human clones.

7.4 Concluding remarks

In this thesis I have assessed and optimised *in utero* surgical techniques for performing genetic manipulation in the developing mouse brain. I have developed two novel retroviral tools for studying clonal relationships in the developing neocortex: a retrovirus encoding

Cre recombinase and an RNA-barcoding retrovirus. I have shown that Cre retrovirus can be used in diverse reporter mouse strains to improve the consistency and versatility of clonal labelling, and that barcoded retrovirus provides a method of confidently and reliably identifying clones in both mouse neocortex and in an *in vitro* model of human neocorticogenesis. I have employed RNA-barcoding retrovirus in mouse to show that clonally related pyramidal neurons in layer 2/3 of somatosensory cortex have more similar dendritic arbors than non-clonally related neurons. Furthermore, I have used RNA-barcoding retrovirus in combination with iPSC technology, and I have been able to demonstrate that human neuronal clones have diverse proliferative behaviour and that they exhibit biased gap junction coupling *in vitro*. This work contributes to the mounting evidence for a relationship between neuronal lineage and neuronal function in the developing neocortex.

References

Abbaci, M., Barberi-Heyob, M., Blondel, W., Guillemin, F., & Didelon, J. (2008). Advantages and limitations of commonly used methods to assay the molecular permeability of gap junctional intercellular communication. *BioTechniques*. http://doi.org/10.2144/000112810

Anastasiades, P. G., & Butt, S. J. B. (2012). A role for silent synapses in the development of the pathway from layer 2/3 to 5 pyramidal cells in the neocortex. *The Journal of Neuroscience : The Official Journal of the Society for Neuroscience*, *32*(38), 13085–99. http://doi.org/10.1523/JNEUROSCI.1262-12.2012

Anastasiades, P. G., Marques-Smith, A., Lyngholm, D., Lickiss, T., Raffiq, S., Kätzel, D., … Miesenbock, G. (2016). GABAergic interneurons form transient layer-specific circuits in early postnatal neocortex. *Nature Communications*, *7*, 10584. http://doi.org/10.1038/ncomms10584

Andrzejowski, J., Hoyle, J., Eapen, G., & Turnbull, D. (2008). Effect of prewarming on post-induction core temperature and the incidence of inadvertent perioperative hypothermia in patients undergoing general anaesthesia. *British Journal of Anaesthesia*, *101*(5), 627–631. http://doi.org/10.1093/bja/aen272

Anthony, T. E., Klein, C., Fishell, G., & Heintz, N. (2004). Radial Glia Serve as Neuronal Progenitors in All Regions of the Central Nervous System. *Neuron*, *41*(6), 881–890. http://doi.org/10.1016/S0896-6273(04)00140-0

Arikkath, J. (2012). Molecular mechanisms of dendrite morphogenesis. *Frontiers in Cellular Neuroscience*, *6*(December), 61. http://doi.org/10.3389/fncel.2012.00061

Arnold, S. J., Huang, G.-J., Cheung, A. F. P., Era, T., Nishikawa, S.-I., Bikoff, E. K., … Groszer, M. (2008). The T-box transcription factor Eomes/Tbr2 regulates neurogenesis in the cortical subventricular zone. *Genes & Development*, *22*(18), 2479–84. http://doi.org/10.1101/gad.475408

Arras, M., Rettich, A., Cinelli, P., Kasermann, H. P., Burki, K., Richardson, C., … Olson, D. (2007). Assessment of post-laparotomy pain in laboratory mice by telemetric recording of heart rate and heart rate variability. *BMC Veterinary Research*, *3*(1), 16. http://doi.org/doi: 10.1186/1746-6148-3-16

Attardo, A., Calegari, F., Haubensak, W., Wilsch-Bräuninger, M., Huttner, W. W. B., Smart, I., … Argraves, W. (2008). Live Imaging at the Onset of Cortical Neurogenesis Reveals Differential Appearance of the Neuronal Phenotype in Apical versus Basal Progenitor Progeny. *PLoS ONE*, *3*(6), e2388. http://doi.org/doi: 10.1371/journal.pone.0002388

Bai, J., Ramos, R. L., Ackman, J. B., Thomas, A. M., Lee, R. V, & LoTurco, J. J. (2003). RNAi reveals doublecortin is required for radial migration in rat neocortex. *Nature Neuroscience*, *6*(12), 1277–1283. http://doi.org/10.1038/nn1153

Bajwa, S. J. S., & Bajwa, S. K. (2013). Anaesthetic challenges and management during pregnancy: Strategies revisited. *Anesthesia, Essays And Researches*. Medknow Publications and Media Pvt. Ltd. http://doi.org/10.4103/0259-1162.118945

Baker, C. A., Elyada, Y. M., Parra-Martin, A., & Bolton, M. (2016). Cellular resolution circuit mapping in mouse brain with temporal-focused excitation of soma-targeted channelrhodopsin. *eLife*, *5*, 1–15. http://doi.org/10.7554/eLife.14193

Bardy, C., van den Hurk, M., Kakaradov, B., Erwin, J. A., Jaeger, B. N., Hernandez, R. V, … Gage, F. H. (2016). Predicting the functional states of human iPSC-derived neurons with single-cell RNA-seq and electrophysiology. *Molecular Psychiatry*, *21*(11), 1573–1588. http://doi.org/10.1038/mp.2016.158

Barmparas, G., Branco, B. C., Schnüriger, B., Lam, L., Inaba, K., & Demetriades, D. (2010). The Incidence and Risk Factors of Post-Laparotomy Adhesive Small Bowel Obstruction. *Journal of Gastrointestinal Surgery*, *14*(10), 1619–1628. http://doi.org/10.1007/s11605-010-1189-8

Bayatti, N., Moss, J. A., Sun, L., Ambrose, P., Ward, J. F. H., Lindsay, S., & Clowry, G. J. (2008). A Molecular Neuroanatomical Study of the Developing Human Neocortex from 8 to 17 Postconceptional Weeks Revealing the Early Differentiation of the Subplate and Subventricular Zone. *Cerebral Cortex*, *18*(7), 1536–1548. http://doi.org/10.1093/cercor/bhm184

Beier, K., Samson, M., Matsuda, T., & Cepko, C. (2011). Conditional expression of the TVA receptor allows clonal analysis of descendents from Cre-expressing progenitor cells. *Developmental Biology*, *353*(2), 309–320. http://doi.org/doi: 10.1016/j.ydbio.2011.03.004

Beltramello, M., Bicego, M., Piazza, V., Ciubotaru, C. D., Mammano, F., & D'Andrea, P. (2003). Permeability and gating properties of human connexins 26 and 30 expressed in HeLa cells. *Biochemical and Biophysical Research Communications*, *305*(4), 1024–1033. http://doi.org/10.1016/S0006-291X(03)00868-4

Betizeau, M., Cortay, V., Patti, D., Pfister, S., Gautier, E., Bellemin-Ménard, A., … Dehay, C. (2013). Precursor Diversity and Complexity of Lineage Relationships in the Outer Subventricular Zone of the Primate. *Neuron*, *80*(2), 442–457. http://doi.org/10.1016/j.neuron.2013.09.032

Bouard, D., Alazard-Dany, D., & Cosset, F.-L. (2009). Viral vectors: from virology to transgene expression. *British Journal of Pharmacology*, *157*(2), 153–65. http://doi.org/10.1038/bjp.2008.349

Brodmann, K. (1910). Vergleichende Lokalisationslehre der Grosshirnrinde. *The Journal of Nervous and Mental Disease*, *37*(12), 783–784. http://doi.org/10.1097/00005053-191012000-00013

Brown, K. N., Chen, S., Han, Z., Lu, C.-H., Tan, X., Zhang, X.-J., … Shi, S.-H. (2011). Clonal production and organization of inhibitory interneurons in the neocortex. *Science (New York, N.Y.)*, *334*(6055), 480–6. http://doi.org/10.1126/science.1208884

Buckingham, M. E., & Meilhac, S. M. (2011). Tracing Cells for Tracking Cell Lineage and Clonal Behavior. *Developmental Cell*, *21*(3), 394–409. http://doi.org/10.1016/j.devcel.2011.07.019

Cai, D., Cohen, K., Luo, T., Lichtman, J., & Sanes, J. (2013). Improved tools for the Brainbow toolbox. *Nat Meth*, *10*(6), 540–547. http://doi.org/doi: 10.1038/nmeth.2450

Camp, J. G., Badsha, F., Florio, M., Kanton, S., Gerber, T., Wilsch-Bräuninger, M., … Treutlein, B. (2015). Human cerebral organoids recapitulate gene expression programs of fetal neocortex development. *Proceedings of the National Academy of Sciences of the United States of America*, *112*(51), 15672–7. http://doi.org/10.1073/pnas.1520760112

Carletti, B., Grimaldi, P., Magrassi, L., & Rossi, F. (2004). Engraftment and differentiation of neocortical progenitor cells transplanted to the embryonic brain in utero. *Journal of Neurocytology*, *33*(3), 309–319.

http://doi.org/10.1023/B:NEUR.0000044192.20397.7e

Cassie, A. B., Chatterjee, A. K., Mehta, S., & Haworth, J. M. (1988). Pain quantum and wound healing: a comparison of interrupted inversion PDS and standard nylon sutures in abdominal skin closure. *Annals of the Royal College of Surgeons of England*, *70*(6), 339–42. Retrieved from http://www.ncbi.nlm.nih.gov/pubmed/2974694

Cepko, C. L., Ryder, E., Austin, C., Golden, J., Fields-Berry, S., & Lin, J. (1998). Lineage analysis using retroviral vectors. *Methods (San Diego, Calif.)*, *14*(4), 393–406. http://doi.org/10.1006/meth.1998.0594

Cesarovic, N., Arras, M., & Jirkof, P. (2014). Impact of inhalation anaesthesia, surgery and analgesic treatment on home cage behaviour in laboratory mice. *Applied Animal Behaviour Science*, *157*, 137–145. http://doi.org/10.1016/j.applanim.2014.04.010

Chen, M. D., Teigen, G. A., Reynolds, H. T., Johnson, P. R., & Fowler, J. M. (1998). Laparoscopy versus laparotomy: an evaluation of adhesion formation after pelvic and paraaortic lymphadenectomy in a porcine model. *American Journal of Obstetrics and Gynecology*, *178*(3), 499–503. Retrieved from citeulike-article-id:14178266

Chenn, A., & McConnell, S. K. (1995). Cleavage orientation and the asymmetric inheritance of Notch1 immunoreactivity in mammalian neurogenesis. *Cell*, *82*(4), 631–41. Retrieved from http://www.ncbi.nlm.nih.gov/pubmed/7664342

Cheung, A. F. P., Kondo, S., Abdel-Mannan, O., Chodroff, R. a, Sirey, T. M., Bluy, L. E., … Molnár, Z. (2010). The subventricular zone is the developmental milestone of a 6-layered neocortex: comparisons in metatherian and eutherian mammals. *Cerebral Cortex (New York, N.Y. : 1991)*, *20*(5), 1071–81. http://doi.org/10.1093/cercor/bhp168

Ciceri, G., Dehorter, N., Sols, I., Huang, Z. J., Maravall, M., & Marín, O. (2013). Lineage-specific laminar organization of cortical GABAergic interneurons. *Nature Neuroscience*, *16*(9), 1199–210. http://doi.org/10.1038/nn.3485

Cornils, K., Thielecke, L., Hüser, S., Forgber, M., Thomaschewski, M., Kleist, N., … Fehse, B. (2014). Multiplexing clonality: combining RGB marking and genetic barcoding. *Nucleic Acids Research*, *42*(7), e56–e56. http://doi.org/doi: 10.1093/nar/gku081

Costa, M. R., Bucholz, O., Schroeder, T., & Götz, M. (2009). Late origin of glia-restricted progenitors in the developing mouse cerebral cortex. *Cerebral Cortex*, *19*(SUPPL. 1), i135-43. http://doi.org/10.1093/cercor/bhp046

Dakin, K., Zhao, Y., & Li, W. H. (2005). LAMP, a new imaging assay of gap junctional communication unveils that Ca2+ influx inhibits cell coupling. *Nat Methods*, *2*(1), 55–62. http://doi.org/10.1038/nmeth730

Dehay, C., Kennedy, H., & Kosik, K. S. (2015). The Outer Subventricular Zone and Primate-Specific Cortical Complexification. *Neuron*, *85*(4), 683–694. http://doi.org/10.1016/j.neuron.2014.12.060

Desai, A. R., & McConnell, S. K. (2000). Progressive restriction in fate potential by neural progenitors during cerebral cortical development. *Development*, *127*(13), 2863–2872.

Díaz-Alonso, J., Aguado, T., Wu, C.-S., Palazuelos, J., Hofmann, C., Garcez, P., … Galve-Roperh, I. (2012). The CB(1) cannabinoid receptor drives corticospinal motor neuron differentiation through the Ctip2/Satb2 transcriptional regulation axis. *Neuroscience*, *32*(47), 16651–65. http://doi.org/10.1523/JNEUROSCI.0681-

12.2012

Díaz, M., & Becker, D. E. (2010). Thermoregulation: physiological and clinical considerations during sedation and general anesthesia. *Anesthesia Progress*, *57*(1), 25–32. http://doi.org/10.2344/0003-3006-57.1.25

Diener, M. K., Voss, S., Jensen, K., Büchler, M. W., & Seiler, C. M. (2010). Elective midline laparotomy closure: the INLINE systematic review and meta-analysis. *Annals of Surgery*, *251*(5), 843–56. http://doi.org/10.1097/SLA.0b013e3181d973e4

Dixit, R., Lu, F., Cantrup, R., Gruenig, N., Langevin, L. M., Kurrasch, D. M., & Schuurmans, C. (2011). Efficient gene delivery into multiple CNS territories using in utero electroporation. *Journal of Visualized Experiments : JoVE*, (52). http://doi.org/10.3791/2957

Dobin, A., Davis, C. A., Schlesinger, F., Drenkow, J., Zaleski, C., Jha, S., … Gingeras, T. R. (2013). STAR: ultrafast universal RNA-seq aligner. *Bioinformatics (Oxford, England)*, *29*(1), 15–21. http://doi.org/10.1093/bioinformatics/bts635

Doufas, A. (2003). Consequences of inadvertent perioperative hypothermia. *Best Practice & Research Clinical Anaesthesiology*, *17*(4), 535–549. http://doi.org/doi: 10.1016/s1521-6896(03)00052-1

Douglas, R. J., & Martin, K. a C. (2004). Neuronal circuits of the neocortex. *Annual Review of Neuroscience*, *27*, 419–51. http://doi.org/10.1146/annurev.neuro.27.070203.144152

Druckmann, S., Feng, L., Lee, B., Yook, C., Zhao, T., Magee, J. C., & Kim, J. (2014). Structured Synaptic Connectivity between Hippocampal Regions. *Neuron*, *81*(3), 629–640. http://doi.org/10.1016/j.neuron.2013.11.026

Duncan, P. G., Pope, W. D., Cohen, M. M., & Greer, N. (1986). Fetal risk of anesthesia and surgery during pregnancy. *Anesthesiology*, *64*(6), 790–794. Retrieved from http://www.ncbi.nlm.nih.gov/pubmed/3717642

Eckwahl, M. J., Sim, S., Smith, D., Telesnitsky, A., & Wolin, S. L. (2015). A retrovirus packages nascent host noncoding RNAs from a novel surveillance pathway. *Genes and Development*, *29*(6), 646–657. http://doi.org/10.1101/gad.258731.115

Elias, L. A. B., & Kriegstein, A. R. (2008). Gap junctions: multifaceted regulators of embryonic cortical development. *Trends in Neurosciences*. http://doi.org/10.1016/j.tins.2008.02.007

Elias, L. A., Wang, D. D., & Kriegstein, A. R. (2007). Gap junction adhesion is necessary for radial migration in the neocortex. *Nature*, *448*(7156), 901–907. http://doi.org/10.1038/nature06063

Englund, C., Fink, A., Lau, C., Pham, D., Daza, R. A. M., Bulfone, A., … Hevner, R. F. (2005). Pax6, Tbr2, and Tbr1 Are Expressed Sequentially by Radial Glia, Intermediate Progenitor Cells, and Postmitotic Neurons in Developing Neocortex. *Journal of Neuroscience*, *25*(1), 247–251. http://doi.org/10.1523/JNEUROSCI.2899-04.2005

Espinosa, J. S., Tea, J. S., & Luo, L. (2014). Mosaic analysis with double markers (MADM) in mice. *Cold Spring Harbor Protocols*, *2014*(2), 182–189. http://doi.org/10.1101/pdb.prot080366

Espuny-Camacho, I., Michelsen, K. A., Gall, D., Linaro, D., Hasche, A., Bonnefont, J., … Vanderhaeghen, P. (2013). Pyramidal Neurons Derived from Human Pluripotent Stem Cells Integrate Efficiently into Mouse Brain Circuits In Vivo. *Neuron*, *77*(3), 440–456. http://doi.org/10.1016/j.neuron.2012.12.011

Esumi, S., Kakazu, N., Taguchi, Y., Hirayama, T., Sasaki, A., Hirabayashi, T., … Yagi,

T. (2005). Monoallelic yet combinatorial expression of variable exons of the protocadherin-[alpha] gene cluster in single neurons. *Nat Genet*, *37*(2), 171–176. http://doi.org/doi: 10.1038/ng1500

Evans, W. H., & Martin, P. E. M. (2002). Gap junctions: structure and function (Review). *Molecular Membrane Biology*, *19*(2), 121–136. http://doi.org/10.1080/09687680210139839

Fernández, V., Llinares-Benadero, C., & Borrell, V. (2016). Cerebral cortex expansion and folding: what have we learned? *The EMBO Journal*, *35*(10), 1021–44. http://doi.org/10.15252/embj.201593701

Ferreira, T. A., Blackman, A. V, Oyrer, J., Jayabal, S., Chung, A. J., Watt, A. J., … van Meyel, D. J. (2014). Neuronal morphometry directly from bitmap images. *Nature Methods*, *11*(10), 982–984. http://doi.org/10.1038/nmeth.3125

Fields-Berry, S. C., Halliday, A. L., & Cepko, C. L. (1992). A recombinant retrovirus encoding alkaline phosphatase confirms clonal boundary assignment in lineage analysis of murine retina. *Proceedings of the National Academy of Sciences of the United States of America*, *89*(2), 693–697. http://doi.org/10.1073/pnas.89.2.693

Fietz, S. A., Kelava, I., Vogt, J., Wilsch-Bräuninger, M., Stenzel, D., Fish, J. L., … Huttner, W. B. (2010). OSVZ progenitors of human and ferret neocortex are epithelial-like and expand by integrin signaling. *Nature Neuroscience*, *13*(6), 690–699. http://doi.org/10.1038/nn.2553

Fietz, S. A., Lachmann, R., Brandl, H., Kircher, M., Samusik, N., Schroder, R., … Huttner, W. B. (2012). Transcriptomes of germinal zones of human and mouse fetal neocortex suggest a role of extracellular matrix in progenitor self-renewal. *Proceedings of the National Academy of Sciences*, *109*(29), 11836–11841. http://doi.org/10.1073/pnas.1209647109

Figueres-Oñate, M., García-Marqués, J., & López-Mascaraque, L. (2016). UbC-StarTrack , a clonal method to target the entire progeny of individual progenitors. *Nature Publishing Group*, *6*(May), 1–13. http://doi.org/10.1038/srep33896

Flores-Maldonado, A., Medina-Escobedo, C. E., Ríos-Rodríguez, H. M., & Fernández-Domínguez, R. (2001). Mild perioperative hypothermia and the risk of wound infection. *Archives of Medical Research*, *32*(3), 227–231. Retrieved from citeulike-article-id:14178292

Flores, L. E., Hildebrandt, T. B., Kühl, A. A., & Drews, B. (2014). Early detection and staging of spontaneous embryo resorption by ultrasound biomicroscopy in murine pregnancy. *Reproductive Biology and Endocrinology : RB&E*, *12*, 38. http://doi.org/10.1186/1477-7827-12-38

Florio, M., & Huttner, W. B. (2014). Neural progenitors, neurogenesis and the evolution of the neocortex. *Development*, *141*(11), 2182–2194. http://doi.org/doi: 10.1242/dev.090571

Földy, C., Darmanis, S., Aoto, J., Malenka, R. C., Quake, S. R., & Südhof, T. C. (2016). Single-cell RNAseq reveals cell adhesion molecule profiles in electrophysiologically defined neurons. *Proceedings of the National Academy of Sciences of the United States of America*, *113*(35), E5222-31. http://doi.org/10.1073/pnas.1610155113

Franco, S. J., Gil-Sanz, C., Martinez-Garay, I., Espinosa, A., Harkins-Perry, S. R., Ramos, C., & Müller, U. (2012). Fate-restricted neural progenitors in the mammalian cerebral cortex. *Science (New York, N.Y.)*, *337*(6095), 746–9. http://doi.org/10.1126/science.1223616

Franco, S. J., & Müller, U. (2013). Shaping our minds: stem and progenitor cell diversity in the mammalian neocortex. *Neuron*, *77*(1), 19–34.

http://doi.org/10.1016/j.neuron.2012.12.022

Frantz, G. D., & McConnell, S. K. (1996). Restriction of late cerebral cortical progenitors to an upper-layer fate. *Neuron*, *17*(1), 55–61. http://doi.org/10.1016/S0896-6273(00)80280-9

Fuentealba, L. C., Rompani, S. B., Parraguez, J. I., Obernier, K., Romero, R., Cepko, C. L., & Alvarez-Buylla, A. (2015). Embryonic Origin of Postnatal Neural Stem Cells. *Cell*, *161*(7), 1644–1655. http://doi.org/10.1016/j.cell.2015.05.041

Gades, N. M., Danneman, P. J., Wixson, S. K., & Tolley, E. A. (2000). The magnitude and duration of the analgesic effect of morphine, butorphanol, and buprenorphine in rats and mice. *Contemporary Topics in Laboratory Animal Science*, *39*(2), 8–13. Retrieved from http://www.ncbi.nlm.nih.gov/pubmed/11487232

Gal, J. S., Morozov, Y. M., Ayoub, A. E., Chatterjee, M., Rakic, P., & Haydar, T. F. (2006). Molecular and morphological heterogeneity of neural precursors in the mouse neocortical proliferative zones. *The Journal of Neuroscience : The Official Journal of the Society for Neuroscience*, *26*(3), 1045–56. http://doi.org/10.1523/JNEUROSCI.4499-05.2006

Gao, P., Postiglione, M. P., Krieger, T., Hernandez, L., Wang, C., Han, Z., … Shi, S.-H. (2014). Deterministic progenitor behavior and unitary production of neurons in the neocortex. *Cell*, *159*(4), 775–788. http://doi.org/doi: 10.1016/j.cell.2014.10.027

Gao, P., Sultan, K. T., Zhang, X.-J., & Shi, S.-H. (2013). Lineage-dependent circuit assembly in the neocortex. *Development*, *140*(13), 2645–2655. http://doi.org/doi: 10.1242/dev.087668

García-García, E., Pino-Barrio, M. J., López-Medina, L., & Martínez-Serrano, A. (2012). Intermediate progenitors are increased by lengthening of the cell cycle through calcium signaling and p53 expression in human neural progenitors. *Molecular Biology of the Cell*, *23*(7), 1167–80. http://doi.org/10.1091/mbc.E11-06-0524

García-Moreno, F., Vasistha, N., Begbie, J., & Molnár, Z. (2014). CLoNe is a new method to target single progenitors and study their progeny in mouse and chick. *Development*, *141*(7), 1589–1598. http://doi.org/doi: 10.1242/dev.105254

Garcia, E. L., Onafuwa-Nuga, A., Sim, S., King, S. R., Wolin, S. L., & Telesnitsky, A. (2009). Packaging of host mY RNAs by murine leukemia virus may occur early in Y RNA biogenesis. *Journal of Virology*, *83*(23), 12526–34. http://doi.org/10.1128/JVI.01219-09

Gargiulo, S., Greco, A., Gramanzini, M., Esposito, S., Affuso, A., Brunetti, A., & Vesce, G. (2012). Mice Anesthesia, Analgesia, and Care, Part I: Anesthetic Considerations in Preclinical Research. *ILAR Journal*, *53*(1), E55–E69. http://doi.org/doi: 10.1093/ilar.53.1.55

Garrett, A. M., Schreiner, D., Lobas, M. A., & Weiner, J. A. (2012). γ-Protocadherins Control Cortical Dendrite Arborization by Regulating the Activity of a FAK/PKC/MARCKS Signaling Pathway. *Neuron*, *74*(2), 269–276. http://doi.org/doi: 10.1016/j.neuron.2012.01.028

Ge, X. (2012). In utero Eletroporation of Mouse Embryo Brains. *BIO-PROTOCOL*, *2*(14). http://doi.org/doi: 10.21769/bioprotoc.231

Gerrits, A., Dykstra, B., Kalmykowa, O., Klauke, K., Verovskaya, E., Broekhuis, M., … Bystrykh, L. (2010). Cellular barcoding tool for clonal analysis in the hematopoietic system. *Blood*, *115*(13), 2610–2618. http://doi.org/doi: 10.1182/blood-2009-06-229757

Gertz, C. C., Lui, J. H., LaMonica, B. E., Wang, X., & Kriegstein, A. R. (2014). Diverse

Behaviors of Outer Radial Glia in Developing Ferret and Human Cortex. *Journal of Neuroscience*, *34*(7).

Glasser, M. F., Coalson, T. S., Robinson, E. C., Hacker, C. D., Harwell, J., Yacoub, E., … Van Essen, D. C. (2016). A multi-modal parcellation of human cerebral cortex. *Nature*, *536*(7615), 171–178. http://doi.org/10.1038/nature18933

Golden, J. A., Fields-Berry, S. C., & Cepko, C. L. (1995). Construction and characterization of a highly complex retroviral library for lineage analysis. *Proceedings of the National Academy of Sciences of the United States of America*, *92*(12), 5704–8. http://doi.org/10.1073/pnas.92.12.5704

Götz, M., & Huttner, W. B. (2005). The cell biology of neurogenesis. *Nature Reviews Molecular Cell Biology*, *6*(10), 777–788. http://doi.org/10.1038/nrm1739

Grove, E. A., Kirkwood, T. B. L., & Price, J. (1992). Neuronal precursor cells in the rat hippocampal formation contribute to more than one cytoarchitectonic area. *Neuron*, *8*(2), 217–229. http://doi.org/10.1016/0896-6273(92)90289-P

Haddad-Tóvolli, R., Szabó, N.-E., Zhou, X., & Alvarez-Bolado, G. (2013). Genetic manipulation of the mouse developing hypothalamus through in utero electroporation. *Journal of Visualized Experiments : JoVE*, (77). http://doi.org/10.3791/50412

Handel, A. E., Chintawar, S., Lalic, T., Whiteley, E., Vowles, J., Giustacchini, A., … Cader, M. Z. (2016). Assessing similarity to primary tissue and cortical layer identity in induced pluripotent stem cell-derived cortical neurons through single-cell transcriptomics. *Human Molecular Genetics*, *25*(5), 989–1000. http://doi.org/10.1093/hmg/ddv637

Hansen, D., Lui, J., Parker, P., & Kriegstein, A. (2010). Neurogenic radial glia in the outer subventricular zone of human neocortex. *Nature*, *464*(7288), 554–561. http://doi.org/doi: 10.1038/nature08845

Hansen, D. V, Lui, J. H., Flandin, P., Yoshikawa, K., Rubenstein, J. L., Alvarez-Buylla, A., & Kriegstein, A. R. (2013). Non-epithelial stem cells and cortical interneuron production in the human ganglionic eminences. *Nature Neuroscience*, *16*(11), 1576–1587. http://doi.org/10.1038/nn.3541

Hansen, D. V, Rubenstein, J. L. R., Kriegstein, A. R., Abematsu, M., Kagawa, T., Fukuda, S., … Wang, F. (2011). Deriving excitatory neurons of the neocortex from pluripotent stem cells. *Neuron*, *70*(4), 645–60. http://doi.org/10.1016/j.neuron.2011.05.006

Harris, K. D., & Shepherd, G. M. G. (2015). The neocortical circuit: themes and variations. *Nature Neuroscience*, *18*(2), 170–181. http://doi.org/10.1038/nn.3917

Hart, S. R., Bordes, B., Hart, J., Corsino, D., & Harmon, D. (2011). Unintended perioperative hypothermia. *The Ochsner Journal*, *11*(3), 259–70. Retrieved from http://www.ncbi.nlm.nih.gov/pubmed/21960760

Harwell, C. C., Fuentealba, L. C., Gonzalez-Cerrillo, A., Parker, P. R. L., Gertz, C. C., Mazzola, E., … Kriegstein, A. R. (2015). Wide Dispersion and Diversity of Clonally Related Inhibitory Interneurons. *Neuron*, *87*(5), 999–1007. http://doi.org/10.1016/j.neuron.2015.07.030

Hau, J., & Van Hoosier, G. L. (2003). *Handbook of laboratory animal science. Vol. 1, Essential principles and practices*. (S. Hau, Jann; Van Hoosier, Gerald; Schapiro, Ed.) (Second). CRC Pres LLC.

Haubensak, W., Attardo, A., Denk, W., & Huttner, W. B. (2004). Neurons arise in the basal neuroepithelium of the early mammalian telencephalon: a major site of

neurogenesis. *Proceedings of the National Academy of Sciences*, *101*(9), 3196–3201. http://doi.org/10.1073/pnas.0308600100

Hayashi, S., & Takeichi, M. (2015). Emerging roles of protocadherins: from self-avoidance to enhancement of motility. *Journal of Cell Science*, jcs.166306. http://doi.org/doi: 10.1242/jcs.166306

Haydar, T. F., Ang, E., & Rakic, P. (2003). Mitotic spindle rotation and mode of cell division in the developing telencephalon. *Proceedings of the National Academy of Sciences*, *100*(5), 2890–2895. http://doi.org/10.1073/pnas.0437969100

Hejtmancik, J. F., Cabrera, P., Chen, Y., M'Hamdi, O., Nickerson, J. M., & Waitzman, D. M. (2017). *Conn's Translational Neuroscience*. *Conn's Translational Neuroscience*. http://doi.org/10.1016/B978-0-12-802381-5.18001-7

Höer, J., Klinge, U., Schachtrupp, A., Töns, C., & Schumpelick, V. (2001). Influence of suture technique on laparotomy wound healing: An experimental study in the rat. *Langenbeck's Archives of Surgery*, *386*(3), 218–223. http://doi.org/10.1007/s004230000196

Höer, J., Töns, C., Schachtrupp, A., Anurov, M., Titkova, S., Oettinger, A., … Schumpelick, V. (2002). Quantitative evaluation of abdominal wall perfusion after different types of laparotomy closure using laser-fluorescence videography. *Hernia : The Journal of Hernias and Abdominal Wall Surgery*, *6*(1), 11–6. Retrieved from http://www.ncbi.nlm.nih.gov/pubmed/12090573

Holzheimer, R. G., Muhrer, K. H., L'Allemand, N., Schmidt, T., & Hennecking, K. (1991). Intraabdominal infections: Classification, mortality, scoring and pathophysiology. *Infection*, *19*(6), 447–452. http://doi.org/10.1007/BF01726463

Horn, E. P., Bein, B., Böhm, R., Steinfath, M., Sahili, N., & Höcker, J. (2012). The effect of short time periods of pre-operative warming in the prevention of peri-operative hypothermia. *Anaesthesia*, *67*(6), 612–617. http://doi.org/doi: 10.1111/j.1365-2044.2012.07073.x

Hou, M., Li, Y., & Paul, D. L. (2013). A novel, highly sensitive method for assessing gap junctional coupling. *Journal of Neuroscience Methods*, *220*(1), 18–23. http://doi.org/10.1016/j.jneumeth.2013.08.007

Howard, B. M., Zhicheng Mo, Z., Filipovic, R., Moore, A. R., Antic, S. D., & Zecevic, N. (2008). Radial glia cells in the developing human brain. *The Neuroscientist : A Review Journal Bringing Neurobiology, Neurology and Psychiatry*, *14*(5), 459–473. http://doi.org/10.1177/1073858407313512

Huang, H., Liu, L., Li, B., Zhao, P.-P., Xu, C.-M., Zhu, Y.-Z., … Wu, Y.-Q. (2015). Ketamine Interferes with the Proliferation and Differentiation of Neural Stem Cells in the Subventricular Zone of Neonatal Rats. *Cellular Physiology and Biochemistry*, *35*(1), 315–325. http://doi.org/doi: 10.1159/000369698

Itah, R., Gitelman, I., Tal, J., & Davis, C. (2004). Viral inoculation of mouse embryos in utero. *Journal of Virological Methods*, *120*(1), 1–8. http://doi.org/10.1016/j.jviromet.2004.02.019

Jaglin, X. H., & Chelly, J. (2009). Tubulin-related cortical dysgeneses: microtubule dysfunction underlying neuronal migration defects. *Trends in Genetics : TIG*, *25*(12), 555–66. http://doi.org/10.1016/j.tig.2009.10.003

Javaherian, A., & Kriegstein, A. (2009). A stem cell niche for intermediate progenitor cells of the embryonic cortex. *Cerebral Cortex (New York, N.Y. : 1991)*, *19 Suppl 1*(suppl 1), i70-7. http://doi.org/10.1093/cercor/bhp029

Jefferis, G., & Livet, J. (2012). Sparse and combinatorial neuron labelling. *Current*

Opinion in Neurobiology, *22*(1), 101–110. http://doi.org/doi: 10.1016/j.conb.2011.09.010

Jirkof, P., Cesarovic, N., Rettich, A., Nicholls, F., Seifert, B., & Arras, M. (2010). Burrowing behavior as an indicator of post-laparotomy pain in mice. *Frontiers in Behavioral Neuroscience*, *4*, 165. http://doi.org/10.3389/fnbeh.2010.00165

Johansson, P. A. (2014). The choroid plexuses and their impact on developmental neurogenesis. *Frontiers in Neuroscience*. http://doi.org/10.3389/fnins.2014.00340

Johnson, M. B., Kawasawa, Y. I., Mason, C. E., Krsnik, Z., Coppola, G., Bogdanović, D., … Sestan, N. (2009). Functional and evolutionary insights into human brain development through global transcriptome analysis. *Neuron*, *62*(4), 494–509. http://doi.org/10.1016/j.neuron.2009.03.027

Johnson, M., Wang, P., Atabay, K., Murphy, E., Doan, R., Hecht, J., & Walsh, C. (2015). Single-cell analysis reveals transcriptional heterogeneity of neural progenitors in human cortex. *Nat Neurosci*, *18*(5), 637–646. http://doi.org/doi: 10.1038/nn.3980

Karus, M., Blaess, S., & Brüstle, O. (2014). Self-organization of neural tissue architectures from pluripotent stem cells. *J. Comp. Neurol.*, *522*(12), 2831–2844. http://doi.org/doi: 10.1002/cne.23608

Katoh, K., Misawa, K., Kuma, K., & Miyata, T. (2002). MAFFT: a novel method for rapid multiple sequence alignment based on fast Fourier transform. *Nucleic Acids Research*, *30*(14), 3059–3066. http://doi.org/10.1093/nar/gkf436

Kim, J.-E., O'Sullivan, M. L., Sanchez, C. A., Hwang, M., Israel, M. A., Brennand, K., … Ghosh, A. (2011). Investigating synapse formation and function using human pluripotent stem cell-derived neurons. *Proceedings of the National Academy of Sciences*, *108*(7), 3005–3010. http://doi.org/10.1073/pnas.1007753108

Kindberg, A. A., Bendriem, R. M., Spivak, C. E., Chen, J., Handreck, A., Lupica, C. R., … Lee, C.-T. (2014). An in vitro model of human neocortical development using pluripotent stem cells: cocaine-induced cytoarchitectural alterations. *Disease Models & Mechanisms*, *7*(12), 1397–405. http://doi.org/10.1242/dmm.017251

Kirkwood, T., Price, J., & Grove, E. (1992). The dispersion of neuronal clones across the cerebral cortex. *Science*, *258*(5080).

Kirwan, P., Turner-Bridger, B., Peter, M., Momoh, A., Arambepola, D., Robinson, H. P. C., & Livesey, F. J. (2015). Development and function of human cerebral cortex neural networks from pluripotent stem cells in vitro. *Development*, *142*(18), 3178–3187. http://doi.org/10.1242/dev.123851

Kohwi, M., & Doe, C. Q. (2013). Temporal fate specification and neural progenitor competence during development. *Nature Reviews Neuroscience*, *14*(12), 823–838. http://doi.org/10.1038/nrn3618

Kolasinski, J., Takahashi, E., Stevens, A. A., Benner, T., Fischl, B., Zöllei, L., & Grant, P. E. (2013). Radial and tangential neuronal migration pathways in the human fetal brain: Anatomically distinct patterns of diffusion MRI coherence. *NeuroImage*, *79*, 412–422. http://doi.org/10.1016/j.neuroimage.2013.04.125

Kornack, D. R., & Rakic, P. (1995). Radial and horizontal deployment of clonally related cells in the primate neocortex: relationship to distinct mitotic lineages. *Neuron*, *15*(2), 311–21. Retrieved from http://www.ncbi.nlm.nih.gov/pubmed/7646888

Kosodo, Y., Toida, K., Dubreuil, V., Alexandre, P., Schenk, J., Kiyokage, E., … Huttner, W. B. (2008). Cytokinesis of neuroepithelial cells can divide their basal process before anaphase. *The EMBO Journal*, *27*(23), 3151–63. http://doi.org/10.1038/emboj.2008.227

Kowalczyk, T., Pontious, A., Englund, C., Daza, R., Bedogni, F., Hodge, R., … Hevner, R. (2009). Intermediate Neuronal Progenitors (Basal Progenitors) Produce Pyramidal–Projection Neurons for All Layers of Cerebral Cortex. *Cerebral Cortex*, *19*(10), 2439–2450. http://doi.org/doi: 10.1093/cercor/bhn260

Kriegstein, A., & Alvarez-Buylla, A. (2009). The glial nature of embryonic and adult neural stem cells. *Annual Review of Neuroscience*, *32*, 149–84. http://doi.org/10.1146/annurev.neuro.051508.135600

Krzymowski, T., & Stefańczyk-Krzymowska, S. (2012). Advances in understanding the physiological mechanism of maternal immune tolerance to the embryo. *Reproductive Biology*, *12*(3), 265–270. http://doi.org/10.1016/j.repbio.2012.10.004

Lake, B. B., Ai, R., Kaeser, G. E., Salathia, N. S., Yung, Y. C., Liu, R., … Zhang, K. (2016). Neuronal subtypes and diversity revealed by single-nucleus RNA sequencing of the human brain. *Science*, *352*(6293), 1586–1590. http://doi.org/10.1126/science.aaf1204

Lam, R. S., Töpfer, F. M., Wood, P. G., Busskamp, V., Bamberg, E., & Wernig, M. (2017). Functional Maturation of Human Stem Cell-Derived Neurons in Long-Term Cultures. *PLOS ONE*, *12*(1), e0169506. http://doi.org/10.1371/journal.pone.0169506

LaMonica, B. E., Lui, J. H., Hansen, D. V, & Kriegstein, A. R. (2013). Mitotic spindle orientation predicts outer radial glial cell generation in human neocortex. *Nature Communications*, *4*, 1665. http://doi.org/10.1038/ncomms2647

Lee, J. H., Zhang, J., Wei, L., & Yu, S. P. (2015). Neurodevelopmental implications of the general anesthesia in neonate and infants. *Experimental Neurology*, *272*, 50–60. http://doi.org/10.1016/j.expneurol.2015.03.028

Lefebvre, J., Kostadinov, D., Chen, W., Maniatis, T., & Sanes, J. (2012). Protocadherins mediate dendritic self-avoidance in the mammalian nervous system. *Nature*, *488*(7412), 517–521. http://doi.org/doi: 10.1038/nature11305

Lefebvre, J., Zhang, Y., Meister, M., Wang, X., & Sanes, J. (2008). gamma-Protocadherins regulate neuronal survival but are dispensable for circuit formation in retina. *Development (Cambridge, England)*, *135*(24), 4141–4151. http://doi.org/doi: 10.1242/dev.027912

Leung, K. K., Lai, A., & Wu, A. (2007). A randomised controlled trial of the electric heating pad vs forced-air warming for preventing hypothermia during laparotomy. *Anaesthesia*, *62*(6), 605–608. http://doi.org/10.1111/j.1365-2044.2007.05021.x

Li, Y., Lu, H., Cheng, P., Ge, S., Xu, H., Shi, S.-H., & Dan, Y. (2012). Clonally related visual cortical neurons show similar stimulus feature selectivity. *Nature*, *486*(7401), 118–21. http://doi.org/10.1038/nature11110

Lo Turco, J., Manent, J. B., & Sidiqi, F. (2009). New and improved tools for in utero electroporation studies of developing cerebral cortex. *Cerebral Cortex*, *19*(SUPPL. 1), i120-5. http://doi.org/10.1093/cercor/bhp033

Lodato, S., & Arlotta, P. (2015). Generating Neuronal Diversity in the Mammalian Cerebral Cortex. *Annual Review of Cell and Developmental Biology*, *31*(1), 699–720. http://doi.org/10.1146/annurev-cellbio-100814-125353

Loulier, K., Barry, R., Mahou, P., Franc, Y. Le, Supatto, W., Matho, K. S., … Livet, J. (2014). Multiplex Cell and Lineage Tracking with Combinatorial Labels. *Neuron*, *81*(3), 505–520. http://doi.org/10.1016/j.neuron.2013.12.016

Lukaszewicz, A., Savatier, P., Cortay, V., Giroud, P., Huissoud, C., Berland, M., … Dehay, C. (2005). G1 Phase Regulation, Area-Specific Cell Cycle Control, and

Cytoarchitectonics in the Primate Cortex. *Neuron*, *47*(3), 353–364. http://doi.org/10.1016/j.neuron.2005.06.032

Luskin, M. B., Pearlman, a L., & Sanes, J. R. (1988). Cell lineage in the cerebral cortex of the mouse studied in vivo and in vitro with a recombinant retrovirus. *Neuron*, *1*(8), 635–47. Retrieved from http://www.ncbi.nlm.nih.gov/pubmed/3272182

Luskin, M., Parnavelas, J., & Barfield, J. (1993). Neurons, astrocytes, and oligodendrocytes of the rat cerebral cortex originate from separate progenitor cells - an ultrastructural analysis of clonally related cells. *J NEUROSCI , 13 (4) 1730 - 1750. (1993)*.

Ma, T., Wang, C., Wang, L., Zhou, X., Tian, M., Zhang, Q., … Yang, Z. (2013). Subcortical origins of human and monkey neocortical interneurons. *Nature Neuroscience*, *16*(11), 1588–97. http://doi.org/10.1038/nn.3536

MacVicar, B. A., & Dudek, F. E. (1981). Electrotonic coupling between pyramidal cells: a direct demonstration in rat hippocampal slices. *Science*, *213*(4509), 782–785. Retrieved from http://www.ncbi.nlm.nih.gov/entrez/query.fcgi?cmd=Retrieve&db=PubMed&dopt=Citation&list_uids=6266013

Madisen, L., Mao, T., Koch, H., Zhuo, J., Berenyi, A., Fujisawa, S., … Zeng, H. (2012). A toolbox of Cre-dependent optogenetic transgenic mice for light-induced activation and silencing. *Nature Neuroscience*, *15*(5), 793–802. http://doi.org/10.1038/nn.3078

Malatesta, P., Hack, M. A., Hartfuss, E., Kettenmann, H., Klinkert, W., Kirchhoff, F., & Götz, M. (2003). Neuronal or Glial Progeny: Regional Differences in Radial Glia Fate. *Neuron*, *37*(5), 751–764. http://doi.org/10.1016/S0896-6273(03)00116-8

Malatesta, P., Hartfuss, E., & Götz, M. (2000). Isolation of radial glial cells by fluorescent-activated cell sorting reveals a neuronal lineage. *Development (Cambridge, England)*, *127*(24), 5253–63. Retrieved from http://www.ncbi.nlm.nih.gov/pubmed/11076748

Malmersjö, S., Rebellato, P., Smedler, E., Planert, H., Kanatani, S., Liste, I., … Uhlén, P. (2013). Neural progenitors organize in small-world networks to promote cell proliferation. *Proceedings of the National Academy of Sciences*, *110*(16), E1524--E1532. http://doi.org/10.1073/pnas.1220179110

Mariani, J., Simonini, M. V., Palejev, D., Tomasini, L., Coppola, G., Szekely, A. M., … Vaccarino, F. M. (2012). Modeling human cortical development in vitro using induced pluripotent stem cells. *Proceedings of the National Academy of Sciences of the United States of America*, *109*(31), 12770–5. http://doi.org/10.1073/pnas.1202944109

Marín, O., & Müller, U. (2014, June). Lineage origins of GABAergic versus glutamatergic neurons in the neocortex. *Current Opinion in Neurobiology*. NIH Public Access. http://doi.org/10.1016/j.conb.2014.01.015

Martínez-Cerdeño, V., Cunningham, C. L., Camacho, J., Antczak, J. L., Prakash, A. N., Cziep, M. E., … Noctor, S. C. (2012). Comparative analysis of the subventricular zone in rat, ferret and macaque: Evidence for an outer subventricular zone in rodents. *PLoS ONE*, *7*(1). http://doi.org/10.1371/journal.pone.0030178

Martínez-Cerdeño, V., Noctor, S. C., & Kriegstein, A. R. (2006). The role of intermediate progenitor cells in the evolutionary expansion of the cerebral cortex. *Cerebral Cortex (New York, N.Y. : 1991)*, *16 Suppl 1*, i152-61. http://doi.org/10.1093/cercor/bhk017

Mayer, C., Bandler, R. C., & Fishell, G. (2016). *Lineage Is a Poor Predictor of*

Interneuron Positioning within the Forebrain. *Neuron* (Vol. 92).

Mayer, C., Jaglin, X., Cobbs, L., Bandler, R., Streicher, C., Cepko, C., … Fishell, G. (2015). Clonally Related Forebrain Interneurons Disperse Broadly across Both Functional Areas and Structural Boundaries. *Neuron*, *87*(5), 989–998. http://doi.org/doi: 10.1016/j.neuron.2015.07.011

McCarthy, M., Turnbull, D. H., Walsh, C. A., & Fishell, G. (2001). Telencephalic neural progenitors appear to be restricted to regional and glial fates before the onset of neurogenesis. *The Journal of Neuroscience*, *21*(17), 6772–6781. http://doi.org/21/17/6772 [pii]

McKenna, A., Findlay, G. M., Gagnon, J. A., Horwitz, M. S., Schier, A. F., & Shendure, J. (2016). Whole-organism lineage tracing by combinatorial and cumulative genome editing. *Science*, *353*(6298), aaf7907-aaf7907. http://doi.org/10.1126/science.aaf7907

Meijering, E., Jacob, M., Sarria, J.-C. F., Steiner, P., Hirling, H., & Unser, M. (2004). Design and validation of a tool for neurite tracing and analysis in fluorescence microscopy images. *Cytometry*, *58A*(2), 167–176. http://doi.org/10.1002/cyto.a.20022

Miller, D. G., Adam, M. A., & Miller, A. D. (1990). Gene transfer by retrovirus vectors occurs only in cells that are actively replicating at the time of infection. *Molecular and Cellular Biology*, *10*(8), 4239–42. Retrieved from http://www.ncbi.nlm.nih.gov/pubmed/2370865

Miller, K. D. (2016). Canonical computations of cerebral cortex. *Current Opinion in Neurobiology*. http://doi.org/10.1016/j.conb.2016.01.008

Mione, M. C., Cavanagh, J. F. R., Harris, B., & Parnavelas, J. G. (1997). Cell fate specification and symmetrical/asymmetrical divisions in the developing cerebral cortex. *Journal of Neuroscience*, *17*(6), 2018–2029.

Mione, M. C., Danevic, C., Boardman, P., Harris, B., & Parnavelas, J. G. (1994). Lineage analysis reveals neurotransmitter (GABA or glutamate) but not calcium-binding protein homogeneity in clonally related cortical neurons. *The Journal of Neuroscience : The Official Journal of the Society for Neuroscience*, *14*(1), 107–123.

Mishchenko, Y. (2010). On optical detection of densely labeled synapses in neuropil and mapping connectivity with combinatorially multiplexed fluorescent synaptic markers. *PLoS ONE*, *5*(1). http://doi.org/10.1371/journal.pone.0008853

Molnár, Z., & Clowry, G. (2012). Cerebral cortical development in rodents and primates. *Progress in Brain Research*, *195*, 45–70. http://doi.org/10.1016/B978-0-444-53860-4.00003-9

Molyneaux, B. J., Goff, L. A., Brettler, A. C., Chen, H. H., Brown, J. R., Hrvatin, S., … Arlotta, P. (2015). DeCoN: Genome-wide analysis of invivo transcriptional dynamics during pyramidal neuron fate selection in neocortex. *Neuron*, *85*(2), 275–288. http://doi.org/10.1016/j.neuron.2014.12.024

Montiel, J. F., Vasistha, N. A., Garcia-Moreno, F., & Molnár, Z. (2016). From sauropsids to mammals and back: New approaches to comparative cortical development. *The Journal of Comparative Neurology*, *524*(3), 630–45. http://doi.org/10.1002/cne.23871

Morrison, M., Klein, C., Clemann, N., Collier, D. A., Hardy, J., Heisserer, B., … Kaye, J. (2015). StemBANCC: Governing Access to Material and Data in a Large Stem Cell Research Consortium. *Stem Cell Reviews*, *11*(5), 681–7. http://doi.org/10.1007/s12015-015-9599-3

Mudge, M., & Hughes, L. E. (1985). Incisional hernia: a 10 year prospective study of incidence and attitudes. *The British Journal of Surgery*. http://doi.org/10.1002/bjs.1800720127

Muldal, A. M. (2016). *The impact of visual experience and lineage relationships on the development of neuronal tuning properties within the Xenopus optic tectum*.

Muldal, A. M., Lillicrap, T. P., Richards, B. A., & Akerman, C. J. (2014). Clonal relationships impact neuronal tuning within a phylogenetically ancient vertebrate brain structure. *Current Biology : CB*, *24*(16), 1929–33. http://doi.org/10.1016/j.cub.2014.07.015

Nicoludis, J., Vogt, B., Green, A., Schärfe, C., Marks, D., & Gaudet, R. (2016). Antiparallel protocadherin homodimers use distinct affinity- and specificity-mediating regions in cadherin repeats 1-4. *eLife*, *5*. http://doi.org/doi: 10.7554/elife.18449

NIH Blueprint. (2011). Cre driver mice: A versatile resource for studying brain circuit development. Retrieved from http://www.neuroscienceblueprint.nih.gov/CRE_driver_mice.htm

Noctor, S. C., Flint, A. C., Weissman, T. A., Dammerman, R. S., & Kriegstein, A. R. (2001). Neurons derived from radial glial cells establish radial units in neocortex. *Nature*, *409*(6821), 714–720. http://doi.org/10.1038/35055553

Noctor, S. C., Martínez-Cerdeño, V., Ivic, L., & Kriegstein, A. R. (2004). Cortical neurons arise in symmetric and asymmetric division zones and migrate through specific phases. *Nature Neuroscience*, *7*(2), 136–44. http://doi.org/10.1038/nn1172

Noctor, S. C., Martínez-Cerdeño, V., & Kriegstein, A. R. (2008). Distinct behaviors of neural stem and progenitor cells underlie cortical neurogenesis. *Journal of Comparative Neurology*, *508*(1), 28–44. http://doi.org/10.1002/cne.21669

Nowakowski, T. J., Pollen, A. A., Sandoval-Espinosa, C., & Kriegstein, A. R. (2016). Transformation of the Radial Glia Scaffold Demarcates Two Stages of Human Cerebral Cortex Development. *Neuron*, *91*(6), 1219–1227. http://doi.org/10.1016/j.neuron.2016.09.005

Ohtsuki, G., Nishiyama, M., Yoshida, T., Murakami, T., Histed, M., Lois, C., & Ohki, K. (2012). Similarity of visual selectivity among clonally related neurons in visual cortex. *Neuron*, *75*(1), 65–72. http://doi.org/10.1016/j.neuron.2012.05.023

Onafuwa-Nuga, A. a, King, S. R., & Telesnitsky, A. (2005). Nonrandom packaging of host RNAs in moloney murine leukemia virus. *Journal of Virology*, *79*(21), 13528–37. http://doi.org/10.1128/JVI.79.21.13528-13537.2005

Ostrem, B., Di Lullo, E., & Kriegstein, A. (2017). oRGs and mitotic somal translocation — a role in development and disease. *Current Opinion in Neurobiology*, *42*, 61–67. http://doi.org/10.1016/j.conb.2016.11.007

Ostrem, B., Lui, J., Gertz, C., & Kriegstein, A. (2014). Control of Outer Radial Glial Stem Cell Mitosis in the Human Brain. *Cell Reports*, *8*(3), 656–664. http://doi.org/doi: 10.1016/j.celrep.2014.06.058

Otani, T., Marchetto, M. C., Gage, F. H., Simons, B. D., & Livesey, F. J. (2016). 2D and 3D Stem Cell Models of Primate Cortical Development Identify Species-Specific Differences in Progenitor Behavior Contributing to Brain Size. *Cell Stem Cell*, *18*(4), 467–480. http://doi.org/10.1016/j.stem.2016.03.003

Palanisamy, A. (2012). Maternal anesthesia and fetal neurodevelopment. *International Journal of Obstetric Anesthesia*, *21*(2), 152–162. http://doi.org/doi: 10.1016/j.ijoa.2012.01.005

Parker, J. M., Austin, J., Wilkerson, J., & Carbone, L. (2011). Effects of multimodal analgesia on the success of mouse embryo transfer surgery. *Journal of the American Association for Laboratory Animal Science : JAALAS*, *50*(4), 466–70. Retrieved from http://www.ncbi.nlm.nih.gov/pubmed/21838973

Peikon, I. D., Gizatullina, D. I., & Zador, A. M. (2014). In vivo generation of DNA sequence diversity for cellular barcoding. *Nucleic Acids Research*, *42*(16), 1–10. http://doi.org/10.1093/nar/gku604

Pierfelice, T., & Gaiano, N. (2010). Ultrasound-Guided Microinjection into the Mouse Forebrain In Utero at E9.5. *Journal of Visualized Experiments*, (45). http://doi.org/doi: 10.3791/2047

Pinkney, T. D., Calvert, M., Bartlett, D. C., Gheorghe, A., Redman, V., Dowswell, G., … Morton, D. (2013). Impact of wound edge protection devices on surgical site infection after laparotomy: multicentre randomised controlled trial (ROSSINI Trial). *BMJ*, *347*.

Pollen, A. A., Nowakowski, T. J., Shuga, J., Wang, X., Leyrat, A. A., Lui, J. H., … West, J. A. A. (2014). Low-coverage single-cell mRNA sequencing reveals cellular heterogeneity and activated signaling pathways in developing cerebral cortex. *Nature Biotechnology*, *32*(10), 1053–8. http://doi.org/10.1038/nbt.2967

Pollen, A., Nowakowski, T., Chen, J., Retallack, H., Sandoval-Espinosa, C., Nicholas, C., … Kriegstein, A. (2015). Molecular Identity of Human Outer Radial Glia during Cortical Development. *Cell*, *163*(1), 55–67. http://doi.org/doi: 10.1016/j.cell.2015.09.004

Polymeneas, G., Theodosopoulos, T., Stamatiadis, A., & Kourias, E. (2001). A comparative study of postoperative adhesion formation after laparoscopic vs open cholecystectomy. *Surgical Endoscopy*, *15*(1), 41–43. Retrieved from citeulike-article-id:14178270

Poulin, J.-F., Tasic, B., Hjerling-Leffler, J., Trimarchi, J. M., & Awatramani, R. (2016). Disentangling neural cell diversity using single-cell transcriptomics. *Nature Neuroscience*, *19*(9), 1131–1141. http://doi.org/10.1038/nn.4366

Price, J., & Thurlow, L. (1988). Cell lineage in the rat cerebral cortex: a study using retroviral-mediated gene transfer. *Development (Cambridge, England)*, *104*(3), 473–82. Retrieved from http://www.ncbi.nlm.nih.gov/pubmed/3151483

Price, J., Turner, D., & Cepko, C. (1987). Lineage analysis in the vertebrate nervous system by retrovirus-mediated gene transfer. *Proceedings of the National Academy of Sciences of the United States of America*, *84*(1), 156–60. http://doi.org/10.1073/pnas.84.1.156

Punzo, C., & Cepko, C. L. (2008). Ultrasound-guided in utero injections allow studies of the development and function of the eye. *Developmental Dynamics : An Official Publication of the American Association of Anatomists*, *237*(4), 1034–42. http://doi.org/10.1002/dvdy.21500

Qi, Y., Zhang, X.-J., Renier, N., Wu, Z., Atkin, T., Sun, Z., … Studer, L. (2017). Combined small-molecule inhibition accelerates the derivation of functional cortical neurons from human pluripotent stem cells. *Nature Biotechnology*, *35*(2), 154–163. http://doi.org/10.1038/nbt.3777

Rakic, P. (1988). Specification of Cerebral Cortical Areas. *Science*, *241*(4862), 170–176.

Rakic, P. (2009). Evolution of the neocortex: a perspective from developmental biology. *Nature Reviews. Neuroscience*, *10*(10), 724–35. http://doi.org/10.1038/nrn2719

Ramon y Cajal, S. (1909). *Histologie du Systeme Nerveux de l'Homme et des*

Vertebres. Maloine, Paris: 1911. chap. II. *Demography* (Vol. v.1). http://doi.org/10.5962/bhl.title.48637

Rash, B. G., & Grove, E. A. (2006). Area and layer patterning in the developing cerebral cortex. *Current Opinion in Neurobiology*, *16*(1), 25–34. http://doi.org/10.1016/j.conb.2006.01.004

Reid, C. B., & Walsh, C. a. (2002). Evidence of common progenitors and patterns of dispersion in rat striatum and cerebral cortex. *The Journal of Neuroscience : The Official Journal of the Society for Neuroscience*, *22*(10), 4002–4014. http://doi.org/20026368

Reillo, I., de Juan Romero, C., Garcia-Cabezas, M. A., & Borrell, V. (2011). A Role for Intermediate Radial Glia in the Tangential Expansion of the Mammalian Cerebral Cortex. *Cerebral Cortex*, *21*(7), 1674–1694. http://doi.org/10.1093/cercor/bhq238

Rembert, M. S., Smith, J. A., & Hosgood, G. (2004). A comparison of a forced-air warming system to traditional thermal support for rodent microenvironments. *Laboratory Animals*, *38*(1), 55–63. http://doi.org/10.1258/00236770460734407

Riou, J.-P. A., Cohen, J. R., & Johnson, H. (1992). Factors influencing wound dehiscence. *The American Journal of Surgery*, *163*(3), 324–330. http://doi.org/10.1016/0002-9610(92)90014-I

Roe, T., Reynolds, T. C., Yu, G., & Brown, P. O. (1993). Integration of murine leukemia virus DNA depends on mitosis. *The EMBO Journal*, *12*(5), 2099–2108.

Rulli, S. J., Hibbert, C. S., Mirro, J., Pederson, T., Biswal, S., & Rein, A. (2007). Selective and Nonselective Packaging of Cellular RNAs in Retrovirus Particles. *Journal of Virology*, *81*(12), 6623–6631. http://doi.org/10.1128/JVI.02833-06

Sagi, H. C., Papp, S., & DiPasquale, T. (2008). The effect of suture pattern and tension on cutaneous blood flow as assessed by laser Doppler flowmetry in a pig model. *Journal of Orthopaedic Trauma*, *22*(3), 171–175. http://doi.org/10.1097/BOT.0b013e318169074c

Saito, T. (2006). In vivo electroporation in the embryonic mouse central nervous system. *Nature Protocols*, *1*(3), 1552–1558. http://doi.org/doi: 10.1038/nprot.2006.276

Saito, T., & Nakatsuji, N. (2001). Efficient Gene Transfer into the Embryonic Mouse Brain Using in Vivo Electroporation. *Developmental Biology*, *240*(1), 237–246. http://doi.org/10.1006/dbio.2001.0439

Sanes, J. R. (1989). Analysing cell lineage with a recombinant retrovirus. *Trends in Neurosciences*. http://doi.org/10.1016/0166-2236(89)90152-5

Schindelin, J., Arganda-Carreras, I., Frise, E., Kaynig, V., Longair, M., Pietzsch, T., … Cardona, A. (2012). Fiji: an open-source platform for biological-image analysis. *Nature Methods*, *9*(7), 676–82. http://doi.org/10.1038/nmeth.2019

Schreiner, D., & Weiner, J. A. (2010). Combinatorial homophilic interaction between γ-protocadherin multimers greatly expands the molecular diversity of cell adhesion. *Proceedings of the National Academy of Sciences of the United States of America*, *107*(33), 14893–14898. http://doi.org/doi: 10.1073/pnas.1004526107

Schütz, M., Auth, T., Gehrt, A., Bosen, F., Körber, I., Strenzke, N., … Willecke, K. (2011). The connexin26 S17F mouse mutant represents a model for the human hereditary keratitis-ichthyosis-deafness syndrome. *Human Molecular Genetics*, *20*(1), 28–39. http://doi.org/10.1093/hmg/ddq429

Seamon, M. J., Wobb, J., Gaughan, J. P., Kulp, H., Kamel, I., & Dempsey, D. T. (2012, April). The effects of intraoperative hypothermia on surgical site infection: an analysis of 524 trauma laparotomies. *Annals of Surgery*.

http://doi.org/10.1097/SLA.0b013e31824b7e35

Shen, Q., Wang, Y., Dimos, J. T., Fasano, C. A., Phoenix, T. N., Lemischka, I. R., … Temple, S. (2006). The timing of cortical neurogenesis is encoded within lineages of individual progenitor cells. *Nature Neuroscience*, *9*(6), 743–751. http://doi.org/doi: 10.1038/nn1694

Shi, Y., Kirwan, P., & Livesey, F. (2012). Directed differentiation of human pluripotent stem cells to cerebral cortex neurons and neural networks. *Nat. Protocols*, *7*(10), 1836–1846. http://doi.org/doi: 10.1038/nprot.2012.116

Shi, Y., Kirwan, P., Smith, J., Robinson, H., & Livesey, F. (2012). Human cerebral cortex development from pluripotent stem cells to functional excitatory synapses. *Nature Neuroscience*, *15*(3), 477–486. http://doi.org/doi: 10.1038/nn.3041

Shimogori, T., & Ogawa, M. (2008). Gene application with *in utero* electroporation in mouse embryonic brain. *Development, Growth & Differentiation*, *50*(6), 499–506. http://doi.org/10.1111/j.1440-169X.2008.01045.x

Shimshek, D. R., Kim, J., Hübner, M. R., Spergel, D. J., Buchholz, F., Casanova, E., … Sprengel, R. (2002). Codon-improved Cre recombinase (iCre) expression in the mouse. *Genesis*, *32*(1), 19–26. http://doi.org/doi: 10.1002/gene.10023

Shitamukai, A., Konno, D., & Matsuzaki, F. (2011). Oblique radial glial divisions in the developing mouse neocortex induce self-renewing progenitors outside the germinal zone that resemble primate outer subventricular zone progenitors. *J Neurosci*, *31*(10), 3683–95. http://doi.org/10.1523/JNEUROSCI.4773-10.2011

Siddiqi, F., Chen, F., Aron, A. W., Fiondella, C. G., Patel, K., & LoTurco, J. J. (2014). Fate mapping by piggybac transposase reveals that neocortical glast+ progenitors generate more astrocytes than nestin+ progenitors in rat neocortex. *Cerebral Cortex*, *24*(2), 508–520. http://doi.org/10.1093/cercor/bhs332

Silver, D. P., & Livingston, D. M. (2001). Self-Excising Retroviral Vectors Encoding the Cre Recombinase Overcome Cre-Mediated Cellular Toxicity. *Molecular Cell*, *8*(1), 233–243. http://doi.org/doi: 10.1016/s1097-2765(01)00295-7

Simmen, H. P., Heinzelmann, M., & Largiadèr, F. (2008). Peritonitis: Classification and Causes. *Digestive Surgery*, *13*(4–5), 381–383. http://doi.org/10.1159/000172468

Smart, I. H. M., Dehay, C., Giroud, P., Berland, M., & Kennedy, H. (2002). Unique Morphological Features of the Proliferative Zones and Postmitotic Compartments of the Neural Epithelium Giving Rise to Striate and Extrastriate Cortex in the Monkey. *Cerebral Cortex*, *12*(1), 37–53. http://doi.org/10.1093/cercor/12.1.37

Smith, S. E. P., Li, J., Garbett, K., Mirnics, K., & Patterson, P. H. (2007). Maternal Immune Activation Alters Fetal Brain Development through Interleukin-6. *The Journal of Neuroscience* , *27*(40), 10695–10702. http://doi.org/10.1523/JNEUROSCI.2178-07.2007

Stancik, E. K., Navarro-Quiroga, I., Sellke, R., & Haydar, T. F. (2010). Heterogeneity in ventricular zone neural precursors contributes to neuronal fate diversity in the postnatal neocortex. *The Journal of Neuroscience : The Official Journal of the Society for Neuroscience*, *30*(20), 7028–36. http://doi.org/10.1523/JNEUROSCI.6131-09.2010

Stolp, H. B. (2013). Neuropoietic cytokines in normal brain development and neurodevelopmental disorders. *Molecular and Cellular Neuroscience*, *53*(0), 63–68. http://doi.org/http://dx.doi.org/10.1016/j.mcn.2012.08.009

Stolp, H. B., Turnquist, C., Dziegielewska, K. M., Saunders, N. R., Anthony, D. C., & Molnár, Z. (2011). Reduced ventricular proliferation in the foetal cortex following

maternal inflammation in the mouse. *Brain : A Journal of Neurology*, *134*(Pt 11), 3236–48. http://doi.org/10.1093/brain/awr237

Stubbs, D., DeProto, J., Nie, K., Englund, C., Mahmud, I., Hevner, R., & Molnar, Z. (2009). Neurovascular Congruence during Cerebral Cortical Development. *Cerebral Cortex*, *19*(suppl 1), i32–i41. http://doi.org/10.1093/cercor/bhp040

Su, X., Chen, J.-J., Liu, L.-Y., Huang, Q., Zhang, L.-Z., Li, X.-Y., … Yu, Y.-C. (2017). Neonatal CX26 removal impairs neocortical development and leads to elevated anxiety. *Proceedings of the National Academy of Sciences of the United States of America*, 201613237. http://doi.org/10.1073/pnas.1613237114

Suo, L., Lu, H., Ying, G., Capecchi, M. R., & Wu, Q. (2012). Protocadherin clusters and cell adhesion kinase regulate dendrite complexity through Rho GTPase. *Journal of Molecular Cell Biology*, *4*(6), 362–376. http://doi.org/doi: 10.1093/jmcb/mjs034

Sussel, L., Marin, O., Kimura, S., & Rubenstein, J. L. (1999). Loss of Nkx2.1 homeobox gene function results in a ventral to dorsal molecular respecification within the basal telencephalon: evidence for a transformation of the pallidum into the striatum. *Development*, *126*(15), 3359–3370. http://doi.org/10393115

Svensson, V., Natarajan, K. N., Ly, L.-H., Miragaia, R. J., Labalette, C., Macaulay, I. C., … Teichmann, S. A. (2017). Power analysis of single-cell RNA-sequencing experiments. *Nature Methods*. http://doi.org/10.1038/nmeth.4220

Swayne, L. A., & Bennett, S. A. L. (2016). Connexins and pannexins in neuronal development and adult neurogenesis. *BMC Cell Biology*, *17 Suppl 1*(Suppl 1), 10. http://doi.org/10.1186/s12860-016-0089-5

Sylvestre, A., Wilson, J., & Hare, J. (2002). A comparison of 2 different suture patterns for skin closure of canine ovariohysterectomy. *The Canadian Veterinary Journal = La Revue Veterinaire Canadienne*, *43*(9), 699–702. Retrieved from http://www.ncbi.nlm.nih.gov/pubmed/12240527

Szczurkowska, J., Cwetsch, A., dal Maschio, M., Ghezzi, D., Ratto, G., & Cancedda, L. (2016). Targeted in vivo genetic manipulation of the mouse or rat brain by in utero electroporation with a triple-electrode probe. *Nature Protocols*, *11*(3), 399–412. http://doi.org/doi: 10.1038/nprot.2016.014

Talan, M. (1984). Body temperature of C57BL/6J mice with age. *Experimental Gerontology*, *19*(1), 25–29. http://doi.org/10.1016/0531-5565(84)90028-7

Tamamaki, N., Nakamura, K., Okamoto, K., & Kaneko, T. (2001). Radial glia is a progenitor of neocortical neurons in the developing cerebral cortex. *Neuroscience Research*, *41*(1), 51–60. Retrieved from http://www.ncbi.nlm.nih.gov/pubmed/11535293

Tan, X., & Shi, S.-H. (2013). Neocortical neurogenesis and neuronal migration. *Wiley Interdisciplinary Reviews. Developmental Biology*, *2*(4), 443–59. http://doi.org/10.1002/wdev.88

Tashiro, K., Teissier, A., Kobayashi, N., Nakanishi, A., Sasaki, T., Yan, K., … Okada, N. (2011). A mammalian conserved element derived from SINE displays enhancer properties recapitulating Satb2 expression in early-born callosal projection neurons. *PLoS ONE*, *6*(12). http://doi.org/10.1371/journal.pone.0028497

Tasic, B., Menon, V., Nguyen, T. N., Kim, T. K., Jarsky, T., Yao, Z., … Zeng, H. (2016). Adult mouse cortical cell taxonomy revealed by single cell transcriptomics. *Nature Neuroscience*, *19*(2), 335–346. http://doi.org/10.1038/nn.4216

Taylor, D. K. (2007). Study of two devices used to maintain normothermia in rats and mice during general anesthesia. *Journal of the American Association for Laboratory*

Animal Science : JAALAS, *46*(5), 37–41.

Telley, L., Govindan, S., Prados, J., Stevant, I., Nef, S., Dermitzakis, E., … Jabaudon, D. (2016). Sequential transcriptional waves direct the differentiation of newborn neurons in the mouse neocortex. *Science*, *351*(6280), 1443–6. http://doi.org/10.1126/science.aad8361

The Jackson Laboratory. (2016a). MOUSE STRAIN DATASHEET - 025524 B6J.B6N(Cg)-Cx3cr1tm1.1(cre)Jung/J. Retrieved November 14, 2016, from https://www.jax.org/strain/000664

The Jackson Laboratory. (2016b). MPD - Phenotype strain survey data listing - reproduction. Retrieved November 14, 2016, from http://phenome.jax.org/db/q?rtn=meas/catlister&req=Creproduction&reqstrainid=7

Thu, C. A., Chen, W., Rubinstein, R., Chevee, M., Wolcott, H., Felsovalyi, K., … Maniatis, T. (2014). Single-cell identity generated by combinatorial homophilic interactions between α, β, and γ protocadherins. *Cell*, *158*(5), 1045–1059. http://doi.org/doi: 10.1016/j.cell.2014.07.012

Toledo-Rodriguez, M., & Markram, H. (2007). Single-Cell RT–PCR, a Technique to Decipher the Electrical, Anatomical, and Genetic Determinants of Neuronal Diversity. In P. Molnar & J. Hickman (Eds.), *Patch-Clamp Methods and Protocols SE - Methods in Molecular Biology™* (Vol. 403, pp. 123–139). Humana Press. http://doi.org/doi: 10.1007/978-1-59745-529-9_8

Toma, K., & Hanashima, C. (2015). Switching modes in corticogenesis: mechanisms of neuronal subtype transitions and integration in the cerebral cortex. *Frontiers in Neuroscience*, *9*(August), 274. http://doi.org/10.3389/fnins.2015.00274

Toyoda, S., Kawaguchi, M., Kobayashi, T., Tarusawa, E., Toyama, T., Okano, M., … Yagi, T. (2014). Developmental Epigenetic Modification Regulates Stochastic Expression of Clustered Protocadherin Genes, Generating Single Neuron Diversity. *Neuron*, *82*(1), 94–108. http://doi.org/doi: 10.1016/j.neuron.2014.02.005

Tsien, J. Z. (2016). Cre-lox neurogenetics: 20 years of versatile applications in brain research and counting... *Frontiers in Genetics*, *7*(FEB). http://doi.org/10.3389/fgene.2016.00019

Tsunekawa, Y., Terhune, R. K., Fujita, I., Shitamukai, A., Suetsugu, T., & Matsuzaki, F. (2016). Developing a de novo targeted knock-in method based on in utero electroporation into the mammalian brain. *Development (Cambridge, England)*, *143*(17), 3216–22. http://doi.org/10.1242/dev.136325

Turrero García, M., Mazzola, E., & Harwell, C. C. (2016). *Lineage Relationships Do Not Drive MGE/PoA-Derived Interneuron Clustering in the Brain*. *Neuron* (Vol. 92).

Tyler, W. A., & Haydar, T. F. (2013). Multiplex Genetic Fate Mapping Reveals a Novel Route of Neocortical Neurogenesis, Which Is Altered in the Ts65Dn Mouse Model of Down Syndrome. *The Journal of Neuroscience*, *33*(12), 5106–5119. http://doi.org/doi: 10.1523/jneurosci.5380-12.2013

Tyler, W. A., Medalla, M., Guillamon-Vivancos, T., Luebke, J. I., & Haydar, T. F. (2015). Neural precursor lineages specify distinct neocortical pyramidal neuron types. *J Neurosci*, *35*(15), 6142–6152. http://doi.org/10.1523/JNEUROSCI.0335-15.2015

Uhlig, C., Krause, H., Koch, T., Gama de Abreu, M., Spieth, P. M., Gargiulo, S., … Beckman, B. (2015). Anesthesia and Monitoring in Small Laboratory Mammals Used in Anesthesiology, Respiratory and Critical Care Research: A Systematic Review on the Current Reporting in Top-10 Impact Factor Ranked Journals. *PLoS ONE*, *10*(8), e0134205. http://doi.org/doi: 10.1371/journal.pone.0134205

Vasistha, N. A., García-Moreno, F., Arora, S., Cheung, A. F. P., Arnold, S. J., Robertson, E. J., & Molnár, Z. (2015). Cortical and clonal contribution of Tbr2 expressing progenitors in the developing mouse brain. *Cerebral Cortex*, *25*(10), 3290–3302. http://doi.org/10.1093/cercor/bhu125

Voigt, T. (1989). Development of glial cells in the cerebral wall of ferrets: direct tracing of their transformation from radial glia into astrocytes. *The Journal of Comparative Neurology*, *289*(1), 74–88. http://doi.org/10.1002/cne.902890106

Walantus, W., Castaneda, D., Elias, L., & Kriegstein, A. (2007). In utero intraventricular injection and electroporation of E15 mouse embryos. *Journal of Visualized Experiments : JoVE*, (6), 239. http://doi.org/10.3791/239

Walsh, C., & Cepko, C. L. (1988). Clonally related cortical cells show several migration patterns. *Science*, *241*(4871), 1342–1345. http://doi.org/doi: 10.1126/science.3137660

Walsh, C., & Cepko, C. L. (1992). Widespread Dispersion of Neuronal Clones Across Functional Regions of the Cerebral Cortex. *Science*, *255*(5043), 434–440. http://doi.org/10.1126/science.1734520

Walsh, C., & Cepko, C. L. (1993). Clonal dispersion in proliferative layers of developing cerebral cortex. *Nature*, *362*(6421), 632–635. http://doi.org/10.1038/362632a0

Walsh, C., & Reid, C. (1995). Cell lineage and patterns of migration in the developing cortex. *Ciba Foundation Symposium*, *193*, 21-40-70. http://doi.org/10.1002/9780470514795.ch2

Wang, C., & Mei, L. (2013). In Utero Electroporation in Mice. In R. Zhou & L. Mei (Eds.), *Neural Development SE - Methods in Molecular Biology* (Vol. 1018, pp. 151–163). Humana Press. http://doi.org/doi: 10.1007/978-1-62703-444-9_15

Wang, X., Tsai, J.-W., LaMonica, B., & Kriegstein, A. R. (2011). A new subtype of progenitor cell in the mouse embryonic neocortex. *Nature Neuroscience*, *14*(5), 555–61. http://doi.org/10.1038/nn.2807

Weber, P. A., Chang, H. C., Spaeth, K. E., Nitsche, J. M., & Nicholson, B. J. (2004). The permeability of gap junction channels to probes of different size is dependent on connexin composition and permeant-pore affinities. *Biophys J*, *87*(2), 958–973. http://doi.org/10.1529/biophysj.103.036350

Wegorzewska, M., Nijagal, A., Wong, C., Le, T., Lescano, N., Tang, Q., & MacKenzie, T. (2014). Fetal Intervention Increases Maternal T Cell Awareness of the Foreign Conceptus and Can Lead to Immune-Mediated Fetal Demise. *The Journal of Immunology*, *192*(4), 1938–1945. http://doi.org/doi: 10.4049/jimmunol.1302403

Weiner, J., & Jontes, J. (2013). Protocadherins, not prototypical: a complex tale of their interactions, expression, and functions. *Frontiers in Molecular Neuroscience*, *6*. http://doi.org/doi: 10.3389/fnmol.2013.00004

Woodruff, A., Xu, Q., Anderson, S. A., & Yuste, R. (2009). Depolarizing effect of neocortical chandelier neurons. *Frontiers in Neural Circuits*, *3*(October), 1–15. http://doi.org/10.3389/neuro.04.015.2009

Wu, S.-X., Goebbels, S., Nakamura, K., Nakamura, K., Kometani, K., Minato, N., … Tamamaki, N. (2005). Pyramidal neurons of upper cortical layers generated by NEX-positive progenitor cells in the subventricular zone. *Proceedings of the National Academy of Sciences*, *102*(47), 17172–17177. http://doi.org/10.1073/pnas.0508560102

Xing, L., Culbertson, E. J., Wen, Y., & Franz, M. G. (2013). Early laparotomy wound failure as the mechanism for incisional hernia formation. *Journal of Surgical*

Research, *182*(1), e35–e42. http://doi.org/10.1016/j.jss.2012.09.009

Yagi, T. (2015). Role of the Clustered Protocadherins in Promoting Neuronal Diversity and Function. In *Neural Surface Antigens: From Basic Biology Towards Biomedical Applications* (pp. 141–151). http://doi.org/10.1016/B978-0-12-800781-5.00012-8

Yang, J., Qin, G., & Chen, J. (2014). [Lentivirus-mediated shRNA interference of Cx26 suppresses epithelial mesenchymal transition and invasion of highly invasive hepatocellular carcinoma cells in vitro]. *Nan Fang Yi Ke Da Xue Xue Bao = Journal of Southern Medical University*, *34*(12), 1743–1747.

Yao, B., Christian, K. M., He, C., Jin, P., Ming, G., & Song, H. (2016). Epigenetic mechanisms in neurogenesis. *Nature Reviews. Neuroscience*, *17*(9), 537–49. http://doi.org/10.1038/nrn.2016.70

Young-Pearse, T. L., Suth, S., Luth, E. S., Sawa, A., & Selkoe, D. J. (2010). Biochemical and Functional Interaction of Disrupted-in-Schizophrenia 1 and Amyloid Precursor Protein Regulates Neuronal Migration during Mammalian Cortical Development. *Journal of Neuroscience*, *30*(31), 10431–10440. http://doi.org/10.1523/JNEUROSCI.1445-10.2010

Yu, Y.-C., Bultje, R. S., Wang, X., & Shi, S.-H. (2009). Specific synapses develop preferentially among sister excitatory neurons in the neocortex. *Nature*, *458*(7237), 501–4. http://doi.org/10.1038/nature07722

Yu, Y.-C., He, S., Chen, S., Fu, Y., Brown, K. N., Yao, X.-H., … Shi, S.-H. (2012). Preferential electrical coupling regulates neocortical lineage-dependent microcircuit assembly. *Nature*, *486*(7401), 113–7. http://doi.org/10.1038/nature10958

Yuste, R., Nelson, D. A., Rubin, W. W., & Katz, L. C. (1995). Neuronal domains in developing neocortex: Mechanisms of coactivation. *Neuron*, *14*(1), 7–17. http://doi.org/10.1016/0896-6273(95)90236-8

Zecevic, N., Chen, Y., & Filipovic, R. (2005). Contributions of cortical subventricular zone to the development of the human cerebral cortex. *The Journal of Comparative Neurology*, *491*(2), 109–122. http://doi.org/10.1002/cne.20714

Zeisel, A., Muñoz-Manchado, A. B., Codeluppi, S., Lönnerberg, P., La Manno, G., Juréus, A., … Linnarsson, S. (2015). Cell types in the mouse cortex and hippocampus revealed by single-cell RNA-seq. *Science*, *347*(6226), 1138–1142. http://doi.org/doi: 10.1126/science.aaa1934

Zhang, F., Wang, L.-P., Boyden, E. S., & Deisseroth, K. (2006). Channelrhodopsin-2 and optical control of excitable cells. *Nature Methods*, *3*(10), 785–792. http://doi.org/10.1038/nmeth936

Zhang, Y., Sloan, S. A., Clarke, L. E., Caneda, C., Plaza, C. A., Blumenthal, P. D., … Barres, B. A. (2016). Purification and Characterization of Progenitor and Mature Human Astrocytes Reveals Transcriptional and Functional Differences with Mouse. *Neuron*, *89*(1), 37–53. http://doi.org/10.1016/j.neuron.2015.11.013

Zhao, C., Teng, E. M., Summers, R. G., Ming, G.-L., & Gage, F. H. (2006). Distinct morphological stages of dentate granule neuron maturation in the adult mouse hippocampus. *The Journal of Neuroscience : The Official Journal of the Society for Neuroscience*, *26*(1), 3–11. http://doi.org/10.1523/JNEUROSCI.3648-05.2006

Zografos, G. C., Martis, K., Morris, D. L., & Anonymous. (1992). Laser Doppler flowmetry in evaluation of cutaneous wound blood flow using various suturing techniques. *Ann Surg*, *215*(3), 266–268. Retrieved from http://www.ncbi.nlm.nih.gov/htbin-post/Entrez/query?db=m&form=6&dopt=r&uid=0001531916

Zong, H., Espinosa, J. S., Su, H. H., Muzumdar, M. D., & Luo, L. (2005). Mosaic analysis with double markers in mice. *Cell*, *121*(3), 479–492. http://doi.org/10.1016/j.cell.2005.02.012

Zufferey, R., Donello, J. E., Trono, D., & Hope, T. J. (1999). Woodchuck hepatitis virus posttranscriptional regulatory element enhances expression of transgenes delivered by retroviral vectors. *J Virol*, *73*(4), 2886–2892. Retrieved from http://www.ncbi.nlm.nih.gov/pubmed/10074136%5Cnhttp://www.pubmedcentral.nih.gov/articlerender.fcgi?artid=PMC104046

Appendix 1

Protocol for *in utero* surgery

This protocol details laparotomy of the dam for *in utero* surgery. Specific manipulation of the embryos is not discussed. This protocol assumes that a single surgeon will be performing the protocol without assistance. Furthermore, this protocol assumes that a dedicated area for preparing the dam for surgery is not available, however this should be made use of if available. Surgical scrubs and a mob cap should be worn.

Equipment

Suppliers are noted in brackets where appropriate. All surgical instruments were sourced from Fine Science Tools.

General Equipment

- 1ml syringe x2
- 23G needle x 4
- 25G needles x 2
- 19G needle
- Meloxicam 5mg/ml solution for injection (Boehringer Ingelheim Vetmedica Gmbh)
- Meloxicam 1.5mg/ml oral suspension (Boehringer Ingelheim Vetmedica Gmbh)
- Buprenorphine 0.3mg/ml (Vetergesic Multidose)
- Isofluorane (Zoetis)
- Sterile water for injection
- Hartmann’s solution
- Water bath
- 15ml Falcon tube
- Sterile Pasteur pipette
- Sterile surgical gloves
- Small clippers
- Chlorhexidine (4 % w/v)
- Gauze swabs

- Cold light source
- Thermal recovery cage

Anaesthesia Equipment

- Carrier gas (100 % O_2)
- Vaporiser
- Induction chamber
- Tubing
- Coaxial tube with nose cone
- Activated charcoal scavenge (Fluosorber Filter Scavenger, Harvard Apparatus)
- Two three-way taps suitable for the anaesthetic system tubing
- Heat pad (HE002, Vet-Tech)
- Eye lubricant (e.g. carbomer: Viscotears Liquid Gel, Novartis)
- Temperature monitor with a flexible probe (MiniTemp, Vetronic)
- Lubricant for the rectal temperature probe

Surgical Kit

The surgical kit should be sterilised and kept sealed until use.

- Individually-wrapped waterproof surgical drape (Transdrape, Millpledge)
- Adson-Brown tissue forceps
- Baby Olsen Hegar needle-holders
- 5” dressing scissors
- 14.5cm blunt-ended straight Metzenbaum scissors
- 8.5cm ring forceps x2
- 6-0 polyglactin 910 suture with a swaged-on, curved, round-bodied needle (75cm)
- Tin foil (approximately an A4-sized sheet)

Preparation

Administration of analgesia

Buprenorphine and meloxicam should be administered by subcutaneous injection 30-60 minutes before the onset of analgesia in order for therapeutic levels to be achieved in the dam before surgery.

- Prepare a 1:5 dilution of meloxicam solution for injection (5mg/ml) by drawing up 0.2ml meloxicam and 0.8ml sterile water for injection into a 1ml syringe with a separate 23G needle for each solution. The bungs of the bottles should be swabbed with ethanol prior to broaching. Replace needle with a 25G needle ready for injection.
- Prepare a 1:10 dilution of 0.3mg/ml buprenorphine solution in sterile water for injection as described above.
- Perform a health check of the dam by observing her in the home cage. Pay attention to factors such as her demeanour, respiratory effort and the condition of her coat. Confirm pregnancy by abdominal palpation.
- Providing the dam is healthy and pregnant, administer buprenorphine and meloxicam by subcutaneous injection at two separate sites (dose according to **Figure 3.5 B**). Place her in a quiet area until the induction of anaesthesia.

Preparation of the surgical area

- Turn on the water bath and set to 48 ^{o}C. This should be accessible when performing surgery
- Clean the surgical area and all non-sterile equipment with 70 % ethanol
- Turn on the heat mat, set at 40 ^{o}C and cover with a disposable absorbent towel, folded over to protect the dam from direct contact with the heat source.
- Assemble and check the anaesthetic circuit using the three-way taps in such a way that the outflow of the fresh anaesthetic gas mixture and the waste gas flow to the scavenger can be directed to either the induction chamber or the nose cone. Place the nose cone onto the heat mat. If using passive scavenge ensure the scavenger is placed below the height of the induction chamber and nose cone.
- Open the 15ml Falcon tube in an aseptic manner. Broach the Hartmann's solution with the 19G needle and carefully fill the Falcon tube with Hartmann's solution. Loosely replace the lid of the Falcon tube and place it in the water bath
- Carefully open the sterile surgical pack, the surgical drape, the suture material, and the Pasteur pipette, in an aseptic manner and place next to the surgery area in such a way that it is covered over within the packaging but accessible.

- Prepare a 1 % (v/v) solution of 50ml chlorhexidine in water in a suitable container.
- Position the cold light source over the site where the mouse will be positioned.
- Line the induction chamber with absorbent towel.
- Set the thermal recovery cage to 35-37 ^{o}C and line with absorbent towel.
- Fill a non-sterile glove with warm water (approximately 37 ^{o}C) and tie closed.

Induction of anaesthesia

- Pre-fill the induction chamber with 96 % O_2, 4 % isofluorane at 2 l/min for 2-3 min. Adjust the time to the size of the induction chamber.
- Place the dam in the induction chamber and monitor for loss of the righting reflex.
- Once the right reflex is absent, transfer the dam from the induction chamber to the heat mat and place her on her back with her face in the nose cone. Ensure the three-way taps directing flow of the fresh anaesthetic gas mixture and the waste gas mixture to the scavenger are changed accordingly. Reduce the flow rate to 1 l/min and the isofluorane concentration to 1.8 %.
- The glove filled with warm water should be positioned near the mouse. Use insulation between the glove and the mouse if necessary to avoid thermal burns (**Figure 3.**1 B)
- Anaesthetic depth should be assessed by checking the pedal withdrawal or tail pinch reflexes and counting the respiratory rate. The concentration of isofluorane should be adjusted to obtain a surgical plane of anaesthesia, indicated by an absence of the tail pinch and pedal withdrawal reflexes and a respiratory rate of 60 – 80 breaths per minute.

Preparation for surgery

- Lubricant should be placed in the dam's eyes and topped up approximately every 20 minutes or as necessary.
- The rectal temperature probe should be inserted using plenty of lubricant and positioned so that it can be monitored during surgery.
- The entire abdomen should be clipped from the sternum to the pelvic brim, taking care to remove all fur without damaging the skin.
- Use swabs soaked in chlorhexidine solution to remove all fur from the surgical site, taking a fresh swab after each pass. Once no fur is evident on the swab, the surgical preparation can begin by cleaning the surgical site in an inside-out fashion

using a fresh swab soaked in chlorhexidine for each pass, prioritising the abdominal midline. This should take 4-5 min. Once the surgical site is prepared, care should be taken not to preserve asepsis.

- Repeat an assessment of the anaesthetic depth and adjust the concentration of isofluorane accordingly.
- Open the sterile surgical gloves away from the surgery area in an aseptic manner and perform a surgical scrub prior to applying the gloves.
- Unpack the surgical drape and use the dressing scissors to make a window approximately 2cm x 1cm in the centre of the drape. Position the drape over the abdominal midline approximately halfway between the sternum and the pelvic brim.
- Unpack the remainder of the surgical kit onto the sterile drape.

Surgery

- The body temperature and anaesthetic depth should be monitored through surgery. Respiratory rate can be relied on primarily to assess anaesthetic depth, and sterile foil can be used to check the pedal withdrawal reflex and make adjustments to the anaesthetic depth if necessary without breaking asepsis. The body temperature should not be allowed to drop below 35^{o}C.
- Use the tissue forceps to raise the skin in the centre of the aperture of the drape away from the body and make a small incision with the Metzenbaum scissors. Alternatively, a scalpel can be used however great care must be taken to avoid incising the underlying viscera. Extend the incision cranially and caudally to approximately 1-1.5cm, depending on the stage of embryonic development. The respiratory rate should be monitored closely for a response to pain suggestive of insufficient anaesthesia, which is indicated by a sharp increase or decrease in respiratory rate.
- Identify the linea alba from the abdominal musculature. The linea alba can be visualised as a translucent line in the midline extending in a cranio-caudal direction. Use the tissue forceps to raise the line alba away from the underlying viscera and make a small incision using the Metzenbaum scissors. As soon as the peritoneum is broached the viscera will drop away from the musculature as air enters the peritoneal cavity. Extend the incision in the linea alba until it is

approximately 1-2mm shorter than the skin incision at the cranial and caudal extent.

- Tear off a section of foil and use it to open the Falcon tube of Hartmann's solution, dedicating one side of the foil as 'dirty' and one side as 'clean'. Place the sterile Pasteur pipette in the Falcon tube in preparation.
- Use the ring forceps to explore the abdomen for the gravid uterus. Once this has been identified, gently exteriorise the uterus by gently grasping it between two embryos.
- Once one uterine horn is exteriorised the embryonic manipulation can be performed. The uterus should be lavaged regularly with warm Hartmann's solution using the Pasteur pipette to prevent desiccation.
- When all embryos in the first uterine horn have been manipulated, this can be gently replaced, beginning with the embryos nearest the ovary. The second uterine horn can then be exteriorised and the process repeated.
- Once both uterine horns have been replaced and the abdominal cavity has been lavaged with approximately 0.5ml of Hartmann's solution, the incision can be closed. This is done in two layers using polyglactin 910. Firstly, the linea alba incorporating the abdominal musculature is closed with simple interrupted or simple continuous sutures. Secondly the skin is closed using either a transdermal or intradermal pattern (see **Figure 3.7**).

Recovery

- Once the skin incision is closed, the dam should be placed in sternal recumbency and the isofluorane turned off. Oxygen delivery should be continued until the dam has regained consciousness.
- Once the dam has regained consciousness she should be placed in the thermal recovery cage and monitored closely until she begins to show signs of normal behaviour such as grooming. If this has not resumed within 30 minutes of her regaining consciousness she should be examined to establish the cause of her slow recovery. Dams should not be kept in a thermal recovery cage for more than 30 minutes. Alternatively, dams can be placed in a home cage placed half onto a heat mat, so that she has the ability to choose her location in order to self-regulate her body temperature.
- Analgesia should be provided in the recovery period according to **Figure 3.5**. Adjustments can be made on an individual basis. Dams should be monitored

closely in the 24 hours following surgery, after which twice-daily checks are sufficient for the following three days. Care should be taken to examine the surgical wound carefully.